

Response of Inhomogeneous DNA to External Twist

Wilber Lim Choon Siang

Oriel College

University of Oxford

A thesis presented for the degree of

Doctor of Philosophy

Trinity 2022

Acknowledgements

I would like to take this opportunity to express my gratitude to my supervisor, Prof. Ard Louis, for the opportunity to work on thought-provoking problems in DNA biophysics. Prof. Jonathan Doye has also been pivotal in shaping the approaches I have taken to study these problems.

I have benefited tremendously from the conversations I had with fellow DPhil students Michael Selby, Hemani Chhabra, Chak Kui Wong, Ian Seet, Shuofeng Zhang, Mehrana Raesian Nejad and Vaibhav Mohanty, as well as subject matter experts such as Prof. Achillefs Kapanidis, Prof. Julia Yeomans, Prof. Jie Yan and Prof. Johan RC van der Maarel. I am also grateful for the mentorship by Dr. Lorenzo Rovigatti and Dr. Ferdinando Randisi.

Finally, I would like to thank my parents, sister and my lovely children, Max and Gwen, for being my motivation to complete this journey.

Abstract

Studies of supercoiled DNA have typically treated DNA as a homogeneous polymer. In reality, however, DNA is highly inhomogeneous. Defects, for example, are an important source of inhomogeneities in DNA. Caused by processes that damage DNA, these defects can have strong effects on local elastic properties. In this thesis, we seek to address the question of how DNA supercoiling affects local defect properties, or, conversely, how the presence of such defects changes global supercoiled structure. Using a model of the thymine dimer (TD) —a major mutagenic photoproduct induced by UV radiation—in the oxDNA forcefield, we performed extensive molecular dynamics (MD) simulations of thymine dimer-containing double-stranded DNA (dsDNA) as a function of external twist and force. Compared to undamaged DNA, the presence of a thymine dimer lowers the supercoiling densities at which plectonemes and bubbles occur. For biologically relevant supercoiling densities and forces, thymine dimers are observed to preferentially segregate to the tips of the plectonemes, where they enhance the probability of a localized tip-bubble. This mechanism increases the probability of highly bent and denatured states at the thymine dimer site, which may facilitate repair enzyme binding. Thymine dimer-induced tip-bubbles are also observed to pin plectonemes, which may help repair enzymes to locate damage.

To understand the physics of how thymine dimers are segregated to the plectoneme tips in an extrahelical arrangement, we develop a free energy model of tip-bubble plectoneme formation. The model is capable of reproducing the major state boundaries in the force-torsion space of negatively supercoiled dsDNA, and predicting how variations in defect properties could affect the probability of plectoneme, bubble and tip-bubble formation in supercoiled dsDNA. The model is further validated by comparing its predictions with our MD simulation findings on thymine dimer-containing dsDNA, and

stress-tested using MD simulations of dsDNA that contains other types of defects, such as base pair mismatches. We also expanded our analysis to the force-torsion space of positively supercoiled dsDNA, and showed that tip-bubbles formed in positively supercoiled dsDNA bear several physical characteristics that are different from its counterpart in negatively supercoiled dsDNA.

We also seek to address, by simulations, the fundamental question of how repair proteins search and identify defects in a crowded cellular environment. To do so, we modelled a crowded intranuclear environment in bacterial cells using the twistable elastic polymer (TEP) model, introduced a DNA defect model by reducing the bending stiffness of several DNA TEP particles, and constructed an actively rotating RNA polymerase model to generate supercoils. We observe that the DNA defect is localised at the tip of a plectonemic supercoil generated by the polymerase model away from the crowded intranuclear environment. This observation strengthens our hypothesis—originally proposed based on MD simulations of a simple molecular tweezer geometry—that the interaction between supercoiling and defects might facilitate damage recognition in living cells.

Finally, we extended our study of defects to DNA nanotubes. These nanotubes are rod-like nanostructures that comprise parallel arrangements of dsDNA. We performed twist simulations of DNA nanotubes similar to the ones we did for dsDNA and showed that the buckling of DNA nanotubes occurs in a defect-driven, non-wormlike chain regime. Our findings raise the question of whether theories based on the wormlike chain model can still be used to study the buckling transition and plectoneme formation in DNA nanotubes, as was done in several experimental studies.

Keywords— DNA damage - Supercoiling - DNA nanotube

Table of Contents

1 Introduction **1**

1.1 DNA supercoiling 1

1.2 Single molecule manipulation of dsDNA 2

1.3 Modelling dsDNA 5

1.4 dsDNA as an inhomogeneous polymer 6

1.5 Thesis objectives and outline 8

2 Methodology **10**

2.1 The oxDNA model 10

2.2 Protocols for molecular tweezer simulations 14

2.3 The Twistable Elastic Polymer (TEP) model 16

3 Thymine Dimers and Supercoiling **19**

3.1 Thymine dimer model in oxDNA 23

3.1.1 Bend angle of TD dsDNA 26

3.1.2 Melting temperature of TD dsDNA 29

3.1.3 Twist absorption by TD 30

3.2 Interplay between DNA supercoiling and the thymine dimer . . . 32

3.2.1 Extrahelical arrangement of the thymine dimer 32

3.2.2 Plectonemic pinning 38

3.2.3 Denaturation probability of the thymine dimer 41

3.2.4 Twist angles 42

3.3 Robustness Analysis 42

3.4 Conclusion 53

4 Statistical Mechanics of Tip-bubble Plectonemes **56**

4.1 Twist-induced buckling . . . 56
4.2 Twist-induced denaturation . . . 60
4.3 Modifications to the Brutzer and Salerno models . . . 64
4.4 Free energy of a tip-bubble plectoneme . . . 68
4.5 State boundary between plectonemes and tip-bubble plectonemes . 73
4.6 State boundary between bubbles and tip-bubble plectonemes . . . 76
4.7 Effects of defects on state boundaries . . . 80
4.7.1 Shift in characteristic force F_c (state boundary between plectonemes and bubbles) . . . 82
4.7.2 Shift in lower characteristic force F_{lc} . . . 83
4.7.3 Shift in buckling transition point . . . 84
4.7.4 Shift in bubble to tip-bubble transition point . . . 85
4.8 Further stress-testing of the theoretical framework . . . 86
4.9 Tip-bubble plectonemes in positively supercoiled dsDNA . . . 90
4.10 P-DNA state in positively supercoiled dsDNA . . . 98
4.11 Conclusion . . . 102

5 Twisting Helix Bundles **105**
5.1 Introduction . . . 105
5.2 oxDNA simulations of plectoneme formation in helix bundles . . . 107
5.2.1 Methods . . . 107
5.2.2 Geometry of plectonemes in helix bundle systems . . . 110
5.2.3 End-to-end extension and Torque response . . . 111
5.3 Theoretical models of plectonemic supercoiling . . . 114
5.4 Comparison between theoretical models and simulation results . . . 119
5.5 A different theoretical model of plectoneme formation . . . 127
5.6 Concluding remarks . . . 130

6 Defects in bacterial nucleoid models **132**

6.1 Introduction 132

6.2 Modelling the bacterial nucleoid 133

6.3 Simulation results 139

6.4 Concluding remarks 147

7 Conclusion **149**

Bibliography **153**

Appendix A Appendix **181**

A.1 DNA sequence used in the thymine dimer simulations 181

A.2 Formula for the rate of change of end-to-end extension with the number of imposed turns 182

A.3 Parameters used in the theoretical treatment of tip-bubble plectonemes 183

A.4 Torque response curve of twist-induced denaturation 184

A.5 Sensitivity analysis 185

A.6 Alternative formulation of the free energy expression for tip-bubble plectoneme 188

A.7 Denaturation transition point for dsDNA with defect X 189

A.8 Supplementary data for bacterial nucleoid simulations 190

List of Figures

1.1 Physical principles behind optical and magnetic tweezers 4

2.1 Schematic representation of the oxDNA 2.0 model 12
2.2 oxDNA simulations of DNA supercoiling by Matek *et al.* 13
2.3 The Twistable Elastic Polymer (TEP) model 16

3.1 The oxDNA thymine dimer model 25
3.2 Defintion of dsDNA bend angle θ_0 26
3.3 Sign convention for the dsDNA bend angle θ_0 27
3.4 Probability density distribution of bend angles for the undamaged and thymine dimer-containing dsDNA 28
3.5 Linear relation between thermalised bend angle θ_0 and roll angle ϕ 29
3.6 Twist angles measurements for a thymine dimer-containing 40-bp duplex 31
3.7 Extrahelical arrangement of the thymine dimer in a 600-bp supercoiled DNA duplex 33
3.8 Force-torsion state diagrams for undamaged and thymine dimer-containing DNA 34
3.9 End-loop of a plectoneme with a tip-bubble for undamaged dsDNA and dsDNA containing a thymine dimer 36
3.10 Definition of the end-loop angle 37
3.11 End-loop angle of the tip-bubble plectoneme in undamaged and thymine dimer-containing dsDNA 38
3.12 Plectoneme position distributions for undamaged DNA and thymine dimer-containing DNA measured at $F = 1.5$ pN and $\sigma \approx -0.073$. 39
3.13 State occupancy of the thymine dimer plectoneme 40

3.14 Average denaturation probability of the thymine dimer base pairs . 41
3.15 A duplex configuration in the bubble state at $F = 1.5\,\text{pN}$ and $\sigma = -0.038$ 42
3.16 Twist angles measurements for the thymine dimer-containing dsDNA at various state points 43
3.17 Twist angles measurements for different TD models 45
3.18 Force-torsion state diagrams for undamaged and thymine dimer-containing dsDNA 47
3.19 Plectoneme position distributions for a negatively supercoiled DNA strand at F = 1.5 pN and $\sigma = -0.073$ 48
3.20 Plectoneme position distributions for supercoiled DNA with TD1 . 48
3.21 Model-specific effects on plectonemic pinning 50
3.22 A comparison of the denaturation probability of thymine-dimer base pairs for the various TD models 51
3.23 Definition of relative orientation of two adjacent bases 52
3.24 Orientation angles between the thymine bases in various TD models 52

4.1 Illustration of the buckling transition and twist-induced denaturation 58
4.2 Variation of the number of denatured base pairs with superhelical density 62
4.3 Comparison of the Brutzer model of buckling with oxDNA simulations 65
4.4 Comparison of the Salerno model of denaturation with oxDNA simulations 67
4.5 Denaturation torque response curve of dsDNA 69
4.6 End-loop angle of a tip-bubble plectoneme as a function of tip-bubble size 71
4.7 An illustration of how the true state boundary is underestimated . 74

4.8 Comparison of the theoretical lower characteristic force with oxDNA simulations . . . 75
4.9 Comparison of the theoretical bubble to tip-bubble transition curve with oxDNA simulations . . . 78
4.10 An illustration of the major state boundaries in the force-torsion space of dsDNA . . . 79
4.11 The theoretical denaturation transition curve for a TD-containing DNA duplex . . . 81
4.12 Shift in the characteristic force for the thymine dimer-containing dsDNA . . . 82
4.13 Shift in the lower characteristic force for the thymine dimer-containing dsDNA . . . 83
4.14 Shift in the position of the buckling transition position for the thymine dimer-containing dsDNA . . . 84
4.15 Shift in the position of the bubble to tip-bubble transition for the thymine dimer-containing dsDNA . . . 85
4.16 Position of the bubble to tip-bubble plectoneme transition σ_t for the dsDNA containing a 2-bp mismatch . . . 87
4.17 Comparison of the theoretical characteristic forces F_c for the undamaged dsDNA, TD-containing dsDNA and defect X-containing dsDNA . . . 88
4.18 Comparison of the theoretical lower characteristic forces F_{lc} for the undamaged dsDNA, TD-containing dsDNA and defect X-containing dsDNA . . . 89
4.19 Force-torsion space for positively supercoiled dsDNA . . . 91
4.20 Tip-bubble size in negatively and positively supercoiled DNA . . . 93
4.21 Tip-bubble plectoneme in positively supercoiled DNA . . . 93

4.22 Position of the buckling transition in positively supercoiled dsDNA 95
4.23 A snapshot of the P-DNA state in positively supercoiled dsDNA . 97
4.24 End-to-end extension and denaturation profiles for positively supercoiled dsDNA in the P-DNA state 97
4.25 Torque response curve of the B-DNA to P-DNA transition in positively supercoiled dsDNA 100
4.26 Position of the B-DNA to P-DNA transition in positively supercoiled ds-DNA 101

5.1 Twist simulation setup of DNA nanotube 108
5.2 Formation of multiple plectonemes in twisted DNA nanotubes . . 109
5.3 Formation of a well-formed plectoneme in a DNA nanotube . . . 110
5.4 Free energy landscape of 6HB-SST as a function of end-to-end separation 111
5.5 End-to-end extension and post-buckling torque plots for 4HB-SST and 6HB-SST systems 112
5.6 Visualisation of plectoneme growth in twisted DNA nanotubes . . 113
5.7 Geometrical description of the plectoneme formed in DNA nanotubes 115
5.8 Predicted superhelical radius R for (A) 4HB-SST and (B) 6HB-SST 121
5.9 Predicted superhelical angle α for (A) 4HB-SST and (B) 6HB-SST 121
5.10 Predicted superhelical pitch P for (A) 4HB-SST and (B) 6HB-SST 122
5.11 Predicted post-buckling torque M for (A) 4HB-SST and (B) 6HB-SST 124
5.12 Predicted linear slope q for (A) 4HB-SST and (B) 6HB-SST . . . 125
5.13 Maximum and minimum possible slope value from a typical end-to-end extension plot 125

5.14 Comparison of the Marko composite model with oxDNA simulations of twisted DNA nanotubes 128
5.15 Variation of the number of intact base pairs with the number of imposed turns on helix bundle systems 129

6.1 1-nucleotide resolution model of E. coli. by Hacker *et al.* 134
6.2 Lattice modelling of a bacterial nucleoid 135
6.3 Equilibrated nucleoid model 137
6.4 Reproduction of the twin supercoiling domain model of transcription using the TEP model 138
6.5 Definition of θ_{TEP} 139
6.6 Representative θ_{TEP} distribution for a nucleoid system with a rotating RNAP 140
6.7 Series of configuration snapshots of a nucleoid model that contains a rotating TEP bead and a defect 141
6.8 Radius of gyration R_g of a bacterial nucleoid system 141
6.9 Twist profiles of a nucleoid model with a rotating RNAP 143
6.10 θ_{TEP} distribution for a nucleoid system with a distant rotating RNAP 145
6.11 Effect of supercoiling-diffusion barriers on defect localisation . . 146

A.1 Denaturation torque response curve of dsDNA with average-sequence oxDNA parameters 184
A.2 Variation of the lower characteristic force F_{lc} with the plectonemic twist stiffness P 185
A.3 Variation of the lower characteristic force F_{lc} with the torsional modulus C 186
A.4 Variation of F_{lc} with a_d 186

A.5 Variation of the slope of the bubble/tip-bubble boundary curve with a_d . . . 187
A.6 Shift in the denaturation transition point for defect X-containing dsDNA . . . 189
A.7 Effect of RNAP rotation period on defect localisation at a plectoneme tip in a nucleoid system . . . 190
A.8 Effect of RNAP rotation period on the θ_{TEP} distributions for nucleoid systems . . . 190

List of Tables

3.1 Features of the thymine dimer models 44
3.2 Melting temperature T_m of the thymine-dimer containing octamer used in the study by Kemmink *et al.* 44

A.1 List of parameters for negatively supercoiled dsDNA 183
A.2 List of parameters for positively supercoiled dsDNA 183

List of Abbreviations

bps . . . . . Base pairs

dsDNA . . . . . Double-stranded DNA

FENE . . . . . Finitely extensible non-linear elastic (spring)

MD . . . . . Molecular dynamics

MT . . . . . Magnetic tweezers

NAP . . . . . Nucleoid-associated protein

NMR . . . . . Nuclear magnetic resonance

sc . . . . . Supercoiled

SEM . . . . . Standard error of the mean

SST . . . . . Single-stranded tile(s)

TD . . . . . Thymine dimer

TEP . . . . . Twistable elastic polymer

Undam . . . . . Undamaged

WLC . . . . . Wormlike-chain

1 | Introduction

1.1 DNA supercoiling

Unstressed double-stranded DNA (dsDNA) in its canonical B-DNA conformation has a helical repeat of approximately 10.4 (closed circular dsDNA) to 10.5 (linear DNA) base pairs (bps) per turn (J. C. Wang, 1979; Rhodes & Klug, 1980; Tullius & Dombroski, 1985). Overwinding (i.e. addition of turns) causes the dsDNA to writhe positively and become positively supercoiled while underwinding (removal of turns) causes dsDNA to become negatively supercoiled. Under strong enough underwinding, the dsDNA can denature, paying the cost of breaking bonds to resolve the energy of twisting by forming single strands. In living cells, dsDNA supercoiling is actively maintained at significant energetic cost. It plays an important role in key biological processes such as transcription and replication, and facilitates the formation of compact structures needed to pack DNA into cellular compartments (Verma et al., 2019; Dekker et al., 2013; Witz & Stasiak, 2010; Postow et al., 2004). Variation in DNA supercoiling is thought to serve as both a sensor and a relay of physiological status that allows the individual cell to optimise its response to changing environmental factors (Dorman & Dorman, 2016). The movement of the RNA polymerases along DNA during transcription generates downstream positive supercoiling and upstream negative supercoiling (L. F. Liu & Wang, 1987; Wu et al., 1988). The negative supercoils that are formed facilitate strand separation in the promoter regions of the genome that enable the formation of an open complex with the RNA polymerase (Ma et al., 2013; Ma & Wang, 2016; Dorman, 2019). In order to avoid misfunction, excess helical stress is relieved by specialist proteins such as topoisomerases. Supercoiling is also thought to affect DNA-protein binding rates (Litwin et al., 2015) by reducing the energy

cost of associated twisting or bending of the DNA (Rohs et al., 2010), and to play a role in juxtaposing linearly distant binding sites on DNA (J. Huang et al., 2001).

1.2 Single molecule manipulation of dsDNA

Much of what we know about supercoiled dsDNA comes from a culmination of decades of experimentation, theoretical developments and computational simulations. Experimental techniques such as electron microscopy (EM) and atomic force microscopy (AFM) enabled the investigation of the topology and geometry of supercoiled DNA under a variety of physiological conditions (Vinograd et al., 1965; A. V. Vologodskii & Cozzarelli, 1994; Lyubchenko & Shlyakhtenko, 1997; Schvartzman et al., 2013), with electron micrographs of the circular genome of polyomavirus providing the first experimental evidence that dsDNA molecules can be supercoiled (Vinograd et al., 1965; Schvartzman et al., 2013). Computer simulations (for example, (Schlick & Olson, 1992; A. V. Vologodskii & Cozzarelli, 1994)) and statistical mechanical theories (J. F. Marko & Siggia, 1994b; J. Marko & Siggia, 1995) of supercoiled dsDNA complement these experimental investigations, which typically treated dsDNA as a simple wormlike chain in the early days.

Single molecule manipulation of dsDNA is one of the experimental techniques that can be used to investigate supercoiled dsDNA. A well-established type of single molecule manipulation comes in the form of magnetic or optical tweezer (MT or OT) experimentation. In a traditional optical tweezer set-up, one end of the dsDNA is tethered to an optically trapped bead via a biotin and/or digoxigenin linkage (M. D. Wang et al., 1997; Pincet & Husson, 2005; Neuman & Nagy, 2008) while depending on the objective(s) of the experiment, the other end can be attached to a surface of a glass slide, a suctioned bead on the micropipette, or

proteins such as RNA polymerases (M. D. Wang et al., 1998). The physics of optical trapping depends on the size of the bead relative to the wavelength of the beam of light (in practice, laser light). If the bead is smaller than the wavelength of the light, then it behaves as a Rayleigh scatterer with an induced electric dipole moment (C. J. Bustamante et al., 2021). In an inhomogeneous electric field (e.g. a Gaussian laser beam), the bead will experience a gradient force that attracts the bead towards higher intensities of the laser beam. The bead will also experience a scattering force due to the absorption and the reflection or refraction of light. Stable trapping is attained when the gradient force on the bead is balanced by the scattering force (Zhao et al., 2018; C. J. Bustamante et al., 2021). Conversely, if the bead is larger than the wavelength of the beam of light used to trap the bead, then geometric optics can be utilised to describe the rays and forces acting on the bead (C. J. Bustamante et al., 2021). Light that is incident onto the bead through a microscope objective lens is reflected and refracted at the same time (Fig. 1.1A). Refracted light generates a recoil force that pulls the bead towards the focal point. Reflected light on the other hand loses forward momentum and thus pushes the bead away from the focal point. The magnitude and direction of these forces can be manipulated by the laser beam to move the trapped bead in the direction of the resultant force.

Angular trapping can also be carried out using optical tweezers (Fig. 1.1B & C). Typically, this requires the use of polarised light and a birefringent trapping particle whose electric susceptibility is anisotropic, such as a quartz crystal (La Porta & Wang, 2004; Gutiérrez-Medina et al., 2010; Ma et al., 2018). In the presence of a linearly polarised electric field $\vec{E}$ which makes an angle θ with the extraordinary axis and has a magnitude of E_0, the quartz crystal develops a polarisation $\vec{P} = \chi_e E_0 \cos\theta \hat{x} + \chi_0 E_0 \sin\theta \hat{y}$. The misalignment between the polarisation and the electric field generates a torque $\tau = \int d^3\vec{r}\vec{P} \times \vec{E} = \hat{z}\frac{1}{2}(\chi_e - \chi_0)\sin 2\theta \int d^3\vec{r}E_0^2$

(La Porta & Wang, 2004). The torque τ will continue to be finite until $\vec{E}$ is aligned with the extraordinary axis of the crystal.

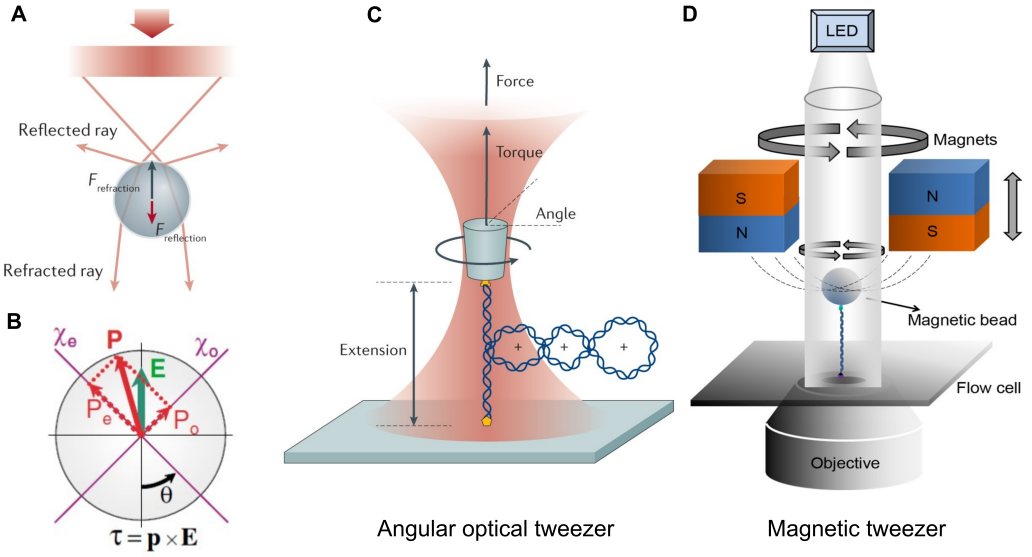


Figure 1.1: Physical principles behind (A) linear displacement and (B) rotation of a trapping particle in optical tweezer set-ups. In (A), the reflected ray imparts a forward momentum to the bead that pushes the spherical bead towards the direction of the laser beam ($\vec{F}_{\text{reflection}}$) while the refracted ray causes a recoil ($\vec{F}_{\text{refraction}}$) towards the focal point of the objective lens. In (B), a polarisation vector $\vec{P}$ is induced in a uniaxial birefringent material by a linearly polarised electric field $\vec{E}$. The extraordinary and ordinary axes are defined along the $\hat{x}$ and $\hat{y}$ direction respectively. Torque is generated when $\theta \neq 0$. Measurement geometries of an angular optical tweezer and a magnetic tweezer are given by (C) and (D) respectively. Figure is reproduced with permission from Refs. (La Porta & Wang, 2004; Zhao et al., 2018; C. J. Bustamante et al., 2021).

Other than the physical principles that underpin the manipulation of the bead attached to the dsDNA molecule, a magnetic tweezer set-up is similar to that of an optical tweezer (Fig. 1.1D). A magnetic bead tethered to the DNA molecule is subjected to an external magnetic field from a pair of permanent magnets above the flow cell. Moving the magnets upwards or downwards alters the magnitude of the force on the bead while rotating the magnets leads to bead rotation. Spatial

information about the bead's position is captured using a charge-coupled device (CCD) camera and a light source that illuminates the magnetic bead (Vilfan et al., 2009). The light that is scattered from the bead creates an interference pattern with the unscattered light, allowing the user to obtain a three-dimensional picture of the bead's position based on the interference pattern's shape and size. Magnetic and optical tweezer manipulations of supercoiled dsDNA each carries its own set of trade-offs. For example, it is easier to conduct a constant force experiment with magnetic tweezers (Zhao et al., 2018), but magnetic tweezers typically have poorer temporal and spatial resolution compared to optical tweezers (Neuman & Nagy, 2008).

1.3 Modelling dsDNA

From a theoretical perspective, it is inevitable that one makes approximations about dsDNA when we try to interpret results from supercoiling experiments of DNA, or when we try to understand DNA supercoiling using a grounds-up approach based on physics.

One of the most commonly used models to study dsDNA is the Wormlike-Chain (WLC) model (Odijk, 1995; Aggarwal et al., 2020). In this model, dsDNA is treated as an elastic rod that bends smoothly under random thermal fluctuations. The deformation energy associated with bending assumes a quadratic form and is characterised by a parameter known as the bending modulus B. For a dsDNA of length L that is stretched by a force F in the $\hat{\mathbf{z}}$ direction, the effective energy E_{wlc} in the WLC approximation can be written as (J. F. Marko & Siggia, 1995; J. F. Marko, 2005):

$$E_{wlc} = \int_0^L ds \left[\frac{B}{2} (\partial_s \hat{\mathbf{t}})^2 - F \hat{\mathbf{z}} \cdot \hat{\mathbf{t}} \right] \tag{1.1}$$

In Eq. 1.1, dsDNA is described by a space curve $\mathbf{r}(s)$ where s is the arc length. In addition, $\hat{\mathbf{t}} = \partial_s \mathbf{r}$ is the unit tangent vector. Eq. 1.1 was famously used by Marko and Siggia to calculate the force-extension curves by Smith *et al.* (Smith et al., 1992; J. F. Marko & Siggia, 1995). Modifications to the WLC model have been made over the years to account for structural transitions and statistical mechanical behaviour that the basic WLC model could not explain. One such example is the incorporation of a twist-stretch coupling term into the WLC model to describe DNA elongation due to changes in twist at intermediate and higher pulling forces (Gross et al., 2011).

Other than the WLC model, atomistic simulations have also been used to study the physical properties of dsDNA (Mazur, 2006; Brown et al., 2015). Atomistic simulations are based on quantum mechanics calculations as well as empirical force fields such as AMBER (Galindo-Murillo et al., 2016) that are parameterized using experimental data for small molecules. Unfortunately, given the limitations of current computational resources, atomistic simulations are ill-suited to study the mesoscale properties of DNA (Minhas et al., 2019) or processes involving long time scales. For such systems, coarse-grained models provide the bridge between the highly detailed atomistic models and the WLC model (Potoyan et al., 2013).

1.4 dsDNA as an inhomogeneous polymer

The lowest order approximation one could make is to treat dsDNA as a homogeneous polymer, with $B(s) = B$ and $C(s) = C$, where B and C are the bending and torsional modulus respectively and s is the arclength along the dsDNA. Such an assumption is common in theoretical treatments of DNA supercoiling, and interpretations of MT/OT experiments. For example, the concept

of Michell's instability in closed circular dsDNA was developed based on the assumption of homogeneity (Michell, 1889; Goriely, 2006). Closed circular dsDNA buckles into a figure of eight when the imposed torsional stress exceeds a critical value that is proportional to B/C. The next order approximation is to consider sequence-dependent effects. This is made possible with the use of appropriate chemical probes and sequencing techniques. A wealth of information about DNA is unearthed when sequence-dependent effects are considered. Supercoiling-induced bubbles (open base pairs), for instance, are known to be highly sequence-dependent with a preference for AT-rich domains in dsDNA (Jeon et al., 2010).

Last but not least, we can consider damages to dsDNA. DNA damage can be categorised into two classes—endogenous or exogenous—depending on its origin. Endogenous damage to DNA is typically caused by processes or reactions that occur naturally within the cellular environment. For example, oxidant by-products from metabolic processes damage DNA (Ames et al., 1993; Poetsch, 2020). Guanine, in particular, is highly susceptible to oxidative modification due to its low redox potential (Cadet et al., 2006; Margolin et al., 2006). Exogenous damage on the other hand is usually caused by environmental agents. Polycyclic aromatic hydrocarbons, a common by-product of tobacco smoke and automobile exhaust, can form intermediates that react and bind with DNA (N. Chatterjee & Walker, 2017). Ionising radiation (alpha, beta, gamma, neutron and X-rays) is another common source of exogenous damage to DNA. It can damage DNA directly by causing single or double strand breaks, or by indirect means, such as the generation of highly reactive hydroxyl radicals in the water surrounding DNA (Desouky et al., 2015; N. Chatterjee & Walker, 2017). The effects on supercoiling are damage/defect-specific since each defect has its own effect on the intrinsic properties of dsDNA. Methylated DNA, for instance, is reported to increase lo-

cal bending stiffness due to steric clashes (Nathan & Crothers, 2002; Pérez et al., 2012; Liebl & Zacharias, 2019). Conversely, base pair mismatches reduces the bending stiffness at the defect site (Sharma et al., 2013; P. R. Desai et al., 2020). These modifications to DNA are not uncommon in living organisms. Contact with oxidative agents, for instance, is estimated to occur at a rate of 10,000 times per cell per day in humans and about 100,000 times per cell per day for rats (Ames et al., 1993). Therefore, to understand the supercoiling of DNA in its most natural state (i.e. within living cells), we need to consider defects or damage as one of the inhomogeneities that DNA possesses as a polymer.

1.5 Thesis objectives and outline

In this thesis, we aim to understand how defect properties can influence the global supercoiled structure of dsDNA, and conversely, how supercoiling can affect the local properties of defects in DNA. We proceed by first incorporating the description of a DNA defect known as the thymine dimer, a photoproduct of UV radiation on DNA, into oxDNA, a coarse-grained model of DNA (Ouldridge et al., 2011). This is followed by oxDNA simulations that emulate a molecular tweezer set-up to study the interactions between the thymine dimer and DNA supercoiling, and a theoretical account of the observations we made from these simulations. Finally, we seek to extrapolate our hypotheses and findings onto an *in-vivo* DNA in a cellular environment by modelling a bacterial nucleoid environment. Interestingly, our findings concerning DNA defects may bear relevance to the study of twisted DNA nanotubes and DNA-based nanotechnology. This study will also be discussed in this report.

The remainder of this report is organised as follows:

Chapter 2 — introduces the oxDNA model and outlines the simulation

protocols for the molecular tweezer set-up. A description of the twistable elastic polymer (TEP) model that we will use to model bacterial nucleoids in Chapter 6 is also provided.

Chapter 3 — focuses on the description of the thymine dimer model in oxDNA and its interactions with DNA supercoiling. The contents are based on a paper that Ferdinando and I worked on together as co-first authors (Lim et al., 2022).

Chapter 4 — details the statistical mechanics of tip-bubble plectonemes and demonstrates how defects such as thymine dimers and base pair mismatches can be represented within the theoretical framework that is outlined in the chapter.

Chapter 5 — investigates the energetics of plectoneme formation in DNA nanotubes and shows that buckling in DNA nanotubes occurs in a defect-dominated, non-WLC regime. The work is carried out in collaboration with Hemani Chhabra from the Doye Group in the Department of Chemistry, University of Oxford.

Chapter 6 — demonstrates how a bacterial nucleoid environment can be modelled using the TEP model and used to test the hypotheses concerning the effect DNA supercoiling has on defects in a biologically-relevant setting.

Chapter 7 — summarises the main findings in this report.

2 | Methodology

2.1 The oxDNA model

oxDNA is a coarse-grained DNA model that bridges the gap between atomistic simulations that rely on quantum mechanical calculations or empirical forcefields to model interactions, and continuum models of DNA that treat DNA as a uniform medium (Sengar et al., 2021). It is developed using a "top-down" approach that is phenomenologically motivated to reproduce as many experimentally relevant properties as possible (Ouldridge, 2012). The model is represented by rigid nucleotides with several interaction sites, namely the backbone, base repulsion, stacking and hydrogen-bonding sites (Fig. 2.1). The functional forms and their corresponding parameters of the various interaction terms are calibrated to reproduce the experimental values of selected structural, thermodynamic, and elastic properties of DNA. For instance, the double helical geometry of dsDNA is achieved by a careful balancing of the hydrogen-bonding, stacking and backbone connectivity interactions (Sengar et al., 2021). The stacking interaction is designed to encourage the nucleotides to form co-planar stacks whose spacings are shorter than the backbone bond length. This results in a tendency to form helical stacked structures. Hydrogen bonding between complementary bases and cross-stacking interactions brings these structures together to form a much more stable double helix.

One's choice along this spectrum of DNA models depends very much on the objective(s) and system(s) of interest. Quantum mechanical calculations can be used to estimate the nucleotide properties from first principles but are ill-suited for larger systems due to its high computational costs (Šponer et al., 2008). Empirical forcefields such as AMBER can be used to simulate larger systems such as

DNA origami but they require continual calibrations as new systems and longer time scales are studied (Pérez et al., 2007). The time scales can also vary depending on whether a solvent is included in the system, further complicating the calibration of the empirical forcefields. Continuum models, which typically treat DNA as an elastic worm-like chain with bending and twisting modes of deformation, are well-suited to understand the geometry of very large-scale systems of DNA, but they lack the granularity or the requisite degrees of freedom in the system to study processes such as DNA duplex melting. Applicability of oxDNA on the other hand is considerably broader: self-assembly, structure and mechanical properties of DNA nanostructures, action of DNA nanodevices, thermodynamics of duplex formation, but it falls short in areas where sequence-dependent elasticity, and where DNA-solvent/solute interactions become crucial (Sengar et al., 2021).

In this thesis, we will be using version 2.0 of the oxDNA model (henceforth known as oxDNA2) that is available in the public domain (dna.physics.ox.ac.uk). Compared to earlier versions of oxDNA, oxDNA2 includes a more accurate structural model that takes into account the asymmetry between the widths of the major and minor grooves of DNA, as well as a screened electrostatic potential energy term that is vital for handling simulations at low monovalent salt concentrations (e.g. 0.1 M) (B. E. Snodin et al., 2015). With these changes, the oxDNA2 interaction potential can be written as:

$$\begin{aligned} V_{\text{oxDNA2}} = & \sum_{\text{nearest neighbours}} \left(V_{\text{backbone}} + V_{\text{stack}} + V_{\text{exc}}^{'} \right) \\ & + \sum_{\text{other pairs}} \left(V_{\text{HB}} + V_{\text{cross stack}} + V_{\text{exc}} + V_{\text{coax stack}} + V_{\text{DH}} \right) \end{aligned} \tag{2.1}$$

The schematic representation of Eq. 2.1 can be found in Fig. 2.1. Details of

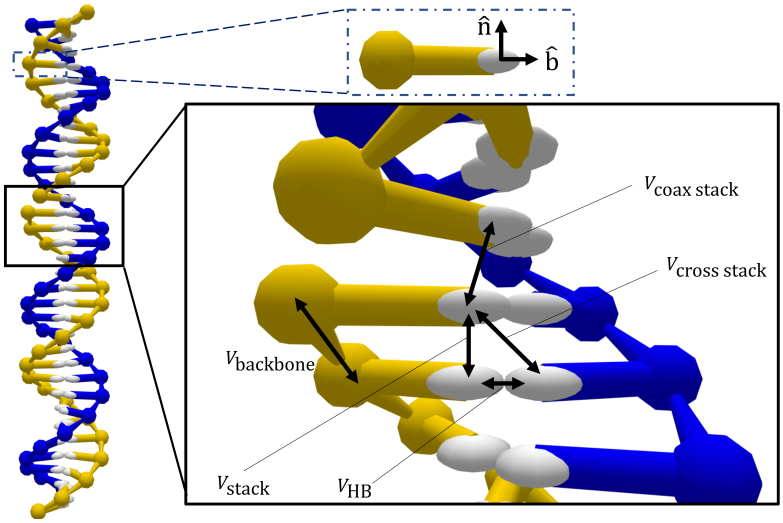


Figure 2.1: Schematic representation of the oxDNA 2.0 model. (Dashed inset) Individual nucleotides have an orientation described by a vector normal to the plane of the base ($\hat{\mathbf{n}}$), and a vector indicating the direction of the hydrogen bonding ($\hat{\mathbf{b}}$). (Solid inset) Main interactions from Eq. 2.1 are highlighted. V_{backbone} is the interaction term associated with backbone connectivity. V_{HB} refers to the hydrogen bonding interaction between complementary bases. V_{stack} represents stacking between neighbouring bases on the same strand. $V_{\text{cross stack}}$ represents the cross-stacking interaction between the bases across the duplex axis. $V_{\text{coax stack}}$ is the stacking interaction potential between bases across a nicked backbone.

the various potential terms used in Eq. 2.1 are available in Ref. (Ouldridge et al., 2011) and (B. E. Snodin et al., 2015). The careful reader may notice that the model is constructed with pairwise interactions. This was a deliberate choice to make effective use of equilibrium sampling algorithms such as the Virtual Move Monte Carlo (VMMC) algorithm, whose cluster building/moving process is based on assessing the change in pairwise interactions.

Given our interest in DNA supercoiling, it is imperative that we examine how well the oxDNA forcefield performs in a molecular tweezer simulation of supercoiled dsDNA. Matek *et al.* were the first to carry out simulation in a molecular tweezer geometry of dsDNA using the oxDNA forcefield (Matek et al., 2015), and demonstrated that oxDNA is capable of reproducing torque response and DNA

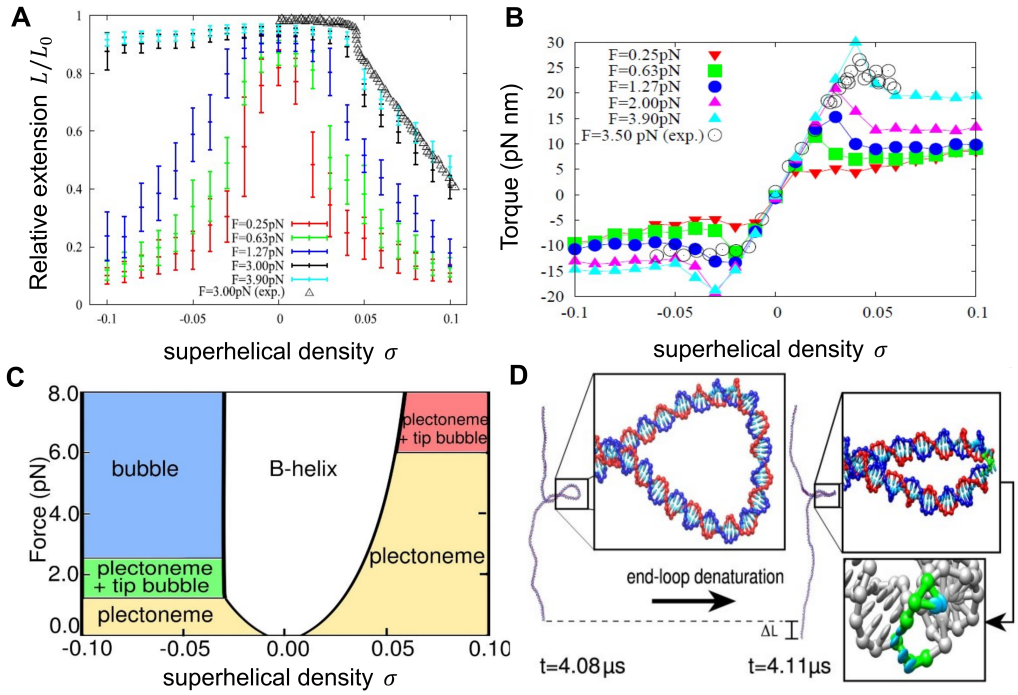


Figure 2.2: Main results from the oxDNA simulations of supercoiling by Matek *et al.* (A) Relative extension L/L_0 data from oxDNA simulations using a monovalent salt concentration of 0.5 M and $L_0 = 600$ bps is compared against L/L_0 experimental data (Black triangles. $[Na^+] = 0.32$ M, $L_0 = 1900$ bps, $F = 3.0$ pN) from Ref. (Brutzer et al., 2010). (B) Torque data from the same set of simulations is compared against experimental data (Black-bordered circles. $[Na^+] = 0.55$ M, $L_0 = 7900$ bps, $F = 3.5$ pN) from Ref. (Janssen et al., 2012). (C) Force-torsion state diagram of supercoiled dsDNA. An intermediate state between bubbles and plectonemes known as the tip-bubble plectoneme state is detected by the simulations. (D) Tip-bubble plectoneme structure. The formation of a bubble at the tip of the plectoneme leads to an end-loop with a lower curvature. Figure is adapted from Ref. (Matek et al., 2015).

end-to-end extension curves that agree well with experimental results (Fig. 2.2A & B). Matek *et al.* also reproduced the force-torsion state diagram of supercoiled dsDNA (Fig. 2.2C) and predicted the existence of an intermediate DNA state between plectonemes and bubbles known as the tip-bubble state (Fig. 2.2D). The existence of the tip-bubble state has yet to be verified by experiments, which raises the question of whether tip-bubbles are an artefact of the oxDNA model. In this

thesis, we aim to provide a more rigorous theoretical justification behind the existence of the tip-bubble state. Note that the simulations carried out by Matek *et al.* were based on an older version of oxDNA model. More recently, Randisi carried out similar molecular tweezer simulations using oxDNA2 and reported results that corroborated well with Matek's findings (Randisi, 2019).

2.2 Protocols for molecular tweezer simulations

The molecular tweezer set-up that we will be using in Chapter 3 and 4 is similar to the one deployed by Matek *et al.* (Matek et al., 2015) and Randisi (Randisi, 2019). A 600-bp DNA duplex, with a randomised sequence with 50% GC content (see Appendix A.1 for the sequence), was simulated with MD at an effective NaCl concentration of 100 mM and T = 300 K. 12 base pairs (bps) were attached at each end of the DNA as "handles" to constrain the linking number of the DNA and its spatial position, and to apply the pulling force F. The nucleotides in the handle at the "surface" end of the DNA were kept in a fixed position by applying harmonic traps to simulate the presence of a fixed surface to which the DNA is tethered; each nucleotide was subject to an external harmonic potential $V_{\text{trap}}(\mathbf{r_n}; \mathbf{r_{n,0}}) = \frac{1}{2}\sum_{i=1}^{3} k^i_{\text{trap}}(r^i_n - r^i_{n,0})^2$,where $\mathbf{r_n} = (r^1_n, r^2_n, r^3_n)$ is the centre-of-mass position of the n-th nucleotide in the harmonic trap, and the position of the trap $\mathbf{r_{n,0}}$ is set to the initial centre-of-mass position of the nucleotide, with k^i_{trap} taking on the value of 571 N/m for all the nucleotides in the handle.

At the other end of the DNA duplex, a harmonic potential with $k^3_{\text{trap}} = 0$ was applied to emulate the freely-moving optical/magnetic bead. This allows the nucleotides to move freely in the direction parallel to the helical axis while remaining constrained in the plane perpendicular to the helical axis. These harmonic traps can also be rotated in the (x, y) plane to achieve the desired superhelical density

σ, here defined as $\sigma = (Lk - Lk_0)/Lk_0$, where Lk is the linking number of the supercoiled DNA and Lk_0, the linking number of the relaxed DNA duplex, is $600/10.55 \approx 56.87$. For these underwinding/overwinding simulations, a rotation period of 10^7 MD simulation steps per turn was applied. A constant external force $F/2$ was also applied to the outermost nucleotides of each strand in this handle to model the presence of an external pulling force totalling F.

To ensure that the nucleotides do not cross the DNA ends and change the linking number of the system, a repulsive external potential $V_{\text{plane}}(\mathbf{r_k}; \mathbf{R}) = \frac{1}{2}k_{\text{plane}}[(\mathbf{r_k} - \mathbf{R}) \cdot \hat{\mathbf{n}}]^2\theta(-(\mathbf{r_k} - \mathbf{R}) \cdot \hat{\mathbf{n}})$ was added to all nucleotides not in the handle. Here, $\mathbf{R}$ is set to the position of one of the nucleotides in the handle that is furthest from the end of the duplex, θ is the Heaviside step function, and $\hat{\mathbf{n}}$ is the normal to the repulsion plane. k_{plane} is set to 571 N/m.

MD trajectories were obtained by integrating Newton's equations of motion with the velocity Verlet algorithm (Swope et al., 1982) using an integration time step of 6.06 fs. A Langevin-like dynamics thermostat was applied to simulate the impact of the solvent (Allen & Tildesley, 2017). The diffusion coefficient was chosen such that the diffusive dynamics of individual nucleotides is accelerated by approximately 2 orders of magnitude compared to experiment (Lapham et al., 1997). This enables the simulation to access longer effective time-scales, accelerating the convergence of the average values of quantities measured during simulations.

To carry out production runs, configurations at the desired superhelical density σ and pulling force F were extracted from the winding simulations at the appropriate time point. An equilibration time τ_{eq} is measured using the decay time of the auto-correlation function of the DNA end-to-end distance. In order to ensure that the observable of interest (i.e. state occupancy, end to-end distance or plectonemic state) is well equilibrated, data was collected for at least $6\tau_{\text{eq}}$ time steps (between

2×10^8 and 1×10^9 steps). Measurements were made after discarding the first $2\tau_{\text{eq}}$ time steps to make sure that initial configurations are averaged out.

At least three independent trajectories were used to ensure the reproducibility and consistency of measurements made. A larger than usual number of trajectories were simulated near state boundaries to ensure good sampling of the conformational states. This is pertinent when we examine the state boundaries associated with tip-bubbles in Chapter 4. The simulations were performed using the GPU-enabled version of the oxDNA simulation code (Rovigatti et al., 2015). Equilibrium data such as the one presented in Fig. 4.18 would require a combined simulation runtime of at least 2 years on a current GPU.

2.3 The Twistable Elastic Polymer (TEP) model

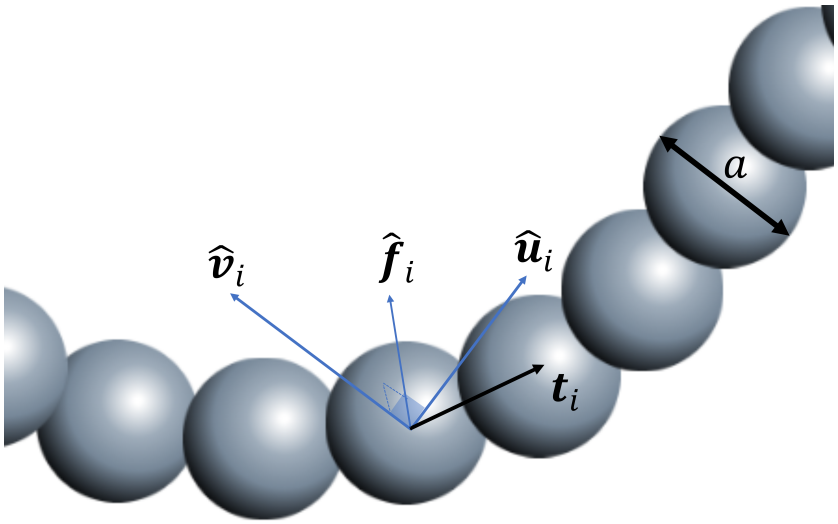


Figure 2.3: The Twistable Elastic Polymer (TEP) model. In this model, DNA is represented as a series of beads connected by springs. Each bead is defined by a position vector $\mathbf{r}_i$ and a set of orthogonal orientation vectors $\{\hat{\mathbf{u}}_i, \hat{\mathbf{v}}_i, \hat{\mathbf{f}}_i\}$. The tangent vector $\mathbf{t}_i$ is defined as $\mathbf{r}_{i+1} - \mathbf{r}_i$.

To simulate large DNA systems such as bacterial chromosome that comprise tens

or hundreds of thousands of base pairs, a different coarse-graining approach may be required. In the Twistable Elastic Polymer (TEP) model, DNA is coarse-grained as a bead-and-spring polymer (Fig. 2.3), with each bead characterised by a position vector $\mathbf{r}_i$ and a set of orthogonal orientation vectors $\{\hat{\mathbf{u}}_i, \hat{\mathbf{v}}_i, \hat{\mathbf{f}}_i\}$ (Chirico & Langowski, 1994; C. A. Brackley et al., 2014). The energy of the system is given by:

$$V_{\text{TEP}} = V_{\text{bend}} + V_{\text{twist}} + V_{\text{align}} + V_{\text{WCA}} + V_{\text{FENE}} \tag{2.2}$$

The bend energy of the polymer V_{bend} can be expressed as:

$$V_{\text{bend}} = \frac{k_b}{a} \sum_{i=1}^{N-1} (1 - \hat{\mathbf{u}}_{i+1} \cdot \hat{\mathbf{u}}_i) \tag{2.3}$$

while the twist energy V_{twist} is given by:

$$V_{\text{twist}} = \frac{k_t}{2a} \sum_{i=1}^{N-1} \left(1 + \hat{\mathbf{u}}_{i+1} \cdot \hat{\mathbf{u}}_i - \hat{\mathbf{f}}_{i+1} \cdot \hat{\mathbf{f}}_i - \hat{\mathbf{v}}_{i+1} \cdot \hat{\mathbf{v}}_i\right) \tag{2.4}$$

In both of these equations (Eq. 2.3 & 2.4), a represents the diameter of the bead, which in our simulations for this thesis is taken to be 2.5 nm or 7.4 bps (C. Brackley et al., 2015). k_b and k_t represent respectively the bending and twisting stiffness of the elastic polymer. In all our TEP simulations of undamaged or homogeneous DNA, $k_b/a = 21\, k_{\text{B}}T$ and $k_t/a = 29.7\, k_{\text{B}}T$ to match the bending persistence length and torsional rigidity of the DNA in the simulation studies by Brackley *et al.* (C. Brackley et al., 2015).

The next term in Eq. 2.2 is the alignment energy that serves to acts to align the vectors $\hat{\mathbf{u}}_i$ along the backbone of the DNA polymer:

$$V_{\text{align}} = k_a \sum_{i=1}^{N-1} \left(1 - \hat{\mathbf{u}}_i \cdot \hat{\mathbf{t}}_i\right) \tag{2.5}$$

$\hat{\mathbf{t}}_i$, the unit tangent vector, is defined as $\frac{\mathbf{r}_{i+1}-\mathbf{r}_i}{|\mathbf{r}_{i+1}-\mathbf{r}_i|}$. Next, V_{WCA}, the Weeks-Chandler-Andersen potential that serves to prevent adjacent beads from overlapping, is given by:

$$V_{\text{WCA}} = \sum_{i \neq j} 4k_{\text{B}}T \left[\left(\frac{a}{|\mathbf{r}_i - \mathbf{r}_j|} \right)^{12} - \left(\frac{a}{|\mathbf{r}_i - \mathbf{r}_j|} \right)^{6} \right] \theta(|\mathbf{r}_i - \mathbf{r}_j| - 2^{1/6}a) \quad (2.6)$$

where θ is the Heaviside step function and a, as defined on the previous page, is the diameter of the bead with a value of 2.5 nm. Finally, the potential energy term for finitely extensible non-linear elastic (FENE) springs V_{FENE} is given by:

$$V_{\text{FENE}} = -\frac{k_{\text{FENE}}R_0^2}{2} \sum_{i=1}^{N-1} \ln \left(1 - \left(\frac{|\mathbf{r}_{i+1} - \mathbf{r}_i|}{R_0} \right)^2 \right) \quad (2.7)$$

where R_0 is defined as the maximum extension of the FENE bond. For our simulations using the TEP model, R_0 and k_{FENE} are set as $1.6a$ and $30\, k_{\text{B}}T$ respectively (C. Brackley et al., 2015).

We will be using the TEP simulation model that is implemented in the oxDNA package by Randisi and Rovigatti (unpublished). In their implementation of the TEP model, a modification is made to the bending energy term in order to mimic the behaviour of a kinked segment in the DNA polymer (Randisi, 2019). This modification is deactivated in our TEP simulations in Chapter 6.

3 | Thymine Dimers and Supercoiling

Thymine dimers are the most common of several types of mutagenic lesions caused by UV irradiation of DNA. They are perhaps the best known and studied DNA damage system (Beukers et al., 2008). Thymine dimers are also called cyclobutane pyrimidine dimers (CPDs), because they are formed via a cyclobutane ring that connects the 5,6 positions of any two adjacent pyrimidine bases (Beukers et al., 2008). While it is possible to form an intrastrand cross-link between any adjacent pyrimidine base (i.e. thymine-thymine, cytosine-thymine, and cytosine-cytosine), thymine-thymine dimerisation is the most common.

The biological effects of these dimers are well documented. Persistent thymine dimers are thought to hinder DNA transcription and replication by stalling the progress of RNA polymerase (Protić-Sabljić & Kraemer, 1985; D. L. Mitchell et al., 1989). This can cause cellular death which manifests, for example, in sunburn. Their presence can also lead to the misreading of the genetic code, causing mutations, which in some cases can lead to cancer. In the context of the current COVID-19 pandemic (Ciotti et al., 2020), the use of UV-C light to induce the formation of thymine dimers in the genomic DNA of the coronavirus and preventing its further replication has become a vital tool in the fight against COVID-19 (Mackenzie, 2020; Bono et al., 2021).

Living organisms possess a variety of mechanisms to repair detrimental lesions in their DNA (Sinha & Häder, 2002). In fact, sunburn only occurs when UV induced thymine dimers are produced at a rate that overwhelms the repair mechanisms. In organisms such as bacteria and plants, thymine dimers can be repaired via enzymatic photoreactivation. A photolyase enzyme binds to thymine dimers and reverses the damage using the energy of light. Mammalian cells, on the

other hand, do not have photolyases to perform the repairs. Instead, thymine dimer repair takes place through a light-independent mechanism known as nucleotide excision repair that excises the region of damaged nucleotides instead of just breaking the bonds of the pyrimidine dimer as is done by photolyase. In humans for instance, the general excision repair pathway begins with the recognition of the lesion site by the Xeroderma pigmentosum group C (XPC) protein in complex with RAD23B (also commonly referred to as XPC). There is accumulating evidence to suggest that XPC is a non-discriminatory damage marker that is non-specific to CPDs (Kusakabe et al., 2019; Chen et al., 2015). Thus, for further confirmation that the lesion is indeed a CPD, the multi-subunit transcription factor TFIIH, including the helicase subunits of XPB and XPD, as well as XPA, are recruited (Sugasawa, 2016; Li et al., 2015). Once the identity and location of the lesion site are verified, XPC dissociates from the complex, and XPG and XPF enters to make the 3' incision and 5' incision around the lesion site respectively. The excised oligodeoxynucleotide has a length of approximately 30 bps (J.-C. Huang et al., 1992), and is removed from the DNA together with the TFIIH-XPG complex and XPF (Hu et al., 2013; Kemp et al., 2012). Apart from XPC, the RNA polymerase can also serve as an initial damage marker (Hu et al., 2017). In this transcription-coupled repair pathway, the RNA polymerase stalls at the lesion site on the transcribed template strand, and, unlike XPC, remains on the strand after the dual incision events by XPF and XPG.

Fundamental to these repair pathways is the question of how repair proteins locate and bind to the DNA lesion (Verdine & Bruner, 1997). In enzymatic photoreactivation for instance, it is generally accepted that the thymine dimer lesion has to be flipped into the active site of the bound photolyase to remove the covalent bond between the two pyrimidine bases (Mees et al., 2004). Yet, it is unclear how this stage of the repair process is achieved in the first place. Two compet-

ing models, namely the passive model and the active "induced fit" model, have been proposed. In the passive model, the thymine dimer base pair has to first flip out of the helix before the enzyme can locate and bind to the lesion site (Parker et al., 2007). On the other hand, in the active model, the repair enzyme first binds to the lesion site, kinks the duplex at the lesion site (reported bend angles range from 42° in the DNA-XPC/Rad4 complex (Min & Pavletich, 2007) to 50° in the DNA-photolyase complex (Mees et al., 2004)), and then flips the thymine dimer bases into an extrahelical arrangement that is fitted into the enzyme's active site (Sancar, 2003; Meulenbroek et al., 2013). The passive model seems to be supported by calorimetric calculations (Wilson et al., 2011) and binding kinetic studies (Schelvis et al., 2015) but it remains unclear how the CPD lesion adopts an extrahelical conformation in the first instance, given that crystal structure and Nuclear Magnetic Resonance (NMR) analyses of thymine dimer-containing DNA typically show an intra-helical arrangement of CPD bases within the double helix (McAteer et al., 1998; Park et al., 2002). In these configurations, the free energy barrier for flipping out the thymine dimer bases has been calculated to be between 6 to 7.5 kcal/mol, and which is most likely too big to be surmounted by thermal fluctuations on time-scales needed for repair (O'Nei & Wiest, 2008).

To the best of our knowledge, many of the experimental and computational studies above that probe the passive/active nature of the repair mechanism use relatively short DNA strands that are unable to mimic the in-vivo conditions of twist. Consequently, they may miss the potential impact of supercoiling. For example, supercoiling can significantly affect binding affinities (Litwin et al., 2015). It may also affect the rate at which repair proteins can locate DNA damage. For example, van den Broek *et al.* (van den Broek et al., 2008) showed that supercoiling accelerated EcoRV's search for its target site. In addition, simulations by Brackley *et al.* (C. A. Brackley et al., 2013, 2012) suggested that for low binding energies,

protein target search is significantly shorter if the target sequence is located on a loop of a DNA rosette instead of in the rosette's centre.

The big question then is how DNA damage interacts with supercoiling to affect protein binding or damage location by repair enzymes. A first step is to ask how damage affects plectonemes. Brutzer *et al.* engineered a kink into DNA and demonstrated experimentally that the kink resulted in an initial loop to be formed (prebuckling) much earlier than for an unkinked DNA molecule (Brutzer et al., 2010). It was suggested in (Matek et al., 2015) that the formation of a bubble at the tip of a plectoneme (a tip-bubble) could pin the plectoneme. Sequences high in AT content were found to be more likely to form tip-bubbles, and intriguingly, RNA polymerase has been shown to segregate to plectoneme tips (ten Heggeler-Bordier et al., 1992), suggesting that there is a co-localization of plectoneme tips with AT rich promotor sequences. Furthermore, it was predicted by simulations (Matek, 2014; P. R. Desai et al., 2020), theory (Brahmachari et al., 2018), and, importantly, shown by magnetic tweezer experiments (Dittmore et al., 2017), that base pair mismatches can also co-localise with plectoneme tips. Preliminary simulations using oxDNA by Randisi suggest that thymine dimers may also co-localise with plectoneme tips (Randisi, 2019). Taken together, theses previous results suggests a number of hypotheses for thymine dimers. *Firstly*, that they may also co-localise with plectoneme tips, which can lead to pinning that may enhance the ability of repair enzymes to locate thymine dimer damage. *Secondly*, such co-localisation may lead to tip-bubbles, which can enhance the probability that the thymine dimer base pair is in an extrahelical arrangement and may provide a possible pathway for the passive model.

This chapter is organised as follows: First, we describe the thymine dimer model that Randisi developed using the oxDNA forcefield. Then, through molecular tweezer simulations, we show that plectoneme tip-bubbles reveal an extra-helical

arrangement of thymine dimers and that these tip-bubbles strengthen the pinning of the plectoneme. Increasing twist increases the probability that thymine dimer base-pairs denature and supercoiling induced plectoneme tip-bubbles further enhances this effect. Finally, we comment on the robustness of our results to model choice, and discuss some potential biological consequences of our findings.

3.1 Thymine dimer model in oxDNA

To demonstrate the feasibility of modelling thymine dimers with oxDNA, we need to ensure that the model can reproduce well-established structural and thermodynamic effects of thymine dimers on DNA. Melting experiments have shown that the presence of a thymine dimer can produce a significant drop in the DNA melting temperature in short oligomers (McAteer et al., 1998; Kemmink et al., 1987; Barone et al., 1995; Taylor et al., 1990), ranging from 8°C for a DNA dodecamer at 0.25 M [NaCl] and a strand concentration of 1 mM (McAteer et al., 1998), to 13°C for an octamer at 0.2 M [NaCl] and a DNA concentration of 3 mM (Kemmink et al., 1987). Thymine dimers are also reported to induce a bend in double-stranded DNA though there is no clear consensus in the magnitude of the bend across these studies. NMR studies suggest a bend angle θ_0 around 10° (McAteer et al., 1998; C.-I. Wang & Taylor, 1991; J.-K. Kim et al., 1995) while the crystal structure of Park *et al.* (Park et al., 2002) and the pioneering gel and electron microscope studies by Husain *et al.* (Husain et al., 1988) suggest that $\theta_0 \approx 30°$. Atomistic simulations of DNA with thymine dimers do not provide much extra insight into the precise value of θ_0, with estimates in the literature ranging from approximately 15° to 30° (Rao et al., 1984; Pearlman et al., 1985; Miaskiewicz et al., 1996).

Estimates of the detailed effects of thymine dimers on the helical parameters are

also available. NMR Studies by McAteer *et al.* (McAteer et al., 1998) suggest an increase of approximately 26° in the roll angle between the thymine dimer-containing base pairs and a decrease of approximately 9° in the tilt between the same base pairs (from $\sim -1°$ in the native DNA, to $\sim -10°$ in the thymine dimer DNA). The crystal structure of Park *et al.* (Park et al., 2002), on the other hand, yields an increase in roll of 22° but did not report the tilt. In both studies, the twist angle between the central thymine base pairs of the CPD is reported to decrease, although the magnitude of the decrease varies, with McAteer *et al.* suggesting a decrease of 15° and Park *et al.* a 9° decrease. Results from atomistic molecular dynamics (MD) simulations also show an increase in roll and a decrease in twist between the thymine dimer base pairs (relative to undamaged base pairs) but no change in tilt for the thymine-dimer base pairs (Knips & Zacharias, 2015).

In creating the thymine dimer model within the oxDNA environment, Randisi focused on reproducing the change in roll angle, DNA melting temperature, and DNA bend angle (Randisi, 2019). There is reasonable consensus on the first two of these properties, but somewhat less agreement on the latter. Changes to tilt were not explicitly incorporated into the model, in part because the introduction of roll is sufficient to generate a bend in DNA, and in part because the results of (Knips & Zacharias, 2015) suggest little change to the tilt.

The modifications introduced into oxDNA to model thymine dimers are illustrated in Fig. 3.1. The stacking and hydrogen bond potentials V_{stack} and V_{HB} as defined in Appendix A of Ref. (Ouldridge et al., 2011) (also see Eq. 2.1) are now replaced via:

$$\begin{aligned} V_{\text{stack}} &\longrightarrow \epsilon_{\text{stack}} V_{\text{stack}} = \epsilon_{\text{stack}} f_1(r_{\text{stack}}) f_4(\theta_4) f_4(\theta_5) f_4(\theta_6) f_5(\cos(\phi_1)) f_5(\cos(\phi_2)) \\ V_{\text{HB}} &\longrightarrow \epsilon_{\text{HB}} V_{\text{HB}} = \epsilon_{\text{HB}} f_1(r_{\text{bond}}) f_4(\theta_1) f_4(\theta_2) f_4(\theta_3) f_4(\theta_4) f_4(\theta_7) f_4(\theta_8) \end{aligned} \tag{3.1}$$

ϵ_{stack} and ϵ_{HB} are the stacking and hydrogen bond strength modifier respectively. The functional forms and variables used in Eq. 3.1 are defined in Ref. (Ouldridge et al., 2011).

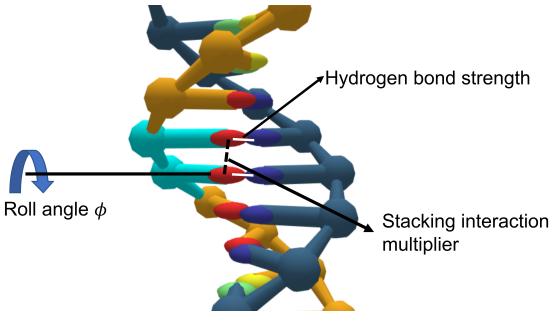


Figure 3.1: The oxDNA thymine dimer model (highlighted in cyan). Nucleotides are represented by the colours: red (T), blue (A), green (C) and yellow (G). The white lines represent the weakened hydrogen bonding while the strengthened stacking interaction is denoted by a dashed black line.

The stacking potential V_{stack} is further modified by introducing an increased roll angle ϕ to the thymine dimer-containing nucleotide, similar to that observed experimentally. Specifically, the base normal $\hat{\mathbf{n}}$ of the nucleotide in the $3'$ direction is rotated by $-\phi$ (right hand rule) around the backbone-base unit vector $\hat{\mathbf{b}}$ of the nucleotide before the interaction potential is computed in a typical MD algorithm or energy minimisation simulation.

$$\hat{\mathbf{n}}_{\text{rotated}} = \hat{\mathbf{n}}\cos\phi - \left(\frac{\hat{\mathbf{b}}}{|\hat{\mathbf{b}}|}\times\hat{\mathbf{n}}\right)\sin\phi + \frac{\hat{\mathbf{b}}}{|\hat{\mathbf{b}}|}\left(\frac{\hat{\mathbf{b}}}{|\hat{\mathbf{b}}|}\cdot\hat{\mathbf{n}}\right)(1-\cos\phi) \tag{3.2}$$

Further details of how $\hat{\mathbf{n}}$ and $\hat{\mathbf{b}}$ are defined can be found in Appendix B of Ref. (Ouldridge et al., 2011). Note that in Randisi's TD model, $\hat{\mathbf{n}}$ in V_{stack} is replaced by $\hat{\mathbf{n}}_{\text{rotated}}$ but the original $\hat{\mathbf{n}}$ is used in all the other oxDNA interaction terms.

To demonstrate that the introduction of a non-zero roll angle can generate a noticeable bending of the DNA, Randisi performed potential energy minimisation using the modified interaction terms (Eq. 3.1 & 3.2) on a 40-bp DNA duplex. This produced the bent DNA shown in Fig. 3.2.

For the thymine dimer model that we are going to use in this chapter, the roll is adjusted in a single base pair by $27.1°$, in part to match the roll and bend angle values reported by McAteer *et al.* (McAteer et al., 1998). The stacking interaction for the thymine dimer-containing base step is enhanced by a factor of ten (i.e. $\epsilon_{\text{stack}} = 10$) to mimic the covalent bonds between the thymines. Finally, hydrogen bonding is weakened in the TD base pairs by setting ϵ_{HB} to be 0.4. As we will show in the subsections below, these parameter choices are sufficient to reproduce the desired bend angle and melting temperature of a TD-containing dsDNA.

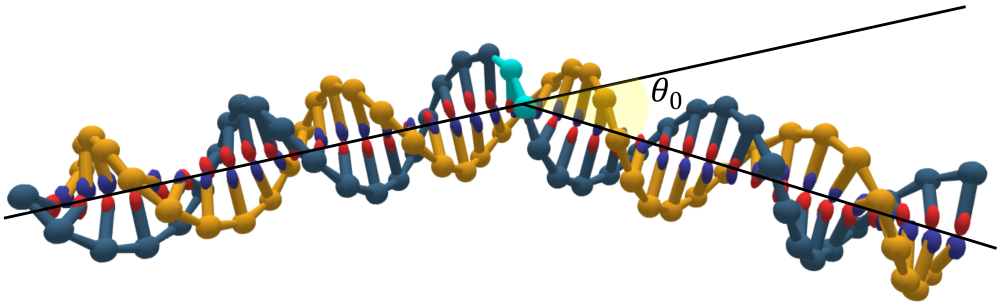


Figure 3.2: The introduction of a finite roll in the thymine dimer model induces a localised dsDNA bend angle of θ_0 after energy minimisation is carried out on a 40-bp DNA duplex that contains the thymine dimer (in cyan) (Randisi, 2019). The angle θ_0 is defined by first assigning each base pair on the DNA into one of two groups, depending on which side of the thymine dimer it is located. Lines are then fitted through the midpoints of the base pairs of each of the two groups, and used to calculate the bend angle, as in Ref. (G. Chatterjee et al., 2017).

3.1.1 Bend angle of TD dsDNA

We seek to measure the thermalised value of the dsDNA bend angle induced by the thymine dimer. MD simulations were carried out at $T = 300\,\text{K}$ and a salt concentration of $0.16\,\text{M}$ on the same 40-bp DNA duplex used in the energy minimisation protocols by Randisi (Randisi, 2019). The length of the simulation runs were 10^8 time steps (using an integration time step of 6.06 fs). For each system of

interest, at least three independent runs were carried out. The dsDNA bend angle reported in the paper is the averaged value obtained from these runs, each with a standard mean error of $1.3°$ or less.

The bend angle's definition follows the one shown in Fig. 3.2. Each base pair on the DNA is assigned into one of two groups, depending on which side of the thymine dimer it is located. Lines are then fitted through the base pairs' centres of mass of each of the two groups, and used to calculate the bend angle θ_0. In defining the centre of mass of a base pair, a small offset in the direction of the major groove is introduced to correct for the helicity of the duplex contour (Chhabra et al., 2020). Because fraying of base pairs at the end of the dsDNA was observed in our simulations, the terminal base pairs were not used in line fitting. The thymine dimer and the base pairs adjacent to the dimer were also not included in the line fitting.

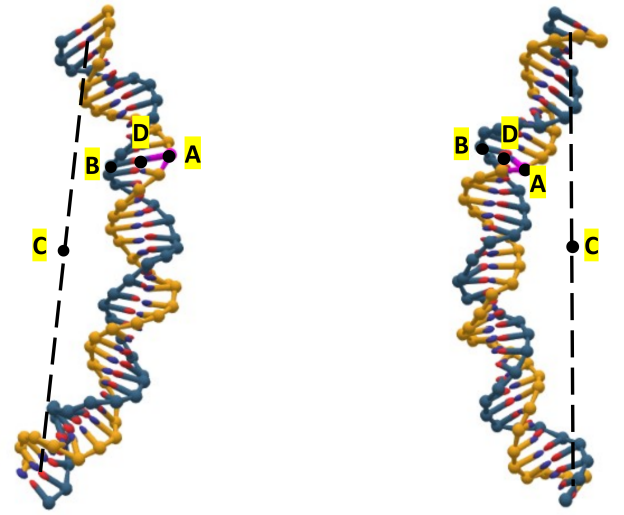


Figure 3.3: Points A and B are taken to be the centre of mass of off-centre nucleotides, while D is the mid-point of A and B. C is taken to be the centre of mass of the second last base pairs on both ends of the dsDNA.

The sign of the bend angle is determined using the convention outlined in Fig. 3.3. When $\vec{AB} \cdot \vec{DC} > 0$, the angle is taken to be positive. Likewise, when $\vec{AB} \cdot \vec{DC} < 0$, the angle becomes negative. The calculated bend angle is observed

to vary sinusoidally with the position of $\vec{AB}$. Thus, we choose to position $\vec{AB}$ at a distance of 7 bps away from the thymine dimer as this gives a maximum calculated bend angle for the damaged DNA. The bending induced by the thymine dimer is roughly towards the major groove. Using this convention, the bend angle of the undamaged dsDNA was found to be a negligible $-0.1 \pm 1.3°$ while the bend angle of the thymine dimer-containing dsDNA was calculated to be $11.3 \pm 0.3°$. This is slightly smaller than the bend angle value of approximately $15.0°$ that Randisi obtained from energy minimisation (Randisi, 2019), suggesting that the bend fluctuations are not symmetric around the potential minimum.

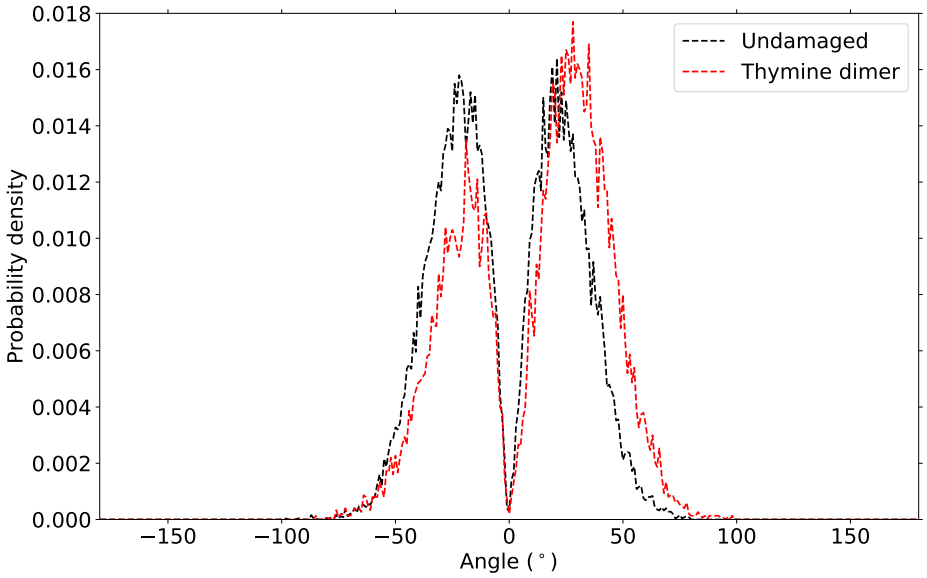


Figure 3.4: Probability density distribution of bend angles for the undamaged and thymine dimer-containing dsDNA. The sharp decrease in probability density at $\theta = 0°$ arises because the number of states with a given θ varies as $\sin\theta$ (see, for instance, Ref. (A. Vologodskii & D. Frank-Kamenetskii, 2013)). A bin width of $1°$ was used.

The standard deviation $\sigma_\theta = \sqrt{\langle\theta_0^2\rangle - \langle\theta_0\rangle^2}$ of the bend angle fluctuations is also measured (Fig. 3.4), but we did not find any significant difference between the standard deviation of the bend angle fluctuations in undamaged dsDNA ($\sigma_\theta =$

$28.5 \pm 0.1°$) and that of the thymine dimer-containing dsDNA ($\sigma_\theta = 31.0 \pm 0.1°$). The full probability distributions for θ are illustrated in Fig. 3.4.

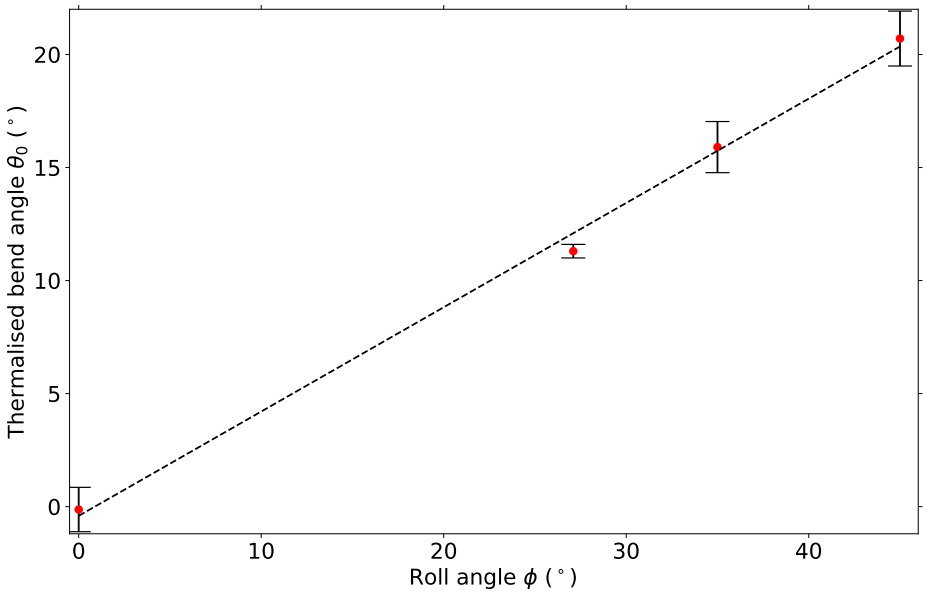


Figure 3.5: Linear relation between the thermalised bend angle θ_0 of the TD duplex and the roll angle ϕ of the TD model. The error bars are statistical errors obtained from block averaging (Frenkel & Smit, 2001).

Finally, we examine the variation of the thermalised bend angle θ_0 with the roll angle ϕ in the TD model. A linear relation between θ_0 and ϕ, similar to the one obtained by Randisi via energy minimisation, is observed (Fig. 3.5).

3.1.2 Melting temperature of TD dsDNA

We use the octamer sequence studied by Kemmink *et al.* (Kemmink et al., 1987) as a benchmark for measuring the change in melting temperature induced by the thymine dimer model. Umbrella sampling simulations using the Virtual Move Monte Carlo (VMMC) algorithm (Whitelam & Geissler, 2007) were carried out (as in (Ouldridge et al., 2010; Šulc et al., 2012)) to measure the melting temperature of both undamaged and thymine dimer-containing octamers. First, we use

a monovalent salt concentration of 0.3 M in the simulations to match the experimental buffer solution of 50 mM potassium phosphate and 0.2 M sodium chloride. Next, we place the duplex–an 8-bp dsDNA–in a cubic periodic box with a side length of 6.52 nm. This gives us a matching dsDNA concentration of 6 mM. To ensure that the standard mean error is below 0.2 K, simulations were carried out for at least 5 independent replicas of each system. This results in a ΔT_m of 12.3 K (with a standard mean error of ± 0.1 K), well within the error margins (± 3 K) of the experimental value of 13 K reported by Kemmink *et al*.

3.1.3 Twist absorption by TD

NMR studies and crystal structure analysis reported a decrease in the twist angle between the central thymine base pairs of the CPD that ranges from 9° (Park et al., 2002) to 15° (McAteer et al., 1998). The thymine dimer model used here is not parametrised against these experimental values of twist in the thymine dimer, but it is still interesting to see how twist angle measurements from our simulations of thymine dimer-containing dsDNA compare against these experimental values.

The definition of twist angle follows from the approach taken by Skoruppa *et al.* (Skoruppa et al., 2017). A rotation vector $\boldsymbol{\Theta}^{(i)}$ represents the rotation of the orthonormal triad $\{\hat{\mathbf{e}}_1(i), \hat{\mathbf{e}}_2(i), \hat{\mathbf{e}}_3(i)\}$ associated with base pair i onto the adjacent triad $\{\hat{\mathbf{e}}_1(i+1), \hat{\mathbf{e}}_2(i+1), \hat{\mathbf{e}}_3(i+1)\}$, where $\hat{\mathbf{e}}_1$ is oriented towards the major groove, $\hat{\mathbf{e}}_2$ is along the direction of base pairing and $\hat{\mathbf{e}}_3$ is along the DNA contour. The twist angle between these two base pairs is given by the third component of the rotation vector Θ_3. In all our twist angle calculations, $\hat{\mathbf{e}}_3$ is defined using "Triad III" that is described in the supplementary materials of Ref. (Skoruppa et al., 2017).

Twist angle measurements on the same thymine dimer-containing 40-bp duplex

used in the bend angle measurements in subsection 3.1.1 are presented in Fig. 3.6. There is a model-specific pattern of slightly reduced twist angles close to the thymine dimer, with the largest decrease of 2° detected at base pair index 20, where the thymine dimer-containing nucleotide in the $3'$ direction is located. The magnitude of decrease in twist angle is too small compared to experimental values but this should not come as a surprise since our parameter choices for the thymine dimer model are not designed to reproduce the experimental twist values. Later, in the robustness analysis section, we will see how variations in the model parameters can alter the amount of twist absorption by the thymine dimer.

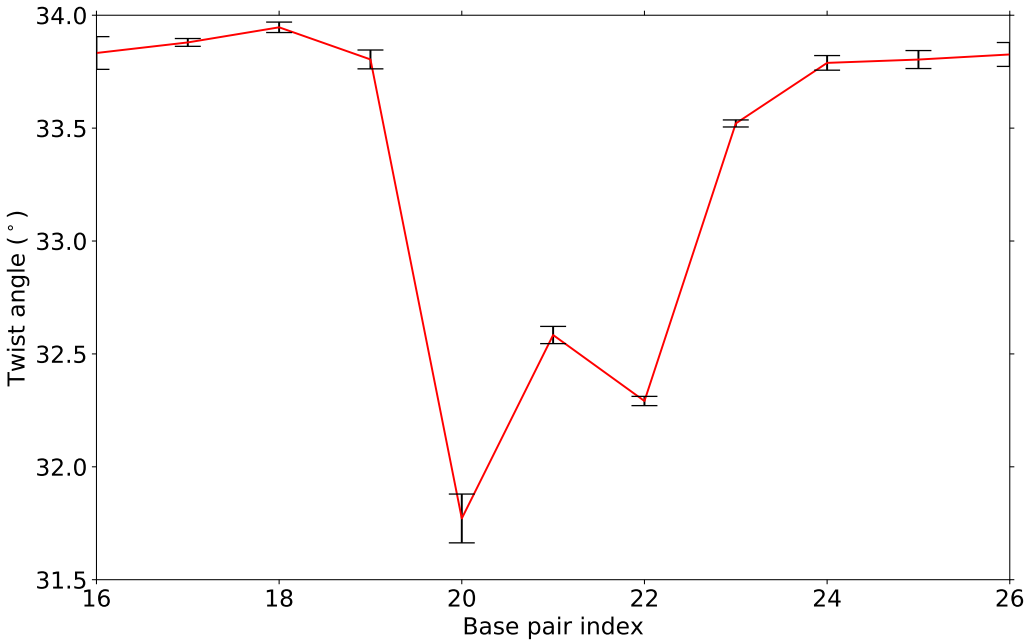


Figure 3.6: Twist angles measurements for the thymine dimer-containing 40-bp duplex used in subsection 3.1.1. The value indicated at base pair index i represents the twist angle between base pair i and base pair $i-1$. Error bars represent standard errors of the mean. The two thymine dimer is located at positions 20 and 21.

3.2 Interplay between DNA supercoiling and the thymine dimer

To test our hypothesis on the effects thymine dimers may have on the global supercoiled structure of DNA and vice versa, we perform molecular tweezer simulations based on the protocol outlined in subsection 2.2. A 600-bp dsDNA with the sequence described in Appendix A.1 has one end fixed in space, and the other end pulled with a force F and simultaneously over/under-twisted at a rotation period of 10^7 MD simulation steps per turn. Configurations at the desired superhelical density σ and force F were extracted from these simulations for further equilibration before observables of interest are measured. Two sets of simulations were carried out: one involving undamaged dsDNA which serves as a reference point, and the other involving thymine dimer-containing dsDNA. The thymine dimer defect is placed 110 bps away from the centre of the DNA. Moving the defect away from the centre helps highlight the effect of plectonemic pinning because the repulsion planes on the duplex ends mean that for homogeneous DNA, the plectoneme is most likely to be near the centre of the DNA, an effect that can be quite pronounced for these lengths (Matek et al., 2015).

3.2.1 Extrahelical arrangement of the thymine dimer

DNA can relieve the imposed twist by buckling to form a plectoneme or by denaturing to form bubbles, which have a much lower twist modulus and so can absorb some of the torsional strain. The relaxation pathway that DNA adopts depends on the applied force. For a given supercoiling density σ, plectonemes are favoured for low forces, and bubbles for larger forces (J. Marko & Siggia, 1995; Strick et al., 2002; Salerno et al., 2012).

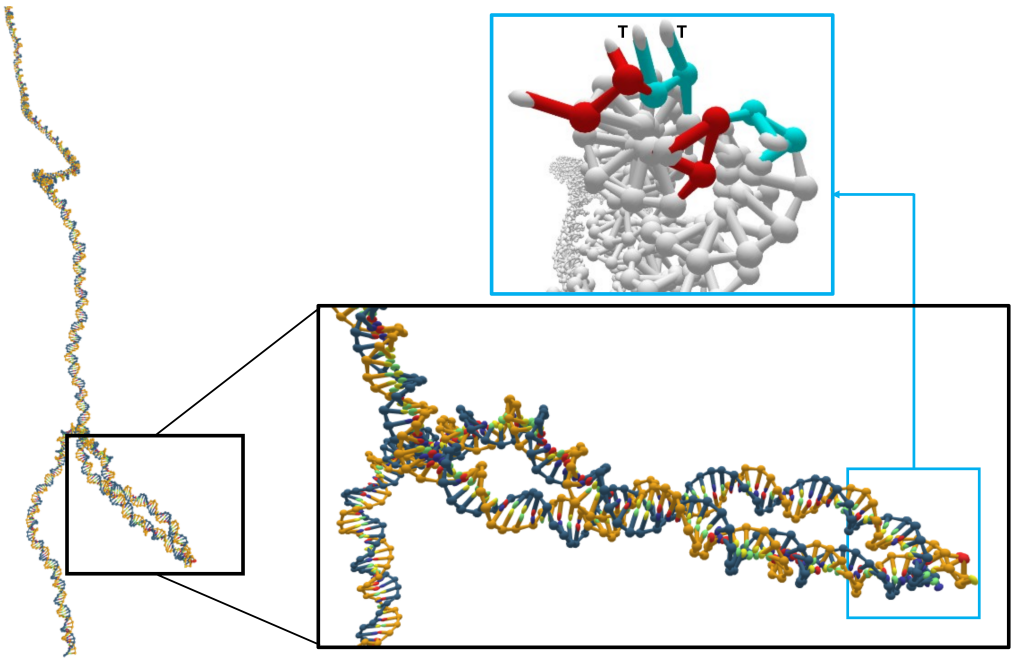


Figure 3.7: Structure of a 600-bp supercoiled DNA duplex with a thymine dimer 110 bps away from the centre for $F = 1.5\,\text{pN}$ and $\sigma = -0.073$. The flipped-out thymine dimer base pairs are coloured in cyan (with the thymine bases labelled as T) while the surrounding denatured base pairs are coloured in red (light blue box).

An intermediate tip-bubble regime where a bubble localizes at the plectoneme tip, was discovered by Matek *et al.* (Matek et al., 2015) using oxDNA simulations. For this state, the cost of breaking bonds to form the bubble is compensated by several effects. Firstly, the denatured tip reduces the overall curvature of the plectoneme end-loop. This leads to a smaller bending cost as well as a reduction ΔL of the loop size, which means an additional energy gain of $F\Delta L$. Secondly, the tip-bubble can absorb some of the torsion just as a normal bubble can. Together, these effects can lead to a tip-bubble regime.

Thymine dimers can enhance plectoneme and tip-bubble formation for two main reasons. Firstly, the intrinsic bending reduces the cost to form an initial loop of the plectoneme. For example, it has also been shown that plectonemes localize at sequences with enhanced curvature (S. H. Kim et al., 2018). Secondly, the reduced

strength of base-pairing lowers the cost of forming a bubble at the thymine-dimer site. Fig. 3.7 depicts such a tip-bubble, illustrating how this mechanism results in the presence of an exposed unbound thymine dimer at the kinked site of the plectonemic tip-bubble.

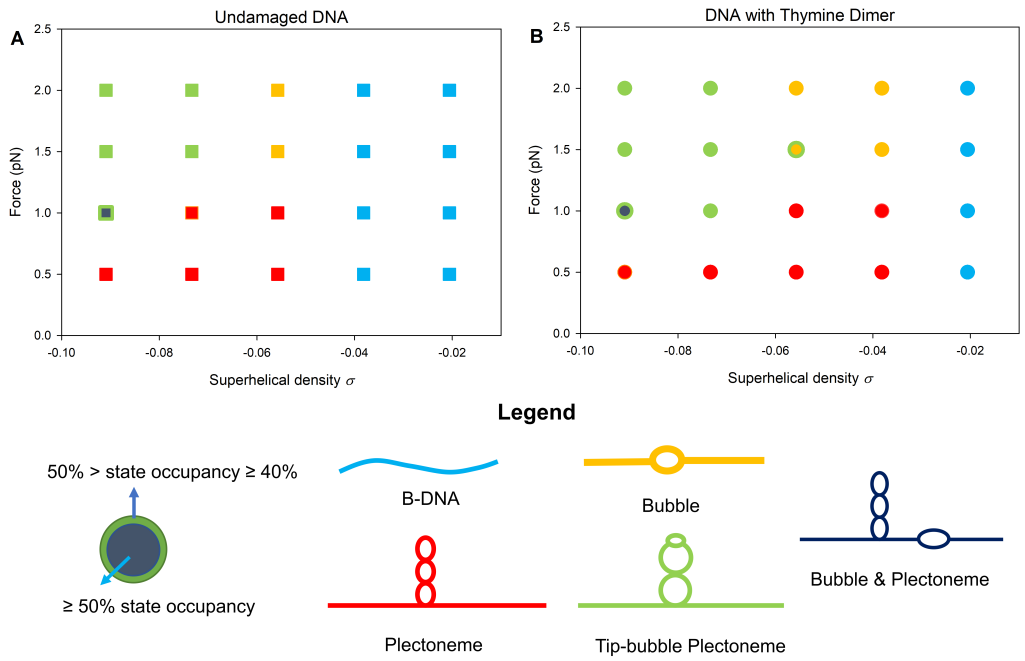


Figure 3.8: Force-torsion state diagrams for (A) undamaged and (B) thymine dimer-containing DNA. For each (σ, F) point simulated the dominant state is identified. A bubble is defined by the denaturation of at least two consecutive base pairs (a base pair is considered denatured if the binding energy is less than 10% of its maximum possible value). Plectonemes are detected using the algorithm described in the supplementary material of Matek *et al.* (Matek et al., 2015). B-DNA is the canonical state where no bubbles or plectonemes are present. A plectoneme is identified as having a tip-bubble, if a kink defect of a few broken base pairs is localised at the tip of the plectoneme (defined here as when the distance between the centre of the bubble and the centre of the plectoneme is less than 20 bps). The dominant states is defined as having a state occupancy $\geq$ 50%; mixed states with occupancy $\geq$ 40% but below 50% are also highlighted. At low forces, the presence of a thymine dimer enhances the occupancy of the plectonemic state (relative to the undamaged DNA) at low superhelical densities. The presence of the thymine dimer also increases the tip-bubble plectoneme and bubble state occupancy at low superhelical densities for F = 1.5 pN and 2 pN.

To quantify the extent of the tip-bubble regime in thymine dimer-containing ds-DNA, we compare, in Fig. 3.8, the force-torsion state diagrams for undamaged and thymine dimer-containing dsDNA. The different states DNA can adopt are characterised as follows:

- B-DNA: the canonical form of DNA where no plectonemes or bubbles are detected. B-DNA can be twisted or unstressed.
- Plectoneme: intertwined extended structure that is detected using the algorithm described in the supplementary material of Matek *et al.* (Matek et al., 2015). In brief, the algorithm operates on the idea that plectonemes bring distant base pairs into close contact with each other. It locates and identifies non-adjacent base pairs N_c bps apart along the strand that are separated by a spatial distance d_c or less. For the salt concentration that we are using for this work, $N_c = 40$ and $d_c = 10.65$ nm.
- Bubble: A base pair is denatured when its binding energy is less than 10% of its maximum possible value (Šulc et al., 2012). A bubble is identified when at least two consecutive base pairs are denatured.
- Tip-bubble plectoneme: A tip-bubble is identified when the centre of the bubble is located within 20 bps on either side of the plectoneme tip (the plectoneme tip is identified by the plectoneme detection algorithm of Matek *et al.*)
- Bubble & plectoneme: Both bubble and plectoneme are detected, but they are not co-localised as per the definition of a tip-bubble plectoneme.

State occupancies are obtained by computing the ratio between the number of times the dsDNA adopts the said state during the sampling process and the total number of times the MD production trajectory is sampled. The state is defined as

being "dominant" for a given superhelical density σ and external force F when its occupancy exceeds 0.5 or 50%. The force-torsion state diagrams in Fig. 3.8 flag out dominant states that the dsDNA adopts at various σ and F.

Not surprisingly, for reasons we had stated above, plectonemes start to form at lower σ for the damaged DNA than for undamaged DNA (compare $\sigma \approx -0.038$). Tip-bubble plectonemes start to form at lower force and σ as can be seen, for example by comparing both diagrams at $\sigma \approx -0.056$, and $\sigma \approx -0.073$, for forces of $F = 1.0\,\text{pN}$ and $F = 1.5\,\text{pN}$, respectively.

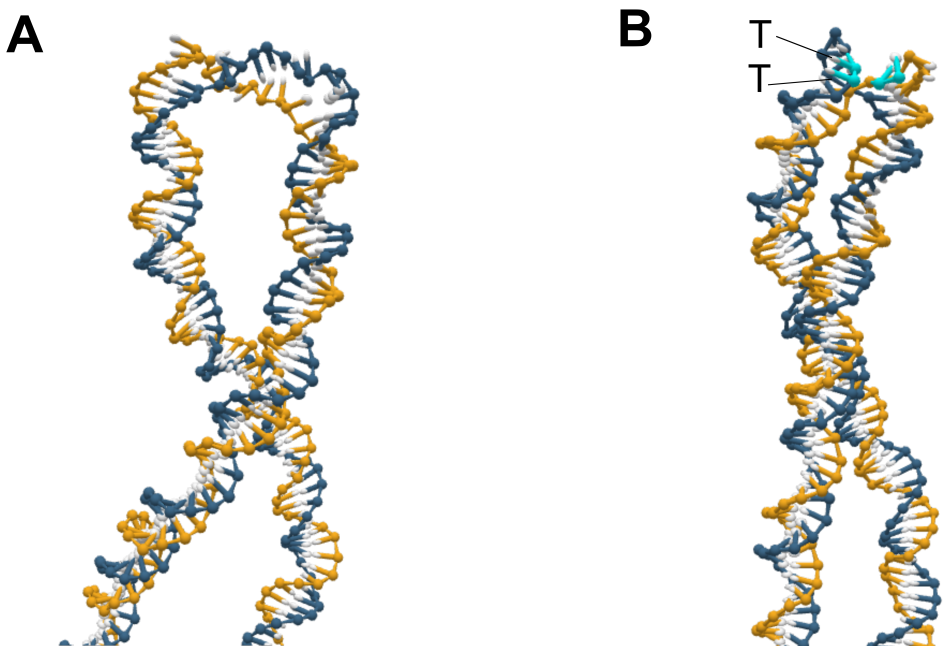


Figure 3.9: End-loop of a plectoneme with a tip-bubble for (**A**) undamaged ds-DNA and (**B**) dsDNA containing a thymine dimer. Both are from simulations at $\sigma \approx -0.091$ and $F = 1.5$ pN. The thymine dimer is highlighted in cyan and the thymine bases are labelled with 'T's.

We also observe from our MD trajectories that the end-loops of tip-bubble plectonemes in thymine dimer-containing dsDNA are more highly bent than that of the undamaged dsDNA (Fig. 3.9). We can quantify this observation by measuring the end-loop angle of tip-bubble plectonemes in undamaged and thymine dimer-

containing dsDNA, following closely the definition of end-loop angle used by Desai *et al.* in their paper (P. R. Desai et al., 2020). Taking the centre of the plectoneme to be i, three blocks of 5 bps are defined along the end-loop: $i-12$ to $i-8$ bp (block 1), $i-2$ to $i+2$ bp (block 2), and $i+8$ to $i+12$ bp (block 3). The end-loop angle is then obtained from the dot product of the vectors connecting the centre of masses of these three blocks (i.e. block 1 and 2, as well as block 3 and 2). Fig. 3.10 illustrates this definition. Since the plectoneme detection algorithm by Matek *et al.* (Matek et al., 2015) does not always pinpoint the exact location of the plectoneme tip, the centre of the plectoneme i is varied by 15 bps on each side. The smallest value of the angle that we obtain from this variation is then set as the end-loop angle (i.e. we are effectively defining the tip of the end-loop as the point with strongest bending).

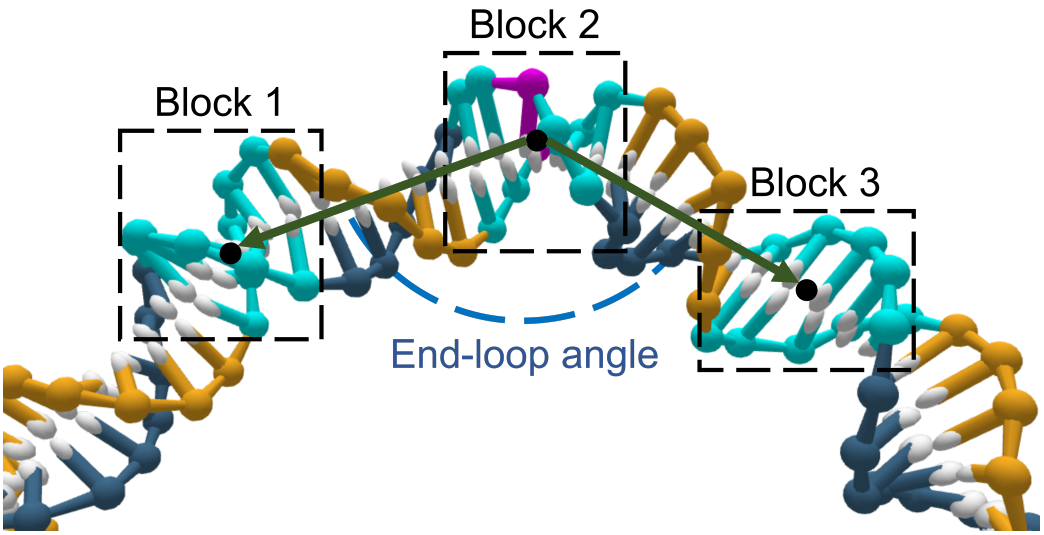


Figure 3.10: Definition of the end-loop angle. In this illustration, the tip of the plectoneme is taken to be the base pair coloured in purple (base pair i). From there, three blocks of 5 bps (coloured in cyan) are defined: $i-12$ to $i-8$ bp (block 1), $i-2$ to $i+2$ bp (block 2), and $i+8$ to $i+12$ bp (block 3). The end-loop angle is then defined as the angle between the vectors connecting the centres of mass of blocks 1 and 2, and blocks 3 and 2.

In Fig. 3.11 we show the results for the end-loop angle in a regime where the tip-bubble plectoneme is the dominant state for both undamaged and TD-containing dsDNA (see Fig. 3.8). The end-loop is much more strongly bent when the thymine dimer is present.

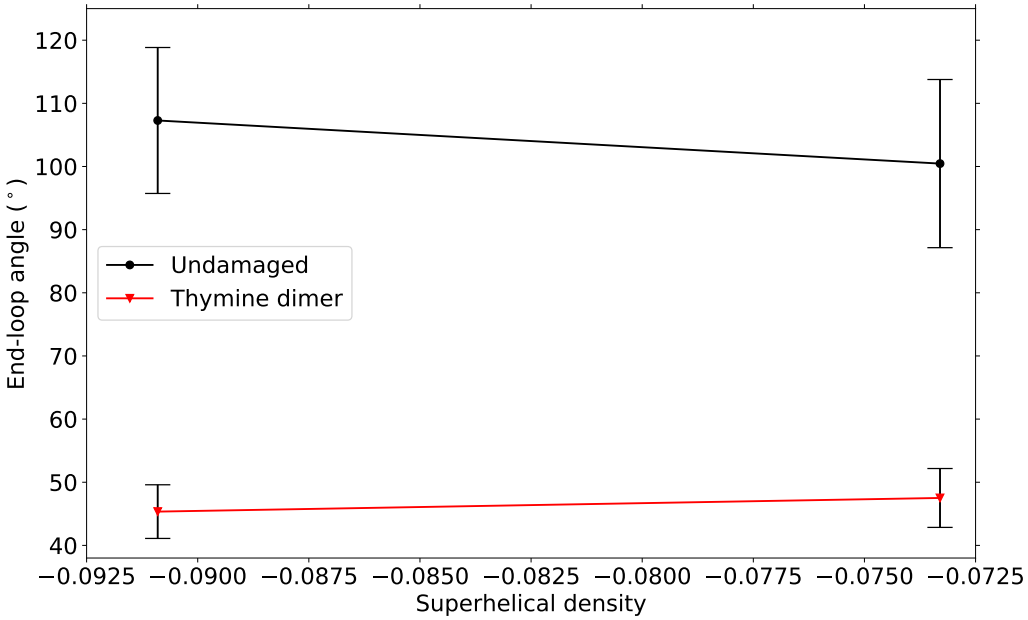


Figure 3.11: The end-loop angle of the tip-bubble plectoneme is measured at $F = 1.5$ pN at two superhelical densities σ where the tip-bubble plectoneme is the dominant state in both undamaged and thymine dimer-containing dsDNA. At $\sigma \approx -0.073$ and $F = 1.5$ pN, the tip-bubble plectoneme occupancy rates are 0.65 and 0.93 for the undamaged and thymine dimer-containing dsDNA respectively. At $\sigma \approx -0.091$ for the same value of F, the occupancies become 0.71 and 0.99 for the undamaged and thymine dimer-containing dsDNA respectively. Error bars represent the standard error of the mean (SEM).

3.2.2 Plectonemic pinning

Using the plectoneme detection algorithm by Matek *et al.* (Matek et al., 2015), we tracked the diffusion of plectonemes with and without damage, and representative results at a state point where tip-bubble plectonemes are also observed for the undamaged case can be seen in Fig. 3.12. While tip-bubble plectonemes have

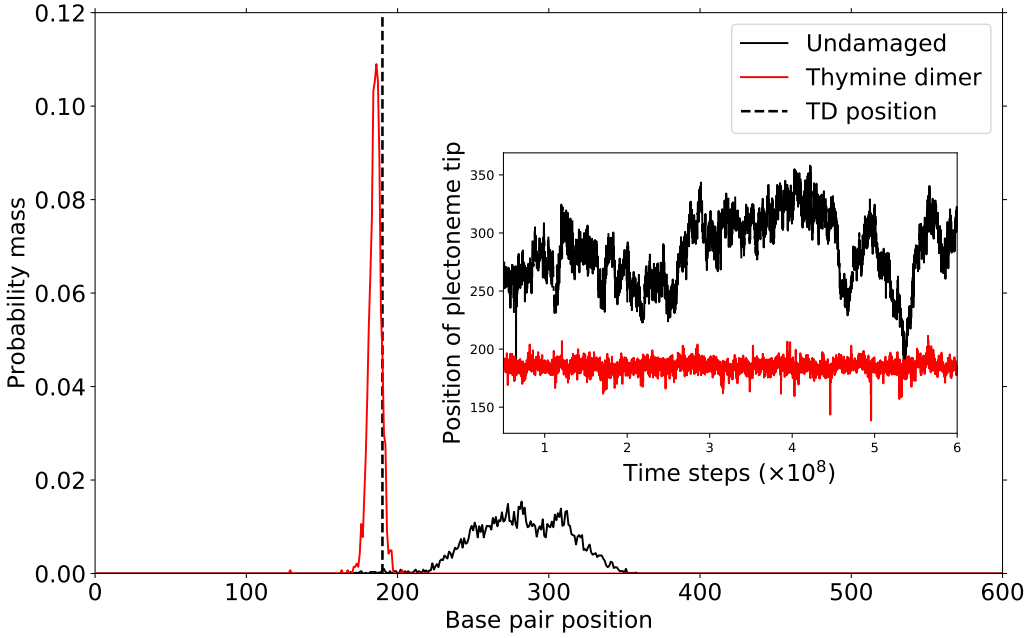


Figure 3.12: Plectoneme position distributions corresponding to state point $F = 1.5\,\text{pN}$ and $\sigma \approx -0.073$. (Inset) The plectoneme position as a function of time. For $F = 1.5\,\text{pN}$ and $\sigma \approx -0.073$, we find that for undamaged DNA the plectoneme can diffuse along the duplex, while when a thymine dimer (TD) is present the plectoneme is strongly localised in one place due to the co-localisation of the tip-bubble with the thymine dimer. Data such as the ones shown here could, in principle, shed some insights on the diffusion dynamics of plectonemes (see, for instance, the report by van Loenhout *et al.* (van Loenhout et al., 2012)).

previously been shown to be more likely to occur in regions with high AT content (Matek et al., 2015), we found that the plectoneme in the undamaged DNA is not strongly localised to a specific part of the duplex for the sequence we used here. By contrast, as can be seen for the thymine-dimer containing duplex in Fig. 3.12, the tip-bubbles preferentially form at the site of the damage, and very strongly pin the plectoneme. We can quantify this observation further by measuring the probability of co-localising the thymine dimer with the tip of the plectoneme (i.e. a TD plectoneme) as a function of superhelical density σ and force F. The probability or state occupancy of the TD plectoneme remains relatively low for the most

part except when the dsDNA is in the tip-bubble plectoneme state at high F and σ (Fig. 3.13). This suggests that the thymine dimer, based on the current set of parameter choices, is unable to pin the plectoneme on its own, and instead relies on tip-bubble formation at high F and σ to drive plectonemic pinning.

To further verify that the reduced plectonemic diffusivity is directly attributed to the tip-bubble instead of the thymine dimer alone, similar simulations were carried out in the positively supercoiled regime at $F = 1.5\,\text{pN}$ and $\sigma \approx 0.067$. Under these circumstances, the plectoneme in the thymine dimer-containing DNA does not have a tip-bubble and possesses much greater diffusivity (also see Fig. 3.21).

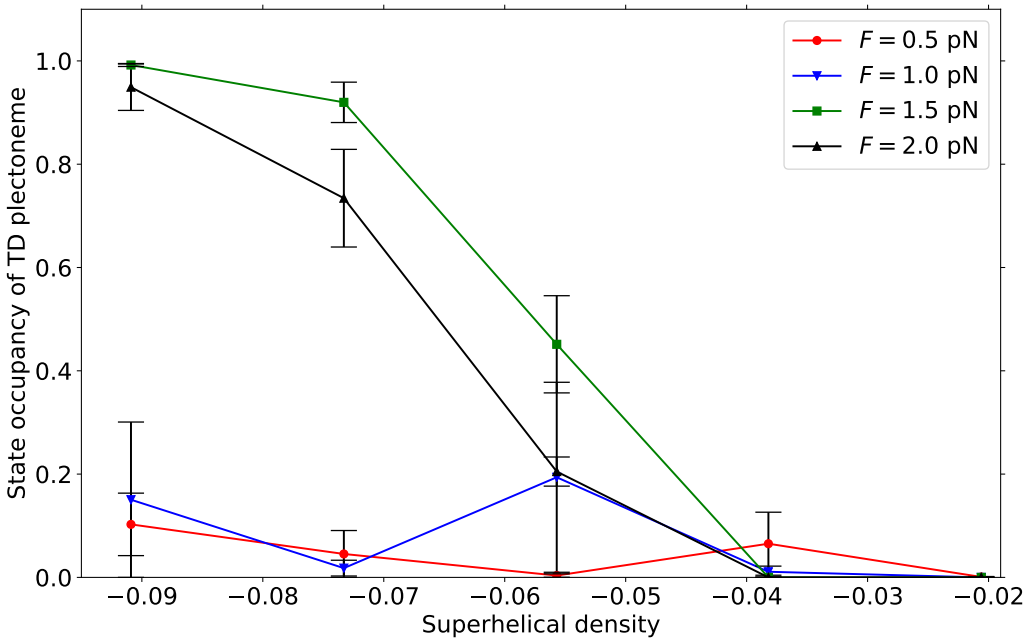


Figure 3.13: The TD plectoneme is defined as a plectoneme with a thymine dimer (TD) within 20 bps on either side of its tip (based on the plectoneme detection algorithm by Matek *et al.* (Matek et al., 2015).). The thymine dimer is shown to be highly localised at the plectoneme tip when the dsDNA is in the tip-bubble plectonemic state at $F = 1.5$ pN and 2.0 pN.

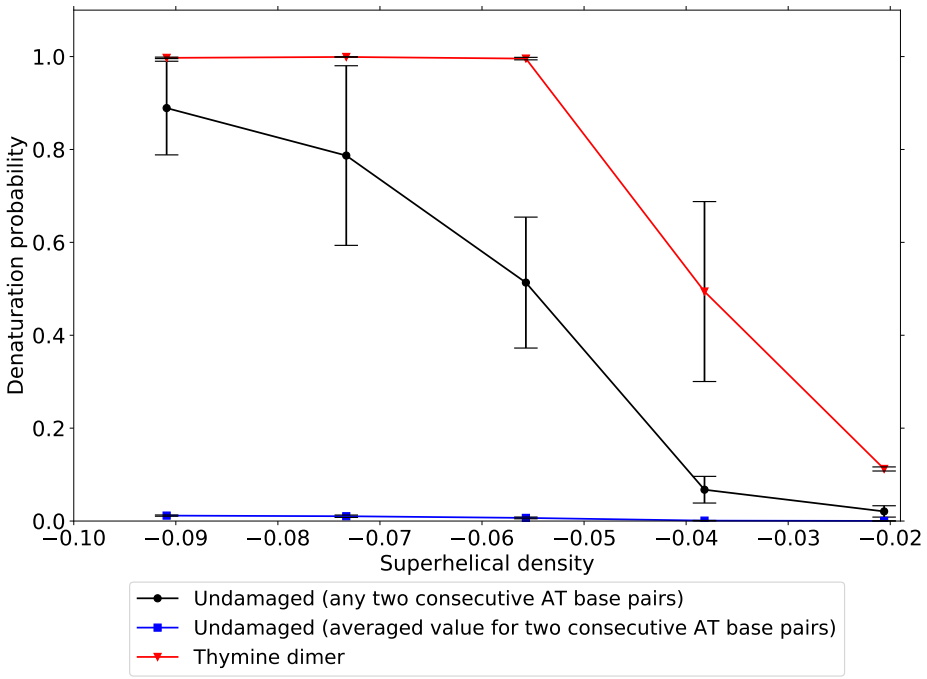


Figure 3.14: Average denaturation probability of the thymine dimer base pairs compared to the probability of *any two* consecutive AT base pairs being open in undamaged DNA at $F = 1.5$ pN. In addition, the blue line shows the averaged probability that a single set of two consecutive AT base pairs is denatured. The thymine dimer base pairs exhibit a higher propensity to denature relative to the undamaged AT base pairs, even at low values of σ where no plectoneme or tip-bubbles are observed. At higher forces and superhelical densities, the co-localisation of the plectoneme tip-bubble and thymine dimer causes the thymine dimer to be part of the denaturation bubble most of the time.

3.2.3 Denaturation probability of the thymine dimer

The stability of the extrahelical arrangement of thymine dimer base pairs can be quantified by measuring the thymine dimer base pairs' denaturation probability (Fig. 3.14). At low forces and $|\sigma|$, the thymine dimer base pairs remain largely in an intra-helical conformation for the values of σ we studied. By contrast, for the applied tensions of 1.5 pN and 2 pN, the thymine dimer base pairs exhibit a much higher propensity to open up at low superhelical densities relative to its un-

damaged counterpart. At these forces, we observe that, as a function of increasing superhelical density, first a bubble forms at the site of the thymine dimer, and then subsequently, plectonemic writhe forms with the bubble at the tip, which then causes the thymine dimer base pair to be denatured most of the time (Fig. 3.15).

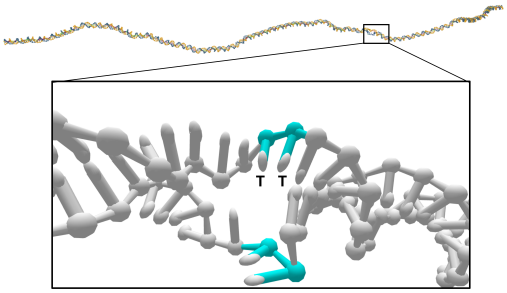


Figure 3.15: A duplex configuration in the bubble state at $F = 1.5\,\text{pN}$ and $\sigma = -0.038$. The bubble preferentially nucleates at the thymine dimer site (coloured in cyan with the thymine bases labelled as T). As more turns are imposed, the denatured site becomes the preferred location for plectoneme formation.

3.2.4 Twist angles

Fig. 3.16 reports the twist angle measurements for the thymine dimer-containing dsDNA in different states (i.e. twisted B-DNA, plectoneme, bubble, tip-bubble plectoneme). In twisted B-DNA and plectonemic DNA when the plectoneme is not localized at the thymine dimer the pattern of twist angle reduction at the thymine dimer is very similar to the reference system of an unstressed dsDNA (Fig. 3.6) albeit with a very small increase in the twist angle reduction. However, when a tip-bubble or bubble is localized at the thymine dimer, the picture is completely different; there is clear absorption of twist at the site of thymine dimer, even leading to large negative left-handed twists close to the thymine dimer.

3.3 Robustness Analysis

As an added layer of checks to ensure that the simulation results are not a peculiarity of the parameters we chose for our thymine dimer model, or an artefact of

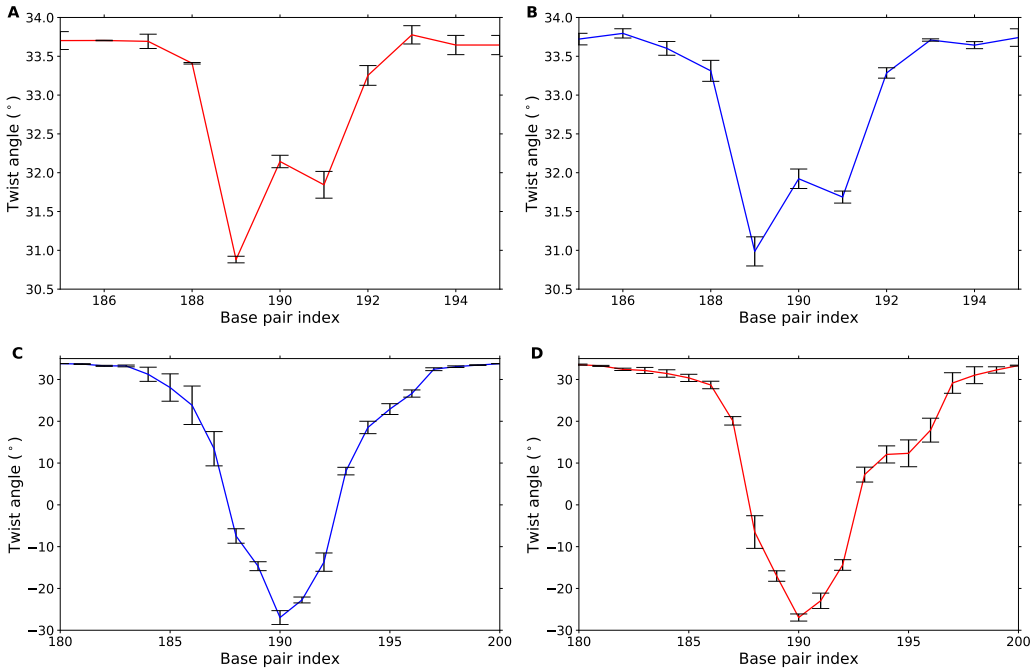


Figure 3.16: Twist angles measurements for the thymine dimer-containing dsDNA at state points (**A**) $F = 0.5$ pN and $\sigma \approx -0.021$ (B-DNA), (**B**) $F = 0.5$ pN and $\sigma \approx -0.056$ (plectoneme), (**C**) $F = 1.5$ pN and $\sigma \approx -0.073$ (tip-bubble plectoneme), and (**D**) $F = 2.0$ pN and $\sigma \approx -0.056$ (bubble). The value indicated at base pair index i represents the twist angle between base pair i and base pair $i - 1$. Error bars represent standard errors of the mean. The two thymine dimer is located at positions 189 and 190.

the particular bending angle experiments we chose to replicate, two other models were created.

The first additional model, dubbed TD1, had the roll angle ϕ adjusted in two adjacent base pairs instead of one and the hydrogen bond strength weakened by 10%. In particular, it produces a larger thermalised bending angle, closer to that which Park *et al*. (Park et al., 2002) observed in their crystal structure. The second model (TD2) generates a bending angle similar to the original model, which we will now call TD0. However, like TD1, it has two base pairs with modified stacking, and like TD0, it has hydrogen-bond weakening of 55%.

Table 3.1: Features of the three thymine dimer models. Standard errors for the mean bending angles obtained using MD simulations are less than 1.3°

	TD0	**TD1**	**TD2**
Roll angle ϕ	27.1°	37.0°	18.3°
Stacking interaction multiplier ϵ_{stack}	10	1	1
Number of base pairs with modified roll	1	2	2
Hydrogen bond weakening	60%	10%	55%
DNA bending angle θ_0	11.3°	30.7°	13.8°

Table 3.1 summarises the features of these three models. Increasing the stacking interaction multiplier ϵ_{stack} or reducing the amount of hydrogen bond weakening in the TD base pair (ϵ_{HB}) stabilises the DNA duplex thermodynamically, while increasing the roll destabilises it. Thus, models with a different balance between these factors can all adequately reproduce the experimental change in melting temperature. The melting temperatures, which were also computed for TD1 and TD2 using the same VMMC protocols as before are presented in Table 3.2. The measured ΔT_m for TD1 and TD2 DNA again fall within the error margins of the experimental value.

Table 3.2: Melting temperature T_m of the thymine-dimer containing octamer used in the study by Kemmink *et al.* (Kemmink et al., 1987) for the three thymine dimer models compared to undamaged DNA and experiment. The melting temperature drop ΔT_m is within the error margins of experimental results for all three models.

	oxDNA				Experiment	
	Undamaged	TD0	TD1	TD2	Undamaged	TD
T_m (°C)	70.4	58.1	58.0	57.0	70	57
ΔT_m (°C)	–	12.3	12.4	13.4	–	13

To extract further insights on the different parameter choices of the thymine dimer models, we measured the amount of twist absorption at the site of TD1 and TD2

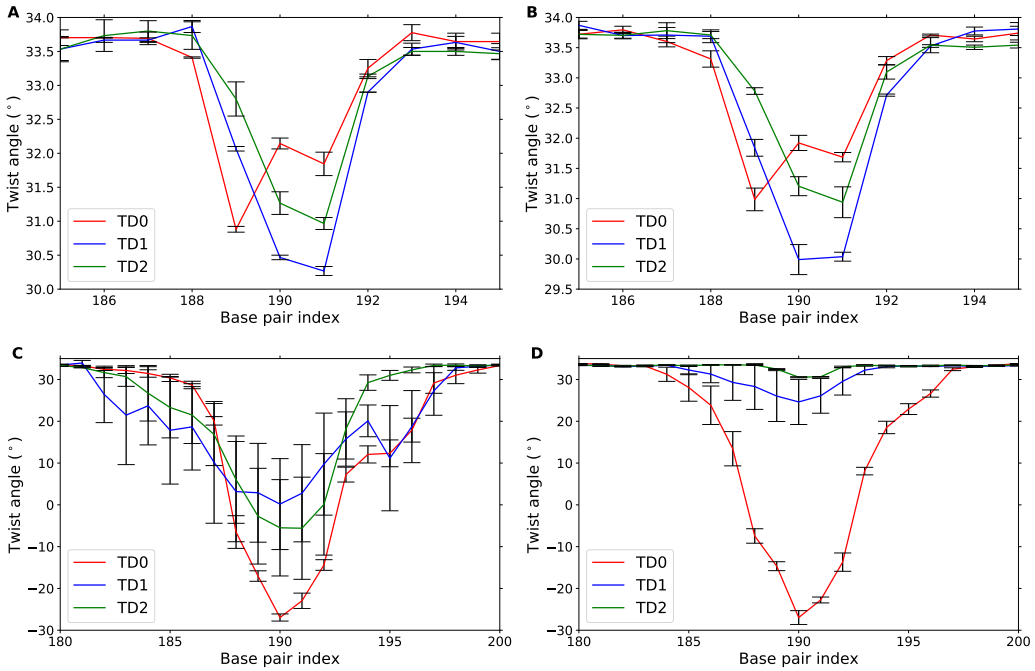


Figure 3.17: Twist angles measurements for the thymine dimer-containing dsDNA at state points (**A**) $F = 0.5$ pN and $\sigma \approx -0.021$ (B-DNA), (**B**) $F = 0.5$ pN and $\sigma \approx -0.056$ (plectoneme), (**C**) $F = 1.5$ pN and $\sigma \approx -0.073$ (tip-bubble plectoneme), and (**D**) $F = 2.0$ pN and $\sigma \approx -0.056$ (bubble). The value indicated at base pair index i represents the twist angle between base pair i and base pair $i-1$. Error bars represent standard errors of the mean. The thymine dimer is located at positions 189 and 190. In the B-DNA and plectonemic state, the largest decrease in twist angle (approximately $3.5°$) is registered by TD1 while the smallest decrease came from TD0. This order changes when we consider the tip-bubble plectoneme and bubble states formed at higher forces, where TD0 registers the largest change in twist angle.

(Fig. 3.17). In the B-DNA and plectonemic state at $F = 0.5$ pN, the decrease in twist angle at the thymine dimer site is comparable across all three models, with TD1 registering the largest decrease in twist angle, likely as a consequence of its relatively enhanced roll and intrinsic bending. On the other hand, in the tip-bubble plectoneme and bubble state at higher forces ($F = 1.5$ pN), the largest decrease in twist angle occurs at the TD0 site. For TD1 and TD2, twist-induced bubbles can be formed at other locations along the DNA strands. These bubbles

can absorb a significant amount of twist. For TD0, which has the largest amount of hydrogen-bond weakening, twist-induced bubbles are strongly localised at the thymine dimer site.

Overwinding/underwinding simulations were also carried out on TD1 and TD2 DNA (Fig. 3.18). We observe a similar increase in state occupancy of plectonemes and tip-bubbles at lower superhelical densities for these models, although there are also some differences in the exact positions of the boundaries between the different states in the three thymine dimer models. With TD1 for instance, bubbles are not the dominant state at F = 2 pN and $\sigma = -0.038$, though its average occupancy at 33% remains higher than its counterpart for the undamaged DNA (23%). On the other hand, TD0 and TD2 exhibit a dominant bubble state at the same point in the force-torsion space. In this particular example, the difference in bubble state occupancy across the three thymine-dimer models can be attributed to the difference in the magnitude of the hydrogen bond strength reduction for these models.

The observation of tip-bubbles at lower $|\sigma|$ than for undamaged DNA gives rise to similar sharply localized plectoneme position distributions for TD1 and TD2-containing plectonemes at F = 1.5 pN and $\sigma = -0.073$ (Fig. 3.19) as found for TD0. With TD1, which is more strongly bent than TD0 or TD2, we also observe plectoneme localization at lower forces and positive σ (Fig. 3.20). At F = 1.5 pN and σ = 0.067, the peak of the probability distribution is approximately half the distribution peak at F = 1.5 pN and $\sigma = -0.073$, and its width (measured at the 50% peak value) is noticeably broader than that of its counterpart at $\sigma = -0.073$. This indicates that TD1 as a defect on its own constrains the position of a plectoneme somewhat less than a tip-bubble. Under the same sets of F and positive σ, localization of the plectoneme by TD0 and TD2 is not readily observed. From an energetics standpoint, it requires more bending energy to form a plectonemic end-loop with TD0 or TD2 as compared to TD1 by virtue of their smaller θ_0 at

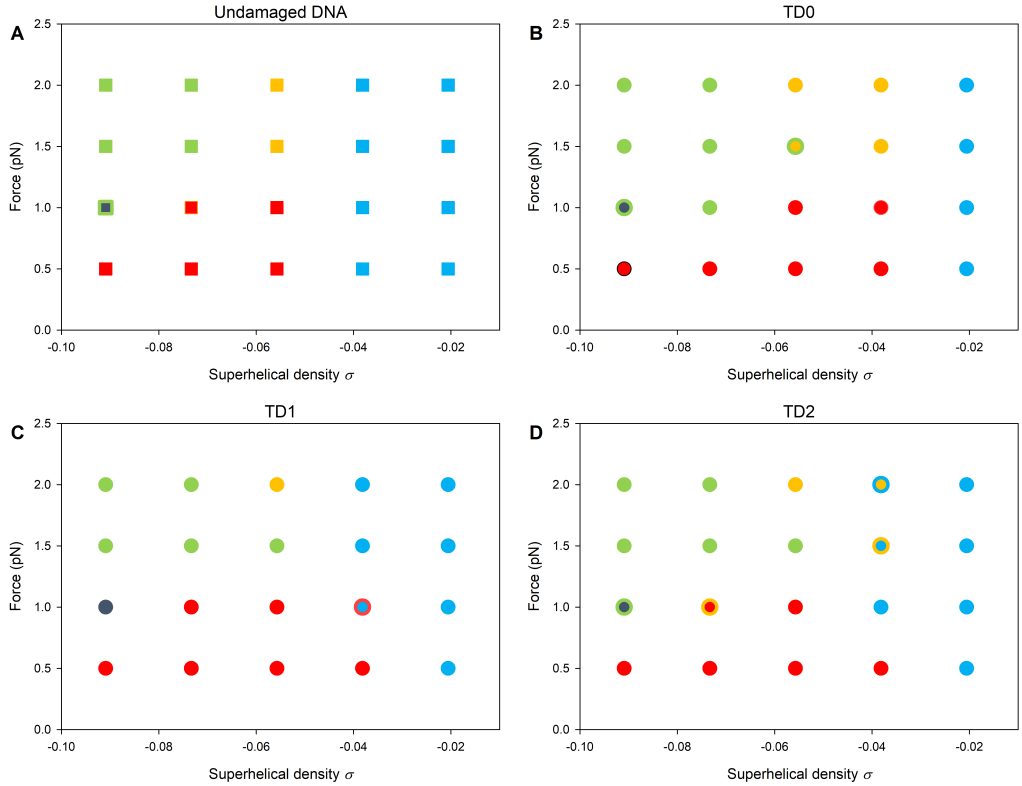


Figure 3.18: Force-torsion state diagrams for (**A**) undamaged and (**B** - **D**) thymine dimer-containing dsDNA. The colour coding can be found in Fig. 3.8. All three thymine dimer models produce similar enhancements in the state occupancy of plectoneme and plectonemic tip-bubble at lower superhelical densities (relative to the undamaged dsDNA).

the defect site in the DNA. This in turn makes it less favourable to nucleate a plectoneme at the TD0 or TD2 site.

We can attempt to quantify the favourability of nucleating a plectoneme at the defect site by examining the free energy of plectonemic loop formation. First, we assume that the reduction in the free energy of loop formation at the defect site (relative to the non-defect site) is largely attributed to the bend angle θ_0 induced by the thymine dimer. Next, using the plectoneme formation energy model by Brutzer *et al.*, we can estimate the free energy reduction as $\theta_0\sqrt{2k_{\mathrm{B}}TpF\bar{z}}$, where

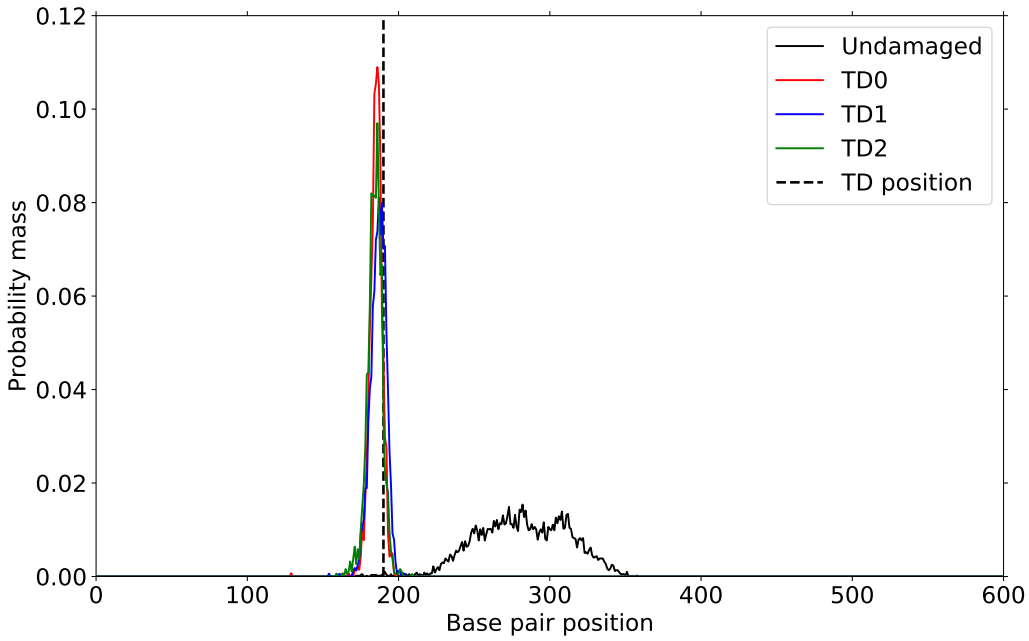


Figure 3.19: Plectoneme position distributions for a negatively supercoiled DNA strand at F = 1.5 pN and $\sigma = -0.073$. All three thymine dimer models yield very similar distributions.

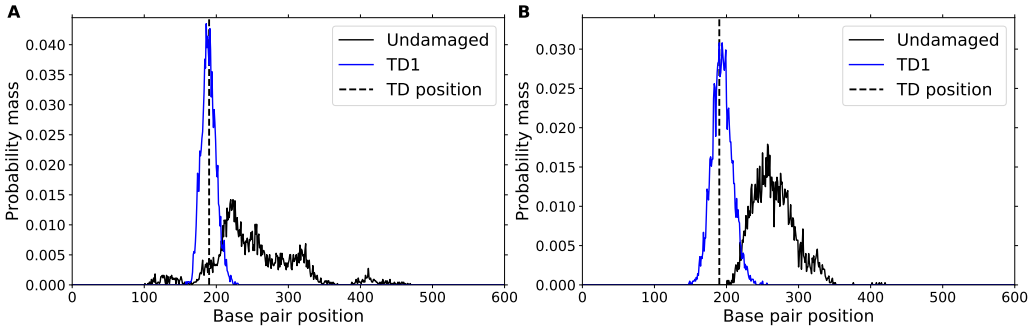


Figure 3.20: (Left) Plectoneme position distribution for a positively supercoiled DNA strand with TD1 at F = 1.5 pN and σ = 0.067. (Right) Plectoneme position distribution for a negatively supercoiled DNA strand with TD1 at F = 1 pN and σ = -0.056. The combination of σ and F here ensures a relatively low tip-bubble state occupancy ($< 40\%$) for the trajectories. Under these state conditions, tip-bubbles are no longer the dominant state in the force-torsion state space, and therefore any observed plectonemic pinning can be directly attributed to the defect itself.

$\bar{z} \approx 0.88$ (at $F = 1.5\,\text{pN}$) is a dimensionless correction term that takes into account writhe fluctuations in B-DNA, and p is the bending persistence length of 45 nm (Brutzer et al., 2010). Using the values of θ_0 from Table 3.1, and $F = 1.5\,\text{pN}$ to ensure a fair comparison with the plectoneme pinning results in Fig. 3.20, we found that the loop formation free energy reduction associated with TD1 is approximately $3.1\,k_\text{B}T$, while the equivalent values for TD0 and TD2 are $1.1\,k_\text{B}T$ and $1.4\,k_\text{B}T$, respectively.

Consequently, the thermodynamic drive for plectoneme localization at the thymine dimer when a tip-bubble is not present is significantly reduced in the TD0 and TD2 models. Consistent with this, in Fig. 3.21 we observe diffusion of the plectoneme centre away from the defect site for TD0 and TD2 in the positively supercoiled regime, whilst it remains pinned for TD1.

We also compared the denaturation probability of the thymine dimer base pairs for all three models (Fig. 3.22). All show a substantial increase in the denaturation probability of the thymine dimer base pairs at F = 1.5 pN when $|\sigma|$ exceeds 0.04. The thymine-dimer denaturation probability is less for TD1 consistent with this model's lower weakening of base pairing (only 10% less than a normal AT base pair). The smaller energetic advantage of opening a bubble at the thymine dimer rather than elsewhere along the duplex offsets less the entropic cost of localization.

Enhancement to the stacking interaction between thymine bases is present in TD0 but absent in TD1 and TD2 (Table 3.1). The increased stacking between the thymine bases better mimics the additional covalent linkages in the thymine dimer, and ensures that the thymine bases remain stacked even if the thymine dimer adopts an extrahelical arrangement in the tip-bubble state (Fig. 3.7).

The stacking of the thymine bases can be quantified indirectly by measuring the relative orientation angle of the thymine nucleotides as defined using their

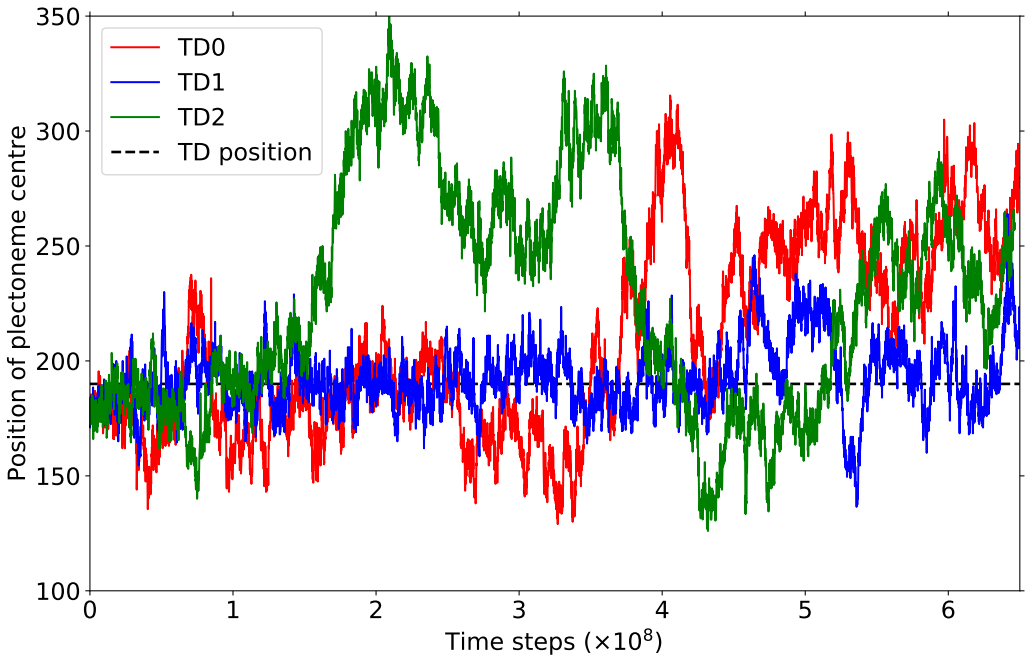


Figure 3.21: Pinning for positive supercoiling: Plectoneme centres are determined using the algorithm described in the supplementary material of Matek *et al.* (Matek et al., 2015). With the exception of the choice of the thymine dimer model, other initial conditions (i.e. starting configuration etc.) for the simulations are identical. TD1 is observed to pin the plectoneme more effectively at the chosen state point of F = 1.5 pN and σ = 0.067 than TD0 or TD2.

backbone-base vectors (Fig. 3.23 for the definition).

To illustrate that the thymine bases in TD0 remain stacked when in an extrahelical arrangement within a tip-bubble, orientation angles between the TD0 thymine bases were extracted from equilibration runs of supercoiled TD0 dsDNA at $F = 1.5\,\text{pN}$ and $\sigma = -0.073$. These conditions were chosen to ensure that the supercoiled dsDNA remained in the plectoneme tip-bubble state. For comparison, the relative orientation of a neighbouring set of (undamaged) bases in the tip-bubble was also measured, and the same approach was repeated for TD1 and TD2.

Fig. 3.24 provides a clear contrast between the thymine bases in TD0 and those of TD1. With an enhanced stacking interaction, the thymine bases in TD0 re-

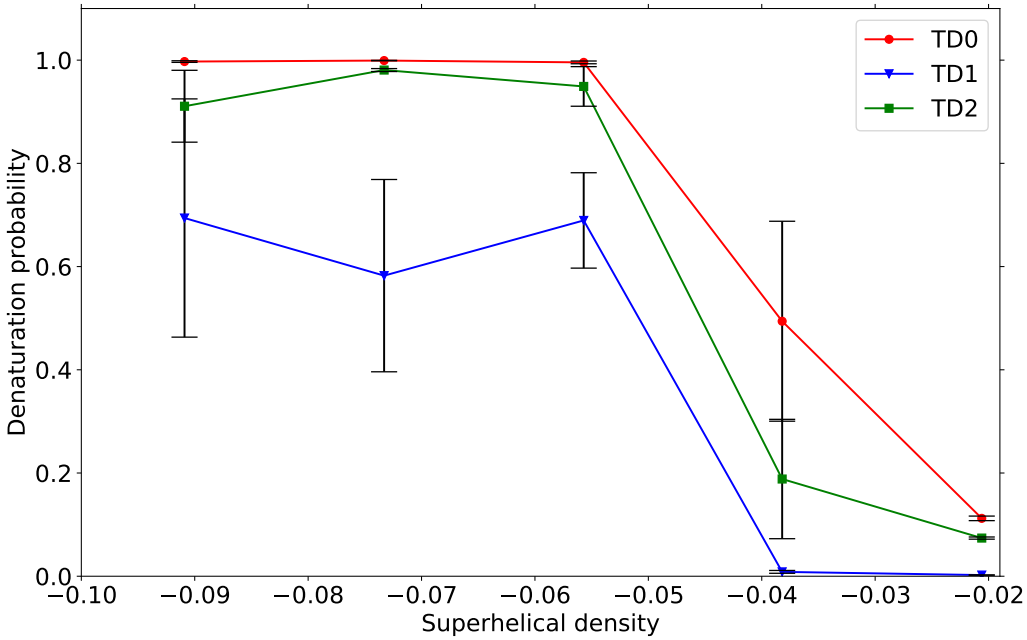


Figure 3.22: Denaturation probability of thymine-dimer base pairs at $F = 1.5$ pN, with error bars corresponding to standard errors in the mean. All three TD models show a marked increase in denaturation probability at the thymine-dimer base pairs when $|\sigma| > 0.04$. The localisation of the tip-bubble at the thymine dimer causes the thymine dimer to be denatured most of the time.

main stacked throughout the equilibration run, as would also be expected for a covalently bonded thymine dimer. Conformational changes associated with the formation of a plectoneme tip-bubble have no impact on the stacking between the thymine bases in TD0. On the other hand, the thymine bases in TD1 lose their stacking when the thymine dimer adopts an extrahelical arrangement within a tip-bubble. The same observation is true for TD2. This behaviour is a weakness of these two alternative models. That being said, variations in the stacking interaction multiplier (up to a value of 10) has a relatively small impact on the global thermodynamic and pinning behaviour of these models.

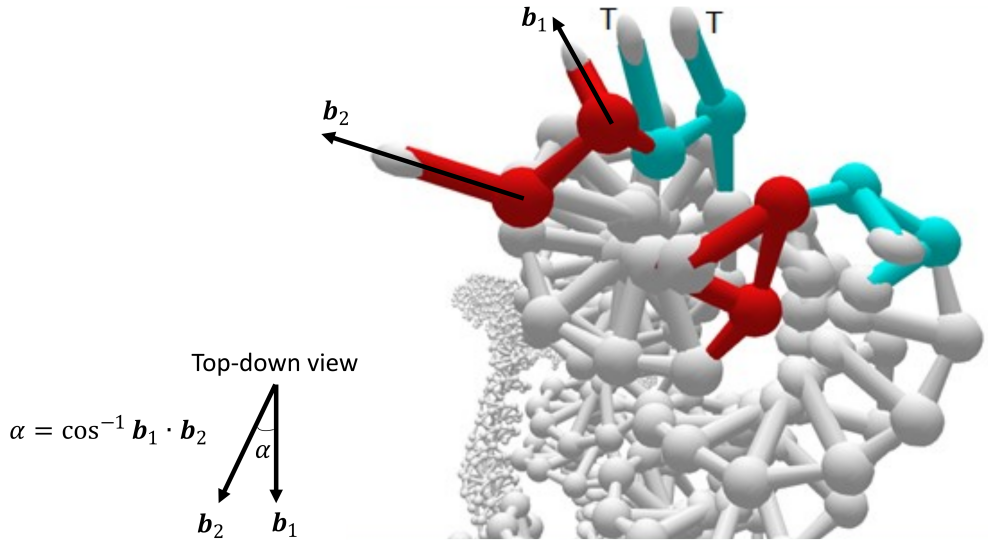


Figure 3.23: The relative orientation of two adjacent bases (in red) is defined by the orientation angle α. $\hat{\mathbf{b}}_\mathbf{1}$ and $\hat{\mathbf{b}}_\mathbf{2}$ are the backbone-base vectors of the bases. The same definition applies for the thymine bases (labelled as T and coloured in cyan).

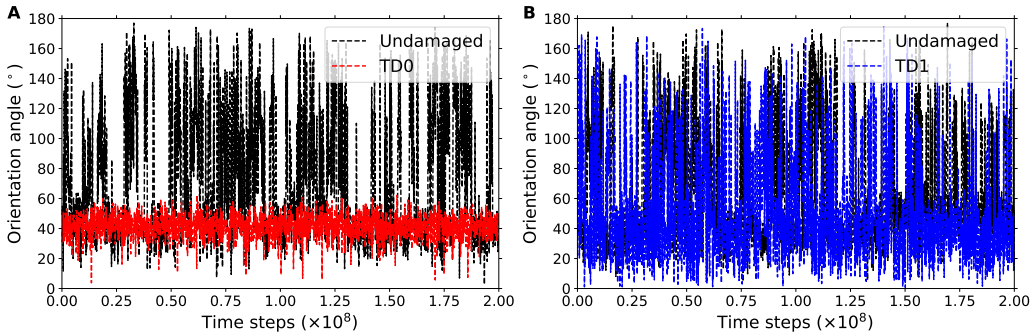


Figure 3.24: (A) The orientation angles between the thymine bases in TD0 remain stable throughout a simulation run at $F = 1.5\,\text{pN}$ and $\sigma = -0.073$ that is initiated with a tip-bubble plectoneme localized at the thymine dimer, whereas significant fluctuations in orientation are observed in the adjacent set of bases. This confirms that the enhanced stacking interaction multiplier in TD0 captures this expected consequence of the covalent bonding between the thymines. (B) Without any enhancement of the stacking interaction in TD1, the thymine bases of TD1 frequently lose their stacking when the thymine dimer adopts an extrahelical arrangement within a tip-bubble at $F = 1.5\,\text{pN}$ and σ = -0.073. A similar behaviour is observed for TD2.

3.4 Conclusion

Our observations of plectonemic pinning by a thymine dimer are consistent with similar pinning by mismatches, as observed in magnetic tweezer experiments (Dittmore et al., 2017) (albeit for positive supercoiling) and also predicted by oxDNA simulations (Matek, 2014; P. R. Desai et al., 2020) and theory (Brahmachari et al., 2018). Taken together, these results suggest that plectonemic pinning may reflect DNA's structural response to a broader range of possible defects in DNA.

For reasons of computational cost, we have only presented results for a fixed length DNA duplex. To first order, the longer the strand is, the larger the relative entropic cost of localising a plectoneme or a bubble at a damaged site. However, entropic costs typically scale with the log of the length (see for example (Brahmachari et al., 2018)), so, although the tendency for localization will be reduced at longer lengths, we can still expect qualitatively similar effects from thymine dimers in longer strands. Typical plectonemic loops in bacteria are thought to be on the order of a few thousand to tens of thousands of base-pairs in size (Postow et al., 2004).

One can imagine that the coupling between supercoiling and DNA damage that we have observed might be exploited by biological systems to help achieve certain tasks. One is DNA damage recognition. In our simulations plectoneme localization at a thymine dimer causes it to adopt a configuration that increases its differentiation from normal double-stranded DNA, be it by being more bent or by opening up a denaturation bubble at the plectoneme tip. In the latter case, the thymine dimer is likely to adopt an extrahelical configuration. These more extreme configurations could well allow the DNA damage to be more easily recognised by the relevant protein.

Unlike in our simulations where a fixed superhelical density is applied, cellular DNA is constantly being subjected to transient local mechanical stresses applied by various proteins. The coupling between their action and the mechanical response of defective DNA might also provide a means to locate DNA damage, such as thymine dimers. For example, in the the twist-open mechanism of damage recognition proposed for the Rad4/XPC nucleotide excision repair complex (Chen et al., 2015; Velmurugu et al., 2016), the requisite repair protein switches between "search" mode (i.e. facilitated diffusion) and "interrogation" mode (i.e. unwinding of the DNA duplex) in its attempt to locate the defect on DNA. One could envisage that a plectoneme is preferentially formed at the defect site when the repair protein interacts with and twists the DNA duplex during the interrogation mode. The structural distortion then serves as a marker for the repair protein, stalling its diffusive motion and enabling it to engage more extensively with the thymine dimer site.

Recent developments in DNA nanotechnology have shown that user-defined placement of thymine dimers in DNA nanostructures can provide an additional level of structural stability. In this approach UV irradiation is used to generate thymine dimers that link strand ends and bridge strand breaks at crossover sites (Gerling et al., 2018). Studying how these thymine dimers affect DNA nanostructures is another avenue of research where the oxDNA model, which has been widely used to study such systems (Doye et al., 2013; B. E. Snodin et al., 2016; B. E. K. Snodin et al., 2019), can now be applied.

Although we have shown that plectoneme pinning by a thymine dimer is robust to variations in our model, it would of course be desirable to further explore these phenomena with more detailed atomistic simulations (Laughton & Harris, 2011; J. Mitchell et al., 2011; Pyne et al., 2021). While larger scale writhing effects such as the formation of plectonemes would be very challenging to study with

atomistic simulations, it may be possible to use multi-scale techniques to treat the writhe on a coarser level, for example with oxDNA, and to then locally treat the thymine dimer with more fine-grained solvent-free atomistic force-fields.

Finally, the best way to test these hypotheses about the interaction between supercoiling and DNA damage is through experiments. One promising direction is through *in-vitro* single-molecule experiments with magnetic tweezers. These can be used to test, as was done in (Dittmore et al., 2017) for mismatches, whether thymine dimers pin plectonemes. Using fluorescent probes, it should also be possible to investigate how imposed force and twist affect the propensity of thymine dimers to denature. It may also be possible to measure the binding constants for key thymine dimer repair proteins as a function of supercoiling density, as was done in (Litwin et al., 2015) for example. Measuring whether or not these mechanisms are at work and assist the location and repair mechanisms of thymine dimers and other defects *in vivo*, is a significantly more complex challenge.

4 | Statistical Mechanics of Tip-bubble Plectonemes

In the previous chapter, we showed how thymine dimers could lower the supercoiling densities at which plectonemes and bubbles occur. At biologically relevant supercoiling densities and forces, thymine dimers can preferentially segregate to the tips of the plectonemes, and enhance the probability of a bubble localised at the tip of the plectoneme. These observations suggest that tip-bubble plectonemes may play an important biological role in facilitating the binding of repair enzymes, and motivate us to provide a firmer theoretical framework to understand how tip-bubbles can be formed in a torsionally stressed and stretched dsDNA. Once such a framework is established, inhomogeneities such as DNA defects can be introduced into the framework to study their effect on the formation of tip-bubble plectonemes.

We begin with a short review of the theoretical approaches that have been taken to study the formation of plectonemes and bubbles in dsDNA under the application of an external torque and force. These theoretical models will subsequently form the basis for the formulation of the free energy model of tip-bubble plectoneme later in the chapter.

4.1 Twist-induced buckling

Buckling occurs when the imposed torsional stress on the dsDNA reaches a critical level, causing the DNA to writhe and cross over itself to form a loop. Using the classical analogy of an elastic rod with twist stiffness C and bending modulus B (Strick et al., 2002), the dsDNA of length L_0 buckles into a loop of radius R

when the system reaches a critical torque value of $\Gamma_b = 2\pi N_b C/L_0$, where N_b is the equivalent critical number of imposed turns. At this point, the torsional energy is converted into the work done against the external pulling force F and the bending energy of the loop:

$$2\pi\Gamma_b = 2\pi RF + 2\pi R\frac{1}{2}\frac{B}{R^2} \tag{4.1}$$

When additional turns are imposed onto the DNA system beyond the critical point, the torque value remains constant at $2\pi\Gamma_b$ and does not increase any further. Excess torsional energy is instead accommodated in the form of additional plectonemic loops until the entire dsDNA is converted into the plectonemic state. We can derive $E_{\text{classical}}$, the energy required to form each of these plectonemic loops, by minimising Eq. 4.1 with respect to R:

$$E_{\text{classical}} = 2\pi\Gamma_b = 2\pi\sqrt{2BF} \tag{4.2}$$

Eqs. 4.1 and 4.2 provide a good qualitative description of the buckling transition in dsDNA observed in magnetic tweezer experiments (Strick et al., 1998). As the pulling force F increases, more turns have to be imposed onto the system before buckling can occur. In addition, the loop radius decreases as $1/\sqrt{F}$, leading to a reduced rate of decrease in the end-to-end extension of the dsDNA with the number of imposed turns.

Despite its success in explaining several broad features of the buckling transition, the classical picture carries a significant oversimplification. It assumes that all the loops in the plectoneme are of the same (circular) geometry and therefore requires the same free energy of formation. Such an assumption stands in contrast with observations of the superhelical geometry of dsDNA from simulations (see, for instance, Fig. 4.1) and the abrupt nature of the buckling transition from ex-

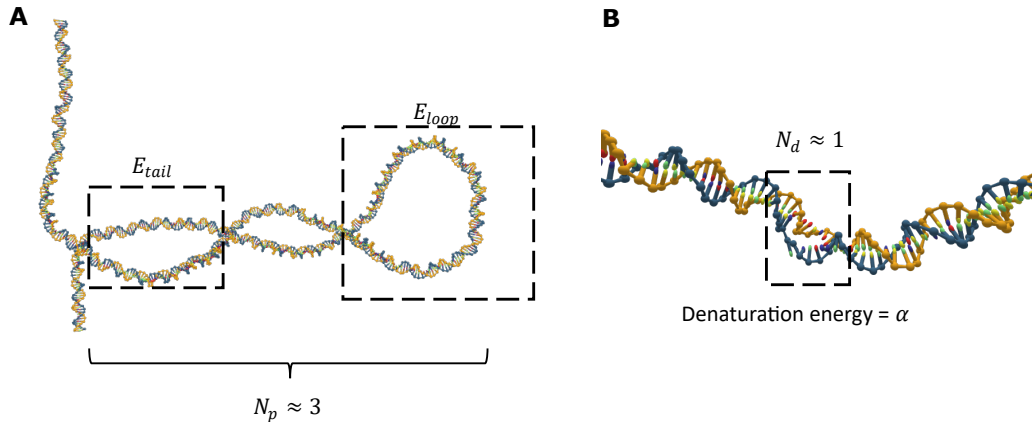


Figure 4.1: Illustration of (A) the buckling transition, and (B) twist-induced denaturation. In (A), N_p reflects the amount of twist in the dsDNA — expressed in terms of the number of imposed turns — that is transferred into writhe upon buckling. In (B), N_d is the number of turns relaxed by twist-induced denaturation.

periments (Forth et al., 2008). As a remedy to this oversimplification, Brutzer *et al.* developed a free energy model (henceforth also known as the Brutzer model) that assumes that the energy required to form the initial plectonemic loop E_{loop} is larger than that (i.e. E_{tail}) of any subsequent superhelical turn (Brutzer et al., 2010):

$$E_{\text{buckled}} = \frac{1}{2}\frac{C_s}{L_0}(2\pi)^2(N - N_p)^2 + E_{loop} + E_{tail}(N_p - 1) \tag{4.3}$$

Fig. 4.1 provides an illustration of the terms involved in Eq. 4.3. In the post-buckled state, the free energy E_{buckled} is partitioned into the twist energy term (first term on the right hand side of Eq. 4.3), and the energy associated with the plectonemic superhelix (second and third term). N_p reflects the amount of twist in the dsDNA that is transferred into writhe upon buckling, and is ≥ 1 in their model since the actual energy landscape for the initial loop formation is unknown. E_{loop} in their model is given by $2\pi\sqrt{2k_{\text{B}}TpF}\bar{z}$, where $\bar{z}$ is a dimensionless, force-dependent correction term that takes into account writhe fluctuations in dsDNA and p is the bending persistence length linked to the bending modulus B via $B =$

$pk_{\mathrm{B}}T$. E_{tail} on the other hand is given by (J. F. Marko, 2007):

$$E_{tail} = 2\pi \left\{ \frac{2P \times \left[F - \left(\frac{k_{\mathrm{B}}T \times F}{p} \right)^{1/2} \right]}{1 - \frac{P}{C_s}} \right\}^{1/2} \tag{4.4}$$

P in Eq. 4.4 refers to the plectonemic twist stiffness, a parameter that depends on the ionic concentration of the solution. For the remainder of this chapter, P is taken to be $23\,k_{\mathrm{B}}T$nm unless stated otherwise. The effective torsional modulus C_s in Eq. 4.3 and 4.4, which takes into account the absorption of twist by the bending fluctuations of dsDNA at low forces, is given by (Moroz & Nelson, 1998): $C_s = C[1 - \frac{C}{4pk_{\mathrm{B}}T}(\frac{k_{\mathrm{B}}T}{pF})^{1/2}]$, where C denotes the DNA torsional modulus and takes on the value of $92\,k_{\mathrm{B}}T$ in this chapter.

By minimising Eq. 4.3 with respect to N_p, Brutzer *et al.* was able to derive the equilibrium writhe $\bar{N}_p$ and the corresponding post-buckling energy $\bar{E}_{\text{buckled}}$:

$$\bar{N}_p = N - \frac{E_{tail}}{\frac{C_s}{L_0}(2\pi)^2} \tag{4.5}$$

$$\bar{E}_{\text{buckled}} = E_{loop} + E_{tail}\left(N - 1 - \frac{1}{2}\frac{E_{tail}}{\frac{C_s}{L_0}(2\pi)^2} \right) \tag{4.6}$$

Equating Eq. 4.6 with the pre-buckled twist energy of $\frac{1}{2}\frac{C_s}{L_0}(2\pi)^2N^2$ gives N_b, the position of the buckling transition where pre- and post-buckled state occupancies are equal:

$$N_b = \frac{E_{tail}}{\frac{C_s}{L_0}(2\pi)^2} + \left[\frac{2(E_{loop} - E_{tail})}{\frac{C_s}{L_0}(2\pi)^2} \right]^{1/2} \tag{4.7}$$

The buckling transition position can also be expressed in terms of superhelical density using the transformation $\sigma_b = N_b d/L_0$, where d is the helical pitch. By making a distinction between the initial loop and the subsequent loops in the plec-

tonemic superhelix, Brutzer *et al.* were able to account for the abrupt nature of the buckling transition via the second term in Eq. 4.7, which represents the average writhe of the abruptly forming plectoneme at the buckling point. Such a distinction also enabled them to account for the torque overshoot observed in the torque response curves of torsionally strained dsDNA, which had been observed and confirmed experimentally by Janssen, Lipfert *et al.* (Janssen et al., 2012). In the model by Brutzer *et al.*, the torque overshoot is a consequence of the additional amount of energy that is required to form the initial loop. The reader may also wish to note that Eq. 4.7 predicts a length-dependent buckling transition position, which was verified by Brutzer *et al.* experimentally (see, for instance, Fig. 4.3).

4.2 Twist-induced denaturation

At a sufficiently high pulling force F, the nucleation of a plectonemic loop, whose energy scales with F, becomes energetically prohibitive, and the torsionally stressed dsDNA denatures instead to accommodate the imposed torsional strain. This picture of twist-induced denaturation underpins the model by Salerno *et al.* (henceforth also known as the Salerno model) (Salerno et al., 2012), which treats the denaturation energy required to relax a single imposed turn as a phenomenological constant α (Fig. 4.1):

$$E_{denatured} = \frac{1}{2}\frac{C_s}{L_0}(2\pi)^2(N - N_d)^2 + \alpha N_d \tag{4.8}$$

In this model, the total free energy $E_{denatured}$ is partitioned into twist energy (first term) and denaturation energy (second term). N_d is the number of turns that is relaxed by twist-induced denaturation. The number of base pairs that is denatured to relax one turn is not known *a priori* but we can estimate it by examining the

change in the number of denatured base pairs over a range of superhelical densities at $F \geq 1.5\,\text{pN}$ from our oxDNA MT simulations (Fig. 4.2). A simple linear regression analysis gives us an estimated change of 6 bps per turn for $F \geq 3.0\,\text{pN}$, while at lower forces (i.e. $F = 1.5\,\text{pN}$ and $2.0\,\text{pN}$), a change of 7 to 8 bps per turn is observed. For comparison, Tempestini *et al.* estimated that 8 denatured bps are required to relax one turn (Tempestini et al., 2013). Such a comparison however has to come with the caveat that their experimental settings and ours are different. For instance, Tempestini *et al.* obtained their estimate based on MT experiments that are carried out with a much longer DNA molecule (7000 bps) at an ionic strength of $0.15\,\text{M}$ [NaCl] while our simulations were carried out with a shorter DNA duplex of 600 bps at a slightly lower salt concentration of $0.1\,\text{M}$.

An intuitively useful feature of the Salerno model is its definition of a characteristic force, above which the buckling transition is replaced by twist-induced denaturation to accommodate the excess torsional stresses. The characteristic force is obtained by equating E_{loop} with α. Since both E_{loop} and α can be altered by a multitude of factors such as salt concentration, temperature and the presence of defects on the DNA, the characteristic force as a concept is useful in helping us understand DNA denaturation in biological settings, and in turn how biological processes that depend on DNA denaturation (e.g. transcription and replication) can be affected by changes in physiological conditions.

The Salerno model, however, does not capture sequence-dependent effects, or the coupling between twist and denaturation. To better characterise these effects, we turn to the denaturation model developed by Fye and Benham (Fye & Benham, 1999). In their model, each base pair j is associated with a binary state variable n_j that takes on a value of either 1 (denatured) or 0 (intact). An imposition of a linking number difference of ΔLk on a dsDNA with N base pairs can lead to the denaturation of n base pairs, causing a change in unstressed helicity of $-n/A$,

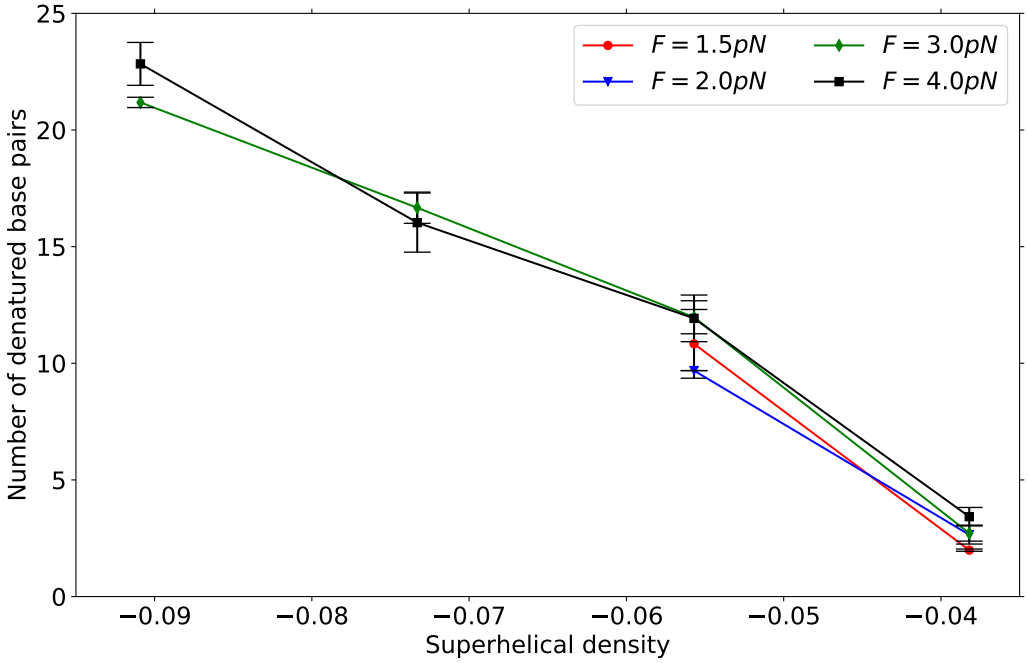


Figure 4.2: Variation of the number of denatured base pairs with superhelical density. The change (increase) in the number of denatured base pairs can be estimated by first fitting the points with the lines of best fit and then calculating the gradients of these lines. At $F \geq 3.0$ pN, we get an estimated change of 6 bps per turn. On the other hand, at $F = 1.5$ pN and 2.0 pN, a change of 7 to 8 bps per turn is observed.

where $A = 10.4$ bps/turn (J. C. Wang, 1979). Because of their high flexibility, the unpaired strands in the denatured regions could interwind, such that their total twist is given by $\sum_{j=1}^{N} \frac{n_j \tau_j}{2\pi}$, with τ_j representing the helical twist of the denatured base pair j. Any remaining linking difference ΔLk_r not accounted for by the change in helicity or interwinding is accommodated by the twisting of the B-form DNA and bending deformations. Taken together, the linking number difference ΔLk can be expressed as $\Delta Lk_r + \sum_{j=1}^{N} \frac{n_j \tau_j}{2\pi} - n/A$. The Hamiltonian H which

describes the total energy of such a DNA system is given by:

$$H = H_t + H_r + H_c = \sum_{j=1}^{N} \frac{C_d n_j \tau_j^2}{2} + \frac{K}{2}\left(\Delta Lk + \frac{n}{A} - \sum_{j=1}^{N} \frac{n_j \tau_j}{2\pi}\right)^2 + \sum_{j=1}^{N} \{(a_{FB} + b_j)n_j - a n_j n_{j+1}\} \tag{4.9}$$

H_t characterises the amount of twist energy associated with the interstrand twisting in the denatured regions. The constant C_d in H_t reflects the torsional stiffness of the denatured regions and is taken to be 9.3×10^{-21} erg cm. The second component of the Hamiltonian $H_r = \frac{K}{2}(\Delta Lk_r)^2$ is the energy associated with superhelical deformations, with K taken to be $2220RT/N$. Finally, the third component H_c is the chemical energy associated with denaturation. $a_{FB} \approx 11$ kcal/mol describes the initiation energy required to nucleate what Fye and Benham call a "run" of denaturation (i.e. a continuous region of denatured base pairs), and arises from the additional hydrophobic stacking interaction that has to be overcome when the first base pair of a run is denatured. Once the initiation barrier is overcome, each base pair in the run is disrupted by an energy input of b_j. The value of b_j depends on the base pair composition as well as environmental conditions such as ionic concentration. In Fye and Benham's model, $b_{\text{AT}} = 0.26$ kcal/mol and $b_{\text{GC}} = 1.31$ kcal/mol. Eq. 4.9 has been applied to study sequence-dependent effects on the size and location of bubbles in supercoiled dsDNA (Hwa et al., 2003), and genomic studies linking mutagenicity to the non B-DNA regions in the human genome (Du et al., 2014). More recent updates to the Fye and Benham model added other conformational transitions that could compete with denaturation to provide a more complete picture of the structural effects of torsional stresses on dsDNA. (Zhabinskaya & Benham, 2011).

4.3 Modifications to the Brutzer and Salerno models

Before we construct the free energy expression for tip-bubble plectonemes in negatively supercoiled dsDNA, we will first need to make a few modifications to the theoretical models that we have highlighted in the previous sections. In the model by Brutzer *et al.*, the initial loop, or equivalently the end-loop of the plectoneme, is treated as a planar circular loop. This geometrical assumption overestimates the actual curvature and in turn the free energy cost of the loop. A teardrop loop is instead a better representation of the initial loop, and its free energy cost can be estimated as $E_{loop} = 2\sqrt{\rho_0 p k_B T F}$, where ρ_0 is a parameter that depends on the geometry of the loop (Brahmachari et al., 2018; Sankararaman & Marko, 2005). For an end-constrained teardrop loop, we will take ρ_0 to be approximately 16 (Sankararaman & Marko, 2005). Such a modification shifts the buckling point to lower superhelical densities $|\sigma|$ since the energetic barrier that the dsDNA has to overcome to form the initial loop is now lowered. This is evident in Fig. 4.3, where we have compared the buckling transition point determined from oxDNA simulations, defined here as the point where the occupancy of the plectonemic state is 50%, with the theoretical predictions made by Brutzer's original model (Eq. 4.7) and the modified version using the geometry of a teardrop loop. A less-than-ideal agreement between oxDNA simulation results and the theoretical predictions is also observed at low forces in Fig. 4.3. A likely reason is that the Brutzer model does not take into account the effects of polymer confinement entropy, which becomes significant at low forces (J. Marko & Siggia, 1995).

The second modification is made to the denaturation model by Salerno *et al.* The first set of base pairs that is denatured to relax a single turn now requires a larger

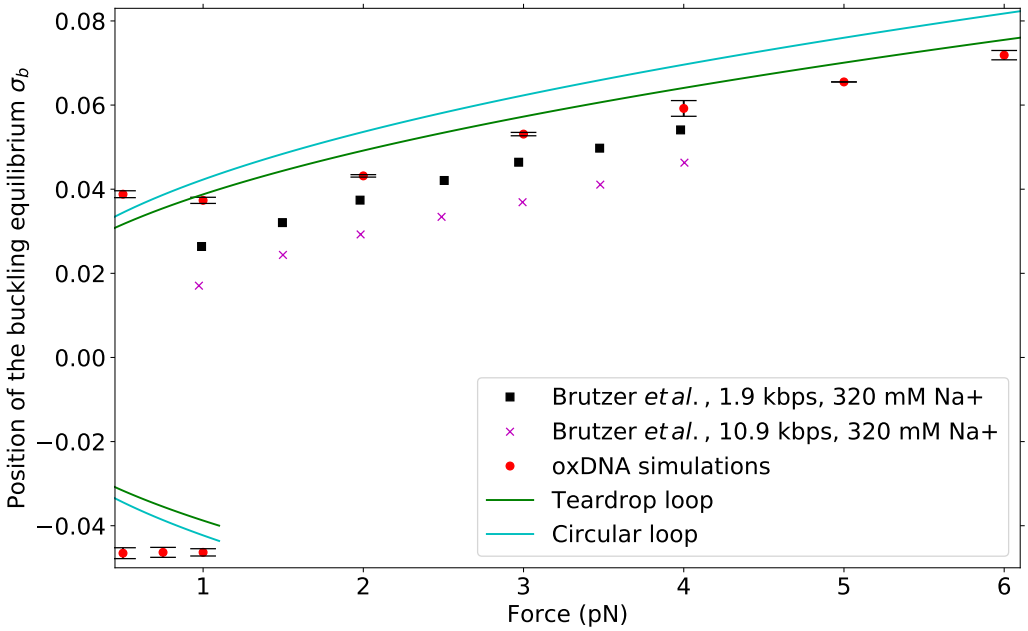


Figure 4.3: Position of the buckling position $\sigma_b = N_b d/L_0$ as measured from oxDNA simulations and predicted using the original (i.e. circular end-loop) model by Brutzer *et al.* and the modified version that uses a teardrop configuration to represent the initial plectonemic loop. Experimental data from Brutzer *et al.* is also included for comparison. The reader may wish to note that the bubble state and tip-bubble plectoneme state dominate at $F > 1$ pN in negatively supercoiled dsDNA. Error bars are SEM.

energy input of $a+b$, where a represents the nucleation barrier that has to be overcome first before a bubble can be formed, and b is the energy required to denature base pairs to accommodate the excess torsional stresses after the nucleation barrier is overcome. Subsequent turns can be relaxed with just an energy input of b since the new denatured base pairs are more likely to be located at the boundaries of the already-denatured regions of the dsDNA. This brings our model into closer agreement with the core concepts behind Fye and Benham's chemical energy formulation of twist-induced denaturation, without sacrificing much of the analytical features offered by the Salerno model, such as the characteristic force F_c, which can now be defined by $E_{loop} = a + b$. We can also derive the state boundary

between B-DNA and the bubble state, starting with the modified definition of the total free energy of the denatured state of dsDNA $E_{\text{denatured}}$:

$$E_{\text{denatured}} = \frac{1}{2}\frac{C_s}{L_0}(2\pi)^2(N - N_d)^2 + a + bN_d \tag{4.10}$$

Note that with this modification to $E_{\text{denatured}}$, the free energy landscape for the formation of the first set of denatured base pairs is unknown, and $E_{\text{denatured}}$ is only well-defined for $N_d \geq 1$. Minimising Eq. 4.10 with respect to N_d gives us:

$$\bar{N}_d = N - \frac{b}{\frac{C_s}{L_0}(2\pi)^2} \tag{4.11}$$

Finally, we adopt the approach taken by Brutzer *et al.* and determine the position of the denaturation transition N_{den} by equating the minimised free energy of the denatured state in Eq. 4.10 with the pre-buckled twist energy:

$$N_{den} = \sqrt{\frac{2a}{\frac{(2\pi)^2 C_s}{L_0}}} + \frac{b}{\frac{(2\pi)^2 C_s}{L_0}} \tag{4.12}$$

For the remainder of this chapter, we choose a to be $5\,k_{\text{B}}T$ and b to be $25\,k_{\text{B}}T$ unless stated otherwise. The theoretical predictions of the characteristic force (1.29 pN) and the boundary between the B-DNA state and the bubble state agree well with the corresponding measurements from oxDNA simulations for this combination of a and b values (Fig. 4.4). Without the inclusion of a nucleation barrier in the model by Salerno *et al.*, the theoretical boundary between the B-DNA state and the bubble state as given by $N_{den}^{Salerno} = \frac{\alpha L_0}{C_s(2\pi)^2}$ would shift to lower superhelical densities $|\sigma|$, resulting in a significant theory-simulation gap (Fig. 4.4B). We can also compare our choices of the values of a and b against the estimates of the same parameters from the denaturation torque response curve of dsDNA (Fig. 4.5). Drawing an analogy with the initial loop model by Brutzer *et al.*

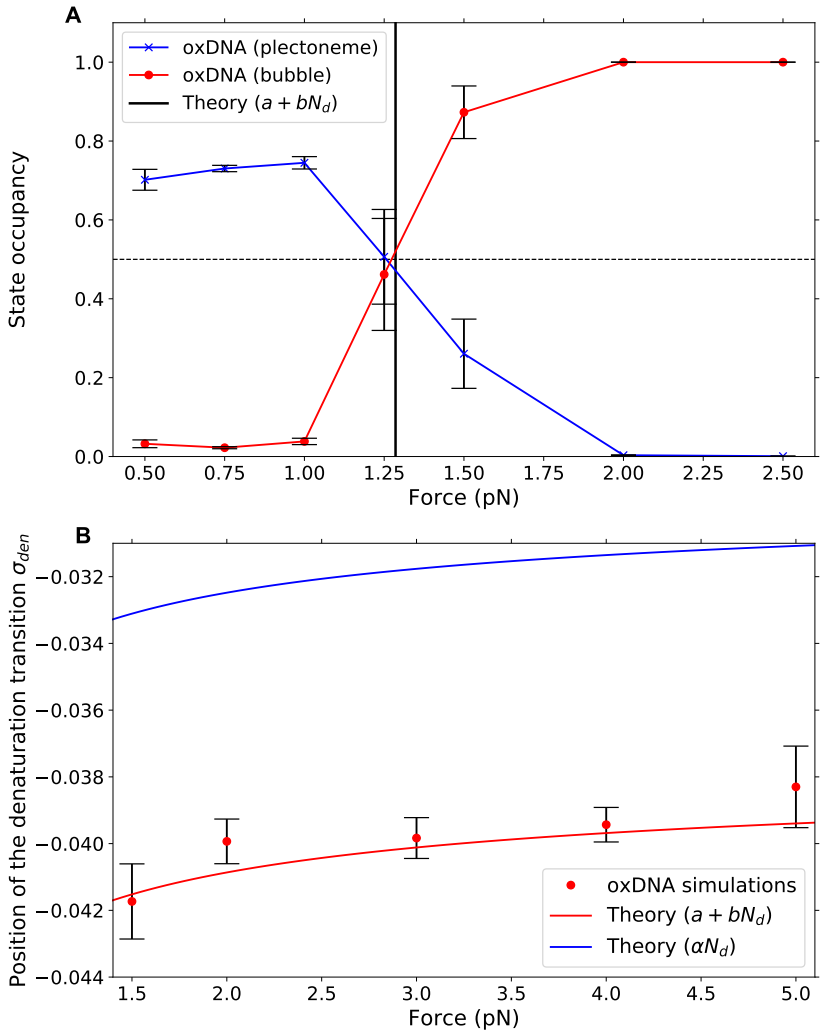


Figure 4.4: (A) Characteristic force as defined by $E_{loop} = a + b$. The theoretical prediction matches well with the plectoneme-bubble crossover point (50% occupancy of the bubble state) measured from oxDNA simulations at $\sigma \approx -0.056$. The variation in plectonemic state occupancy with force F at the same σ is also included for reference. (B) Position of the denaturation position σ_{den} as measured from oxDNA simulations and predicted using the original (αN_d) and modified ($a + bN_d$) model by Salerno *et al.* The value of α is taken to be $a + b$ for a fair comparison. The modification to the Salerno model results in a better fit with oxDNA simulation measurements as it takes into account the additional energy barrier that has to be overcome before twist-induced denaturation occurs. Error bars in the figure are SEM.

(Brutzer et al., 2010), the area between the torque overshoot and post-denaturation torque in our denaturation model is characterised by $\frac{a}{2\pi}$ while the post-denaturation torque is given by $\frac{b}{2\pi}$. It is difficult to get an estimate of the torque overshoot's area (in part due to sequence-dependent effects) and in turn a directly from Fig. 4.5, but for the purpose of illustration, we will estimate the area as a triangle bounded horizontally by $\sigma \approx -0.031$ and $\sigma \approx -0.056$ and vertically by $\Gamma \approx 14$ pNnm and $\Gamma \approx 17$ pNnm. This gives $a \approx 3.2\, k_{\mathrm{B}}T$. To get an estimate of b, we take the average of the torque values between $\sigma \approx -0.073$ and $\sigma \approx -0.108$. This gives us $b \approx 23\, k_{\mathrm{B}}T$. Both estimates of a and b from the torque response curve are in good agreement with our choices of parameter values in this study (i.e. $a = 5\, k_{\mathrm{B}}T$ and $b = 25\, k_{\mathrm{B}}T$). We also note that a more distinct torque overshoot can be obtained using the average-sequence parameterization of oxDNA (Fig. A.1). This also strengthens our earlier claim that a nucleation barrier is present in the oxDNA simulations of twist-induced denaturation.

4.4 Free energy of a tip-bubble plectoneme

In tip-bubble plectonemes, the co-localisation of the denatured base pairs with the tip of the plectoneme reduces the overall geometric curvature of the plectonemic end-loop (Matek et al., 2015). We can quantify such an interaction between the denatured base pairs and the plectonemic loop using the kinked loop model originally developed by Sankararaman and Marko (Sankararaman & Marko, 2005), and subsequently applied to the study of defects (Dittmore et al., 2017; Brahmachari et al., 2018; P. R. Desai et al., 2020). In this model, the energy of a kinked loop under tension F, E_{kinked}, is given by:

$$E_{kinked} = 2(1-\epsilon)\sqrt{\rho_0 p k_{\mathrm{B}}TF} \tag{4.13}$$

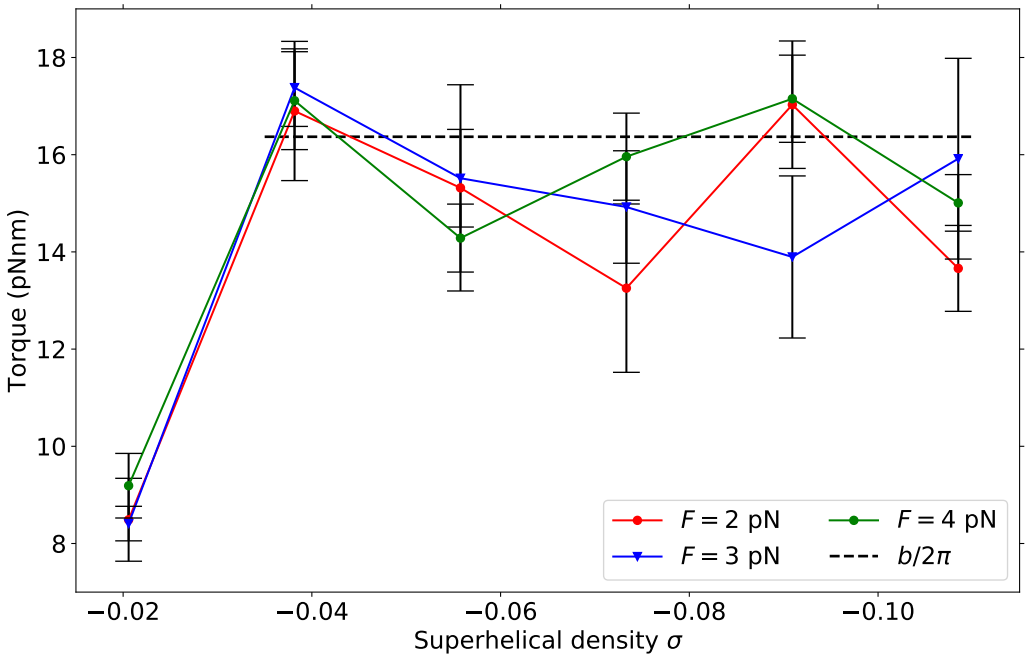


Figure 4.5: Denaturation torque response curve of dsDNA, with error bars representing the standard error of the mean absolute-valued torque. b is taken to be $25\,k_{\mathrm{B}}T$ in this figure.

The factor of 2 in Eq. 4.13 arises from energetic contributions due to the work done against the pulling force F and the bending energy of the loop. ϵ is an empirical kink parameter that was reported to scale approximately linearly with the size of the mismatch n, for $n \leq 6$ bps (Brahmachari et al., 2018; P. R. Desai et al., 2020). For a larger mismatch size, higher order terms involving n would have to be introduced since the linear relation between n and ϵ is not expected to hold indefinitely. Because these experiments and simulations were carried out on positively supercoiled dsDNA that contains mismatches, we need to verify whether a similar relation between ϵ and the size of a bubble holds for negatively supercoiled dsDNA. As a proxy, we measure the end-loop angle of tip-bubble plectonemes as a function of the tip-bubble size. The end-loop angle measurement follows the approach taken by Desai *et al.* (P. R. Desai et al., 2020), which we

have detailed in subsection 3.2.1. If ϵ increases with n, we would expect the end-loop angle to decrease as n increases.

Measurements of the end-loop angle and the corresponding tip-bubble size are carried out using equilibration trajectories simulated at $F = 1.5$ pN with tip-bubble plectonemes as the dominant state. In these trajectories, the DNA duplexes are held at a fixed linking number deficit ΔLk using stationary harmonic traps. Since the change in ΔLk is strongly correlated with the size of the tip-bubble (See, for e.g., Fig. 4.2 and 4.20), by tuning the magnitude of ΔLk, the size of the tip-bubble in these duplexes can be adjusted. The results are presented in Fig. 4.6, which shows a decrease in end-loop angle as the size of the tip-bubble increases. These results are similar to the reported decrease in end-loop angle with an increase in the number of mismatched base pairs by Desai *et al.*. In turn, a smaller end-loop angle is also shown to be positively correlated with an increase in ϵ (Sankararaman & Marko, 2005; P. R. Desai et al., 2020). We can therefore reasonably assume, to the lowest order, that for negatively supercoiled dsDNA, ϵ increases linearly with the size of a tip-bubble. In arriving at this conclusion, we have assumed that the decrease in end-loop angle is largely attributed to the change in tip-bubble size instead of the change in linking number deficit. This is a reasonable assumption, which we can verify by measuring the variation of end-loop angle with linking number deficit using trajectories that are simulated at $F = 0.5$ pN where no bubbles or tip-bubbles are observed. In this regime, the percentage change in end-loop angle is approximately 11 % as σ goes from -0.056 to -0.073. A similar set of calculations is also made for positively supercoiled dsDNA simulated at $F = 1.5$ pN, where the percentage change in end-loop angle is approximately 4.8 % as σ goes from 0.050 to 0.103. These percentage change values are too small to fully account for the decrease in end-loop angle that we observe in Fig. 4.6.

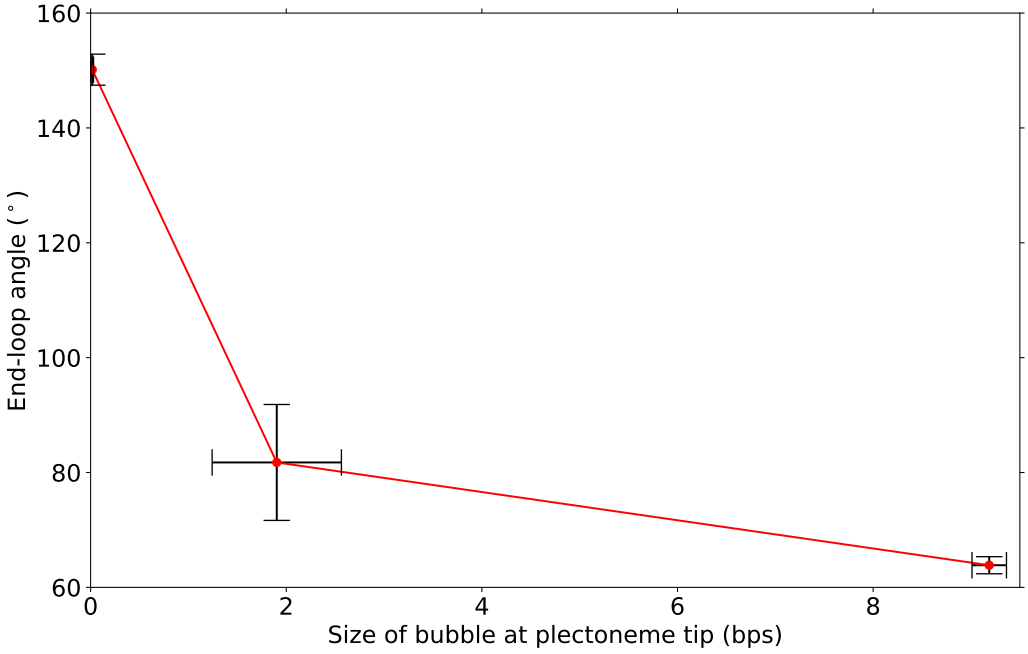


Figure 4.6: End-loop angle of a tip-bubble plectoneme as a function of tip-bubble size. Error bars are statistical errors obtained from block averaging. These measurements are taken from trajectories simulated at $F = 1.5$ pN.

Armed with this assumption, we can now state the total free energy cost of the plectonemic tip-bubble state in negatively supercoiled dsDNA E_{tip} as:

$$\begin{aligned} E_{tip} =& \frac{1}{2}\frac{C_s}{L_0}(2\pi)^2(N - N_d - N_p)^2 + a + bN_d \\ &+ 2(1 - a_d N_d)\sqrt{\rho_0 p k_\mathrm{B} T F} + E_{tail}(N_p - 1) \end{aligned} \tag{4.14}$$

In Eq. 4.14, ϵ in the energy expression for the kinked end-loop is recast as $a_d N_d$, where a_d is a constant of proportionality. This stems from our observation that N_d is proportional to the size of the twist-induced bubble (see, for instance, Fig. 4.20). Unless stated otherwise, a_d is taken to be 0.3, which is equivalent to saying that $\epsilon(N_d = 1) \approx 0.04$ if $N_d = 1$ corresponds to 7 denatured base pairs. This is comparable to the values of ϵ reported by Desai *et al.* for a similar mismatch size at low salt conditions (P. R. Desai et al., 2020).

For plectoneme tip-bubbles which are induced and pinned by defects, the translational entropic cost of pinning the plectoneme, ΔS, would have to be considered (J. F. Marko & Neukirch, 2012; Brahmachari & Marko, 2017; Brahmachari et al., 2018):

$$\Delta S = k_{\mathrm{B}}T \ln\left(\frac{L}{D}\right) = k_{\mathrm{B}}T \ln\left[\frac{(L_0 - \Delta L_1 - (N_p - 1)\frac{dL}{dN})\bar{z}}{D}\right] \tag{4.15}$$

Here, $\bar{z} = 1 - \frac{1}{2}\left[\frac{pF}{k_{\mathrm{B}}T} - \frac{1}{32}\right]$ is a correction factor that accounts for incomplete stretching due to writhe fluctuations (Moroz & Nelson, 1998; Clauvelin et al., 2008; Brutzer et al., 2010). L represents the amount of free length on the dsDNA that is available for the plectoneme to slide along. D discretises the number of configurational states that the plectoneme can adopt along the dsDNA, and can be represented by a natural cutoff such as the helical repeat (Emanuel et al., 2013), or the formula $D = p^{1/4}\left(k_{\mathrm{B}}T/F\right)^{3/4}$ (J. F. Marko & Neukirch, 2012; Brahmachari et al., 2018). $\Delta L_1 = \sqrt{\rho_0 p k_{\mathrm{B}}T/F}$ is the length of the end-loop in a normal plectoneme and $\frac{dL}{dN}$ is given by Eq. A.1 in Appendix A.2. Together, ΔL_1 and $(N_p - 1)\frac{dL}{dN}$ add up to the length of the plectoneme L_p (J. F. Marko, 2007; Forth et al., 2008; Brutzer et al., 2010). The translational entropic cost of pinning is a relatively small quantity for the length scales and forces we are considering here. Using the formula by Marko and Neukirch to describe D (J. F. Marko & Neukirch, 2012), at $L \approx 200$ nm, $\Delta S \approx 3\,k_{\mathrm{B}}T$ or smaller. Even if we take $L \approx 2000$ nm, $\Delta S \approx 7\,k_{\mathrm{B}}T$. In contrast, $a + b = 30\,k_{\mathrm{B}}T$ in our model. We will leave Eq. 4.15 out in our subsequent calculations of the various state boundaries, as we have observed, through our calculations, that the inclusion of ΔS has a very small effect on the positions of the state boundaries in the force-torsion state space. As such, its exclusion would not affect our general conclusions.

4.5 State boundary between plectonemes and tip-bubble plectonemes

We can now proceed to derive the boundaries between tip-bubble plectonemes and other states in the force-torsion space. The first state boundary that we are deriving is the plectoneme/tip-bubble plectoneme boundary. We can do so by taking the following approach. At/near the state boundary N^*, an imposition of a single turn on the dsDNA currently in state A would cause the dsDNA to relax the additional imposed turn and transition to state B. Mathematically, we can express this as:

$$E_A(N^* + 1) = E_B(N^*) \tag{4.16}$$

Note that this method of deriving state boundaries introduces a bias in the value of N^* (see Fig. 4.7 for a detailed illustration). This bias in principle can be eliminated by equating $E_A(N^* + \delta)$ with $E_B(N^*)$ and taking the limit of $\delta \to 0$. However, because Eq. 4.14 includes a term that is independent of N, taking such a limit introduces divergences that cannot be easily removed. Moreover, the initial loop model by Brutzer *et al.*—upon which the free energy of the tip-bubble plectoneme is based—is constrained by the condition $N_p \geq 1$ since the energy landscape of the initial plectoneme loop is not known in Brutzer's model (Brutzer et al., 2010). This constraint invalidates the use of $E_A(N^* + \delta) = E_B(N^*)$ to study state transitions where N_p could potentially be smaller than 1, such as the bubble to tip-bubble plectoneme transition. A similar issue arises when we consider the modified free energy model of denaturation, which is valid for $N_d \geq 1$.The use of Eq. 4.16 circumvents the above-mentioned issues. Despite the trade-off in the accuracy of N^*, this method is still capable of providing us with a good sense of how the state boundaries vary with the pulling force and superhelical density.

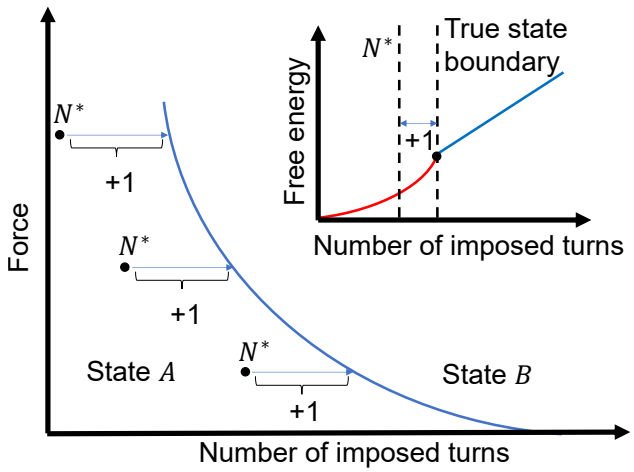


Figure 4.7: An illustration of how the true boundary is underestimated when a full additional turn is required for the transition from state A to state B. (Inset) The same representation of the underestimation of the true state boundary from the free energy perspective.

By taking state A to be the plectonemic state (Eq. 4.6) and state B to be the tip-bubble plectoneme state (Eq. 4.14), we can express Eq. 4.16 as:

$$E_{loop} + E_{tail}(N^* - \frac{1}{2}\frac{E_{tail}}{\frac{C_s}{L_0}(2\pi)^2}) = E_{loop} + E_{tail}(N^* - \frac{1}{2}\frac{E_{tail}}{\frac{C_s}{L_0}(2\pi)^2} - 1) - a_d E_{loop} + a + b \tag{4.17}$$

Eq. 4.17 can be simplified to give:

$$E_{tail} = a + b - a_d E_{loop} \tag{4.18}$$

Because E_{tail} and E_{loop} are force-dependent quantities, Eq. 4.18 can be numerically solved to give $F = F_{lc}$, which we will subsequently term as the lower characteristic force, since its value is typically smaller than the characteristic force F_c under normal physiological conditions. Eq. 4.18 can be interpreted physically as follows: At a pulling force that is below the characteristic force F_c, twisted DNA will first buckle and nucleate an initial plectonemic loop when the imposed torsional strain exceeds a critical value. With additional imposed turns, DNA can have either one of these two responses. If E_{tail} is smaller than the net energetic cost of forming a kink at the tip of the plectoneme (i.e. $a + b - a_d E_{loop}$), the

plectoneme will continue to grow to accommodate the additional torsional strain. Otherwise, DNA relaxes the additional torsional stresses by kinking at the tip of the plectoneme, thus forming a tip-bubble plectoneme. Which response dsDNA takes depends on the pulling force F, since E_{tail} is force-dependent. Below F_{lc}, plectoneme formation is the energetically preferred mode of relaxation for twisted DNA. Above it, tip-bubbles are formed to relieve the torsional strain. Note that an expression similar to Eq. 4.18 can be obtained even if we use the original Salerno model (Eq. 4.8) to describe the formation of a bubble at the plectoneme tip (see Appendix A.6).

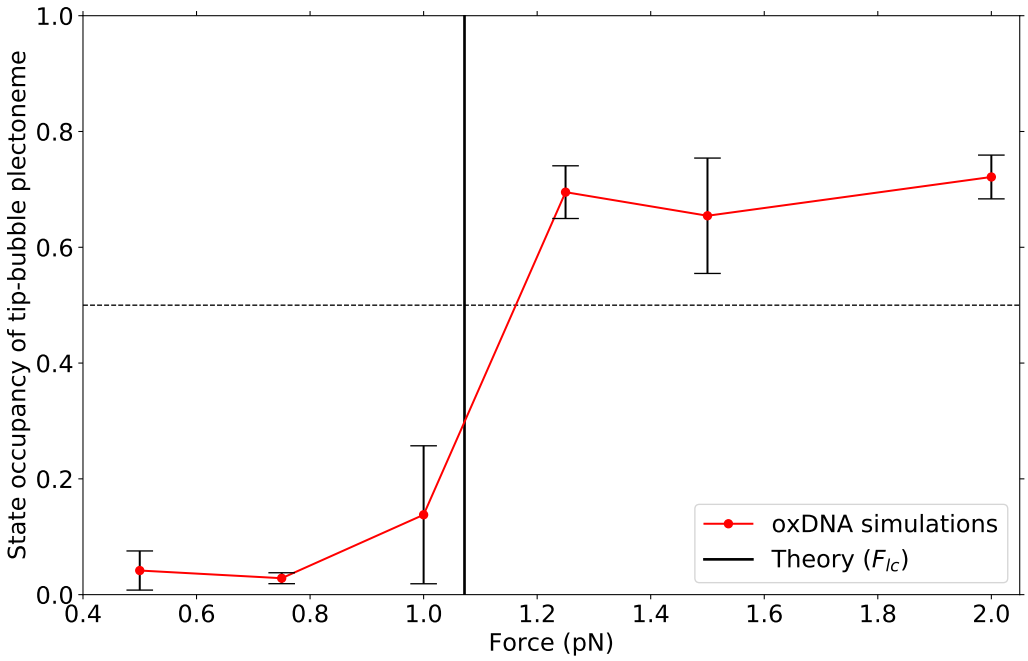


Figure 4.8: Comparison of the theoretical lower characteristic force (Eq. 4.18) with oxDNA simulations. The theoretical F_{lc} of 1.07 pN slightly underestimates the plectoneme/tip-bubble plectoneme crossover point (defined as 50% of the tip-bubble plectoneme state occupancy) measured from oxDNA simulations at $\sigma \approx -0.073$.

In Fig. 4.8, we compare the theoretical lower characteristic force F_{lc} with the state occupancy of tip-bubble plectonemes that we have measured from oxDNA

simulations of dsDNA at $\sigma \approx -0.073$. The choice of σ here is a considered one. At high superhelical densities (e.g. $\sigma \approx -0.091$) and relatively low forces (e.g. $F = 1.0$ pN), the 600 bps dsDNA would have expended its entire length to form a plectoneme. Any further torsional stresses would result in the formation of bubbles, alongside what Salerno *et al.* referred to as a plectoneme at zero DNA extension (Salerno et al., 2012). In our oxDNA simulations, this co-existence of bubbles and plectonemes takes the form of tip-bubble plectonemes as it is energetically optimal to form a bubble at the plectoneme tip. Consequently, we need to make a distinction between tip-bubble plectonemes that are formed when the DNA extension reaches zero (i.e. when $L_0 - \Delta L_1 - (N_p - 1)\frac{dL}{dN} \approx 0$), and tip-bubble plectonemes that are formed when E_{tail} is larger than the net energetic cost of kinking the end-loop of the plectoneme. For the purpose of calculating and measuring the lower characteristic force F_{lc} from oxDNA simulations, we are only concerned with the latter category of tip-bubble plectonemes. F_{lc} is found to be approximately 1.07 pN after solving Eq. 4.18 numerically, which slightly underestimates the cross-over from the plectonemic state to the tip-bubble plectoneme state shown in Fig. 4.8.

4.6 State boundary between bubbles and tip-bubble plectonemes

The second boundary that we can derive is that between the bubble state and tip-bubble plectoneme state, N_t:

$$\begin{aligned} a + b(N_t + 1) - \frac{1}{2}\frac{b^2}{\frac{C_s(2\pi)^2}{L_0}} =& a + bN_t - \frac{1}{2}\frac{b^2}{\frac{C_s(2\pi)^2}{L_0}} \\ &+ \left[1 - a_d\left(N_t - \frac{b}{\frac{C_s(2\pi)^2}{L_0}}\right)\right] E_{loop} \end{aligned} \tag{4.19}$$

The left-hand side of Eq. 4.19 represents the minimised free energy (Eq. 4.10 and 4.11) of the denatured DNA that has an additional imposed turn near the state boundary N_t. The additional imposed turn is relaxed by the formation of a bubble-containing plectonemic loop instead of further denaturation. This process is represented by the right-hand side of Eq. 4.19. Solving Eq. 4.19 for N_t gives us:

$$N_t = \frac{1}{a_d} + \frac{b}{\frac{C_s}{L_0}(2\pi)^2} - \frac{b}{a_d E_{loop}} \tag{4.20}$$

We can interpret Eq. 4.20 as follows: The twist-induced bubble, given its increased bending flexibility, provides an energetically favourable nucleation site for the initial plectonemic loop. The initial loop, when fully formed, would therefore possess a bubble at its tip which kinks the loop and reduces its overall curvature and bending energy (Eq. 4.13). As the pulling force increases in magnitude, the nucleation cost of the initial plectonemic loop increases. This requires a larger bubble to be formed first (Fig. 4.6) in order to compensate for the increase in the nucleation cost of the loop.

Eq. 4.20 is plotted against oxDNA simulation measurements of σ_t in Fig. 4.9. Without any surprise, due to the use of Eq. 4.16 to derive the state boundaries, the theoretical boundary as given by Eq. 4.20 underestimates the boundary measured from oxDNA simulations. Moreover, local elastic properties and twist absorption effects due to the unpaired strands are likely to play a more significant role in this regime with larger bubble sizes. These effects are not adequately captured by the kinked loop model (Eq. 4.13) and are also neglected in the derivation of Eq. 4.20. Nevertheless, the oxDNA measurements show an agreement with the prediction that $|\sigma_t|$ increases with the magnitude of the pulling force.

Our simulations of twisted dsDNA at $F \geq 3$ pN reveal a pure bubble state across a wide range of $|\sigma|$ where no plectonemes or loops are detected. This is simi-

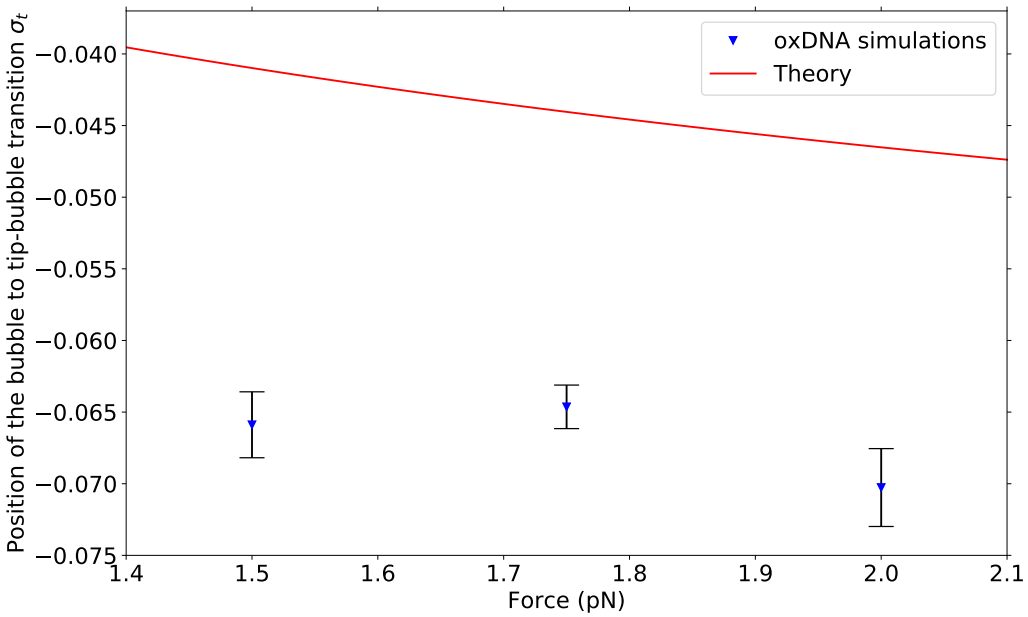


Figure 4.9: The theoretical bubble to tip-bubble plectoneme transition point σ_t underestimates the σ_t measured from oxDNA simulations (defined as 50% of the tip-bubble plectoneme state occupancy). Local elastic properties and twist absorption effects due to the unpaired strands are likely to play a more significant role in this regime with larger bubble sizes. These effects are not adequately captured in our model.

lar to the results obtained by Matek *et al.* (Matek et al., 2015). The theoretical model that we have developed provides us with the physical basis to interpret this result. The linearity between ϵ in Eq. 4.13 and the bubble size n is not expected to hold indefinitely. As n tends to a large number, ϵ is likely to plateau at ϵ_m. What this implies is that above a critical pulling force F_m, growing the bubble by $N_d = 1$ will always be more energetically favourable than nucleating a kinked plectonemic loop at the site of the bubble. We can use this insight to estimate ϵ_m by equating $2(1-\epsilon_m)\sqrt{\rho_0 p k_\mathrm{B} T F_m}$ with b. Using $F_m \approx 2.5$ pN, ϵ_m is calculated to be approximately 0.4. In terms of the number of base pairs, this means that any increment in bubble size beyond 9 bps would no longer yield a significant reduction in the free energy of the plectonemic loop.

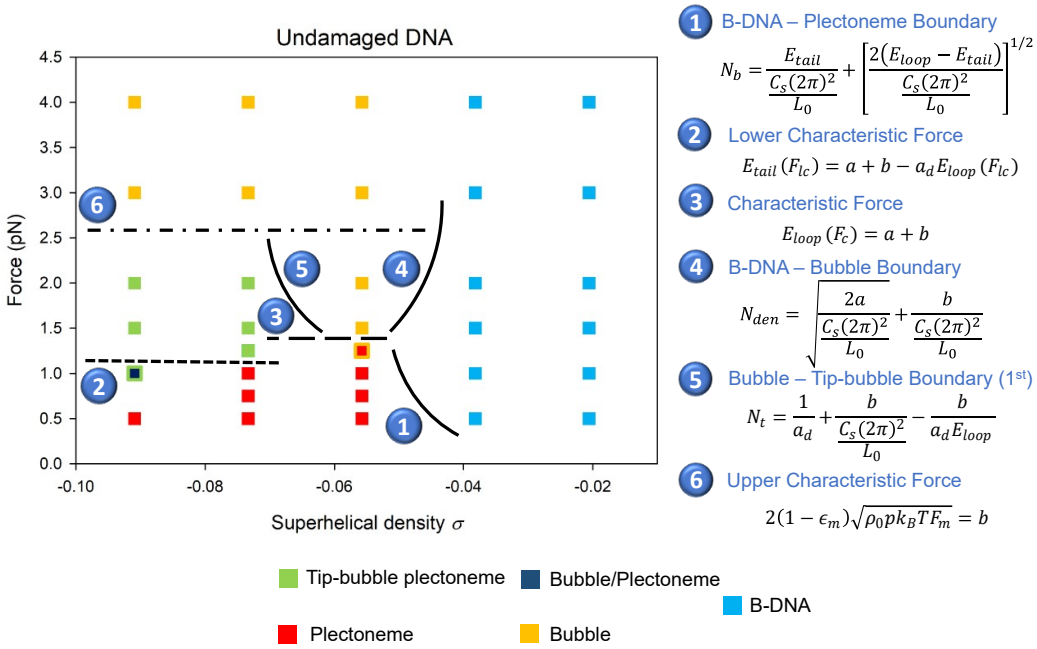


Figure 4.10: An illustration of the six state boundaries in the force-torsion space of dsDNA without permanent damage: (1) The B-DNA – plectoneme boundary is based on the DNA buckling model by Brutzer *et al.* (Brutzer et al., 2010) but with $E_{loop} = 2\sqrt{\rho_0 p k_B T F}$ to represent the teardrop geometry of the initial loop. (2) The lower characteristic force refers to the boundary between plectonemes and tip-bubble plectonemes and is governed by the competition between the net energetic cost of forming a tip-bubble ($a + b - a_d E_{loop}$) and the energy cost of forming a plectoneme loop E_{loop} (see Section 4.5 for more details). (3) The characteristic force is defined by $E_{loop} = a + b$, similar to the definition used in the denaturation model by Salerno *et al.* (Salerno et al., 2012). (4) The B-DNA – bubble boundary is derived theoretically by incorporating a nucleation barrier a into the denaturation by Salerno *et al.* (further details can be found in Section 4.3) (5) The bubble – tip-bubble boundary exists in this region of the force-torsion space because the twist-induced bubble, given its increased bending flexibility, provides an energetically favourable nucleation site for the initial plectonemic loop (see Section 4.6 for more details). (6) The upper characteristic force marks the boundary above which no tip-bubble plectonemes can be observed (i.e. it is always more energetically favourable to form bubbles instead of tip-bubbles in this region). The simulation results for the twisted, undamaged dsDNA (as represented by the coloured squares in this figure) are consistent with the oxDNA simulation results of an earlier study on supercoiled dsDNA by Matek *et al.* (Matek et al., 2015).

Fig. 4.10 provides a graphical summary of the main state boundaries in the force-torsion space of a negatively supercoiled dsDNA, superimposed against the simulation results for the twisted, undamaged dsDNA that we had earlier obtained in the previous chapter. The parameters that we have used to perform the various calculations in the preceding sections can also be found in Appendix A.3. Values used for the DNA torsional modulus C, bending persistence length p and the plectonemic twist stiffness P in our theoretical model are in line with experimentally-obtained values at a salt concentration of 0.1 M [NaCl] (J. F. Marko, 2007; Mosconi et al., 2009; Brutzer et al., 2010; Kriegel et al., 2017). The theoretical model is also reasonably robust against variations in the values of these parameters (see Appendix A.5). The value of $a + b = 30\,k_{\mathrm{B}}T$ is slightly higher than the value of $26.8\,k_{\mathrm{B}}T$ obtained experimentally at a salt concentration of 0.15 M [NaCl] by Tempestini *et al.* for their denaturation parameter α (Salerno et al., 2012; Tempestini et al., 2013), though it is likely that this disagreement is a consequence of the way oxDNA is parametrised that tends to overestimate the value of the characteristic force (see, for instance, the state boundary between plectonemes and bubbles in the paper by (Matek et al., 2015)).

4.7 Effects of defects on state boundaries

We now have an analytical framework that will enable us to predict how the presence of defects can change the global supercoiled structure. Once again, we will use the thymine dimer model in oxDNA to examine the predictive capability of this framework. The localised bend that the thymine dimer induces in the DNA duplex can be quantified in energetic terms by $\Delta E_{loop} \approx \frac{\theta_0}{\pi}\sqrt{\rho_0 p k_{\mathrm{B}} T F}$ (Randisi, 2019), with $\theta_0 = 11.7°$, while the weakening of the hydrogen bonding between the AT base pairs can be represented in the framework by the reduction in denat-

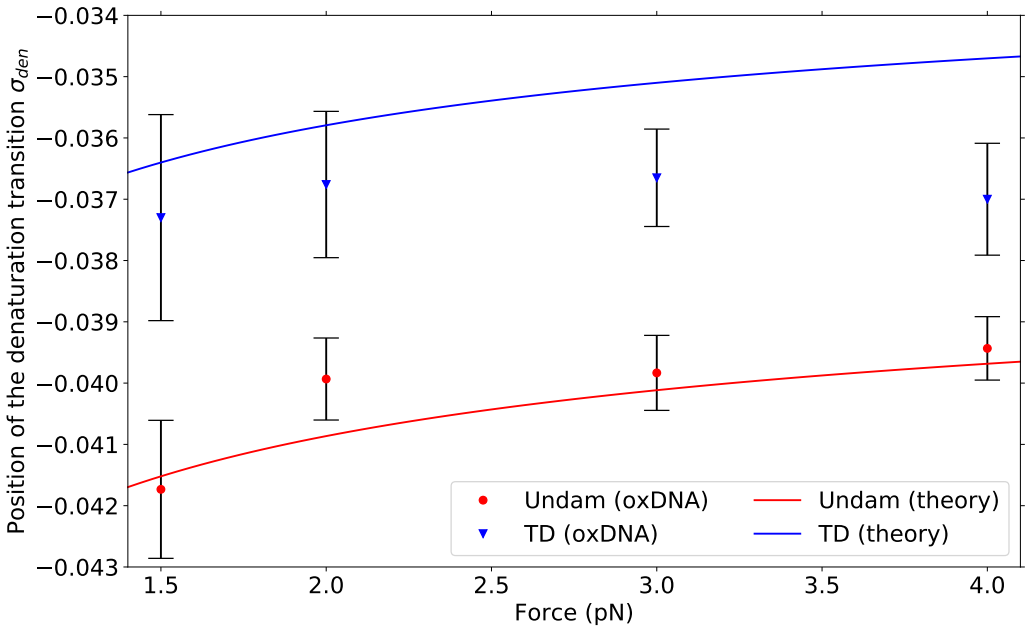


Figure 4.11: The theoretical denaturation transition position is calculated using Eq. 4.12 and compared against oxDNA simulation measurements. For thymine dimer (TD)-containing duplexes, the initiation energy a_{TD} differs from the undamaged (Undam) duplexes' initiation energy by $\Delta a = 3\,k_{\mathrm{B}}T$ by virtue of the weakened hydrogen bonding at the TD site.

uration nucleation energy Δa (assuming that the thymine dimer does not affect distal sites of denaturation and thus affects b).

In this analysis, we will set Δa to be equal to $3\,k_{\mathrm{B}}T$. This value of Δa provides a reasonable fit to the shift in the position of the denaturation transition σ_{den} when the thymine dimer is present in the dsDNA at $F = 1.5$ and 2.0 pN (Fig. 4.11). The shift in σ_{den} appears to be smaller at higher forces of $F = 3.0$ and 4.0 pN, but since we are predominantly interested in state boundary shifts that are occurring at forces below 2.5 pN, these force-dependent effects should not have a significant influence on the rest of our analysis below.

4.7.1 Shift in characteristic force F_c (state boundary between plectonemes and bubbles)

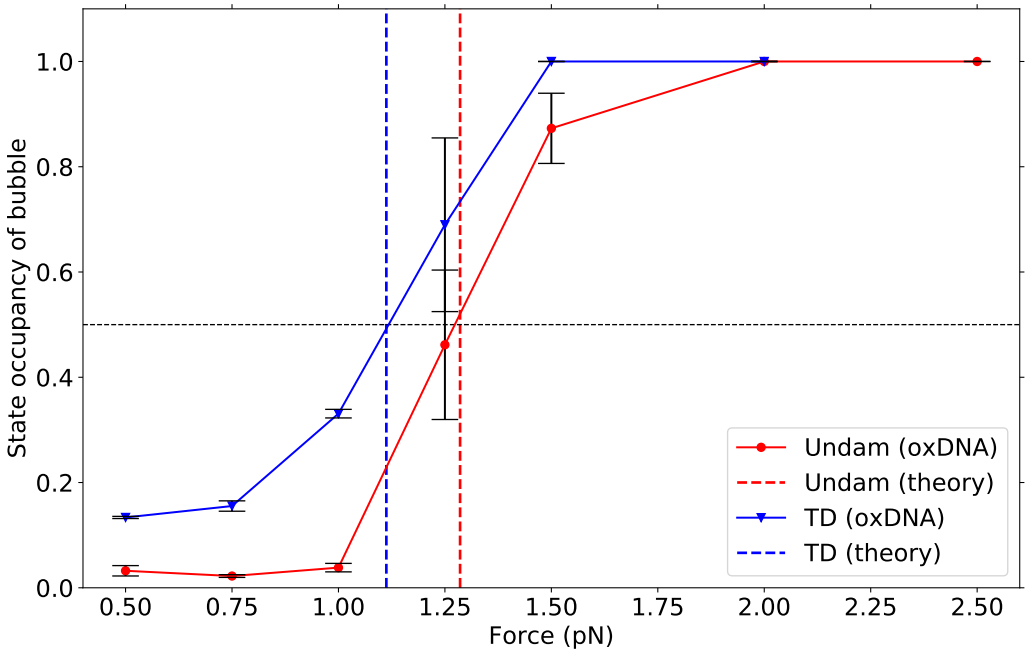


Figure 4.12: Shift in the characteristic force for the thymine dimer-containing dsDNA. The theoretical prediction of a 0.17 pN reduction in the characteristic force agrees well with measurements from oxDNA simulations of negatively supercoiled dsDNA at $\sigma \approx -0.056$. Error bars represent SEM.

The shift in the characteristic force for the thymine dimer-containing dsDNA can be described as a competition between ΔE_{loop} and Δa. An induced localised bend of θ_0 at the thymine dimer site reduces the cost of forming a plectonemic loop by ΔE_{loop} and allows plectonemes to be formed at higher forces than usual, but a reduction in the bubble initiation energy Δa allows twist-induced bubbles to be nucleated at lower forces. For the thymine dimer-containing dsDNA, since $\Delta a = 3\,k_{\mathrm{B}}T$ is significantly larger than $\Delta E_{loop} = 0.98\,k_{\mathrm{B}}T$ at the theoretical characteristic force of 1.29 pN, our model predicts a net reduction in the characteristic force. The calculated value of 0.17 pN reduction in the theoretical F_c matches well

with the measured shift in the plectoneme-bubble crossover point from oxDNA simulations of negatively supercoiled dsDNA at $\sigma \approx -0.056$ (Fig. 4.12).

4.7.2 Shift in lower characteristic force F_{lc}

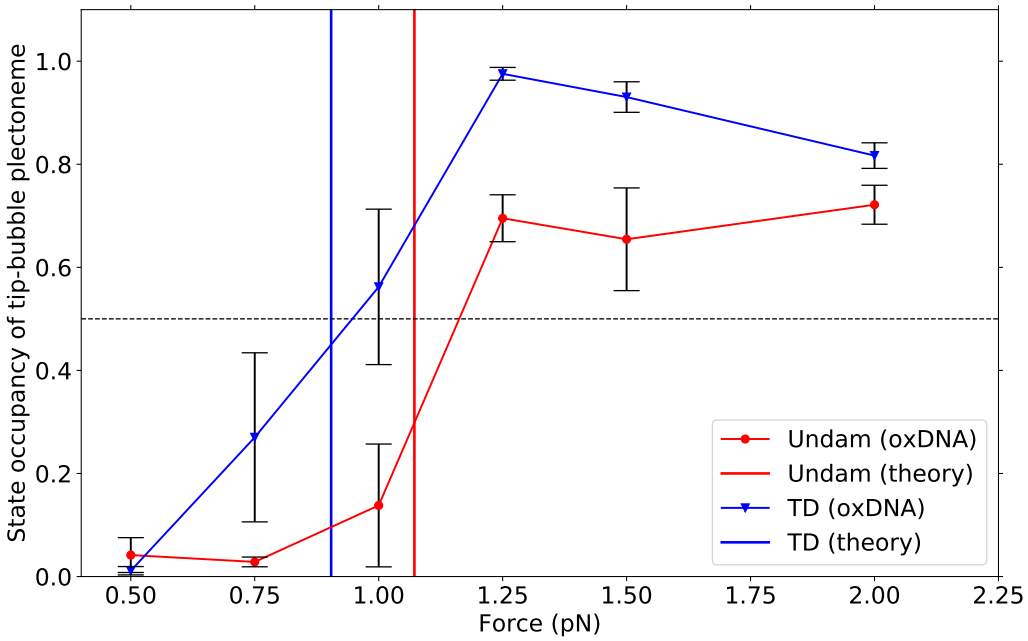


Figure 4.13: Shift in the lower characteristic force for the thymine dimer-containing dsDNA. A reduction in the lower characteristic force is correctly predicted by our tip-bubble model based on measurements of tip-bubble plectoneme occupancies made from oxDNA simulations of negatively supercoiled dsDNA, with and without the thymine dimer, at $\sigma \approx -0.073$. Error bars represent SEM.

A reduction in the bubble initiation energy a makes tip-bubbles energetically more favourable at lower F while the presence of a natural rest angle θ_0 at the thymine dimer site would reduce the energetic savings that kinking the end-loop brings. Analogous to the argument for the shift in the characteristic force, since Δa is larger than ΔE_{loop}, the net effect based on Eq. 4.18 is a reduction in F_{lc} (by 0.17 pN). This theoretical prediction is shown to quite accurately predict the shift that we measured for the thymine dimer-containing dsDNA simulated with the

oxDNA forcefield (Fig. 4.13).

4.7.3 Shift in buckling transition point

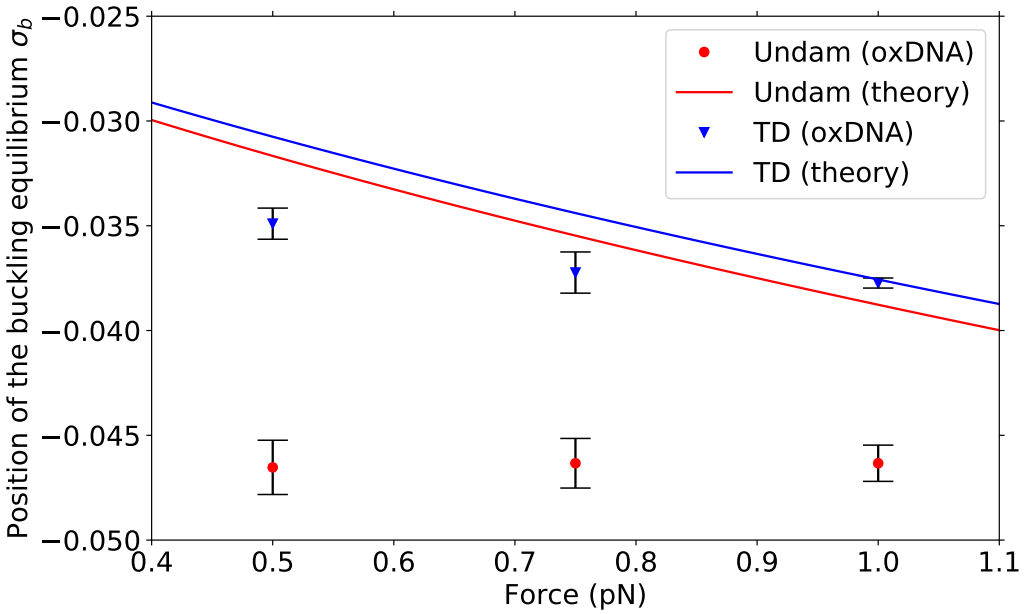


Figure 4.14: The model by Brutzer *et al.* (Eq. 4.7) predicts a shift in the position of the buckling transition to lower superhelical densities $|\sigma|$ when a thymine dimer is present. Error bars represent SEM.

The model by Brutzer *et al.* predicts that a reduction in the initial loop energy E_{loop} would shift the buckling transition point σ_b to lower superhelical densities $|\sigma|$. Using $\Delta E_{loop} \approx \frac{\theta_0}{\pi}\sqrt{\rho_0 p k_B T F}$ with $\theta_0 = 11.7°$, we can calculate the magnitude of the shift in σ_b (and therefore the σ_b for the TD dsDNA) and compare that against the measured σ_b of TD dsDNA from oxDNA simulations (Fig. 4.14). At $F \leq 1$ pN, the direction of shift in σ_b is correctly predicted by the Brutzer model, though the magnitude of the shift measured from oxDNA simulations is larger than the prediction by an order of magnitude of 1.

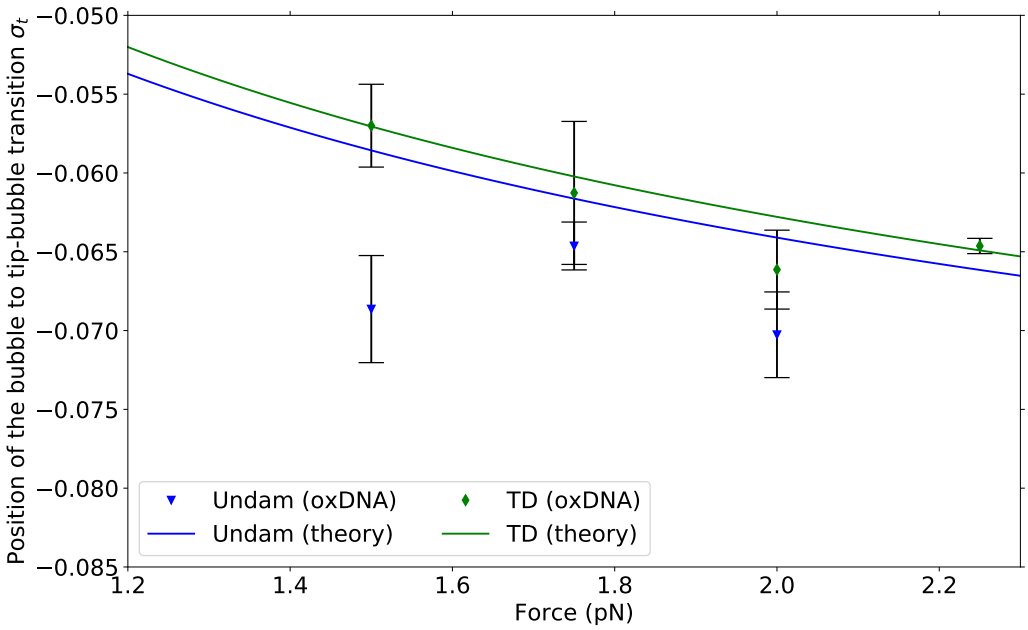


Figure 4.15: Eq. 4.20 predicts a shift in the position of the bubble to tip-bubble transition σ_t to lower superhelical densities $|\sigma|$ when a thymine dimer is present. For ease of comparison, an offset of $\Delta\sigma = 0.0176$ (or equivalently, $N = 1$) has been applied to the theoretical state boundaries. Error bars represent SEM.

4.7.4 Shift in bubble to tip-bubble transition point

The reduction in the bubble initiation energy Δa by the thymine dimer has no bearing on the position of the bubble to tip-bubble plectoneme transition σ_t, since a bubble is already formed in the first instance. ΔE_{loop} on the other hand affects the transition point by reducing the energetic cost of nucleating a loop at the thymine dimer site. Given that a bubble is typically nucleated at the TD site, writhing of the bubble-containing segment to form a tip-bubble plectoneme, which now requires less energy, could occur at a lower superhelical density. These effects are captured by Eq. 4.20, which we will use to calculate the theoretical bubble to tip-bubble plectoneme transition point for a dsDNA that contains a thymine dimer (Fig. 4.15). Two observations can be made from Fig. 4.15. Firstly, the

variation of the theoretical σ_t for the TD dsDNA with F compares well with the σ_t measured from oxDNA simulations. Secondly, the shift in σ_t towards lower superhelical densities when the TD is present is correctly predicted by our model. At $F = 1.5$ pN, oxDNA measurements show a larger-than-expected shift in σ_t, but that is likely due to the computational difficulty of equilibrating (undamaged) dsDNA configurations at a state point close to multiple state boundaries (i.e. the characteristic force and bubble to tip-bubble transition boundary). With a single state boundary, achieving a proper equilibration of the dsDNA near that boundary would require us to sample the pre-transition and post-transition states adequately as the dsDNA jumps back and forth between these two states (see, for instance, (Ott et al., 2020)). On the other hand, with two or more state boundaries in the vicinity, equilibration would mean sampling each of the multiple (i.e. > 2) states that the dsDNA jump into for a period of time that is significantly longer than what current computational resources could afford.

4.8 Further stress-testing of the theoretical framework

To further stress-test our theoretical model, we examined a similar dsDNA that contains a 2-bp mismatch instead of a thymine dimer. In oxDNA, a base pair mismatch has its hydrogen bond strength reduced to zero. Using the same bend angle measurement protocols in the previous chapter on a 40-bp duplex with a 2-bp mismatch, the bend angle θ_0 of the mismatch-containing duplex was found to be $-0.7 \pm 2.5^\circ$. Taken together, this means that the 2-bp mismatch introduces a large Δa and a negligible ΔE_{loop}. Consequently, we would expect the position of the bubble to tip-bubble transition σ_t to be unperturbed by the presence of a 2-bp mismatch.

Fig. 4.16 shows the comparison between the position of the bubble to tip-bubble plectoneme transition σ_t for undamaged dsDNA, and σ_t for the 2-bp mismatch dsDNA. Unlike the TD-containing dsDNA, there is no clear shift in σ_t to either higher or lower superhelical densities for the dsDNA with 2-bp mismatch. In addition, the σ_t for the 2-bp mismatch dsDNA varies with F in the manner that is consistent with Eq. 4.20. The anomalous gap between the σ_t for undamaged dsDNA and the σ_t for the 2-bp mismatch dsDNA at $F = 1.5$ pN can be partially attributed to the same computational difficulties associated with equilibrating DNA configurations near critical points in the state space. These observations do not contradict the predictions from our theoretical framework for tip-bubble plectonemes.

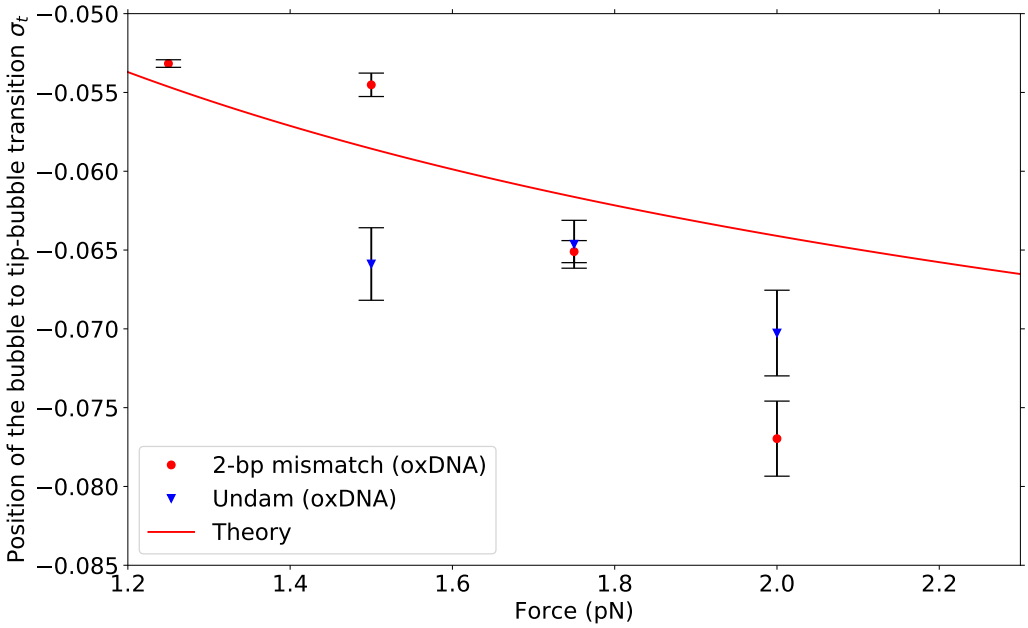


Figure 4.16: Position of the bubble to tip-bubble plectoneme transition σ_t for the 2-bp mismatch dsDNA, alongside the σ_t for undamaged dsDNA and the theoretical prediction. For ease of comparison, an offset of $\Delta\sigma = 0.0176$ (or equivalently, $N = 1$) has been applied to the theoretical state boundary. Error bars represent SEM.

An artificial defect (henceforth termed as defect X) is also introduced to stress-

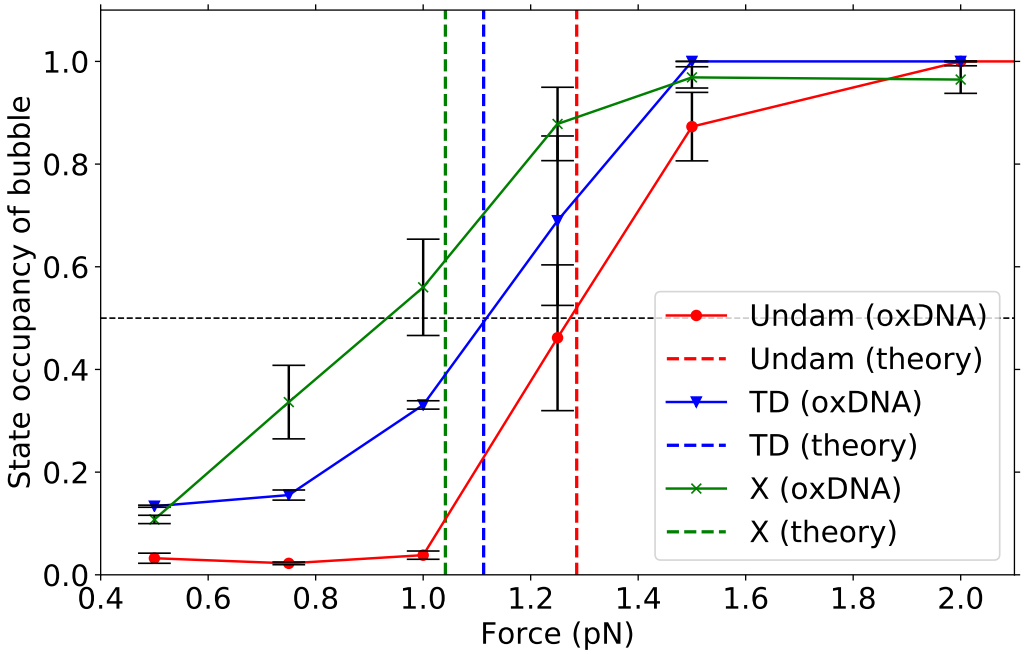


Figure 4.17: Comparison of the theoretical characteristic forces F_c for the undamaged dsDNA, TD-containing dsDNA and defect X-containing dsDNA with the occupancy of the bubble state over a range of forces at $\sigma \approx -0.056$. Error bars represent SEM.

test the theoretical framework. This defect reduces the hydrogen bonding strength of the AT base pairs by the same amount as the thymine dimer (and shifts the denaturation transition position by the same amount. See Appendix A.7), but unlike the thymine dimer, it does not introduce any localised change in roll or twist to the DNA duplex, and in turn any noticeable duplex bending (Randisi, 2019). Application of the bend angle measurement protocols highlighted in sub-section 3.1.1 on a 40-bp X-containing duplex indeed yields a bend angle θ_0 of $0.04 \pm 1.70°$. For such a defect, since θ_0 is negligible, we would expect a larger reduction in the characteristic force compared to the reduction in the characteristic force caused by the presence of the thymine dimer. Simulations of X-containing dsDNA under the same environmental conditions corroborates this prediction (Fig. 4.17), thus strengthening the justification of the use of Δa and ΔE_{loop} to characterise defects

such as mismatches and the thymine dimer.

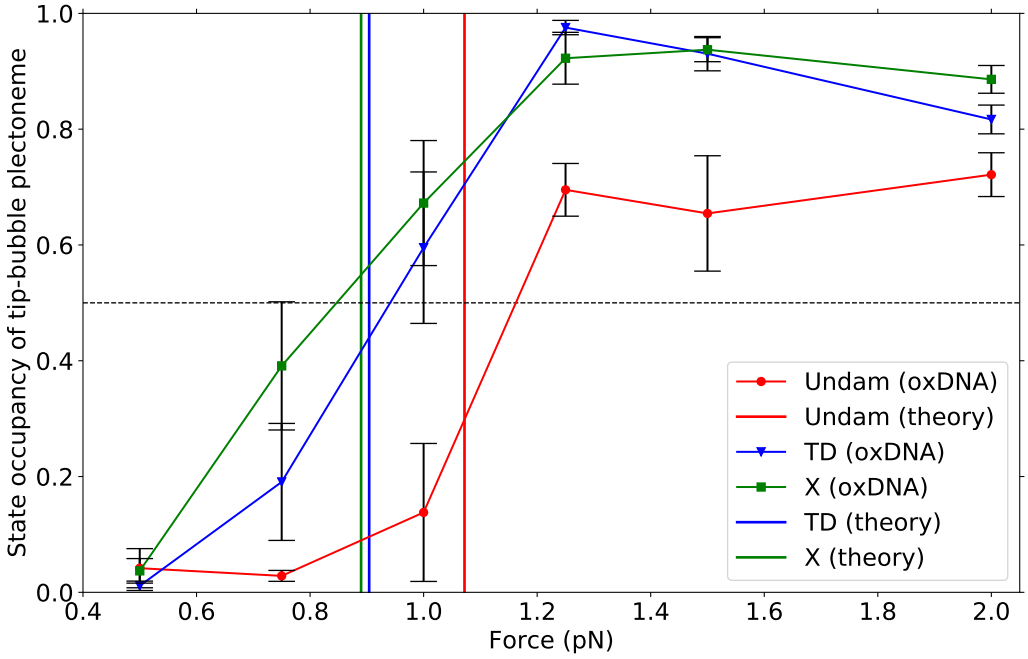


Figure 4.18: Comparison of the theoretical lower characteristic forces F_{lc} for the undamaged dsDNA, TD-containing dsDNA and defect X-containing dsDNA with the occupancy of the tip-bubble state over a range of forces at $\sigma \approx -0.073$. Error bars represent SEM.

Compared to the lower characteristic force F_{lc} of a TD-containing dsDNA, our theoretical model also predicts a smaller F_{lc} for the X-containing dsDNA. The presence of defect X reduces the nucleation cost of forming a bubble at the defect site but, unlike the thymine dimer, achieves the same amount of energetic savings in kinking the end-loop as the undamaged dsDNA. The shift in F_{lc} is however very small, which makes obtaining a statistically significant comparison between the state occupancies of plectoneme tip-bubbles in X-containing dsDNA and that of TD-containing dsDNA a very difficult task for the computational resources at our disposal. That being said, we were still able to identify a statistically significant increase in the state occupancy of the tip-bubble state at $F = 0.75$ pN in X-containing dsDNA (Fig. 4.18), which can be regarded as an indication pointing to

a reduced F_{lc}.

4.9 Tip-bubble plectonemes in positively supercoiled dsDNA

We now turn our attention to the characterisation of tip-bubbles in positively supercoiled dsDNA. While it is generally accepted that homeostatic DNA in most organisms is negatively supercoiled at a global level (Sinden et al., 1980; Hirose & Matsumoto, 2005; Luijsterburg et al., 2008; Corless & Gilbert, 2017), transient positive supercoils have been shown to be pervasive in genomic DNA as a result of transcription activities (M. S. Guo et al., 2021). The advancing RNA polymerase along the DNA track generates positive supercoils ahead of it and negative supercoils behind it (L. F. Liu & Wang, 1987). The downstream positive supercoils have been reported to destabilise nucleosomes and disrupt road-block proteins to increase the DNA's accessibility to RNA polymerase (Sheinin et al., 2013), and may also facilitate the detection of DNA damage that is otherwise hidden in the compact chromatin structure (Gerasimova et al., 2016).

OxDNA simulations of overtwisted DNA by Matek *et al.* and Randisi reveal an intermediate regime between the plectonemic and P-DNA state where tip-bubble plectonemes dominate (Matek et al., 2015; Randisi, 2019). We have reproduced their findings in Fig. 4.19. At forces ≤ 6 pN, dsDNA relaxes into the pure plectonemic state as more torsional energy is injected into the system. For $6 \text{ pN} < F < 9 \text{ pN}$, the dsDNA buckles into tip-bubble plectonemes instead of plectonemes. This represents a key difference between positively supercoiled dsDNA and its negatively supercoiled counterpart. In negative supercoiling, the dsDNA first forms either a pure plectonemic or a pure bubble state depending on the

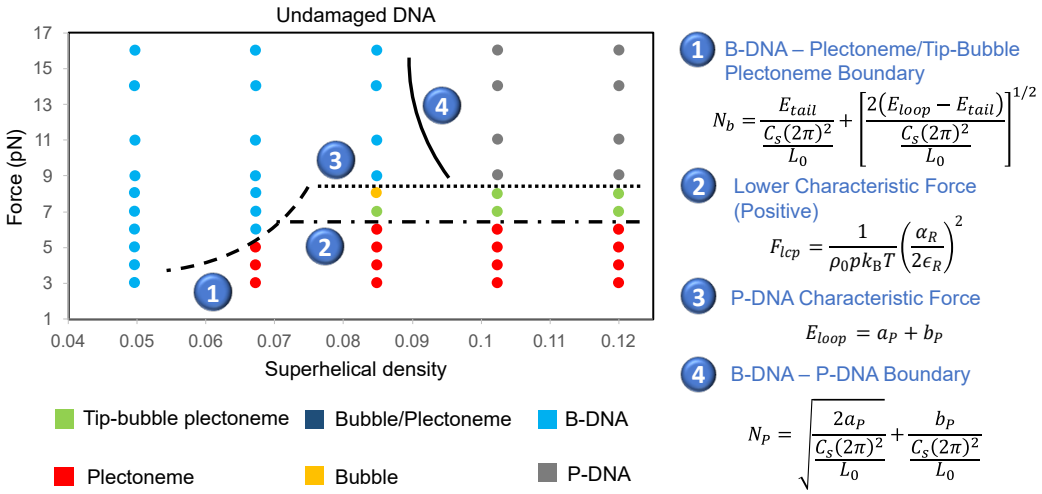


Figure 4.19: Force-torsion space for positively supercoiled dsDNA. The theoretical formulation of the (1) B-DNA – plectoneme/tip-bubble plectoneme boundary is based on the DNA buckling model by Brutzer *et al.* (Brutzer et al., 2010), with E_{loop} defined by Eq. 4.21. When $F < F_{lcp}$, the (2) lower characteristic force for positively supercoiled dsDNA, the formation of a tip-bubble plectoneme during the buckling transition is energetically unfavourable since the net energetic saving is smaller than the cost, α_R, of kinking the end-loop in the plectoneme. Conversely, when $F > F_{lcp}$, the energetic saving is large enough to justify the formation of a tip-bubble plectoneme over a plectoneme during the buckling transition. At higher forces above the (3) P-DNA characteristic force, the P-DNA state is energetically favoured over the plectoneme or tip-bubble plectoneme state in positively supercoiled dsDNA. The theoretical treatment of the (4) B-DNA – P-DNA boundary is similar to that of the denatured state in negatively supercoiled dsDNA (see Section 4.10 for more details).

size of the pulling force or tension. With further twisting of the dsDNA, the pure plectonemic or bubble state transits into the tip-bubble state if the pulling force is larger than the lower characteristic force such that the energetic cost of forming a tip-bubble is smaller than E_{tail}, the free energy of every subsequent writhe other than the first within the plectoneme. On the other hand, in positively supercoiled dsDNA, the transition from the B-DNA state to the tip-bubble plectoneme state can occur without first requiring the B-DNA to form either a pure buckled state

or a pure denatured state. The careful reader will note that in Fig. 4.19, the state point at $F = 8$ pN and $\sigma \approx 0.085$ is represented by the bubble state. But in actuality, the state point is a mixed one, with the bubble state as the dominant state (i.e. state occupancy $> 50\%$), and a relatively high state occupancy of the tip-bubble/plectoneme states (close to 40%). This stands in contrast to the pure plectonemic and bubble states (where concurrent occupancy of other states is less than a percent) observed in our simulations of negatively supercoiled dsDNA.

In addition, tip-bubbles in positively supercoiled dsDNA possess several characteristics that differ from tip-bubbles in negatively supercoiled dsDNA:

- The size of the tip-bubble in positively supercoiled dsDNA does not grow linearly with the number of imposed turns. This stands in contrast to the near-linear variation of the tip-bubble size with the superhelical density observed in negatively supercoiled DNA (Fig. 4.20).
- Tip-bubbles in positively supercoiled dsDNA are also smaller in size compared to their counterpart in negatively supercoiled dsDNA. The tip-bubble size is measured to be around 3 to 5 base pairs, which is approximately half of the size of the tip-bubble observed at $\sigma \approx -0.073$. The smaller tip-bubble size could reflect the high energetic cost of denaturation in overwound DNA, and represent the optimal number of base pairs required for the DNA strands at the tip of the plectonemic loop to bend backwards in order to minimise the loop curvature at high pulling forces (Fig. 4.21).

These observations suggest that tip-bubbles are not formed in positively supercoiled DNA solely to accommodate the excess torsional strain imposed on the DNA. Instead, they serve to facilitate the nucleation of the plectonemic loop in the buckling transition by reducing its curvature and therefore the energetic penalty of forming a loop at higher forces. We can capture this hypothesis in the formulation

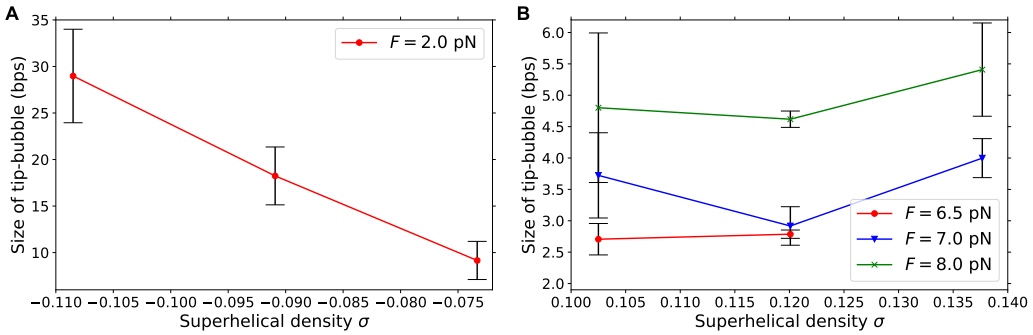


Figure 4.20: (A) Size of tip-bubbles in negatively supercoiled dsDNA. (B) Size of tip-bubbles in positively supercoiled dsDNA. Error bars represent SEM. In negatively supercoiled dsDNA, there is a near-linear relation between tip-bubble size and superhelical density $|\sigma|$. In positively supercoiled dsDNA on the other hand, the size of the tip-bubbles does not vary significantly over a similar interval of superhelical densities.

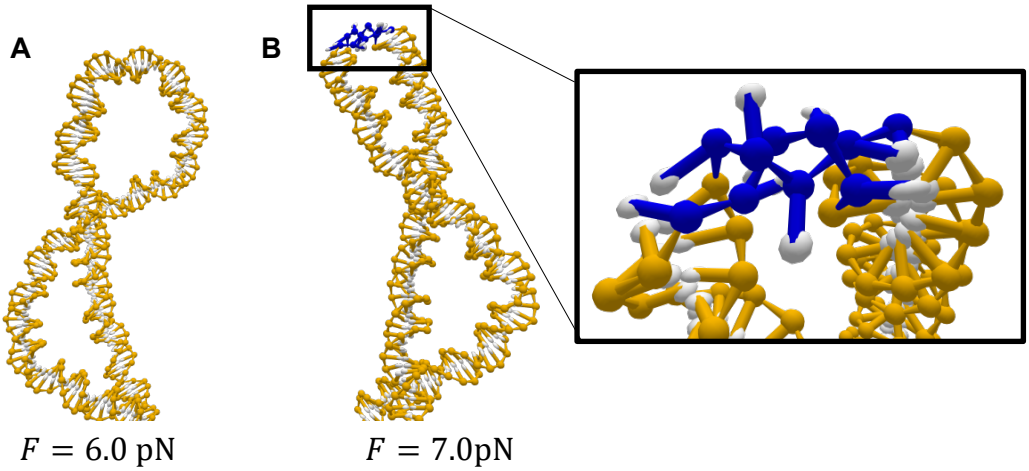


Figure 4.21: End-loop of (A) plectoneme at $F = 6.0$ pN and $\sigma \approx 0.138$, and (B) plectoneme at $F = 7.0$ pN and $\sigma \approx 0.138$, with inset focusing on the kinked tip and the denatured base pairs (highlighted in blue). Strong bending of the DNA end-loop is already observed when $F = 6.0$ pN. Increasing the magnitude of the pulling force further would require a kink in the end-loop to relieve the bending stresses.

of the free energy of the plectonemic end-loop for positively supercoiled dsDNA:

$$E_{loop} = \begin{cases} 2\sqrt{\rho_0 p k_B T F}, & \text{if } F < F_{lcp} \\ 2(1-\epsilon_R)\sqrt{\rho_0 p k_B T F} + \alpha_R, & \text{otherwise} \end{cases} \tag{4.21}$$

α_R is the cost of forming a kink in the plectonemic end-loop. ϵ_R, like its counterpart definition in Eq. 4.13, reflects the reduction in curvature energy due to the presence of a kink at the tip of the end-loop. The slight increase in tip-bubble size with the magnitude of the pulling force in Fig. 4.20 suggests that α_R is a force-dependent quantity, but as a simplifying assumption, we will neglect the force dependence in α_R and take it to be a constant as a lowest order approximation. ϵ_R is also taken to be a constant since the size of the tip-bubble does not vary significantly over the range of forces and superhelical densities that we are considering here. F_{lcp} in Eq. 4.21 serves as a state boundary (i.e. a characteristic force) between the plectonemic state and the tip-bubble plectonemic state in positively supercoiled dsDNA:

$$F_{lcp} = \frac{1}{\rho_0 p k_{\mathrm{B}} T} \left(\frac{\alpha_R}{2\epsilon_R} \right)^2 \tag{4.22}$$

Together with Eq. 4.21, Eq. 4.22 can be interpreted in the following manner: Introducing a kink in the end-loop brings about energetic savings that comes from the concurrent reduction in the curvature energy of the loop and the work done against the pulling force F. In mathematical terms, these energetic savings as a whole is equivalent to $2\epsilon_R\sqrt{\rho_0 p k_{\mathrm{B}} T F}$. When $F < F_{lcp}$, the formation of a tip-bubble plectoneme during the buckling transition is energetically unfavourable since the net energetic saving is smaller than the cost, α_R, of kinking the end-loop in the plectoneme. Conversely, when $F > F_{lcp}$, the energetic saving is large enough to justify the formation of a tip-bubble plectoneme over a plectoneme during the buckling transition.

Substituting Eq. 4.21 into Eq. 4.7 gives us the position of the buckling transition from the B-DNA state to the plectoneme or the tip-bubble plectoneme state. Because $\alpha_R - 2\epsilon_R\sqrt{\rho_0 p k_{\mathrm{B}} T F} < 0$, the theory predicts a shift in the buckling curve

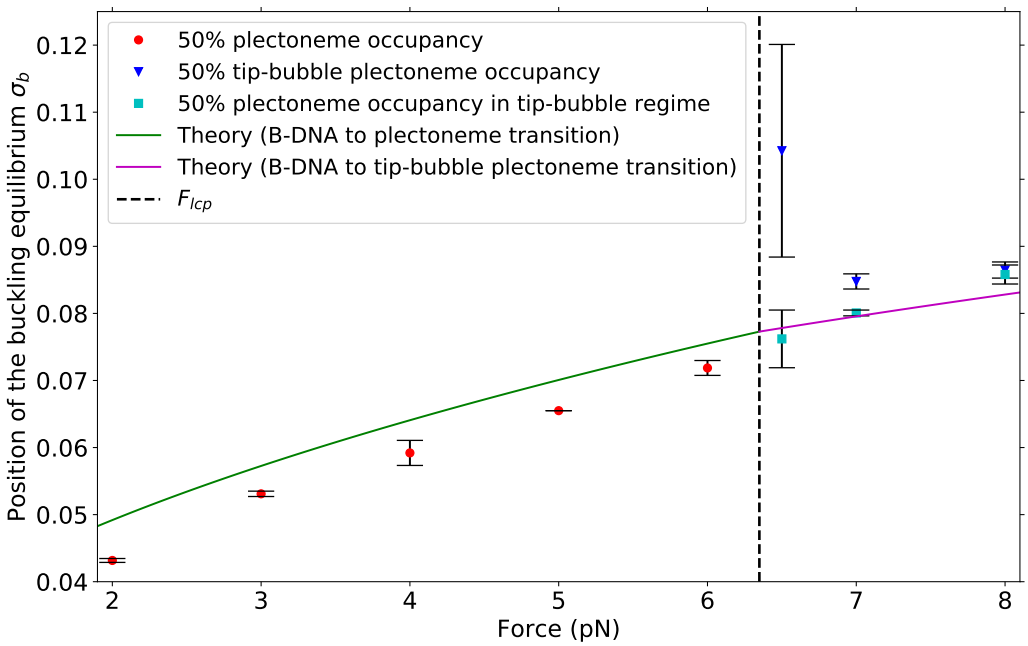


Figure 4.22: Position of the buckling equilibrium in positively supercoiled dsDNA. In oxDNA simulations, this position is defined as the state point where 50% occupancy rate of the plectonemic or tip-bubble plectonemic state is detected. Error bars represent SEM.

to lower values of σ when $F > F_{lcp}$. Fig. 4.22 shows the comparison between the buckling position measured from oxDNA simulations and our theoretical prediction, obtained using $\epsilon_R = 0.21$ and $\alpha_R = 14\,k_{\mathrm{B}}T$. As far as we are aware, there is no established experimental data concerning the denaturation energy of bubbles in positively supercoiled DNA for us to make a direct comparison against our choice of value for α_R. Instead, we could compare α_R against the cost of forming a tip-bubble in negatively supercoiled dsDNA. For a tip-bubble in negatively supercoiled dsDNA that has a size of approximately 10 bps, the energetic cost of formation is approximately $30\,k_{\mathrm{B}}T$ (see Fig. 4.4), or roughly $3\,k_{\mathrm{B}}T$ per base pair. In contrast, for tip-bubbles in positively supercoiled dsDNA that has a size of approximately 4 bps, the energetic cost of formation per base pair is approximately $3.5\,k_{\mathrm{B}}T$. This is comparable, if not slightly larger than the cost of

denaturing a base pair in undertwisted dsDNA. Our choice of the value for ϵ_R on the other hand is similar to the value of ϵ (0.24) derived from oxDNA simulations of a similarly-sized, positively supercoiled dsDNA with a 4-bps mismatch at 0.2 M salt concentration (P. R. Desai et al., 2020).

This combination of values for ϵ_R and α_R in Eq. 4.22 yields $F_{lcp} \approx 6.35$ pN, a value which is close to the state boundary between plectonemes and tip-bubble plectonemes observed in our oxDNA simulations of positively supercoiled dsDNA (Fig. 4.22). One could argue that the state boundary is closer to $F = 6.5$ pN than $F = 6.0$ pN, given the anomalous jump in the 50% tip-bubble plectoneme occupancy mark at $F = 6.5$ pN relative to the rest of our measurements. Such a deviation from expected behaviour could once again reflect the computational difficulty of equilibrating the dsDNA at a state point near multiple state boundaries, similar to what we had observed in the simulations of negatively supercoiled dsDNA at $F = 1.5$ pN in Fig. 4.15.

Our choices for ϵ_R and α_R also predict a very slight shift in the buckling curve when $F > F_{lcp}$, but this effect is very small (see Fig. 4.22) and difficult to observe or measure in such complex numerical simulations. It is also noteworthy that the simulations show a close proximity between the 50% plectoneme occupancy and 50% tip-bubble plectoneme occupancy in the tip-bubble regime at $F = 7.0$ pN and 8.0 pN. Barring, again, the anomaly that we have seen earlier at $F = 6.5$ pN, this observation strengthens our earlier hypothesis about the role of tip-bubbles in positively supercoiled dsDNA, and reinforces the approximation made in equating the tip-bubble formation with the buckling transition via Eq. 4.21.

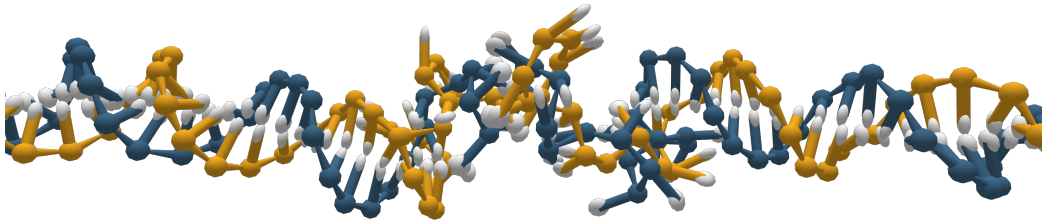


Figure 4.23: A snapshot of the P-DNA state in positively supercoiled dsDNA at $F = 16$ pN and $\sigma \approx 0.155$. The bases are exposed on the outside while the backbones are tightly interwound.

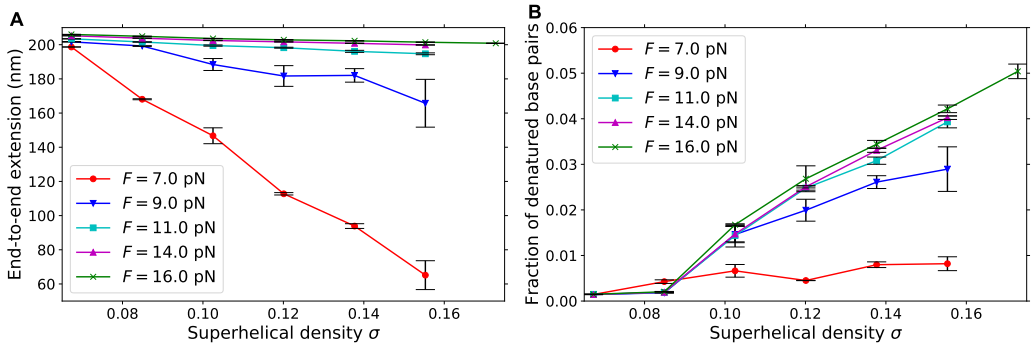


Figure 4.24: (A) End-to-end extensions for positively supercoiled dsDNA in the P-DNA state show little change over a wide range of σ, similar to what we observe for negatively supercoiled dsDNA in the denatured state. (B) To a good approximation, the fraction of base pairs in the P-DNA state grows linearly with σ. The case of $F = 7$ pN is included in both plots to serve as a reference point. At $F = 7$ pN, the end-to-end extension decreases due to the formation of a plectoneme. The fraction of denatured base pairs also remains relatively unchanged at $F = 7$ pN, which reinforces our earlier observation in Fig. 4.20 that the size of the tip-bubble in positively supercoiled dsDNA is constant over a wide range of σ. Error bars represent SEM.

4.10 P-DNA state in positively supercoiled dsDNA

Our oxDNA simulations show that at $F = 9$ pN and beyond, dsDNA relaxes into the P-DNA state instead of the plectoneme or tip-bubble plectoneme state to relieve the imposed torsional strain (Fig. 4.23). The letter "P" in P-DNA pays homage to Linus Pauling, as its structural features, first modelled by Allemand *et al.* (Allemand et al., 1998), bear striking resemblance to Pauling's proposed model of an inside-out DNA structure with bases exposed and the phosphate backbones located in the middle of the helix (Pauling & Corey, 1953). Randisi in his thesis provided a detailed characterisation of the P-DNA conformation using oxDNA simulations (Randisi, 2019). He demonstrated that the critical superhelical density σ_c at which the entire dsDNA is converted into the P-DNA state varies from 2.5 for a pulling force F of 10 pN to 2.1 for $F = 40$ pN, and also made the observation that the P-DNA state in dsDNA adopts the solenoidal configuration, whose radius and pitch increases when the pulling force F decreases, or when σ increases. Because a great deal has been reported about P-DNA's structural features and elastic properties, we will instead focus, for this chapter, on the free energy characterisation of the P-DNA state in the regime before the entire dsDNA is converted into P-DNA state (i.e. when $\sigma << \sigma_c$). In this regime, the P-DNA state is similar to the denatured/bubble state in underwound dsDNA, both in terms of its end-to-end extension profile as well as the approximately linear relation between the fraction of base pairs in the P-DNA state and the degree of supercoiling (Fig. 4.24). These parallels with twist-induced denaturation suggest that we could use Eq. 4.10 as the basis to characterise the free energy of P-DNA $E_{\text{P-DNA}}$ as:

$$E_{\text{P-DNA}} = \frac{1}{2}\frac{C_s}{L_0}(2\pi)^2(N - N_{LP})^2 + a_P + b_P N_{LP} \tag{4.23}$$

N_{LP} is defined as the number of turns stored in the P-DNA form to accommodate the imposed torsional stresses. Following the definitions of a and b in Eq. 4.10, a_P refers to the energy needed to initiate a "run" of P-DNA base pairs while b_P is the energy needed to convert the base pairs at the boundaries of the existing run into the P-DNA conformation. With Eq. 4.23, we can obtain the P-DNA characteristic force F_{LP}, the post-transition torque Γ_{LP} and the B-DNA–P-DNA state boundary N_P:

$$E_{loop}\left(F_{LP}\right) = a_P + b_P \tag{4.24}$$

$$\Gamma_{LP} = \frac{b_P}{2\pi} \tag{4.25}$$

$$N_P = \sqrt{\frac{2a_P}{\frac{(2\pi)^2 C_s}{L_0}}} + \frac{b_P}{\frac{(2\pi)^2 C_s}{L_0}} \tag{4.26}$$

We can use Eq. 4.25 and the torque response curve for the B-DNA to P-DNA transition (Fig. 4.25) to obtain estimates of a_P and b_P. Starting with b_P, its value can be estimated from the post-transition torque of approximately 49 pNnm from the torque response curve in Fig. 4.25. This gives us $b_P \approx 75\, k_{\mathrm{B}}T$. The value of a_P can be obtained using the same measurement protocols for the torque overshoot's area outlined in Sect. 4.3. First, we use the torque response curve at $F = 9$ pN as a gauge for the torque overshoot area. Next, we use a triangle to represent the torque overshoot area. The triangle is bounded horizontally by $\sigma \approx 0.074$ and $\sigma \approx 0.102$ and vertically by $\Gamma \approx 50$ pNnm and $\Gamma \approx 60$ pNnm. This yields an approximate value of $11.7\, k_{\mathrm{B}}T$ for a_P.

With these values of a_P and b_P, F_{LP} is computed using Eq. 4.24 to give an approximate value of 12 pN. N_P is also plotted in Fig. 4.26 using Eq. 4.26. Our estimate of F_{LP} is much larger than the observed P-DNA characteristic force of approximately 9 pN from our simulations. N_P on the other hand yields a good fit

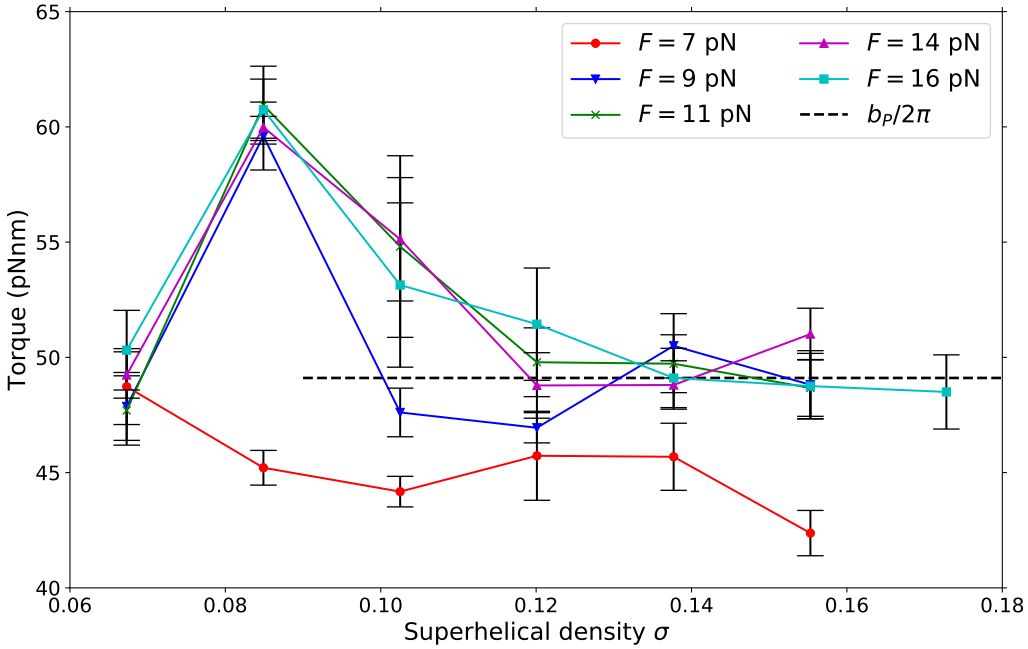


Figure 4.25: Torque response curve of the B-DNA to P-DNA transition in positively supercoiled dsDNA at $F = 9$ pN to 16 pN, with error bars representing SEM. As a reference, the $F = 7$ pN torque response curve for the B-DNA to tip-bubble plectoneme transition is included as well. A large torque overshoot is detected for the range of forces that we have considered here. The post-transition torque for these curves converges at an approximate value of 49 pNnm.

with the measured 50% occupancy rate of the P-DNA state in oxDNA trajectories (albeit with a small over-estimation). The discrepancy between the simulation measurement and the theoretical calculation of the characteristic force should not come as a surprise since, in this simple model of the P-DNA state, we did not consider alternative means or configurations that the dsDNA can adopt to accommodate the additional turns (e.g. additional turns can be stored as writhe in the P-DNA state) or the reduced bending stiffness of the DNA segment stored in the P-DNA conformation.

It is also useful, at this juncture, to make a comparison between the torque response curve in Fig. 4.25 and the corresponding experimental measurements. Op-

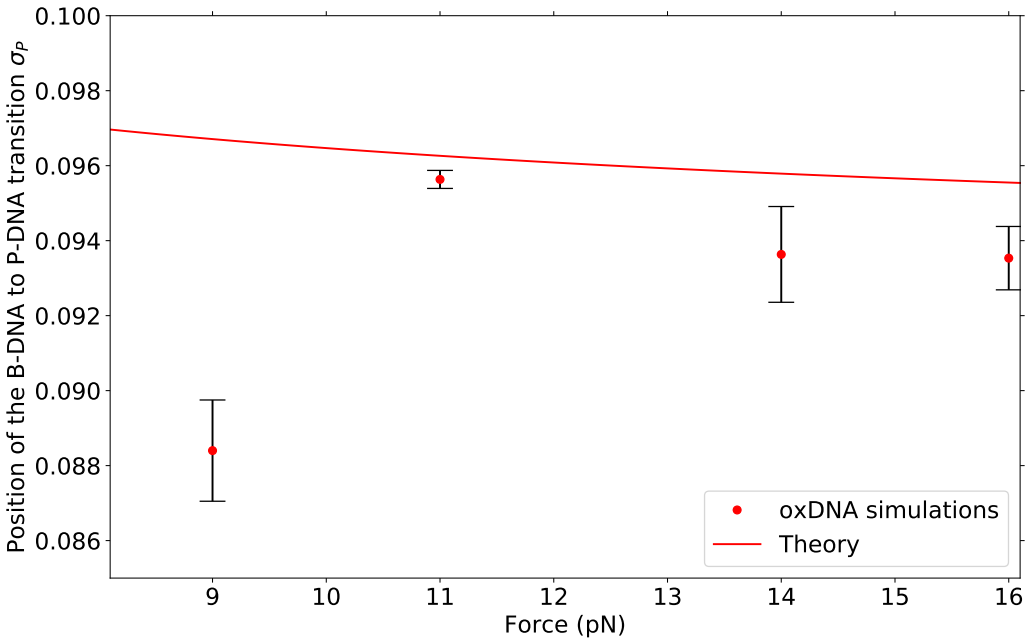


Figure 4.26: Position of the B-DNA to P-DNA transition in positively supercoiled ds-DNA. In oxDNA simulations, this position is defined as the state point where 50% occupancy rate of the P-DNA is detected. The theoretical position σ_P is computed using Eq. 4.26. Error bars represent SEM.

tical tweezer experiments by Bryant *et al.* reported a critical torque of 34 pNnm for the B-DNA to P-DNA transition under a constant tension of 45 pN (Bryant et al., 2003). This value is comparable to the critical torque measurements for the B-DNA to scP-DNA (supercoiled P-DNA) from the magnetic tweezer experiments by Lipfert *et al.* (36 ± 2 pNnm at a tension of 6.5 pN (Lipfert et al., 2010)) and the optical tweezer experiments by Deufel *et al.* (33 pNnm at a tension of 10 pN (Deufel et al., 2007)). These experimental values are smaller than our measured post-transition torque of approximately 50 pNnm by nearly 30%. Moreover, the torque overshoot in Fig. 4.25 is conspicuously absent in the torque response curves of these experiments (see, for instance, Fig. 3 in the paper by (Bryant et al., 2003) or (Deufel et al., 2007)). The choice of salt concentration alone is insufficient to account for these discrepancies since some of these single-molecule ma-

nipulations were carried at arguably what one might consider to be relatively low salt concentrations (e.g. 100 mM NaCl and 40 mM Tris-HCl (Bryant et al., 2003), and 137 mM NaCl, 2.7 mM KCl and 10 mM phosphate (Lipfert et al., 2010)). The absence of a torque overshoot in the experiments' torque output could be caused by a lack of high resolution measurements at the time, compared to more recent torque measurement techniques (Janssen et al., 2012; Oberstrass et al., 2012) that are sensitive enough to pick up the torque overshoot in the buckling transition, which, relative to the torque overshoot for the the B-DNA to P-DNA transition that we obtained from our simulations, has a much smaller vertical height (in pNnm) and area. One plausible explanation for these discrepancies is that the oxDNA2 force field has not been calibrated to reproduce the twist-induced P-DNA form accurately at high F and high σ. A potential source of issues is the way oxDNA2 handles electrostatic interactions using a simplified Debye-Hückel treatment (B. E. Snodin et al., 2015; Sengar et al., 2021). This issue may become critical when the negatively-charged phosphate backbones are closely intertwined, similar to what we observe when the dsDNA adopts the P-DNA conformation.

4.11 Conclusion

The theoretical framework that we have outlined in this chapter to describe the energetics of tip-bubbles and the influence of defects on DNA supercoiling is a simple one. The model ignores, for instance, the interwinding of unpaired strands when bubbles are formed (Benham, 1992; W. R. Bauer & Benham, 1993; Fye & Benham, 1999) and the changes in bend or twist moduli associated with bubbles and defects. The model also does not factor in anisotropic mechanical properties such as the twist-stretch coupling that becomes important when large forces are at play (J. F. Marko, 1997; Lionnet et al., 2006; Gore et al., 2006), or the effect

of twist-bend coupling on the shape of the DNA loops (J. F. Marko & Siggia, 1994a; Nomidis et al., 2019). Its simplicity is a deliberate choice, designed to elucidate the main factors that drive the behaviour of supercoiled dsDNA in the force-torsion space, and to provide a quick, back-of-the-envelope approach for experimentalists and theorists alike to interpret single-molecule manipulations or simulations of dsDNA with defects. Even though we have only applied the framework to the computational study of thymine dimers and mismatches, we expect the characterisation of defects based on their effect on the bubble initiation energy a and the plectonemic loop energy E_{loop} to work well on other defects that similarly induce duplex bending or weaken the hydrogen bonding in base pairs. Examples of such defects include the single-nucleoside gap created by ionising radiation, which induce a directional bend in the DNA duplex (H. Guo & Tullius, 2003), as well as the wobble base-pair between guanine and uracil in DNA (Seibert et al., 2003).

The framework could also shed some insight into the difficulty of detecting tip-bubble plectonemes using conventional magnetic or optical tweezer manipulation techniques. For tip-bubble plectonemes to be formed in negatively supercoiled dsDNA, E_{tail} has to be larger than the net energetic cost of kinking the plectonemic end-loop. This implies that the tip-bubble plectonemes are unlikely to grow to a length that becomes comparable to the contour length of the dsDNA since the dominant mode of accommodating the additional torsional stresses in the tip-bubble plectoneme regime is the nucleation and growth of DNA bubble(s), similar to the manner by which the pure bubble state accommodates excess twist. Consequently, tracking end-to-end extension changes (C. Bustamante et al., 2003) on its own is not a reliable method of ascertaining the presence of tip-bubble plectonemes in negatively supercoiled dsDNA.

On the other hand, in positively supercoiled dsDNA, the tip-bubble does not grow

in size with increasing σ to accommodate the additional torsional stresses. Instead, the tip-bubble plectoneme continues to grow in length as σ increases, making it indistinguishable from ordinary plectonemes from the perspective of tracking state transitions based on the end-to-end extension of dsDNA. A combination of end-to-end extension tracking, and the use of appropriate nucleases to probe exposed bases (N. A. Desai & Shankar, 2003) could be employed to distinguish these tip-bubble plectonemes from the P-DNA conformation when σ is sufficiently small.

One of the unanswered questions in this work is how the variation in salt concentration might affect the defect parameter ϵ. Desai *et al.* had reported that a 2-bp mismatch in their oxDNA simulations could pin the plectoneme with the imposition of a high force (2 pN) and a high salt concentration, and appreciably less so in a low force and low salt scenario (P. R. Desai et al., 2020). It is unclear from their simulations if the application of a high or low force plays a more important role than the choice of salt concentration in determining the plectoneme pinning probability and in turn the value of ϵ.

Future investigations can also focus on examining the mechanical properties of the P-DNA state in dsDNA. We have some sense of what the torsional modulus C of the P-DNA conformation should be in the oxDNA forcefield (i.e. $5\,k_{\mathrm{B}}T$nm), based on Randisi's calculations using torque outputs at $\sigma > \sigma_c$ (Randisi, 2019), but it is less clear what the bending modulus B should be. Measuring the value of B could help us understand the energy costs associated with the formation of loops and solenoids in the P-DNA state and in turn the state boundaries of positively supercoiled dsDNA at high F and σ.

5 | Twisting Helix Bundles

5.1 Introduction

The buckling transition that we examined in Chapter 3 and 4 is not a phenomenon that is unique to torsionally stressed dsDNA in the biological context. On the contrary, buckling, in its broadest definition, is one of the possible manifestations of instabilities in elastic rods subjected to external stresses (Duprat & Shore, 2015; J. M. T. Thompson, 2017), and has implications for various scientific and engineering disciplines. Petroleum engineers, for instance, are concerned with the buckling of drill strings in a drilling rig (J. Thompson et al., 2012) while medical practitioners may rely on the buckling of the guidewire to negotiate a lesion in the coronary artery during an endovascular intervention (Schneider, 2003).

In this chapter, we will examine the buckling of DNA-based nanotubes. DNA's high thermodynamic stability, reliable base-pairing and the nearly limitless combination of sequences makes it an ideal material for the synthesis of complex nanostructures (Seeman & Sleiman, 2017). In particular, DNA nanotubes (which in our context refers to bundled dsDNA arranged in a parallel fashion) have attracted significant attention in recent years, in part due to the relative ease of synthesising them using the origami approach and in part due to their wide range of applicability as building blocks of mechanical scaffolds and in mechanoresponsive devices (Castro et al., 2011; Wei et al., 2012; Mohammed et al., 2017; Liedl et al., 2010). Consequently, considerable efforts have gone into characterising the mechanical properties of DNA nanotubes (Schiffels et al., 2013; Kauert et al., 2011). Understanding mechanical properties such as the bend and twist moduli of DNA nanotubes allows for more refined control of their structure and behaviour under external stresses. Case in point is the proof-of-concept design of a nano-

scale sigmoidal switch that utilises the pre- and post-buckled states of closed helix bundle rings to designate the off and on states of the switch (Y.-J. Kim et al., 2021). Calibrated introduction of gaps into the ring structures tunes the ratio of the bend to twist moduli of these rings and in turn controls their buckling transition point .

The theoretical analysis of these experiments were typically carried out with the assumption that the nanotubes' responses and behaviour can be accounted for within the elastic regime using the wormlike chain (WLC) model (Kauert et al., 2011; Y.-J. Kim et al., 2021). However, because the nanotubes possess relatively high bending and twisting stiffness compared to the dsDNA, it remains unclear if this assumption continues to be valid in all scenarios. The sharp and abrupt decrease in the end-to-end extension of the four- and six-helix bundles in the magnetic tweezer experiments by Kauert *et al.* hints at a possible deviation from the WLC model. Similarly, cyclization experiments on dsDNA suggest that the WLC model's assumption of a homogenous elastic response breaks down due to denaturation of bonds or other local defects when $p > \frac{2\pi R}{K}$, where R is the radius of curvature, p is the bending persistence length as before, s is the arclength, l is the contour length of the WLC strand, and K is a numerical factor of order 1 (Qu et al., 2011). The typical length scales of these nanotubes used in experiments (for instance, the closed six-helix bundle rings in the paper by Kim *et al.* has a radius of gyration of less than 70 nm (Y.-J. Kim et al., 2021)) and their bending persistence lengths that range in the thousands of nanometres would fulfil the above-mentioned WLC breakdown criterion.

Therefore, we seek to address the question of whether the buckling of nanotubes can be characterised in the elastic regime using the WLC model. To do so, we turn to the use of oxDNA to simulate the buckling transition in helix bundles. OxDNA has also been shown to provide a very good structural description of DNA origami

and other large DNA nanostructures (Doye et al., 2020), including granular physical features that are not easily accessible by experiments or simulations that are highly coarse-grained. We will simulate 4-helix bundle (4HB) and 6-helix bundle (6HB) made from single-stranded tiles (SST) to match the type of nanotubes used in the tweezer experiment by Klaurt *et al.* (Kauert et al., 2011).

The rest of this chapter is divided into the following sections. First, we will outline the simulation protocols for twisting helix bundles. Next, we will provide a summary of the physics behind plectoneme geometry based on the WLC model. Finally, we will compare the theoretical predictions (of the plectoneme geometry and energetics) from the WLC model with simulation results, and discuss the implications of these results.

5.2 oxDNA simulations of plectoneme formation in helix bundles

5.2.1 Methods

Twist simulations of 4HB and 6HB systems made from single-stranded tiles were carried out by Hemani Chhabra using a protocol that is a variant to the one described in Chapter 2. Harmonic twist traps are applied on 40 slices of each end of the approximately 350 nm-long nanotube (see Fig. 5.1 for the definition of a nanotube slice and the description of the simulation set-up). 2 sets of 20 twist traps are spaced 20 slices apart. 40-45 slices on each end are left free (from the application of the twist traps) as the ends will typically be somewhat more flexible. The twist traps rotate in opposite direction on each end about an axis that passes through the centre of mass of the slices and lies along the tubular axis. Initial trajectories are simulated using the MD approach for 1×10^8 simulation steps with a force F

acting on both ends of the nanotube and a twisting rate of $2\pi \times 10^{-7}$ per time step. The applied force F ranges from 0.5 pN to 10 pN. Configurations at the requisite number of imposed turns N are extracted from these trajectories and equilibrated for at least 1×10^9 simulation steps. Simulations are carried out at a temperature of 300 K and a monovalent salt concentration of 1 M. An Andersen-like thermostat is also used in all the simulations.

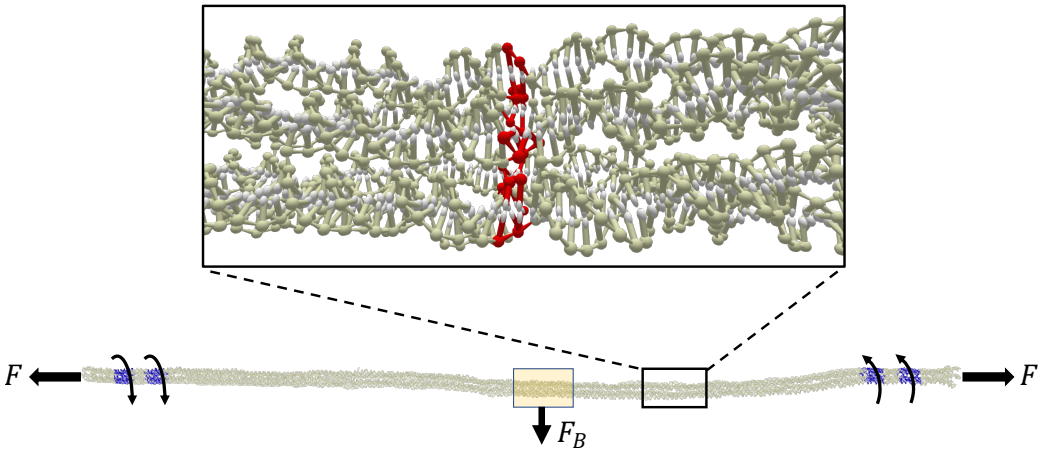


Figure 5.1: Twist simulation setup of DNA nanotube. An external force F is applied onto the outermost nucleotides on both ends of the nanotube. Harmonic traps are placed on two sets of 20 slices (highlighted in blue) near each end of the nanotube. These traps are rotated about an axis that passes through the centre of mass of the slices and lies in the same direction as F. After two turns are imposed onto the nanotube, a force $F_B = 4$ pN, perpendicular to the nanotube, is applied to 60 to 65 slices (yellow box) in the centre of the nanotube. (Inset) A slice is bounded by two layers of nucleotides (example in red).

We expect kink defects to form more easily in twisted or buckled helix bundles due to their high bend and twist moduli. These defects, like tip-bubbles in dsDNA, could immobilise the plectoneme and prevent its translational diffusion. Because the buckling site can be located along any part of the helix bundle, care has to be taken to minimise finite-size effects that arise from pinned buckling that occurs at the edge of the helix bundle. To reduce the chances of such a scenario,

a slightly twisted configuration of the nanotube is first extracted at $t = 1 \times 10^7$ simulation steps (when the tube contains 4π twist). Then, a force F_B is applied (perpendicular to the length of the tube) on 60-65 slices in the very centre of the nanotube. The force cannot be too large as it would cause irreversible changes to the physical characteristics of the nanotube. Eventually, we settled on $F_B = 4$ pN, after comparing the equilibrium end-to-end extension of the nanotube that is subjected to a finite F_B, against the reference extension of an unbent nanotube in the pre-buckled state (the two extensions should be similar).

Generating well-equilibrated and representative structures of helix bundle plectonemes remains a challenge nonetheless. 4HB-SST systems, in particular, have a tendency to form multiple buckling sites for reasons that are still being investigated, and the presence of kink defects prevent the diffusion and merger of the multiple plectonemes that are formed (see Fig. 5.2 for an example). Thus, in order to achieve representative end-to-end extension and post-buckling torque data from 4HB-SST systems, untwist simulations that use the final configurations from the twist simulations as starting points were also carried out. The end-to-end extension z and torque M are then taken to be the average of the corresponding equilibrium measurements from the production runs — i.e. $\overline{z}(N, F) = (z_{twist}(N, F) + z_{untwist}(N, F))/2$, $\overline{M}(N, F) = (M_{twist}(N, F) + M_{untwist}(N, F))/2$.

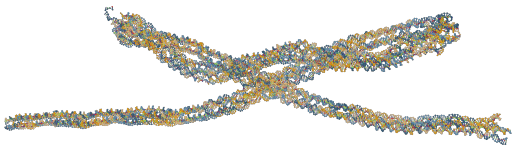


Figure 5.2: An example of how multiple plectonemes can be formed on twisted DNA nanotubes. The kinked end-loops slowed down the diffusion and merger of plectonemes. The example highlighted here is from a 4HB-SST system subjected to 8 imposed turns and $F = 2$ pN.

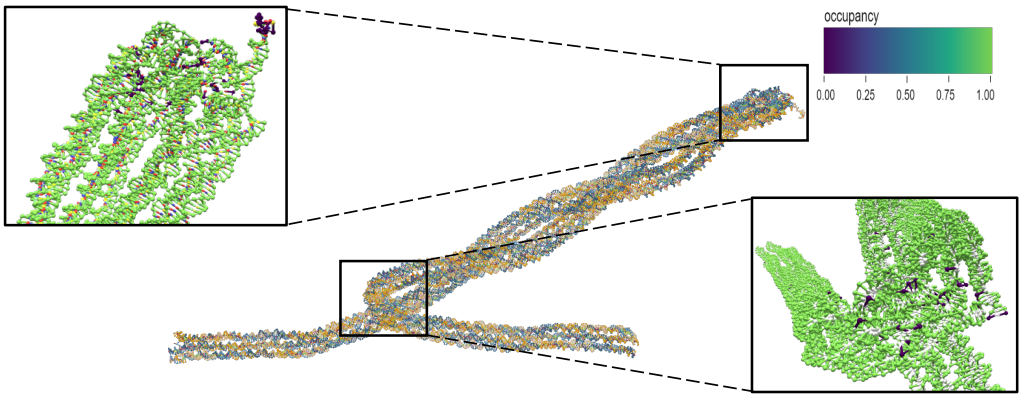


Figure 5.3: Formation of a well-formed plectoneme in a DNA nanotube. Kink defects are present in the end-loop and the connecting region between the plectoneme and the tail of the nanotube. (Inset) Open base pairs are identified using scripts from Ref. (Poppleton et al., 2020) and visualised in blue.

5.2.2 Geometry of plectonemes in helix bundle systems

Fig. 5.3 shows an example of a plectoneme that is formed from a helix bundle. Two geometrical features stand out in this example. Firstly, the plectoneme is characterised by strong, localised bending at its tip, creating a kink defect that contains dozens of broken base pairs (much like a tip-bubble in dsDNA). Secondly, the filaments in the plectoneme are connected to the straight and unwrithed tails of the nanotube in a manner that is atypical of what we would expect in a wormlike chain — one of the filaments connects smoothly to a tail with a small geometric curvature while the other is highly bent and kinked at the connecting point. The net effect is a plectoneme with a superhelical axis that is oblique relative to the unwrithed portion of the nanotube. In contrast, the filaments of a WLC plectoneme are, on average, equally bent at the connecting points, resulting in a superhelical axis that is perpendicular to the unwrithed tails. Virtually all the plectonemes produced by our twist simulations adopt the slanted configuration, suggesting that the slanted configuration is a minimum energy configuration. We can explain this

observation using results from Wong *et al.* (Wong et al., 2022) who compared the free energy of a bent 6HB-SST to that of a WLC theory (see Fig. 5.4). When the nanotube is weakly or moderately bent (i.e. the end-to-end distance $R_{ee} > 160$ nm), the free energy landscape with R_{ee} as the order parameter can be characterised using the WLC model. This picture changes when R_{ee} crosses the 160 nm threshold and the nanotube experiences strong bending. In this regime, the variation in free energy with R_{ee} no longer follows the WLC model. The strong bending kinks the nanotube and redistributes the bending stresses along the nanotube. Bending the kinked nanotube further does not increase the free energy cost significantly. For example, in Fig. 5.4, a $\Delta R_{ee} = 100$ nm in the WLC regime corresponds to a free energy change of $64\,k_{\mathrm{B}}T$ whereas the same ΔR_{ee} in the non-WLC, kink-mediated regime gives rise to a much smaller free energy change of $33\,k_{\mathrm{B}}T$. Thus, in forming a plectoneme from a nanotube, it is energetically favourable to create a sharp bent in one of the filaments instead of bending two filaments equally at the plectoneme base.

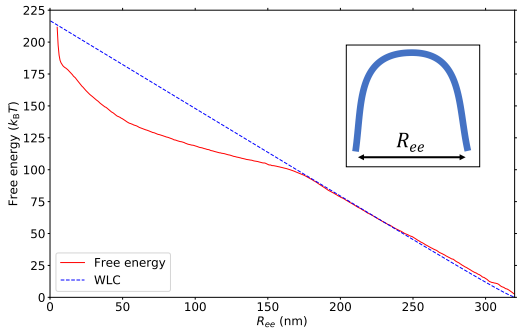


Figure 5.4: Free energy landscape of 6HB-SST as a function of R_{ee}. This is computed using umbrella sampling by Wong *et al.* (Wong et al., 2022). The WLC free energy is calculated using the formula given in Ref. (Qu & Zocchi, 2011) and fitted using a bending modulus B of $7200\,k_{\mathrm{B}}T$. The nanotube has a length of approximately 320 nm. (Inset) Illustration of the definition of R_{ee}.

5.2.3 End-to-end extension and Torque response

The end-to-end extension curves and post-buckling torque response for 4HB-SST and 6HB-SST systems are shown in Fig. 5.5. For 4HB-SST systems, the end-

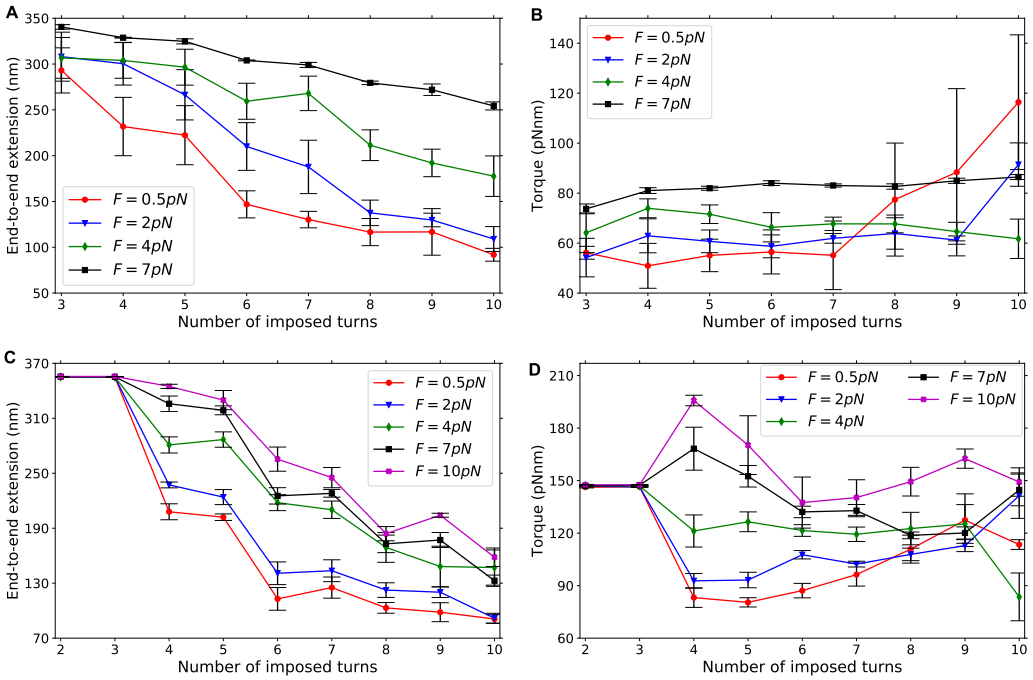


Figure 5.5: (A) and (B) End-to-end extension and post-buckling torque plots for 4HB-SST. (C) and (D) End-to-end extension and post-buckling torque plots for 6HB-SST. Error bars represent the standard error of the mean. In the case of 4HB-SST, the mean is obtained from both twist and untwist trajectories. Edge effects become apparent when the number of imposed turns is large. Plectonemes are pinned down by the kink defect at their tips. If these plectonemes are formed near the edge of the helix bundle, then their continuous lengthening will be prevented as the number of imposed turns increases, leading to the formation of secondary plectonemes which results in a deviation from the expected trends in the end-to-end extension and torque plots.

to-end extension and torque response are averaged using production runs from both twist and untwist trajectories, as described in subsection 5.2.1. The end-to-end extension and torque response for 6HB-SST systems on the other hand are averaged using production runs from the twist trajectories. Despite the difference in averaging methods, the end-to-end extension and torque response curves of both helix bundle systems exhibit similar characteristics. First, the decrease in the end-to-end extension of the nanotubes in the post-buckled state is approximately

linear, with every injected twist of 2π roughly corresponding to the formation of a plectonemic loop (see Fig. 5.6). The decrease in the end-to-end extension is also observed to become more gradual as the pulling force increases. A larger pulling force means that more work (against the external force) has to be carried out before a plectonemic loop is formed. Consequently, each plectonemic loop that is formed to accommodate the additional twist is smaller in size to reduce the amount of external work that is required, leading to a gentler reduction in the end-to-end extension. In Fig. 5.6, we can clearly see a reduction in the superhelical pitch at $F = 10$ pN, as compared to the case for $F = 0.5$ pN. Second, the post-buckling

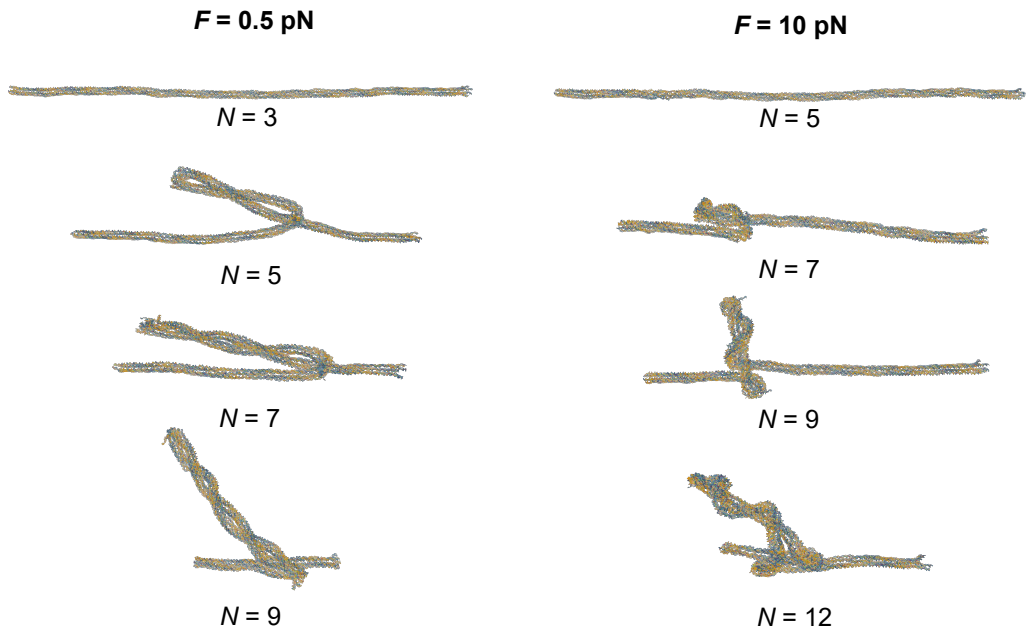


Figure 5.6: Visualisation of plectoneme growth in twisted DNA nanotubes. Plectoneme formed in nanotubes held at a tension of $F = 0.5$ pN has a larger pitch compared to its counterpart at $F = 10$ pN. Rebuckling with the formation of a second kinked end-loop is observed when $N = 9$ (at $F = 0.5$ pN) and $N = 12$ (at $F = 10$ pN) . Examples shown here are for 6HB-SST systems.

torque is observed to stay approximately constant as more turns are imposed, until the nanotube rebuckles (E.g. At $F = 0.5$ pN, rebuckling occurs at $N \gtrsim 7$).

The torsional energy injected into the system is balanced by the loop's bending energy and the work done against the pulling force (Strick et al., 2002), both of which are a function of the loop geometry that remains (on average) constant throughout the process as the plectoneme grows. In addition, the magnitude of the (constant) post-buckling torque is observed to increase with the pulling force. The reduced loop size at a larger applied force is accompanied by an increase in the loop curvature that increases its bending energy. The net effect is an increase in post-buckling torque with a larger applied force.

Finally, the end-to-end extension curves for both systems lack the characteristic inverse quadratic curve ("hat") commonly seen in the end-to-end extension curves of dsDNA. Hats are formed as a consequence of chiral fluctuations (J. F. Marko, 2005). The absence of such hats in the end-to-end extension curves for helix bundle systems is thus an indication of the suppression of these chiral fluctuations due to the high bending stiffness of the nanotubes.

As a whole, it might be tempting to regard these features in the end-to-end extension curves and torque responses as an indication of elastic or WLC buckling, given their many similarities. However, the parallels that we see here contain a number of subtleties. For instance, the small helical pitch and the high loop curvature that we observed at $F = 10$ pN in Fig. 5.6 suggests that the plectoneme formation is occurring in a non-WLC regime for the given F, based on the free energy landscape outlined in Fig. 5.4. In the next two sections, we will attempt to capture and quantify these non-WLC responses by the buckled DNA nanotubes.

5.3 Theoretical models of plectonemic supercoiling

We begin with a description of a mechanical model of plectoneme formation by Clauvelin *et al.* (Clauvelin et al., 2008, 2009). In their model, buckling is assumed

to have taken place (i.e. the number of imposed turns $N > N_b$, the buckling equilibrium point). The plectoneme in question is composed of an inextensible elastic rod with a circular cross-sectional area, a bending modulus B and a torsional rigidity C. The plectoneme assumes a helical geometry, characterised by a superhelical radius R, pitch P and a superhelical angle α (Fig. 5.7). The local curvature of the plectoneme is given by $\kappa(s) = |d\vec{t}/ds|$, where s is the arclength of the rod that ranges from 0 to l, the contour length of the rod. $\vec{t}(s)$ is the unit vector that is tangent to the rod's centreline. Twist $\tau(s) = \tau$ is taken to be uniform since the rod has a circular cross-section.

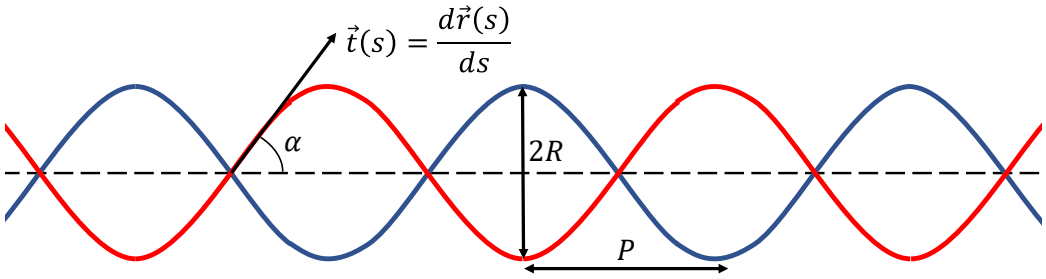


Figure 5.7: Geometrical description of the plectoneme formed in DNA nanotubes. The superhelical angle, radius and pitch are denoted as α, R and P respectively. The filament centreline (coloured in red and blue) is parametrized by the position vector $\vec{r}(s)$, from which we can define the tangent unit vector $\vec{t}(s)$.

There are three components to the total mechanical energy of this system. First, the elastic energy V_{el} is:

$$V_{el} = \frac{B}{2}\int_0^l \kappa^2(s)ds + \frac{C}{2}\int_0^l \tau^2 ds = \frac{B}{2}\frac{\sin^4\alpha}{R^2}l_p + \frac{C}{2}\tau^2 l \tag{5.1}$$

In deriving the final expression for Eq. 5.1, the "tail" portion of the elastic rod is assumed to have zero curvature. The curvature in the plectonemic part of the rod (with length l_p) on the other hand is taken to be constant. Variations in the

curvature at the plectoneme end-loop and the connecting regions between the tail and the plectoneme are also neglected. Next, the pulling force F and the external torque M are characterised using the following potential energy expression:

$$V_{ext} = -F\left(z(l) - z(0)\right) - 2\pi MN = -F\left(l - l_p\right) - 2\pi MN \tag{5.2}$$

The extension of the rod in the z direction $(z(l) - z(0))$ is taken to be $l - l_p$ since thermal fluctuations, as well as the connecting regions between the tail and the plectoneme are ignored in this mechanical model. N is constrained by the following relation:

$$N = Lk = Tw + Wr = \frac{1}{2\pi}\int_0^l \tau ds - \chi\frac{\sin 2\alpha}{4\pi R}l_p = \frac{1}{2\pi}\left(\tau l - \chi\frac{\sin 2\alpha}{2R}l_p\right) \tag{5.3}$$

$\chi = \pm 1$ is the chirality of the two helices in the plectonemic state. The sign of the chirality is defined such that it is always opposite to the sign of the rotation N. For example, a positive rotation $N > 0$ will result in the formation of left-handed superhelices ($\chi = -1$). In deriving the final expression for Eq. 5.3, writhe fluctuations in the tail portion of the rod are ignored.

Finally, the self-interaction of the superhelices is expressed as:

$$V_{int} = l_p U(R, \alpha) \tag{5.4}$$

Together, the total energy of the system is:

$$\begin{aligned} V_{total} &= V_{el} + V_{ext} + V_{int} \\ &= \frac{B}{2}\frac{\sin^4\alpha}{R^2}l_p + \frac{C}{2}\tau^2 l + -F\left(l - l_p\right) - 2\pi MN + l_p U(R,\alpha) \\ &= \frac{C}{2}\tau^2 l + (2\pi N - \tau l)\left[\frac{-2\chi}{\sin 2\alpha}\left(\frac{B}{2}\frac{\sin^4\alpha}{R} + RF + RU(R,\alpha)\right)\right] \end{aligned} \tag{5.5}$$

In obtaining the final expression for Eq. 5.5, both $2\pi MN$ and Fl are dropped since the energy minimisation protocol is carried out for a fixed N, and Fl is also invariant to the minimisation protocol. In addition, Eq. 5.3 is used to replace l_p in favour of N.

Energy minimisation is carried out with respect to α, R and τ (i.e. $\partial V_{total}/\partial\alpha = 0$, $\partial V_{total}/\partial R = 0$ and $\partial V_{total}/\partial\tau = 0$). As a simplifying assumption, we will ignore U's dependence on α:

$$2B\frac{\cos\alpha\sin^3\alpha}{R^2} - \frac{2}{\tan 2\alpha}\left(\frac{B}{2}\frac{\sin^4\alpha}{R^2} + F + U(R)\right) = 0 \tag{5.6a}$$

$$F - \frac{B}{2R^2}\sin^4\alpha + R\frac{\partial U(R)}{\partial R} + U(R) = 0 \tag{5.6b}$$

$$M + \frac{2\chi}{\sin 2\alpha}\left(\frac{B}{2}\frac{\sin^4\alpha}{R} + RF + RU(R)\right) = 0 \tag{5.6c}$$

The constitutive relation $M = C\tau$ has been used to replace τ in Eq. 5.6c. This set of equations has to be solved to get the equilibrium values of α, R and M.

The model by Neukirch and Marko (Neukirch & Marko, 2011) builds on the model by Clauvelin *et al.* by factoring in conformational fluctuations (J. F. Marko & Siggia, 1995; Moroz & Nelson, 1997):

$$\begin{aligned} G(\alpha,\lambda_s,R,\tau_p,l_p) = &- g(F)(l-l_p) + \frac{1}{2}C_s\lambda_s^2(l-l_p) \\ &+ \left[\frac{1}{2}C\tau_p^2 + \frac{B}{2}\frac{\sin^4\alpha}{R^2} + U(R,\alpha)\right]l_p \\ &- 2\pi M\left(\frac{\lambda_s(l-l_p)}{2\pi} + \frac{\tau_p l_p}{2\pi} + \frac{\sin 2\alpha}{4\pi R}l_p\right) \end{aligned} \tag{5.7}$$

Eq. 5.7 is partitioned into three parts – the free energy of the extended region of the system, the free energy of the plectonemic state, and a constraint on ΔLk, the linking number deficit. The first two terms are concerned with the free energy of

the extended state. $g(F)$ is the free energy (per unit length) of the extended WLC rod (Eq. A.2). The second term refers to the twist energy in the extended region of the system, with $\lambda_s = 2\pi\Delta Lk_s/(l - l_p)$ (ΔLk_s being the excess linking number in the extended region). C_s, the Moroz-Nelson result for the effective torsional modulus (Moroz & Nelson, 1997, 1998), takes into account writhe fluctuations in the stretched region of the system. The next three terms in square brackets pertain to the free energy of the plectonemic part of the system, starting with the twist energy in the plectonemic part of the system, with $\tau_p = 2\pi\Delta Tw_p/l_p$ (ΔTw_p being the excess twist in the plectonemic region). This is followed by the bending energy of the plectoneme and the self-interaction term $U(R, \alpha)$. Last but not least, a constraint on $\Delta Tw + Wr$ is applied, with $2\pi M$ serving as the Lagrange multiplier (and M takes on the physical interpretation of torque).

Numerical solutions to $\nabla G(\alpha, \lambda_s, R, \tau_p, l_p, M) = 0$, where $\nabla = (\partial_\alpha, \partial_{\lambda_s}, \partial_R, \partial_{\tau_p}, \partial_p, \partial_M)$ provide the equilibrium values of the six variables in Eq. 5.7. To obtain closed-form solutions for the variables α, R and M, several simplifying assumptions have to be made. First, the α dependence in the self-interaction U is ignored. Second, C_s is approximated as C, which takes the value of $370\,k_\mathrm{B}T$nm and $750\,k_\mathrm{B}T$nm for the 4HB-SST and 6HB-SST respectively (Chhabra et al., 2020). This is valid in the high force limit. The result is a reduced set of equilibrium equations that can be solved analytically with the appropriate choice of $U(R)$:

$$-B\frac{\sin^4\alpha}{R^3} + \frac{\partial U(R)}{\partial R} + M\frac{\sin 2\alpha}{2R^2} = 0 \tag{5.8a}$$

$$2B\frac{\cos\alpha\sin^3\alpha}{R^2} - M\frac{\cos 2\alpha}{R} = 0 \tag{5.8b}$$

$$g + \frac{1}{2}B\frac{\sin^4\alpha}{R^2} + U(R) - M\frac{\sin 2\alpha}{2R} = 0 \tag{5.8c}$$

At this juncture, it is useful to compare Eq. 5.8 with Eq. 5.6. Both sets of equi-

librium equations are essentially identical when B is large (i.e. when $g(F) \approx F$). This is not surprising since a high bending stiffness suppresses conformational fluctuations that differentiate Eq. 5.7 from Eq. 5.5. Thus, in the analysis of plectoneme formation in DNA helix bundles, choosing between the model by Clauvelin *et al.* and the model by Neukirch and Marko becomes inconsequential since both 4HB-SST and 6HB-SST systems have very high bending stiffness relative to the applied forces. Solving either Eq. 5.6 or 5.8 would yield the same equilibrium values of α, R and M for the said systems.

5.4 Comparison between theoretical models and simulation results

In order to obtain equilibrium values of α, R and M that can be compared with simulation results, we need to first choose an appropriate form of $U(R)$ (here, we have dropped U's dependence on α). Two representative interaction energies are considered in this chapter. The first is an interaction energy term based on the Debye-Hückel approximation of the Poisson -Boltzmann equation (J. Marko & Siggia, 1995; Neukirch & Marko, 2011):

$$U(R) = k_{\mathrm{B}} T v^2 L_B K_0(2\kappa R) \tag{5.9}$$

L_B is the Bjerrum length of 0.7 nm in water. κ^{-1} is the Debye length. v is the effective charge:

$$v = Z \frac{1}{\gamma(b, \kappa a, L_B)} \frac{1}{\kappa a K_1(\kappa a)} \tag{5.10}$$

In deriving Eq. 5.10, the charge is assumed to be distributed evenly on the surface of a cylindrical rod with radius a and the Gouy potential is matched with the Debye-Hückel potential at large R (Stigter, 1975). Z is the linear charge density

in electron charge units (E.g. $Z = 1/0.17$ for dsDNA since there are two negative charges for each base pair). $\gamma(b, \kappa a, L_B)$ is the correction factor that is used to match the Debye-Hückel potential with the Gouy potential at the cylinder surface (Stigter, 1975).

We proceed to compute v for the helix bundles systems as follows: The helix bundles are assumed to be charged cylinders with a given by the sum of the nanotube radius computed in Ref. (Chhabra et al., 2020) and the radius of dsDNA (1 nm). This gives us $a = 2.75$ nm and 3.5 nm for the 4HB-SST and 6HB-SST respectively. The linear charge density Z is taken to be $4/0.17$ (4HB-SST) and $6/0.17$ (6HB-SST). Since the simulations were carried out using a monovalent salt concentration of 1 M, κ is computed to be 3.29 nm^{-1}. Finally, $\gamma(b, \kappa a, L_B)$ is obtained from Table III in Ref. (Stigter, 1975). This gives $\gamma \approx 1.49$ (4HB-SST) and 1.32 (6HB-SST).

Neukirch and Marko had derived closed-form approximate solutions to Eq. 5.8, valid for moderate to large values of κR and small values of α, which we can use to obtain the equilibrium geometry of the helix bundles. The equilibrium radius R and superhelical angle α are respectively given by (Neukirch & Marko, 2011):

$$R \approx \frac{1}{2\kappa}\left(\ln K + \frac{\ln(\ln K)}{2 - 1/\ln K}\right) \tag{5.11}$$

$$\alpha \approx \left(\frac{2R^2 g(F)}{3B}\right)^{1/4} \tag{5.12}$$

$K := \sqrt{9\pi/8} v^2 L_B k_B T / g(F)$, and B is taken to be $2030\, k_B T$nm and $7620\, k_B T$nm for the 4HB-SST and 6HB-SST respectively (Chhabra et al., 2020). The pitch P can be obtained from Eq. 5.11 and 5.12 via $P = 2\pi R \cot\alpha$ (Zakharova et al., 2002). Figs. 5.8 - 5.10 show the equilibrium values of R, α and P respectively. The results are not surprising. A plectonemic system with a high bending stiffness

will seek to reduce its curvature by having a large pitch and a small superhelical angle. This behaviour is also evident from the approximate solution to α (Eq. 5.12) with its explicit dependence in B, where we can clearly see that a large B gives rise to a small value of α. On the other hand, R as given by Eq. 5.11 is not a function of B explicitly but instead depends on the strength of the interaction energy $U(R)$ (through the choice of v etc.).

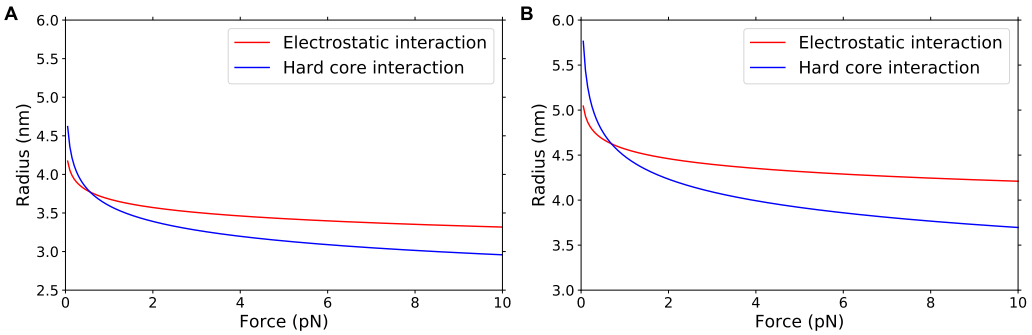


Figure 5.8: Predicted superhelical radius R for (A) 4HB-SST and (B) 6HB-SST. According to these theoretical models, the filaments in the plectoneme are essentially in close contact with each other.

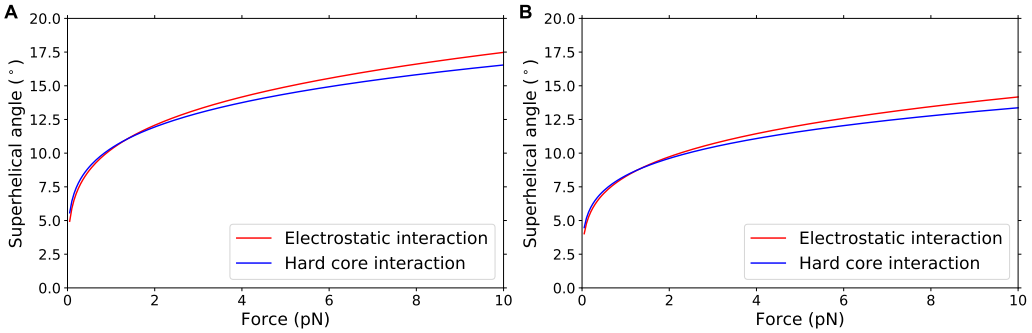


Figure 5.9: Predicted superhelical angle α for (A) 4HB-SST and (B) 6HB-SST. For comparison, the predicted superhelical angle for dsDNA is close to 30° for $F < 3.5$ pN (Clauvelin et al., 2009).

To ascertain the veracity of these results, we also considered a hard core interac-

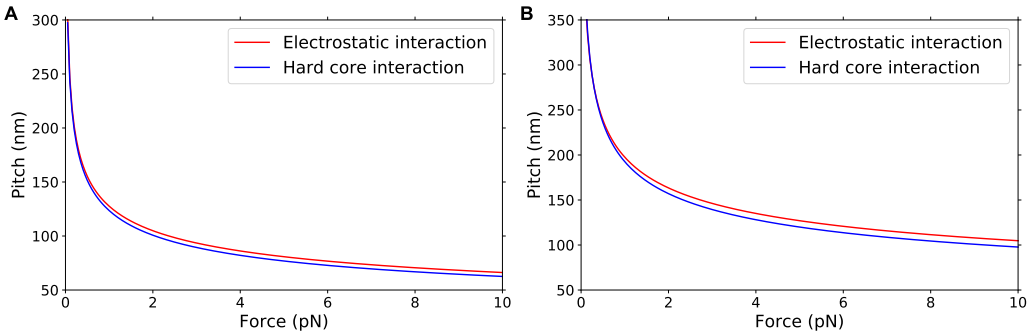


Figure 5.10: Predicted superhelical pitch P for (A) 4HB-SST and (B) 6HB-SST.

tion energy term (J. F. Marko & Siggia, 1994b):

$$U(R) = \frac{1}{a}\left(\frac{a}{R}\right)^{12} \tag{5.13}$$

a has the same definition as before in Eq. 5.10. Together with Eq. 5.6, equilibrium values of R, α and P can be extracted numerically. The results are also plotted in Figs. 5.8 - 5.10, alongside the ones obtained using an electrostatic interaction energy term (i.e. Eq. 5.9). Both choices of $U(R)$ yield similar values of α, P and R for the range of forces that are under consideration here.

We can also extract theoretical predictions of the linear slope q and post-buckling torque M from these models. The end-to-end extension z is given by:

$$z = l - l_p = \left(1 - \chi\frac{2R}{\sin 2\alpha}\tau\right) l + \chi\frac{4\pi R}{\sin 2\alpha}N \tag{5.14}$$

In deriving Eq. 5.14, Eq. 5.3 is used to eliminate l_p. For dsDNA, a correction factor $\rho_{WLC} \in [0, 1]$ was introduced in Eq. 5.14 to account for thermal fluctuations in the tails of the dsDNA (Clauvelin et al., 2008, 2009). This rescaling is not necessary for the much stiffer DNA nanotubes that we are examining here.

z's linear dependence on N is evident in the second term of the final expression

in Eq. 5.14. Since the linear slope q is defined as $|\frac{dz}{dN}|$, we get:

$$q = \frac{4\pi R}{\sin 2\alpha} \tag{5.15}$$

Notice that the linear slope values (as given by Eq. 5.15) are nearly identical to that of the helical pitch. This is because the equilibrium values of α are very small. Using the small angle approximation, $q \approx \frac{2\pi R}{\alpha}$. Since $P = 2\pi R \cot \alpha \approx \frac{2\pi R}{\alpha}$ for small α, $q \approx P$.

Next, M can be solved numerically using Eq. 5.6c, or, for the case of an electrostatic interaction potential, analytically using Eq. 5.11 and 5.12 via this equation:

$$M = \frac{2B}{R} \frac{\sin^3 \alpha \cos \alpha}{\cos 2\alpha} \tag{5.16}$$

The theoretical post-buckling torque M and linear slope q are plotted in Fig. 5.11 and 5.12 respectively. oxDNA-derived measurements of post-buckling torque and slope are extracted from the end-to-end extension and torque response curves in Fig. 5.5. Several precautions were taken to ensure that the torque and slope values extracted from the graphs were not from nanotubes in their pre-buckled or rebuckled state. First, we use the torque overshoot observed in Fig. 5.5 and the point at which the end-to-end extension of the nanotube starts to decrease as a (collective) reference point for the onset of nanotube buckling. Next, we avoid the rebuckled states in our measurements by determining when the rate of change in the end-to-end extension of the nanotube starts to decrease, and when the torque output starts to increase again (E.g., at $F = 0.5$ pN, a shift in the gradient of the end-to-end extension curve and a gradual increase in the torque output can be observed at $N \gtrsim 6$). Finally, as a last layer of check, visual inspection of all the configurations is carried out. Still, in estimating the linear slope from the end-to-end extension curves using linear regression, we notice that the value of the linear slope is highly

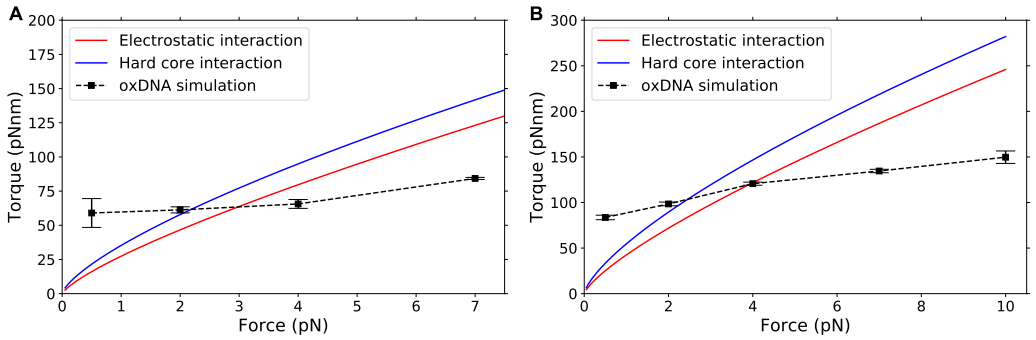


Figure 5.11: Predicted post-buckling torque M for (A) 4HB-SST and (B) 6HB-SST. The theoretical M tends to zero as F approaches zero; the bending energy becomes negligible as the superhelical pitch increases asymptotically with a vanishing F. Work done against the external F also tends to zero as F approaches zero. In our simulated systems, the post-buckling torque outputs at $F = 0.5$ and 2 pN are larger than the predicted values. The finite size of the nanotubes constrains the maximum possible pitch that the system can adopt at very low forces, resulting in a non-negligible bending energy. At much larger forces, we observed a non-WLC behaviour in our nanotube systems. In this regime, the strong bending has kinked the nanotube, resulting in a smaller-than-expected increase in the free energy of the nanotube.

sensitive to the number of points we choose for the linear fitting. This prompted us to implement a search protocol that is designed to identify the maximum and minimum linear gradient of a end-to-end extension scatter plot, based on linear regressions that are fitted to at least 3 consecutive points (see Fig. 5.13 for an example). The constraint of gradient < 0 is imposed to ensure physically relevant results (i.e. end-to-end extension is decreasing during buckling). The search algorithm also excludes the pre-buckled and rebuckled states of the helix bundles (i.e. $N = 2, 9$ and 10 where N is the number of imposed turns) to give a more accurate estimate of the possible upper and lower limits of the linear slope measurements. The protocol is applied to all the simulated trajectories, and the results (for a given F and choice of nanotube system) are averaged across the relevant trajectories to produce the dashed lines we see in Fig. 5.12.

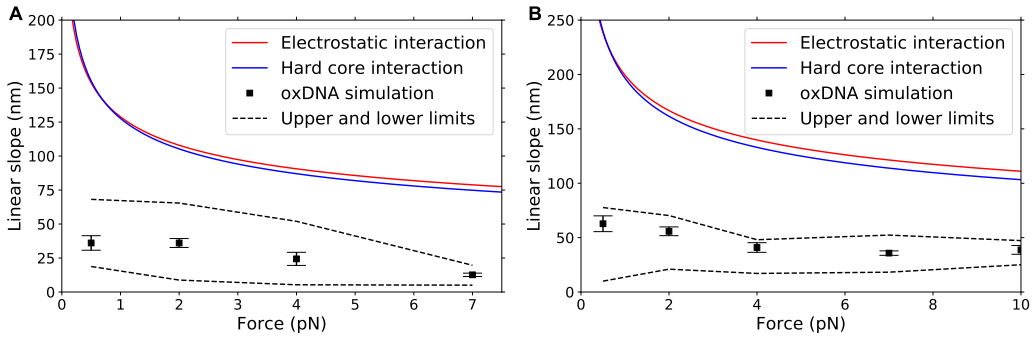


Figure 5.12: Predicted linear slope q for (A) 4HB-SST and (B) 6HB-SST. The linear slope values calculated using Eq. 5.15 are nearly identical to that of the helical pitch, and overestimate the measured slopes from the oxDNA simulations. The smaller pitch/linear slope values from the oxDNA simulations is an indication of the non-WLC behaviour of the nanotubes. A shorter superhelical pitch (and a larger superhelical angle) corresponds to a stronger bending of the nanotubes, which can be accommodated in the non-WLC regime by a smaller increase in the free energy of the nanotube relative to the corresponding increment in the WLC free energy.

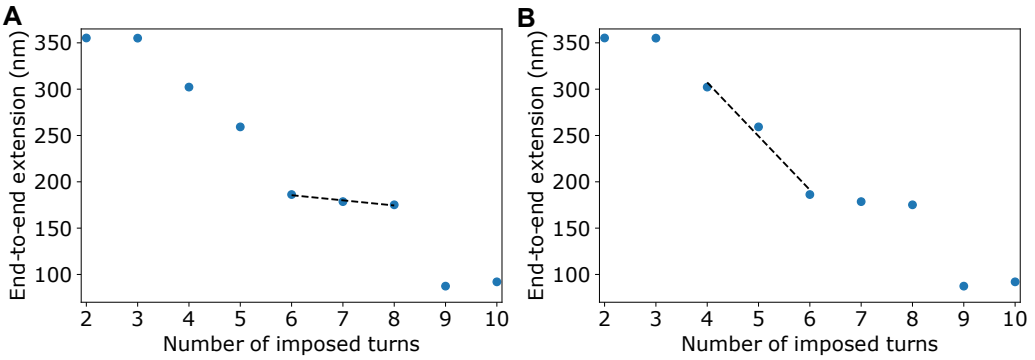


Figure 5.13: Maximum and minimum possible slope value from a typical end-to-end extension plot. Example shown here is from a 6HB-SST system subjected to $F = 4$ pN. A search algorithm identifies the maximum and minimum linear gradient of a end-to-end extension scatter plot by comparing linear regressions which are fitted to at least 3 consecutive points. Linear fits that give rise to a positive gradient (i.e. increasing end-to-end extension during buckling) are discarded. The linear fitting also excludes the pre-buckled and rebuckled states of the helix bundles at $N = 2$, 9 and 10.

With Figs. 5.11 and 5.12 alongside Figs. 5.8, 5.9 and 5.10, we could now attempt to formulate a comprehensive picture of the energetics of plectoneme formation in our DNA nanotubes. At very low forces, the amount of nanotube length that is available for supercoiling is unable to accommodate the equilibrium superhelical pitch of the plectoneme, which is derived from theoretical models that essentially assume a superhelix of unbridled lengths. The result is a helix bundle plectoneme with a much larger superhelical curvature and therefore a larger bending energy cost. This finite-size effect at low forces is evident in Fig. 5.11. At $F = 0.5$ pN and 2 pN, the post-buckling torque values measured from our oxDNA simulations of both 4HB-SST and 6HB-SST systems are larger than the theoretical equilibrium torque values since each plectonemic loop is now associated with a larger energetic cost. At larger forces, the non-WLC behaviour of the nanotubes takes over and becomes more evident. The plectonemes formed in this force regime are made from strongly bent loops with a smaller superhelical pitch and a larger superhelical angle to minimise the work done against the external force. The stronger bending kinks the nanotube and, as depicted in Fig. 5.4, results in a non-WLC behaviour of the DNA nanotube. In this kink-mediated regime, the free energy cost of each plectonemic loop is smaller than the corresponding WLC free energy. Consequently, the post-buckling torque as measured from our simulations is smaller than what the elastic models of plectoneme formation would predict.

The same interpretations apply to Fig. 5.12, since the linear slope of the end-to-end extension curve reflects the length of the superhelical pitch of the plectoneme. At very low forces, it is not physically feasible to attain the theoretical linear slope values in our finite-size helix bundle systems. On the other hand, at larger forces, the nanotubes can possess much stronger bending at a fraction of the WLC free energy cost. This is manifested in the form of linear slope values that are smaller than the theoretical ones.

5.5 A different theoretical model of plectoneme formation

There are also other theoretical models of plectoneme formation that we can use to compare against our oxDNA simulation results. One such example is Marko's composite model of plectonemically supercoiled DNA (J. F. Marko, 2007), which serves as the theoretical basis for the energetics model of DNA supercoiling transition by Brutzer *et al.* (Brutzer et al., 2010). In this model, the plectonemic free energy (per unit length) is treated as a quadratic function of the linking number deficit ΔLk:

$$P(\Delta\text{Lk}) = \frac{P}{2}\left(\frac{2\pi\Delta\text{Lk}}{l}\right)^2 \tag{5.17}$$

The twist stiffness P of the plectonemic state is not known *a priori* but is expected to be smaller than the elastic rod's torsional stiffness C due to writhing. In the case of dsDNA, P is determined experimentally to be in the range of 21 to 27 $k_\text{B}T$nm depending on the salt concentration (W. Bauer & Vinograd, 1970; Hsieh & Wang, 1975; Rybenkov et al., 1997; J. F. Marko, 2007), or approximately a quarter of the value of C. For helix bundles, it is unclear if Eq. 5.17 is a valid approximation of the plectonemic state in helix bundle systems, and if so, what value P would assume relative to the torsional stiffness C of the helix bundle.

On the other hand, the free energy per unit length of the non-plectonemic, extended state in the model is given by:

$$S(\Delta\text{Lk}) = -g + \frac{C_s}{2}\left(\frac{2\pi\Delta\text{Lk}}{l}\right)^2 \tag{5.18}$$

g and C_s take on the same definition as before in Eq. A.2 and Ref. (Moroz & Nelson, 1998). The post-buckling torque can be derived from the minimisation of

the free energy of the co-existing domains of the plectonemic and extended states to give: (J. F. Marko, 2007, 2009; Brutzer et al., 2010):

$$M = \sqrt{\frac{2Pg}{1 - \frac{P}{C_s}}} \tag{5.19}$$

A similar calculation would yield the linear slope of the end-to-end extension curve as given by Eq. A.1 in Appendix A.2. We can attempt to get a better sense

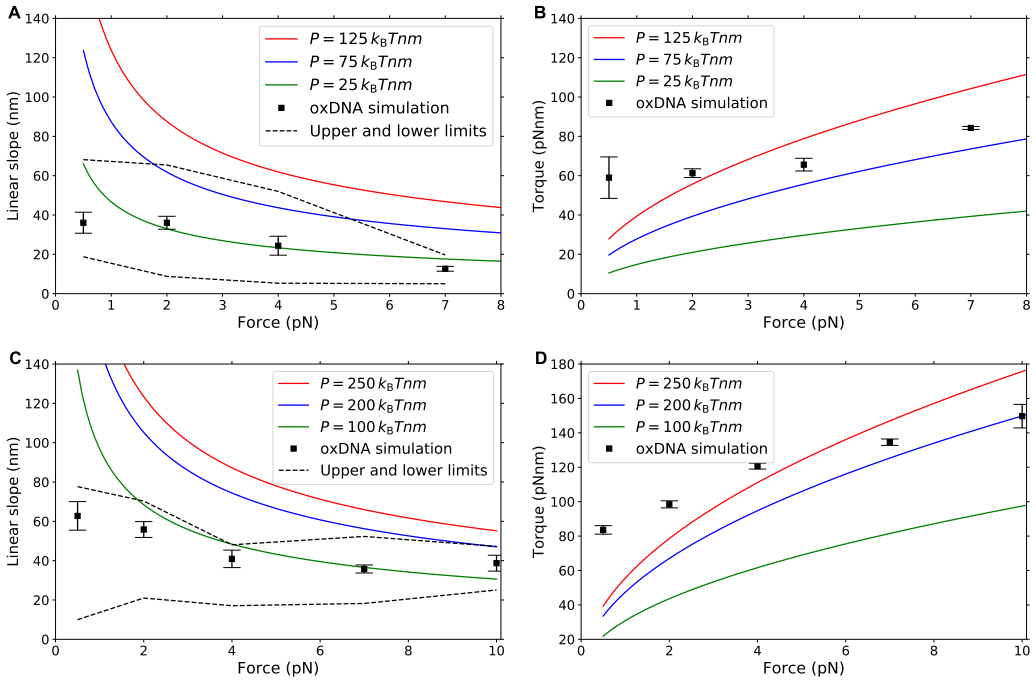


Figure 5.14: Comparison of the Marko composite model (J. F. Marko, 2007) with (A) linear slope of the end-to-end extension curve and (B) post-buckling torque for 4HB-SST systems, and (C) linear slope of the end-to-end extension curve and (D) post-buckling torque for 6HB-SST systems. Parameter values for the bending modulus B and torsional rigidity C which are used to plot the theoretical curves are obtained from Ref. (Chhabra et al., 2020).

of the value of the plectonemic twist stiffness P for the helix bundles from Fig. 5.14. This proves to be non-trivial as a single value for P does not ensure a good fit with both post-buckling torque and linear slope plots in Fig. 5.14 simultaneously.

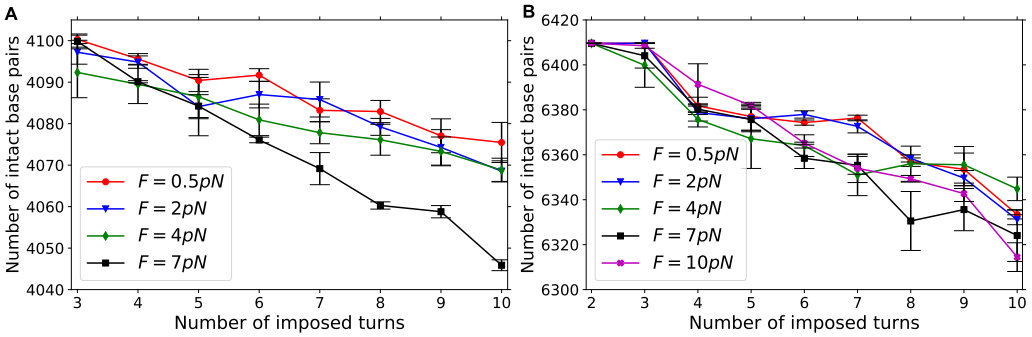


Figure 5.15: Variation of the number of intact base pairs with the number of imposed turns in (A) 4HB-SST, and (B) 6HB-SST. A base pair is considered denatured if the binding energy falls below 10% of its maximum possible value. In 4HB-SST systems, approximately 5 base pairs are broken per turn whereas in 6HB-SST systems, this number goes up to approximately 10 base pairs per turn.

It might be possible that the free energy of the helix bundle's plectonemic state cannot be described by Eq. 5.17. Another possibility is that the model has not incorporated the energetics of the melted/bubble state as a co-existing domain alongside the plectonemic and extended, twisted states. We have observed, in the simulations, a continuous disruption of hydrogen bonds along the undulating filaments of the plectoneme as more turns are imposed onto the nanotubes (Fig. 5.15). Analogous to the theoretical treatment of bubble formation in Chapter 4, such disruptions cost α_{HB} (in $k_{\mathrm{B}}T$) per imposed turn N and contribute $\alpha_{HB}/2\pi$ to the post-buckling torque on average. If this were to be a valid hypothesis, and if the base pair disruptions are assumed to have a relatively small effect on the nanotube's end-to-end extension, then we would expect a persistent discrepancy between oxDNA's post-buckling torque measurements and the theoretical values from Eq. 5.19, and a much closer fit between the measured linear slope (from the simulations) and the theoretical predictions from Eq. A.1. Even though this might explain why the model is unable to provide a good fit to both post-buckling torque and linear slope plots in Fig. 5.14 simultaneously with a single value for P, it remains unclear if a better explanation for the discrepancies lies with the

(yet-to-be determined) modification of mechanical properties (e.g. bend and twist moduli B and C, as well as P) by these base pair disruptions. These hypotheses are the subject of ongoing investigations.

5.6 Concluding remarks

To the best of our knowledge, the buckling of DNA nanotubes was only briefly studied by Kauert *et al.* at a relatively low pulling force of 0.6 pN (Kauert et al., 2011). There is yet to be a systematic experimental study of the plectonemic state of the DNA nanotubes that will allow us to make an apple-to-apple comparison with our simulation findings (i.e. end-to-end extensions and torque response) and to explore DNA nanotube buckling in both the WLC regime (at low forces) and the non-WLC regime (at higher pulling forces).

One could seek to explore the effect of the non-WLC behaviour of 4HB-SST and 6HB-SST systems on other features of the buckling transition in twisted and stretched DNA nanotubes. For instance, the kinked end-loop that we observed in the buckled nanotubes (Fig. 5.3) is indicative of an E_{loop} that is smaller than what we would expect from an elastic rod with the same bend and twist moduli. Consequently, using the model for buckling by Brutzer *et al.* (Eq. 4.7) is expected to lead to a lower buckling transition point for the DNA nanotubes than what we would have estimated using an equivalent WLC rod. For the same reasons, the overshoot in the torque response curve of a buckled DNA nanotube is also likely to be smaller than that of its elastic counterpart. Another related area to investigate is the effect of end-loop kinking on the buckling transition kinetics for DNA nanotubes. The findings could also be compared against similar studies conducted on buckling dsDNA with defects (Dittmore et al., 2018). That being said, it is difficult to investigate these effects directly using oxDNA simulations,

given how computationally expensive it is to carry out the twist simulations of nanotubes (relative to dsDNA), and how difficult it is to equilibrate these systems due to the formation of defects and kinks in the system.

6 | Defects in bacterial nucleoid models

6.1 Introduction

In Chapter 3, we postulated that the coupling between supercoiling and DNA damage might facilitate DNA damage recognition in living cells. Negative supercoiling, induced by proteins such as RNA polymerase, could potentially aid the discovery of defects by favouring the location of the damage in the relatively easy-to-find plectonemic loop away from the crowded environment at the centre of the chromosome.

To explore this hypothesis by simulation, much longer DNA duplexes in more complex and biologically-relevant configurations must be treated than the simple molecular tweezer geometry used in Chapter 3. In eukaryotic cells, DNA is typically condensed into a complex and hierarchical toroidal form that is restrained by histones through the formation of nucleosomes (Barbi et al., 2012). In prokaryotic organisms such as bacteria, genomic DNA assumes a less structured supercoiled configuration, with about half of the chromosomal DNA organized in the form of free, plectonemic supercoils while the remaining half is restrained in alternative configurations via nucleoid-associated proteins (NAPs) (Bliska & Cozzarelli, 1987; Postow et al., 2004).

In this work, we choose to examine the above-mentioned hypothesis by modelling bacterial DNA. Bacterial DNA configurations are often used as a model system to study broader biological effects (Blount, 2015) and its configurations have been studied extensively over the years. By contrast, much less is known about the detailed configurations of the eukaryotic genome, although much progress has recently been made, for example, through HiRes measurements (Mirny & Dekker,

2022). Moreover, the use of eukaryotic DNA models introduces additional variables such as the coupling between DNA supercoiling and nucleosome stability (Gilbert & Allan, 2014; Kaczmarczyk et al., 2020) that could potentially complicate the hypothesis testing process. In addition, minichromosome maintenance (MCM) complexes, a replicative helicase found in eukaryotes but not prokaryotes (Forsburg, 2004), have recently been reported to obstruct the formation of DNA loops (Dequeker et al., 2022), a key feature of the hypothesis that we seek to test. These complications can be ignored in bacterial DNA models for the time being, especially given the prevalence of free unrestrained plectonemic loops in bacterial DNA configurations.

6.2 Modelling the bacterial nucleoid

There are various approaches one could take to model bacterial nucleoids. Some of the simulation studies of bacterial DNA or the intranuclear environment place an emphasis on reproducing the intrinsic mechanical properties of DNA. In these instances, bacterial DNA is modelled using a discretised version of the wormlike chain model that takes into account the electrostatic interaction between the chain segments and/or the twist deformation of the WLC (Jian et al., 1997; Johnson et al., 2015; Lepage & Junier, 2017). Because these simulations tend to be computationally expensive, modellers typically do not construct the entire bacterial nucleoid (often comprising millions of base pairs) but instead choose to mimic the environment of a nucleoid or specific characteristics of nucleoid DNA using a much smaller number of base pairs (C. A. Brackley et al., 2014; Chow & Skolnick, 2017).

Another approach focuses on reproducing the mesoscale characteristics of genomic DNA. In the nucleotide-resolution molecular model of the Escherichia coli

(E. coli.) chromosome by Hacker *et al.* for instance (Hacker et al., 2017), a highly coarse-grained, 500 base pair per bead model is gradually compacted to achieve the desired nucleoid density and concurrently refined to exact a highly resolved one nucleotide per bead structure (Fig. 6.1). The model is also deliberately constructed to reproduce the transcriptional profile of E. coli. by partitioning the chromosome into a series of plectoneme-rich and plectoneme-free regions whose locations match experimental data-sets for E. coli in slow-growth conditions (Grainger et al., 2006). The plectonemes in the model also have lengths and branches that correspond to experimentally observed distribution profiles (Boles et al., 1990; Postow et al., 2004). Such a modelling strategy can be considered to be "top-down" in the sense that model construction is carried out with a specific set of end-state characteristics and properties in mind.

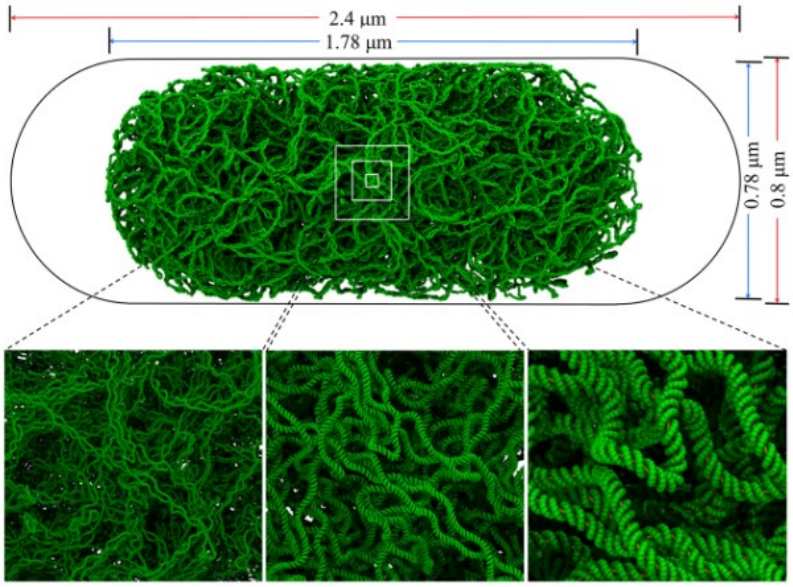


Figure 6.1: A 1-nucleotide resolution model of the 4.6 Mbps E. coli. chromosome by Hacker *et al.* (Hacker et al., 2017). (Insets) Magnified images of the chromosomes. The major and minor grooves of the DNA are visible in the rightmost panel. Figure is reproduced with permission from Ref. (Hacker et al., 2017).

The lattice model of bacterial nucleoid by Goodsell *et al.* serves as another exam-

ple of such a "top-down" approach (Goodsell et al., 2018; Klein et al., 2019). In their model, a random walk is first applied to generate a closed backbone of the genomic DNA, from which plectonemes branch off at randomised locations (Fig. 6.2). The random walk process is calibrated to reproduce various global features of the bacterial nucleoid, such as the average plectoneme length and spacing, persistence length and the distribution of close contact. A common feature of these mesoscale models is the use of a highly simplified forcefield to reduce computational expenses during the relaxation stage. For instance, the total potential energy expression for the model by Hacker *et al.* does not take into account the degrees of freedom associated with twist as well as the electrostatic interaction between the polymer segments.

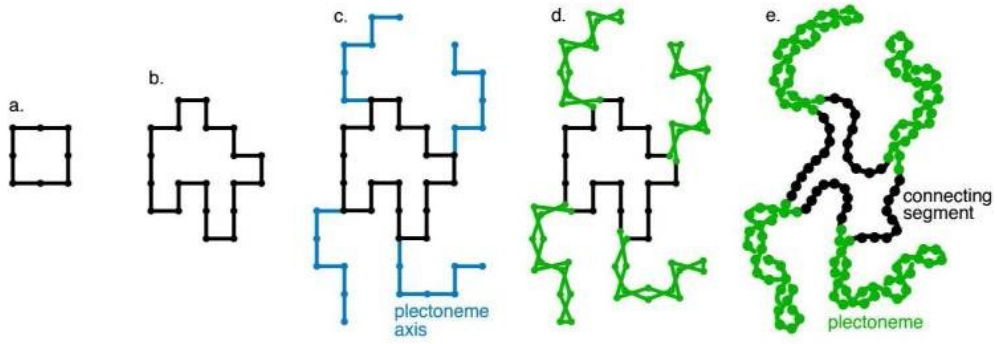


Figure 6.2: Lattice modelling of a bacterial nucleoid. A (a) closed loop is (b) enlarged and refined with the addition of lattice points until the desired number of bps per lattice spacing is achieved. Plectonemes are then (c) added using a random walk, (d) refined into a superhelix by splitting each lattice point into two and rotating them accordingly to achieve the desired superhelical density. Finally, the structure undergoes a (e) relaxation protocol to remove steric overlaps. Figure is reproduced with permission from Ref. (Goodsell et al., 2018).

Which modelling approach to take is ultimately a question of what the study objectives are. Given that our hypothesis-testing is contingent on the generation of twist-induced supercoiling, it is essential that we choose a model that gives the correct mechanical response to a change in twist or linking number. The TEP

model that we introduced in Chapter 2 is a suitable choice. Since the simulation of an entire bacterial nucleoid using the TEP model carries a high computational cost, we have decided to create a representative intranuclear environment, with a few simplifications made to conduct the hypothesis-testing in a more controlled fashion. Firstly, we ensure that the volume fraction of DNA (i.e. volume of DNA/volume of nucleoid) in our model matches physiological values. For this study, we choose to use a volume fraction of 0.13 as quoted by Chow and Skolnick in their paper (Chow & Skolnick, 2017). Secondly, we exclude the presence of nucleoid-associated proteins (NAPs) and various topoisomerases in our model, except for a single RNA polymerase (RNAP) that serves to generate plectonemic supercoils. Thirdly, topological domains (a region of plectonemic supercoils that is flanked by supercoiling-diffusion barriers) are not explicitly considered in our nucleoid architecture. The origin of the supercoiling-diffusion barriers and the size of topological domains remain very much the subject of active investigations (Sinden & Pettijohn, 1981; Higgins et al., 1996; Postow et al., 2004; Deng et al., 2005; Yan et al., 2018). Finally, we set σ to be -0.05 in order to match the physiological supercoiling density value of deproteinised plasmids from bacterial cells (Benedetti et al., 2015).

We begin with a closed DNA loop comprising N TEP beads. The DNA loop is characterised by a linking number deficit ΔLk that is introduced into the system with the following choice of the Euler angles (Chirico & Langowski, 1994):

$$\beta_i = -\frac{2\pi}{N} \tag{6.1a}$$

$$\alpha_i = -\frac{(i-1)2\pi\Delta Lk}{N} \tag{6.1b}$$

$$\gamma_i = \frac{i2\pi\Delta Lk}{N} \tag{6.1c}$$

Most of the systems we simulate for this work consist of $N = 1430$ TEP beads which is equivalent to 10,582 bps. This matches the size of a topological domain quoted in (Postow et al., 2004). Thus, for a loop with $N = 1430$ beads and a helical repeat of 10.6 bps/turn, $\Delta Lk \approx -49.97$. To model the confinement of the rest of the DNA and the cell, and in order to aid with equilibration, the DNA loop is enclosed within a sphere with a radius $R = 227.6$ TEP units (equivalent to 569 nm) that is slightly larger than the initial loop radius, and with a quadratic potential that has a stiffness of $k_{\text{sphere}} = 50$ TEP units. Molecular dynamics simulation of the 1430-bead system is then carried out with R decreasing at a rate of 1.027×10^{-5} nm/time step for 5.0×10^{7} time steps until the volume fraction of 0.13 is achieved. Once the desired volume fraction is achieved, the system is further equilibrated for another 1.0×10^{8} time steps (Fig. 6.3).

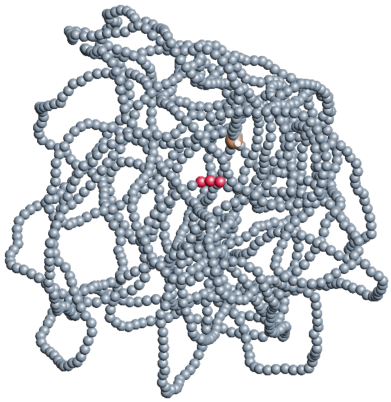


Figure 6.3: Equilibrated nucleoid model comprising of 1430 TEP beads (10,582 bps) enclosed in a hard sphere with a radius of 55.5 nm. Also visible are the defect (in red) and the stationary RNA polymerase (in brass).

Modelling the DNA defect

The defect is modelled by reducing the bending stiffness k_b of three TEP beads to 10% of its original value. The reduction in bending stiffness is significantly larger than what we would expect of a typical defect such as base pair mismatch or thymine dimer (for instance, in Ref. (Randisi, 2019), the bending stiffness of a 10-bp mismatch was determined to be 35% of the corresponding undamaged value). The tendency for plectonemes to be localised at the defect site is depen-

dent on the length of the dsDNA and the tension in the DNA strands. Plectonemic pinning in a longer DNA strand incurs a larger entropic cost while the probability of pinning increases with the applied force (Randisi, 2019; P. R. Desai et al., 2020). Since the DNA system that we are examining here comprises tens of thousands of base pairs and is not subjected to any external force(s), the typical defect parameters are insufficient to provide the thermodynamic drive necessary for plectoneme localisation at the defect site. Consequently, in order to observe and to understand how plectoneme localisation can be attained in such a system, a much "stronger" defect model is required.

To mimic the occurrence of DNA damage in a crowded chromosomal environment, we also place the defect close to the middle of the nucleoid (see Fig. 6.3).

Modelling the RNA polymerase

The RNA polymerase (RNAP) is represented by an actively rotating TEP bead fixed in space with a harmonic trap ($k^i_{\text{trap}} = 100$ TEP units, $i = 1, 2, 3$). This is placed 186 beads away from the centre of the defect site. The rotating TEP bead is capable of generating negative and positive supercoils similar to the twin supercoiling model of transcription by Liu and Wang (L. F. Liu & Wang, 1987; Wu et al., 1988) (Fig. 6.4).

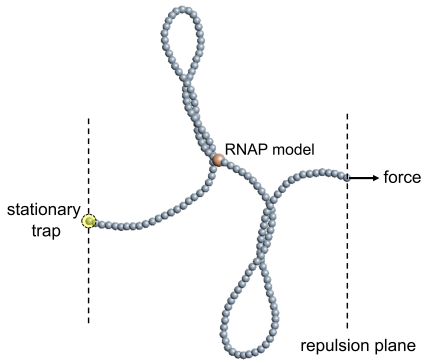


Figure 6.4: Reproduction of the twin supercoiling domain model of transcription by Liu and Wang (L. F. Liu & Wang, 1987) in a molecular tweezer set-up. An actively rotating TEP bead (in brass colour) mimics the rotation of the RNA polymerase-RNA complex around the DNA.

6.3 Simulation results

Rotating RNAP facilitates plectonemic pinning of defects

The plectoneme detection algorithm by Matek *et al.* (Matek et al., 2015), which relies on the identification of close contact between DNA segments, is ill-suited for locating the plectoneme that is pinned at the defect site due to the closely-packed nature of the bacterial nucleoid. Thus, to determine if the defect is segregated at the tip of a plectoneme, we define θ_{TEP}, as shown in Fig. 6.5. Taking the index of a defect TEP bead to be i, two vectors are defined: one connecting bead i to bead $i + 2$, and the other connecting i to bead $i - 2$. The angle θ_{TEP} is then calculated from the dot product of these two vectors. The algorithm is repeated for the other two defect beads, and the smallest value of θ_{TEP} that arises from this variation in the choice of i is selected to be the finalised value for θ_{TEP}. If the defect is localised at the tip of a plectoneme throughout the entire MD trajectory, we would expect θ_{TEP} to be narrowly distributed about an angle that is significantly smaller than $180°$ (since the plectoneme tip has a high geometrical curvature). Otherwise, the distribution of θ_{TEP} is expected to be broad and approximately uniform (given a sufficiently long simulation run).

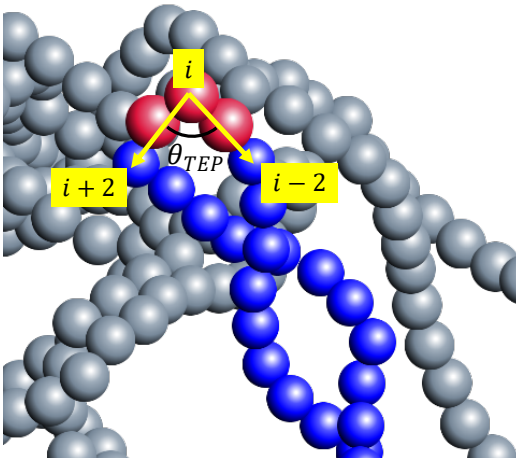


Figure 6.5: Definition of θ_{TEP}. A defect TEP bead (in red) assumes an index i. Two vectors connecting bead i to bead $i + 2$ and bead $i - 2$ are constructed, from which θ_{TEP} is calculated using the dot product of these two vectors. The algorithm is repeated for the other two defect beads. The smallest value of θ_{TEP} that arises from this variation in the choice of i is selected to be the finalised value for θ_{TEP}.

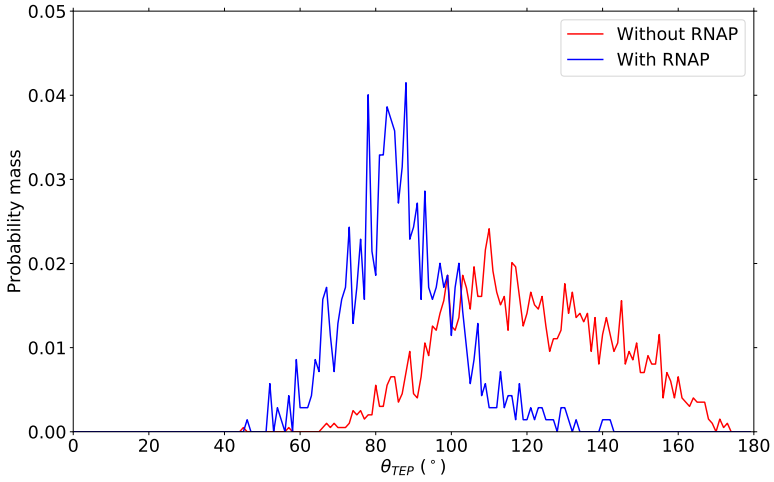


Figure 6.6: Representative θ_{TEP} distribution (in blue colour) for a nucleoid system with a rotating RNAP. For comparison, the reference distribution for a nucleoid system without a RNAP is shown in red. The mean θ_{TEP} of $87.8°$ for a nucleoid system with a rotating RNAP is suggestive of a defect that is localised at the tip of a plectoneme.

Fig. 6.6 compares the θ_{TEP} distribution for a nucleoid system that contains an RNAP with a rotational period of 5.0×10^4 time steps (we will quantify what this rate means later) and the θ_{TEP} distribution for a similar system without an RNAP. In generating these θ_{TEP} distributions, the first 5.0×10^7 time steps — which is approximately the time needed for plectonemes to be formed in the presence of an RNAP — were ignored. The much narrower θ_{TEP} distribution (in blue) centred at $\sim 90°$ suggests that the defect is segregated most of the time at the tip of a plectoneme when an active RNAP is present. We can verify this effect visually from Fig. 6.7 as well. The defect, initially placed in the middle of the nucleoid, is gradually pushed to the surface by the nucleation of a plectoneme that carries the defect at its tip. Other than the localisation of the defect at the plectoneme tip, we also observe a compaction of the bacterial DNA configuration in Fig. 6.7 caused by the formation of multiple plectonemic loops. This observation can be quantified by tracking the variation in the radius of gyration R_g (Fixman, 1962) of

the system with time (see Fig. 6.8). Such an effect could complement plectonemic pinning in making the defect more visible to the repair proteins.

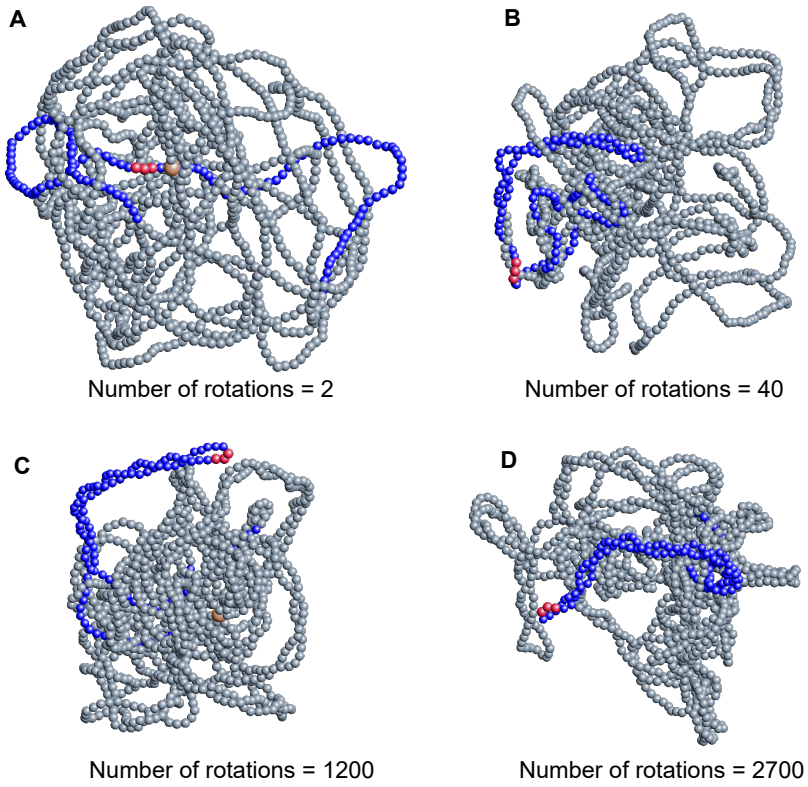


Figure 6.7: Series of configuration snapshots of the nucleoid model that contains a rotating TEP bead (in brass) and a defect (in red). The defect is yet to be localised in (A) and (B), but as torsional stresses build up, the defect is observed (in (C) and (D)) to be segregated to the tip of a plectoneme (highlighted in blue).

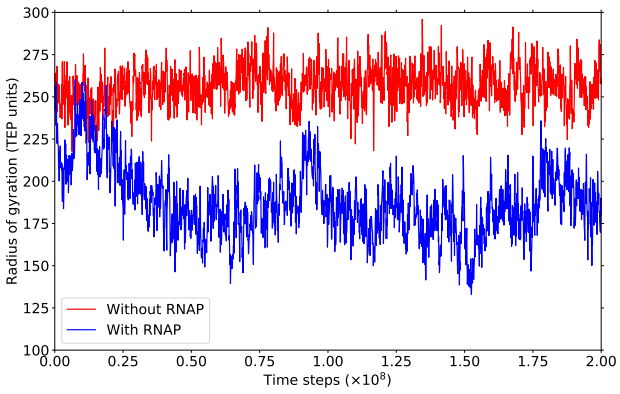


Figure 6.8: The radius of gyration R_g of the bacterial nucleoid system is observed to decrease by approximately 29% in the presence of an actively rotating RNAP.

Localisation of defect at the plectoneme tip is dependent on the rotational speed of the RNAP model

Plectonemic pinning of the defect model and the reduction in R_g can still be observed when the rotation period of the RNAP is increased to 1.0×10^6 time steps (see Figs. A.7 and A.8). When the rotation period is further increased to 1.0×10^7 time steps, these effects are no longer observed. We can explain this observation with Fig. 6.9, where the local twist angle associated with each TEP bead i is calculated using $\alpha_i + \gamma_i$ (C. A. Brackley et al., 2014), with α and γ being Euler angles. A high rotational speed of the RNAP is required to sustain adjacent domains of positive and negative twist in the absence of topological barriers, and induce the formation of plectonemic supercoils. Otherwise, the rate of twist dissipation is greater than the rate of accumulation of positive/negative twist (Racko et al., 2015), and no plectonemic supercoils can be formed.

We shall now attempt to make a real-time estimate of the rotation speed of the RNAP in our simulations by following the approach taken by Racko *et al.* in Ref. (Racko et al., 2015). First, we track the time evolution of the orientation vector $\hat{u}(t)$ of individual, stand-alone TEP beads and perform a linear fit using the formula $\langle|\hat{u}(t) - \hat{u}_0|^2\rangle = 2(1 - e^{-2D_r t}) \approx 4D_r t$ at $D_r t \ll 1$ to obtain a rotational diffusion constant D_r of 5.0×10^{-4} rad^2/time step (Jain & Sebastian, 2017). In pure water, a DNA 8-mer (the closest experimental equivalent of a TEP bead that represents 7.4 bps) is reported to have a D_r of 6×10^7 rad^2/s (Niermann et al., 1999). Assuming that D_r is inversely proportional to the viscosity, the rotational diffusion constant of the same 8-mer is expected to be smaller in an intranuclear environment that is more viscous than pure water. Experimentally-determined values of viscosity in intranuclear environments μ_{cell} however vary significantly. Measurements based on nano-particle tracking of fluorescent nanospheres in the intranuclear region of Swiss 3T3 fibroblasts yielded an intranuclear

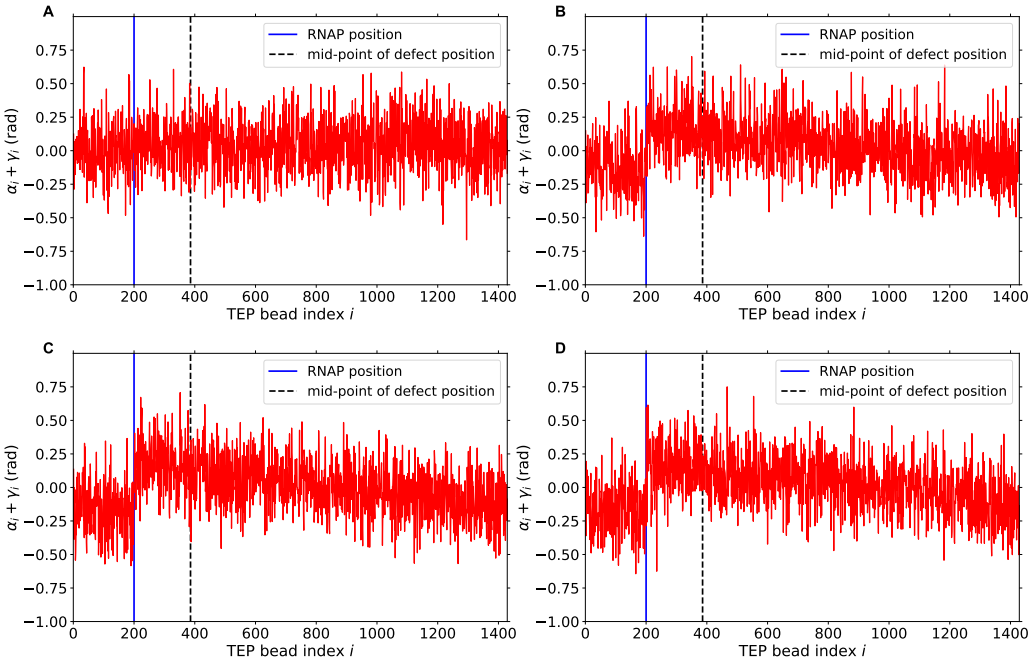


Figure 6.9: Twist profile of the nucleoid model when the RNAP has completed (A) 2 rotations, (B) 80 rotations, (C) 1000 rotations and (D) 2000 rotations. The local twist angle associated with each TEP bead i is obtained using $\alpha_i + \gamma_i$. The high rotational speed (period of 50,000 time steps) sustains a region of positive twist on one side of the RNAP and a region of negative twist on the other side.

viscosity μ_{cell} of 520 P (Tseng et al., 2004) while a similar technique applied to developing Caenorhabditis elegans (C. elegans) embryos reported a μ_{cell} of 10 P (Daniels et al., 2006). A different technique based on the entropic relaxation of chromosomal DNA in yeast cells estimated μ_{cell} at 140 P (Fisher et al., 2009). If we use the lowest value, then μ_{cell} is a thousand times larger than that of water (water has a viscosity of approximately 0.01 P), and then the D_r of a DNA 8-mer in a cell is approximately 6×10^4 rad^2/s, and each TEP time step would correspond to 8.3×10^{-9} s. For an RNAP with a rotational period of 1.0×10^6 time steps, the conversion between TEP time steps and real-time units would imply an angular speed of 120 rotations per second. A similar series of calculations using the highest reported value of 520 P for μ_{cell} would instead yield an angular speed

of 2.3 rotations per second.

A comparison with the experimental values of the RNAP's rotation rate is unfortunately not straightforward, as its rotation speed has been reported to be dependent on multiple factors, such as the RNAP's distance from the transcription start site, GC content of the gene, concentration of nucleoside triphosphates and the choice of experimental technique (Harada et al., 2001; Veloso et al., 2014; Kosuri et al., 2019; Tripathi et al., 2021). That being said, it is still useful to examine a few of these reported values to see where our simulated speed stands. In the study by Kosuri *et al.*, the maximum elongation rate was measured to be 17.5 bp/s (Kosuri et al., 2019). Assuming that the polymerase faithfully tracks the DNA helix, the rotation speed would be given by the elongation rate divided by 10.5. This gives us a value of 1.67 rotations per second. On the other hand, in the study by Harada *et al.*, the maximum elongation rate was reported to be 22 bp/s (Harada et al., 2001). This translates to a rotation rate of 2.1 turns per second under the same assumptions. Both values are comparable to our lower bound estimate of the RNAP model's angular speed. For these kinds of coarse-grained models, one should always be careful not to overinterpret these numbers. The upshot is that we believe that our simulations are roughly capturing the correct physical regime for how RNAP induces plectonemes.

Localisation of defect at the plectoneme tip is dependent on the separation between the defect and the RNAP model

We find, from Fig. 6.9, that $\alpha_i + \gamma_i$ decays with increasing distance from the rotating RNAP. By placing the defect at a distance of 700 bps away from the RNAP, we discover that the defect no longer segregates to a plectonemic tip (Fig. 6.10). This strengthens our earlier assertion that the sustained overtwisted/undertwisted regions generated by the RNAP in the DNA model is responsible for driving defect

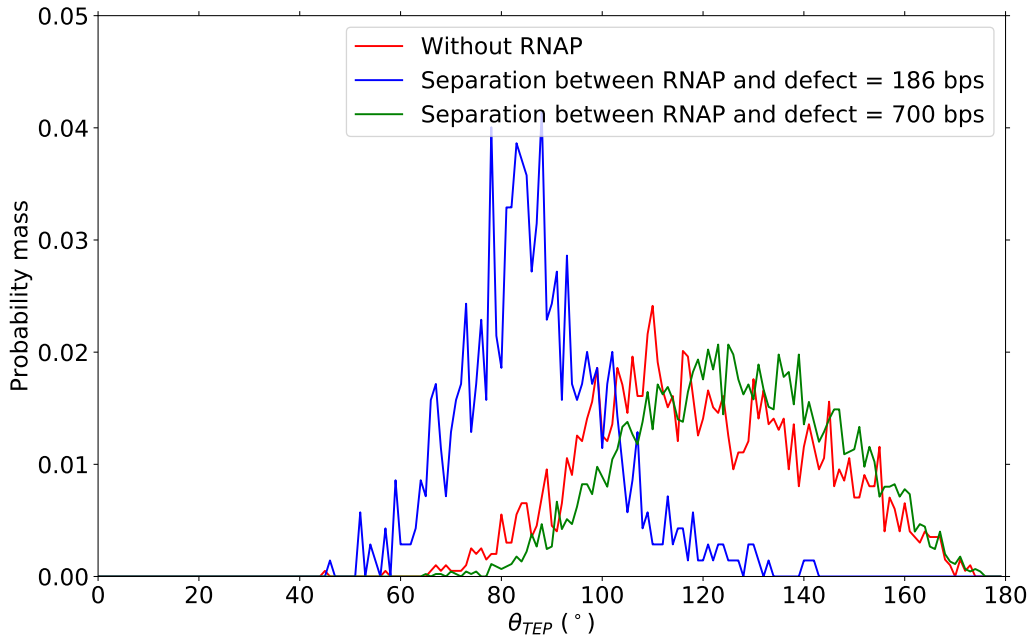


Figure 6.10: The θ_{TEP} distribution (in green) for a nucleoid system with a rotating RNAP that is 700 bps away from the defect is similar to the θ_{TEP} distribution for a nucleoid system without a RNAP (in red). The RNAPs in both systems have the same rotational period.

localisation.

Supercoiling-diffusion barriers facilitate defect segregation at the plectoneme tip

Topological domains in DNA are flanked by supercoiling-diffusion barriers (otherwise also known as topological barriers) which block the dissipation of torsional stresses generated by processes such as replication and transcription (Postow et al., 2004; Joyeux & Junier, 2020; Visser et al., 2022). In this work, topological barriers are represented using TEP beads whose orientations and positions are constrained. The TEP beads located at particle indices 700 and 1200 in our 1430-bead model (refer to Fig. 6.9 for particle location) are designated as topological barriers. The constrained orientation vectors of these topological barriers

block the diffusion of excess twist generated by the rotating RNAP model. Consequently, accumulation of excess positive and negative twists adjacent to the RNAP model—an important factor in the formation of plectonemes that localise the defect at their tips—can still be observed even for a slowly rotating RNAP model (Fig. 6.11). Alternative methods of representing topological barriers, such as significantly increasing the torsional moduli of several adjacent TEP beads, are currently being explored. The inclusion of supercoiling-diffusion barriers in our DNA model effectively reduces the overall length of supercoiled DNA. This in turn lowers the entropic cost of plectonemic pinning by a defect, which scales with the log of the DNA length (Brahmachari et al., 2018). As a result, it may be possible to model our defect more realistically (instead of using three beads with a highly reduced bending stiffness k_b). This is currently under investigation.

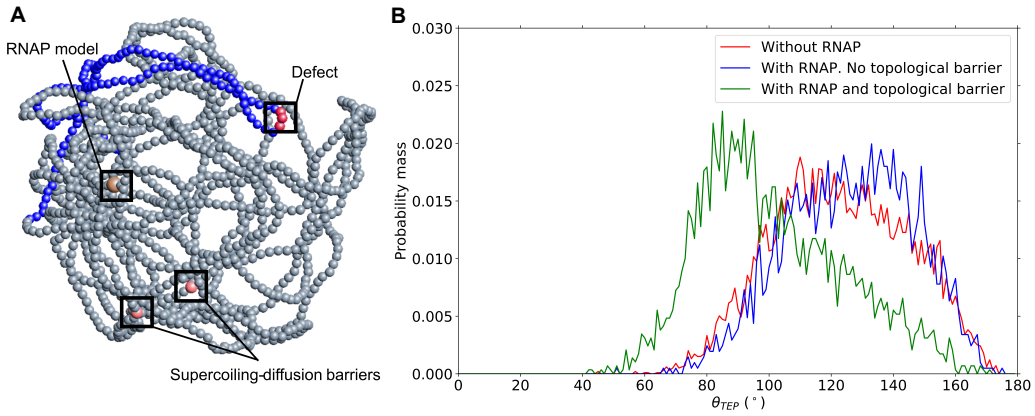


Figure 6.11: (A) The presence of supercoiling-diffusion or topological barriers allows defect localisation at the plectoneme tip to be achieved for a slowly rotating RNAP model. The RNAP model has a rotational period of 1.0×10^7 time steps. (B) In the absence of topological barriers, the θ_{TEP} distribution (in blue) for a nucleoid system with a slowly rotating RNAP (period of 1.0×10^7 time steps) is similar to the θ_{TEP} distribution for a nucleoid system without a RNAP (in red). The inclusion of topological barriers into the nucleoid system shifts the peak of the θ_{TEP} distribution (in green) to a lower value of approximately $80°$, indicating the presence of defect segregation at a plectonemic tip.

6.4 Concluding remarks

Our findings are consistent with experimental studies which suggest that a stalled RNA polymerase near a damage site serves as a damage marker and a signal for DNA repair (Lindsey-Boltz & Sancar, 2007; Derheimer et al., 2007; Sanij et al., 2019; S. Liu et al., 2021). A moving RNAP generates downstream positive supercoils and upstream negative supercoils that are relieved by topoisomerases in order for elongation to continue (L. F. Liu & Wang, 1987; Dorman, 2019). When a defect is encountered in close proximity, the generated supercoil is pinned by the defect, which in turn is localised at the tip of the plectonemic supercoil. The topoisomerase that is responsible for relieving the supercoils aborts its action when it encounters the defect and stays attached to the supercoil (McKinnon, 2016). This is interpreted as a type of DNA damage that has to be removed before the supercoils are relaxed (Swan et al., 2022).

This study is intended to serve as a precursor and a test of feasibility for studying the very rich and complex question of how supercoiling affects defect recognition in a large-scale, complex bacterial nucleoid model. There are several modifications that could improve the current model. Firstly, we could construct a more realistic RNAP model that represents the mechanical action of an elongating RNAP. One possibility is to follow the approach taken by Fosado *et al.*, who modelled the RNAP as a ring that encircles the DNA strand (Fosado et al., 2021). The DNA segment that passes through the ring experiences a force that is perpendicular to the plane of the ring. This force then drives the relative motion between the ring and the DNA strand. Secondly, we can introduce NAPs into the system. NAPs such as H-NS or Fis are thought to serve as supercoiling-diffusion barriers since they have been observed to bind to distinct sites on the chromosome to form a topologically isolated DNA loop (Skoko et al., 2005, 2006; Verma et al., 2019;

Japaridze et al., 2021). By treating these proteins as a set of separate particle that could bind to or dissociate from the TEP beads (similar to the methods employed by Johnson *et al.* (Johnson et al., 2015)), we could generate a variable amount of topological domains in our system, which effectively reduces the length of the supercoiling DNA strand and in turn reduces the entropic cost of plectonemic pinning by a defect. NAPs at a sufficiently high concentration have also been reported to compact DNA into a condensed form (Zhu et al., 2010; Zhang et al., 2013; Jiang et al., 2015; Gupta & van der Maarel, 2017), which in our current study is modelled using a repulsive hard sphere.

Finally, we could replicate the same study using the oxDNA model instead of the TEP model. The current study assumes that the transient torsional stresses introduced by the rotating RNAP do not affect defect properties. This is not true. A sufficiently large torsional stress could rupture base pairs around a DNA defect such as base pair mismatch—similar to how bubbles are preferentially nucleated at a defect site—and modify the local bending and torsional moduli at the defect site.

7 | Conclusion

In this thesis we have studied a number of different topics related to the effect of supercoiling on inhomogeneous DNA. While the study of how twist affects homogeneous DNA has a long and illustrious history, much less is known about what happens when we include defects in the DNA. Given that in-vivo, we expect DNA to often have defects, and is subject to torques, it is important to study this problem.

To summarise, we have carefully demonstrated a working model of thymine dimers in oxDNA that can reproduce known experimental results. There is a certain amount of robustness in the choice of model parameters, constrained by experiments on melting temperatures and bending angles. Within this range of parameters, we achieve consistent results on DNA's response to twist, namely a preferential co-localization of the thymine dimer with the tips of supercoiled plectonemic structures and the enhanced probability for the thymine dimer to be in a bubble state. This robustness suggests that the results are not a peculiarity of the parameters used in our model, but are instead reflective of a more general interaction between supercoiling and the thymine dimer. By exposing the thymine dimer in a plectoneme tip-bubble, negative supercoiling could play a bigger role than previously thought in facilitating the repair of thymine dimers. Moreover, our results here are suggestive of a much richer set of possible mechanisms that could be driven by the coupling between supercoiling and DNA damage. Future workstreams can focus on adapting the approach taken to model thymine dimers to construct other types of DNA damage such as methylated bases in an oxDNA environment or to explore the phenomenon of plectonemic pinning by a thymine dimer with more detailed atomistic simulations.

We also used relatively simple statistical mechanics models to study the fundamental processes that underlie the interaction between supercoiling and the thymine dimer. By calculating the energetic savings that arise from kinking a plectonemic end-loop, we were able to derive a free energy expression for a plectoneme tip-bubble. We compared our predictions of how the state occupancy of a plectoneme tip-bubble, as a function of force and superhelical density, can be modified by the presence of a defect, to measurements made with oxDNA of the thymine dimer-containing dsDNA. The predictive ability of the model is also stress-tested successfully with other defects such as base pair mismatches. This strengthens our argument that the coupling between negatively supercoiled tip-bubbles and the thymine dimer that we observe in Chapter 3 is a specific example of a more general mechanism that facilitates DNA repair. As next steps, we could extend this study to positively supercoiled dsDNA and examine if the statistical mechanics models that we have developed continue to apply to positively supercoiled dsDNA with damage.

These observations may have implications for damage search and recognition in living cells. It may be possible that plectonemic supercoils—positive or otherwise—are responsible for moving the DNA defect away from the crowded intranuclear environment. To test this hypothesis, we constructed an intranuclear environment within a prokaryotic bacterial cell using the twistable elastic polymer (TEP) model. An actively rotating TEP bead that represents a stationary RNAP and TEP beads with reduced bending stiffness to represent DNA damage were introduced into this environment. With this model, we found that the supercoils generated by the RNAP were capable of separating the defect away from the crowded region of the nucleoid. The results are promising but the model carries a number of assumptions that have to be examined thoroughly or removed with a more accurate representation of the nucleoid. Nucleoid-associated proteins, for instance,

can be added to the system. These proteins could help our chromosome model organise itself into distinct topological domains that would reduce the entropic cost of pinning the defect-containing plectoneme. In addition, we could modify our RNAP model to make it move and behave like an actual elongating polymerase. Such a modification could have implications on the size of the plectonemic supercoil (Fosado et al., 2021). These modifications are being considered as future extensions of this work.

Finally, we examine the formation of plectonemes in DNA nanotubes using MD simulations in the oxDNA forcefield. Unlike dsDNA, buckling in DNA nanotubes is mediated in the kink-dominated regime due to the nanotubes' high bending and torsional moduli. Strong bending of the nanotube—to form a plectonemic loop for instance—kinks the nanotube and reduces the overall cost of bending relative to a WLC. We showed, as a consequence of this phenomenon, that typical plectoneme formation theories based on the WLC model are ill-suited to characterise the plectoneme geometry and energetics in buckled DNA nanotubes. For instance, the WLC theories predict a much longer plectoneme pitch and a much smaller superhelical angle than what we have observed from the simulations. This is because in the WLC regime, the nanotube is expected to minimise its overall bending energy by simultaneously maximising its pitch and minimising its superhelical angle in response to its high bending stiffness. In our simulations however, the kinks that are formed from the bending stresses alleviate some of these energetic costs and enable plectonemic loops with a higher geometric curvature to be formed. These findings prompted us to re-evaluate the validity of using the WLC model to characterise the findings of recent experimental studies involving twisted/bent DNA nanotubes, and warranted further tweezer experimentations to quantify the buckling transition of DNA nanotubes (e.g. measuring the magnitude of the torque overshoot and position of the buckling transition point) so that

predictions from the WLC model can be stress-tested.

To conclude, our study of inhomogeneous DNA's response to twist has brought forth a number of possibilities for future investigations. The question of how the WLC model (Eq. 1.1) can be modified to account for DNA inhomogeneities remains open. Early attempts to do this by treating DNA defects as a segment of the WLC with a bending modulus B_1 that differs from that of the rest of the WLC had yielded promising results (Randisi, 2019), though challenges remain in the treatment of the boundaries between the inhomogeneous segment and the rest of the WLC under conditions of extreme twist. The hypothesis that DNA damage repair is facilitated by the co-localisation of DNA damages and the tip-bubbles in supercoiled dsDNA requires further testing. It may be possible, for instance, for the tip-bubble plectonemes to be preferentially formed on certain DNA sequences (Matek et al., 2015) instead of the DNA damage site itself. This competition between DNA sequences and DNA damages for the co-localisation of tip-bubbles could impact the efficiency of damage recognition and repair (Hill et al., 2023).

Bibliography

Aggarwal, A., Naskar, S., Sahoo, A. K., Mogurampelly, S., Garai, A., & Maiti, P. K. (2020). What do we know about DNA mechanics so far? *Current Opinion in Structural Biology*, *64*, 42–50.

Allemand, J. F., Bensimon, D., Lavery, R., & Croquette, V. (1998). Stretched and overwound DNA forms a Pauling-like structure with exposed bases. *Proceedings of the National Academy of Sciences*, *95*(24), 14152–14157.

Allen, M. P., & Tildesley, D. J. (2017). *Computer simulation of liquids*. Oxford University Press.

Ames, B. N., Shigenaga, M. K., & Hagen, T. M. (1993). Oxidants, antioxidants, and the degenerative diseases of aging. *Proceedings of the National Academy of Sciences*, *90*(17), 7915–7922.

Barbi, M., Mozziconacci, J., Victor, J.-M., Wong, H., & Lavelle, C. (2012). On the topology of chromatin fibres. *Interface Focus*, *2*(5), 546–554.

Barone, F., Bonincontro, A., Mazzei, F., Minoprio, A., & Pedone, F. (1995). Effect of thymine dimer introduction in a 21 base pair oligonucleotide. *Photochem. Photobiol.*, *61*, 61–67.

Bauer, W., & Vinograd, J. (1970). Interaction of closed circular DNA with intercalative dyes: Ii. the free energy of superhelix formation in sv40 DNA. *Journal of Molecular Biology*, *47*(3), 419–435.

Bauer, W. R., & Benham, C. J. (1993). The free energy, enthalpy and entropy of native and of partially denatured closed circular DNA. *Journal of Molecular Biology*, *234*(4), 1184–1196.

Benedetti, F., Japaridze, A., Dorier, J., Racko, D., Kwapich, R., Burnier, Y., … Stasiak, A. (2015). Effects of physiological self-crowding of DNA on shape and biological properties of DNA molecules with various levels of

supercoiling. *Nucleic Acids Research*, *43*(4), 2390–2399.

Benham, C. J. (1992). Energetics of the strand separation transition in superhelical DNA. *Journal of Molecular Biology*, *225*(3), 835–847.

Beukers, R., Eker, A. P., & Lohman, P. H. (2008). 50 years thymine dimer. *DNA Repair*, *7*(3), 530–543.

Bliska, J. B., & Cozzarelli, N. R. (1987). Use of site-specific recombination as a probe of DNA structure and metabolism in vivo. *Journal of Molecular Biology*, *194*(2), 205–218.

Blount, Z. D. (2015). The natural history of model organisms: The unexhausted potential of E. coli. *Elife*, *4*, e05826.

Boles, T. C., White, J. H., & Cozzarelli, N. R. (1990). Structure of plectonemically supercoiled DNA. *Journal of Molecular Biology*, *213*(4), 931–951.

Bono, N., Ponti, F., Punta, C., & Candiani, G. (2021). Effect of UV irradiation and TiO2-photocatalysis on airborne bacteria and viruses: an overview. *Materials*, *14*(5), 1075.

Brackley, C., Allan, J., Keszenman-Pereyra, D., & Marenduzzo, D. (2015). Topological constraints strongly affect chromatin reconstitution in silico. *Nucleic Acids Research*, *43*(1), 63–73.

Brackley, C. A., Cates, M. E., & Marenduzzo, D. (2012). Facilitated diffusion on mobile DNA: configurational traps and sequence heterogeneity. *Physical Review Letters*, *109*(16), 168103.

Brackley, C. A., Cates, M. E., & Marenduzzo, D. (2013). Effect of DNA conformation on facilitated diffusion. *Biochemical Society Transactions*, *41*(2), 582–588.

Brackley, C. A., Morozov, A. N., & Marenduzzo, D. (2014). Models for twistable elastic polymers in Brownian dynamics, and their implementation for LAMMPS. *The Journal of Chemical Physics*, *140*(13), 04B603_1.

Brahmachari, S., Dittmore, A., Takagi, Y., Neuman, K. C., & Marko, J. F. (2018). Defect-facilitated buckling in supercoiled double-helix DNA. *Physical Review E*, *97*(2), 022416.

Brahmachari, S., & Marko, J. F. (2017). Torque and buckling in stretched intertwined double-helix DNAs. *Physical Review E*, *95*(5), 052401.

Brown, R. F., Andrews, C. T., & Elcock, A. H. (2015). Stacking free energies of all DNA and RNA nucleoside pairs and dinucleoside-monophosphates computed using recently revised AMBER parameters and compared with experiment. *Journal of Chemical Theory and Computation*, *11*(5), 2315–2328.

Brutzer, H., Luzzietti, N., Klaue, D., & Seidel, R. (2010). Energetics at the DNA supercoiling transition. *Biophysical Journal*, *98*(7), 1267–1276.

Bryant, Z., Stone, M. D., Gore, J., Smith, S. B., Cozzarelli, N. R., & Bustamante, C. (2003). Structural transitions and elasticity from torque measurements on DNA. *Nature*, *424*(6946), 338–341.

Bustamante, C., Bryant, Z., & Smith, S. B. (2003). Ten years of tension: single-molecule DNA mechanics. *Nature*, *421*(6921), 423–427.

Bustamante, C. J., Chemla, Y. R., Liu, S., & Wang, M. D. (2021). Optical tweezers in single-molecule biophysics. *Nature Reviews Methods Primers*, *1*(1), 1–29.

Cadet, J., Douki, T., & Ravanat, J.-L. (2006). One-electron oxidation of DNA and inflammation processes. *Nature Chemical Biology*, *2*(7), 348–349.

Castro, C. E., Kilchherr, F., Kim, D.-N., Shiao, E. L., Wauer, T., Wortmann, P., … Dietz, H. (2011). A primer to scaffolded DNA origami. *Nature Methods*, *8*(3), 221–229.

Chatterjee, G., Dalchau, N., Muscat, R. A., Phillips, A., & Seelig, G. (2017). A spatially localized architecture for fast and modular DNA computing.

Nature Nanotechnology, *12*(9), 920–927.

Chatterjee, N., & Walker, G. C. (2017). Mechanisms of DNA damage, repair, and mutagenesis. *Environmental and Molecular Mutagenesis*, *58*(5), 235–263.

Chen, X., Velmurugu, Y., Zheng, G., Park, B., Shim, Y., Kim, Y., ... others (2015). Kinetic gating mechanism of DNA damage recognition by Rad4/XPC. *Nature Communications*, *6*(1), 1–10.

Chhabra, H., Mishra, G., Cao, Y., Prešern, D., Skoruppa, E., Tortora, M. M., & Doye, J. P. K. (2020). Computing the elastic mechanical properties of rod-like DNA nanostructures. *Journal of Chemical Theory and Computation*, *16*, 7748–7763.

Chirico, G., & Langowski, J. (1994). Kinetics of DNA supercoiling studied by Brownian dynamics simulation. *Biopolymers: Original Research on Biomolecules*, *34*(3), 415–433.

Chow, E., & Skolnick, J. (2017). DNA internal motion likely accelerates protein target search in a packed nucleoid. *Biophysical Journal*, *112*(11), 2261–2270.

Ciotti, M., Ciccozzi, M., Terrinoni, A., Jiang, W.-C., Wang, C.-B., & Bernardini, S. (2020). The COVID-19 pandemic. *Critical reviews in Clinical Laboratory Sciences*, *57*(6), 365–388.

Clauvelin, N., Audoly, B., & Neukirch, S. (2008). Mechanical response of plectonemic DNA: An analytical solution. *Macromolecules*, *41*(12), 4479–4483.

Clauvelin, N., Audoly, B., & Neukirch, S. (2009). Elasticity and electrostatics of plectonemic DNA. *Biophysical Journal*, *96*(9), 3716–3723.

Corless, S., & Gilbert, N. (2017). Investigating DNA supercoiling in eukaryotic genomes. *Briefings in Functional Genomics*, *16*(6), 379–389.

Daniels, B. R., Masi, B. C., & Wirtz, D. (2006). Probing single-cell microme-

chanics in vivo: the microrheology of C. elegans developing embryos. *Biophysical Journal*, *90*(12), 4712–4719.

Dekker, J., Marti-Renom, M. A., & Mirny, L. A. (2013). Exploring the three-dimensional organization of genomes: interpreting chromatin interaction data. *Nature Reviews Genetics*, *14*, 390–403.

Deng, S., Stein, R. A., & Higgins, N. P. (2005). Organization of supercoil domains and their reorganization by transcription. *Molecular Microbiology*, *57*(6), 1511–1521.

Dequeker, B. J., Scherr, M. J., Brandão, H. B., Gassler, J., Powell, S., Gaspar, I., ... others (2022). MCM complexes are barriers that restrict cohesin-mediated loop extrusion. *Nature*, 1–7.

Derheimer, F. A., O'Hagan, H. M., Krueger, H. M., Hanasoge, S., Paulsen, M. T., & Ljungman, M. (2007). RPA and ATR link transcriptional stress to p53. *Proceedings of the National Academy of Sciences*, *104*(31), 12778–12783.

Desai, N. A., & Shankar, V. (2003). Single-strand-specific nucleases. *FEMS Microbiology Reviews*, *26*(5), 457–491.

Desai, P. R., Brahmachari, S., Marko, J. F., Das, S., & Neuman, K. C. (2020). Coarse-grained modelling of DNA plectoneme pinning in the presence of base-pair mismatches. *Nucleic Acids Research*, *48*(19), 10713–10725.

Desouky, O., Ding, N., & Zhou, G. (2015). Targeted and non-targeted effects of ionizing radiation. *Journal of Radiation Research and Applied Sciences*, *8*(2), 247–254.

Deufel, C., Forth, S., Simmons, C. R., Dejgosha, S., & Wang, M. D. (2007). Nanofabricated quartz cylinders for angular trapping: DNA supercoiling torque detection. *Nature Methods*, *4*(3), 223–225.

Dittmore, A., Brahmachari, S., Takagi, Y., Marko, J. F., & Neuman, K. C. (2017). Supercoiling DNA locates mismatches. *Physical Review Letters*, *119*(14),

147801.

Dittmore, A., Silver, J., & Neuman, K. C. (2018). Kinetic pathway of torsional DNA buckling. *The Journal of Physical Chemistry B*, *122*(49), 11561–11570.

Dorman, C. J. (2019). DNA supercoiling and transcription in bacteria: a two-way street. *BMC Molecular and Cell Biology*, *20*(1), 1–9.

Dorman, C. J., & Dorman, M. J. (2016). DNA supercoiling is a fundamental regulatory principle in the control of bacterial gene expression. *Biophysical Reviews*, *8*(3), 209–220.

Doye, J. P., Fowler, H., Prešern, D., Bohlin, J., Rovigatti, L., Romano, F., ... others (2020). The oxDNA coarse-grained model as a tool to simulate DNA origami. *arXiv preprint arXiv:2004.05052*.

Doye, J. P., Ouldridge, T. E., Louis, A. A., Romano, F., Šulc, P., Matek, C., ... others (2013). Coarse-graining DNA for simulations of DNA nanotechnology. *Physical Chemistry Chemical Physics*, *15*(47), 20395–20414.

Du, X., Gertz, E. M., Wojtowicz, D., Zhabinskaya, D., Levens, D., Benham, C. J., ... Przytycka, T. M. (2014). Potential non-B DNA regions in the human genome are associated with higher rates of nucleotide mutation and expression variation. *Nucleic Acids Research*, *42*(20), 12367–12379.

Duprat, C., & Shore, H. A. (2015). *Fluid-structure interactions in low-reynolds-number flows*. Royal Society of Chemistry.

Emanuel, M., Lanzani, G., & Schiessel, H. (2013). Multiplectoneme phase of double-stranded DNA under torsion. *Physical Review E*, *88*(2), 022706.

Fisher, J., Ballenger, M., O'Brien, E., Haase, J., Superfine, R., & Bloom, K. (2009). DNA relaxation dynamics as a probe for the intracellular environment. *Proceedings of the National Academy of Sciences*, *106*(23), 9250–9255.

Fixman, M. (1962). Radius of gyration of polymer chains. *The Journal of Chemical Physics*, *36*(2), 306–310.

Forsburg, S. L. (2004). Eukaryotic MCM proteins: beyond replication initiation. *Microbiology and Molecular Biology Reviews*, *68*(1), 109–131.

Forth, S., Deufel, C., Sheinin, M. Y., Daniels, B., Sethna, J. P., & Wang, M. D. (2008). Abrupt buckling transition observed during the plectoneme formation of individual DNA molecules. *Physical Review Letters*, *100*(14), 148301.

Fosado, Y. A., Michieletto, D., Brackley, C. A., & Marenduzzo, D. (2021). Nonequilibrium dynamics and action at a distance in transcriptionally driven DNA supercoiling. *Proceedings of the National Academy of Sciences*, *118*(10).

Frenkel, D., & Smit, B. (2001). *Understanding molecular simulation: from algorithms to applications* (Vol. 1). Elsevier.

Fye, R. M., & Benham, C. J. (1999). Exact method for numerically analyzing a model of local denaturation in superhelically stressed DNA. *Physical Review E*, *59*(3), 3408.

Galindo-Murillo, R., Robertson, J. C., Zgarbova, M., Sponer, J., Otyepka, M., Jurecka, P., & Cheatham III, T. E. (2016). Assessing the current state of AMBER force field modifications for DNA. *Journal of Chemical Theory and Computation*, *12*(8), 4114–4127.

Gerasimova, N., Pestov, N., Kulaeva, O., Clark, D., & Studitsky, V. (2016). Transcription-induced DNA supercoiling: New roles of intranucleosomal DNA loops in DNA repair and transcription. *Transcription*, *7*(3), 91–95.

Gerling, T., Kube, M., Kick, B., & Dietz, H. (2018). Sequence-programmable covalent bonding of designed DNA assemblies. *Science Advances*, *4*, eaau1157.

Gilbert, N., & Allan, J. (2014). Supercoiling in DNA and chromatin. *Current Opinion in Genetics & Development*, *25*, 15–21.

Goodsell, D. S., Autin, L., & Olson, A. J. (2018). Lattice models of bacterial nucleoids. *The Journal of Physical Chemistry B*, *122*(21), 5441–5447.

Gore, J., Bryant, Z., Nöllmann, M., Le, M. U., Cozzarelli, N. R., & Bustamante, C. (2006). DNA overwinds when stretched. *Nature*, *442*(7104), 836–839.

Goriely, A. (2006). Twisted elastic rings and the rediscoveries of Michell's instability. *Journal of Elasticity*, *84*(3), 281–299.

Grainger, D. C., Hurd, D., Goldberg, M. D., & Busby, S. J. (2006). Association of nucleoid proteins with coding and non-coding segments of the Escherichia coli genome. *Nucleic Acids Research*, *34*(16), 4642–4652.

Gross, P., Laurens, N., Oddershede, L. B., Bockelmann, U., Peterman, E. J., & Wuite, G. J. (2011). Quantifying how DNA stretches, melts and changes twist under tension. *Nature Physics*, *7*(9), 731–736.

Guo, H., & Tullius, T. D. (2003). Gapped DNA is anisotropically bent. *Proceedings of the National Academy of Sciences*, *100*(7), 3743–3747.

Guo, M. S., Kawamura, R., Littlehale, M. L., Marko, J. F., & Laub, M. T. (2021). High-resolution, genome-wide mapping of positive supercoiling in chromosomes. *Elife*, *10*, e67236.

Gupta, A. N., & van der Maarel, J. R. (2017). Compaction of plasmid DNA by macromolecular crowding. *Macromolecules*, *50*(4), 1666–1671.

Gutiérrez-Medina, B., Andreasson, J. O., Greenleaf, W. J., LaPorta, A., & Block, S. M. (2010). An optical apparatus for rotation and trapping. *Methods in Enzymology*, *475*, 377–404.

Hacker, W. C., Li, S., & Elcock, A. H. (2017). Features of genomic organization in a nucleotide-resolution molecular model of the Escherichia coli chromosome. *Nucleic Acids Research*, *45*(13), 7541–7554.

Harada, Y., Ohara, O., Takatsuki, A., Itoh, H., Shimamoto, N., & Kinosita, K. (2001). Direct observation of DNA rotation during transcription by Escherichia coli RNA polymerase. *Nature*, *409*(6816), 113–115.

Higgins, N. P., Yang, X., Fu, Q., & Roth, J. R. (1996). Surveying a supercoil domain by using the gamma delta resolution system in Salmonella typhimurium. *Journal of Bacteriology*, *178*(10), 2825–2835.

Hill, V. E., Noy, A., & Craggs, T. D. (2023). DNA damage competes with sequence to pin a plectoneme. *Biophysical Journal*, *122*(3), 214a.

Hirose, S., & Matsumoto, K. (2005). Possible roles of DNA supercoiling in transcription. In *DNA conformation and transcription* (pp. 138–143). Springer.

Hsieh, T.-S., & Wang, J. C. (1975). Thermodynamic properties of superhelical DNAs. *Biochemistry*, *14*(3), 527–535.

Hu, J., Choi, J.-H., Gaddameedhi, S., Kemp, M. G., Reardon, J. T., & Sancar, A. (2013). Nucleotide excision repair in human cells: fate of the excised oligonucleotide carrying DNA damage in vivo. *Journal of Biological Chemistry*, *288*, 20918–20926.

Hu, J., Selby, C. P., Adar, S., Adebali, O., & Sancar, A. (2017). Molecular mechanisms and genomic maps of DNA excision repair in escherichia coli and humans. *Journal of Biological Chemistry*, *292*(38), 15588–15597.

Huang, J., Schlick, T., & Vologodskii, A. (2001). Dynamics of site juxtaposition in supercoiled DNA. *Proceedings of the National Academy of Sciences*, *98*(3), 968–973.

Huang, J.-C., Svoboda, D. L., Reardon, J. T., & Sancar, A. (1992). Human nucleotide excision nuclease removes thymine dimers from DNA by incising the 22nd phosphodiester bond 5'and the 6th phosphodiester bond 3'to the photodimer. *Proceedings of the National Academy of Sciences*, *89*, 3664–3668.

Husain, I., Griffith, J., & Sancar, A. (1988). Thymine dimers bend DNA. *Proceedings of the National Academy of Sciences*, *85*(8), 2558–2562.

Hwa, T., Marinari, E., Sneppen, K., & Tang, L.-h. (2003). Localization of denaturation bubbles in random DNA sequences. *Proceedings of the National Academy of Sciences*, *100*(8), 4411–4416.

Jain, R., & Sebastian, K. (2017). Diffusing diffusivity: Rotational diffusion in two and three dimensions. *The Journal of Chemical Physics*, *146*(21), 214102.

Janssen, X. J., Lipfert, J., Jager, T., Daudey, R., Beekman, J., & Dekker, N. H. (2012). Electromagnetic torque tweezers: a versatile approach for measurement of single-molecule twist and torque. *Nano letters*, *12*(7), 3634–3639.

Japaridze, A., Yang, W., Dekker, C., Nasser, W., & Muskhelishvili, G. (2021). DNA sequence-directed cooperation between nucleoid-associated proteins. *Iscience*, *24*(5), 102408.

Jeon, J.-H., Adamcik, J., Dietler, G., & Metzler, R. (2010). Supercoiling induces denaturation bubbles in circular DNA. *Physical Review Letters*, *105*(20), 208101.

Jian, H., Vologodskii, A. V., & Schlick, T. (1997). A combined wormlike-chain and bead model for dynamic simulations of long linear DNA. *Journal of Computational Physics*, *136*(1), 168–179.

Jiang, K., Zhang, C., Guttula, D., Liu, F., van Kan, J. A., Lavelle, C., … others (2015). Effects of Hfq on the conformation and compaction of DNA. *Nucleic Acids Research*, *43*(8), 4332–4341.

Johnson, J., Brackley, C., Cook, P., & Marenduzzo, D. (2015). A simple model for DNA bridging proteins and bacterial or human genomes: bridging-induced attraction and genome compaction. *Journal of Physics: Condensed Matter*, *27*(6), 064119.

Joyeux, M., & Junier, I. (2020). Requirements for DNA-bridging proteins to act as

topological barriers of the bacterial genome. *Biophysical Journal*, *119*(6), 1215–1225.

Kaczmarczyk, A., Meng, H., Ordu, O., Noort, J. v., & Dekker, N. H. (2020). Chromatin fibers stabilize nucleosomes under torsional stress. *Nature Communications*, *11*(1), 1–12.

Kauert, D. J., Kurth, T., Liedl, T., & Seidel, R. (2011). Direct mechanical measurements reveal the material properties of three-dimensional DNA origami. *Nano Letters*, *11*(12), 5558–5563.

Kemmink, J., Boelens, R., Koning, T., Van der Marel, G., Van Boom, J., & Kaptein, R. (1987). 1 H NMR study of the exchangeable protons of the duplex d (gcgttgcg). d (cgcaacgc) containing a thymine photodimer containing a thymine photodimer. *Nucleic Acids Research*, *15*(11), 4645–4653.

Kemp, M. G., Reardon, J. T., Lindsey-Boltz, L. A., & Sancar, A. (2012). Mechanism of release and fate of excised oligonucleotides during nucleotide excision repair. *Journal of Biological Chemistry*, *287*, 22889–22899.

Kim, J.-K., Patel, D., & Choi, B.-S. (1995). Contrasting structural impacts induced by cis-syn cyclobutane dimer and (6–4) adduct in DNA duplex decamers: implication in mutagenesis and repair activity. *Photochemistry and Photobiology*, *62*(1), 44–50.

Kim, S. H., Ganji, M., Kim, E., van der Torre, J., Abbondanzieri, E., & Dekker, C. (2018). DNA sequence encodes the position of DNA supercoils. *Elife*, *7*, e36557.

Kim, Y.-J., Park, J., Lee, J. Y., & Kim, D.-N. (2021). Programming ultrasensitive threshold response through chemomechanical instability. *Nature Communications*, *12*(1), 1–8.

Klein, T., Mindek, P., Autin, L., Goodsell, D. S., Olson, A. J., Gröller, E., & Viola, I. (2019). Parallel generation and visualization of bacterial genome

structures. In *Computer graphics forum* (Vol. 38, pp. 57–68).

Knips, A., & Zacharias, M. (2015). Influence of a cis, syn-cyclobutane pyrimidine dimer damage on DNA conformation studied by molecular dynamics simulations. *Biopolymers*, *103*(4), 215–222.

Kosuri, P., Altheimer, B. D., Dai, M., Yin, P., & Zhuang, X. (2019). Rotation tracking of genome-processing enzymes using DNA origami rotors. *Nature*, *572*(7767), 136–140.

Kriegel, F., Ermann, N., Forbes, R., Dulin, D., Dekker, N. H., & Lipfert, J. (2017). Probing the salt dependence of the torsional stiffness of DNA by multiplexed magnetic torque tweezers. *Nucleic Acids Research*, *45*(10), 5920–5929.

Kusakabe, M., Onishi, Y., Tada, H., Kurihara, F., Kusao, K., Furukawa, M., ... Sugasawa, K. (2019). Mechanism and regulation of DNA damage recognition in nucleotide excision repair. *Genes and Environment*, *41*, 1–6.

Lapham, J., Rife, J. P., Moore, P. B., & Crothers, D. M. (1997). Measurement of diffusion constants for nucleic acids by NMR. *Journal of Biomolecular NMR*, *10*(3), 255–262.

La Porta, A., & Wang, M. D. (2004). Optical torque wrench: angular trapping, rotation, and torque detection of quartz microparticles. *Physical Review Letters*, *92*(19), 190801.

Laughton, C. A., & Harris, S. A. (2011). The atomistic simulation of DNA. *Wiley Interdisciplinary Reviews: Computational Molecular Science*, *1*, 590–600.

Lepage, T., & Junier, I. (2017). Modeling bacterial DNA: simulation of self-avoiding supercoiled worm-like chains including structural transitions of the helix. In *The bacterial nucleoid* (pp. 323–337). Springer.

Li, C.-L., Golebiowski, F. M., Onishi, Y., Samara, N. L., Sugasawa, K., & Yang, W. (2015). Tripartite DNA lesion recognition and verification by XPC,

TFIIH, and XPA in nucleotide excision repair. *Molecular Cell*, *59*, 1025–1034.

Liebl, K., & Zacharias, M. (2019). How methyl–sugar interactions determine DNA structure and flexibility. *Nucleic Acids Research*, *47*(3), 1132–1140.

Liedl, T., Högberg, B., Tytell, J., Ingber, D. E., & Shih, W. M. (2010). Self-assembly of three-dimensional prestressed tensegrity structures from DNA. *Nature Nanotechnology*, *5*(7), 520–524.

Lim, W., Randisi, F., Doye, J. P., & Louis, A. A. (2022). The interplay of supercoiling and thymine dimers in DNA. *Nucleic Acids Research*, *50*(5), 2480–2492.

Lindsey-Boltz, L. A., & Sancar, A. (2007). RNA polymerase: the most specific damage recognition protein in cellular responses to DNA damage? *Proceedings of the National Academy of Sciences*, *104*(33), 13213–13214.

Lionnet, T., Joubaud, S., Lavery, R., Bensimon, D., & Croquette, V. (2006). Wringing out DNA. *Physical Review Letters*, *96*(17), 178102.

Lipfert, J., Kerssemakers, J. W., Jager, T., & Dekker, N. H. (2010). Magnetic torque tweezers: measuring torsional stiffness in DNA and recA-DNA filaments. *Nature Methods*, *7*(12), 977–980.

Litwin, T. R., Solà, M., Holt, I. J., & Neuman, K. C. (2015). A robust assay to measure DNA topology-dependent protein binding affinity. *Nucleic Acids Research*, *43*(7), e43–e43.

Liu, L. F., & Wang, J. C. (1987). Supercoiling of the DNA template during transcription. *Proceedings of the National Academy of Sciences*, *84*(20), 7024–7027.

Liu, S., Hua, Y., Wang, J., Li, L., Yuan, J., Zhang, B., … Kong, D. (2021). RNA polymerase iii is required for the repair of DNA double-strand breaks by homologous recombination. *Cell*, *184*(5), 1314–1329.

Luijsterburg, M. S., White, M. F., van Driel, R., & Dame, R. T. (2008). The major architects of chromatin: architectural proteins in bacteria, archaea and eukaryotes. *Critical Reviews in Biochemistry and Molecular Biology*, *43*(6), 393–418.

Lyubchenko, Y. L., & Shlyakhtenko, L. S. (1997). Visualization of supercoiled DNA with atomic force microscopy in situ. *Proceedings of the National Academy of Sciences*, *94*(2), 496–501.

Ma, J., Bai, L., & Wang, M. D. (2013). Transcription under torsion. *Science*, *340*(6140), 1580–1583.

Ma, J., Tan, C., & Wang, M. D. (2018). Single-molecule angular optical trapping for studying transcription under torsion. In *Molecular motors* (pp. 301–332). Springer.

Ma, J., & Wang, M. D. (2016). DNA supercoiling during transcription. *Biophysical Reviews*, *8*(1), 75–87.

Mackenzie, D. (2020). Ultraviolet light fights new virus. *Engineering (Beijing, China)*, *6*(8), 851.

Margolin, Y., Cloutier, J.-F., Shafirovich, V., Geacintov, N. E., & Dedon, P. C. (2006). Paradoxical hotspots for guanine oxidation by a chemical mediator of inflammation. *Nature Chemical Biology*, *2*(7), 365–366.

Marko, J., & Siggia, E. (1995). Statistical mechanics of supercoiled DNA. *Physical Review E*, *52*(3), 2912.

Marko, J. F. (1997). Stretching must twist DNA. *EPL (Europhysics Letters)*, *38*(3), 183.

Marko, J. F. (2005). Course 7 introduction to single-DNA micromechanics. In *Les houches* (Vol. 82, pp. 211–270). Elsevier.

Marko, J. F. (2007). Torque and dynamics of linking number relaxation in stretched supercoiled DNA. *Physical Review E*, *76*(2), 021926.

Marko, J. F. (2009). Micromechanics of single supercoiled DNA molecules. In *Mathematics of DNA structure, function and interactions* (pp. 225–249). Springer.

Marko, J. F., & Neukirch, S. (2012). Competition between curls and plectonemes near the buckling transition of stretched supercoiled DNA. *Physical Review E*, *85*(1), 011908.

Marko, J. F., & Siggia, E. D. (1994a). Bending and twisting elasticity of DNA. *Macromolecules*, *27*(4), 981–988.

Marko, J. F., & Siggia, E. D. (1994b). Fluctuations and supercoiling of DNA. *Science*, *265*(5171), 506–508.

Marko, J. F., & Siggia, E. D. (1995). Stretching DNA. *Macromolecules*, *28*(26), 8759–8770.

Matek, C. (2014). *Statistical mechanics of nucleic acids under mechanical stress.* (PhD thesis, University of Oxford). Retrieved from https://ora.ox.ac.uk/objects/uuid:ce44cf50-2001-4f54-8e57-d1757f709fd6

Matek, C., Ouldridge, T. E., Doye, J. P., & Louis, A. A. (2015). Plectoneme tip bubbles: coupled denaturation and writhing in supercoiled DNA. *Scientific Reports*, *5*(1), 1–4.

Mazur, A. K. (2006). Evaluation of elastic properties of atomistic DNA models. *Biophysical Journal*, *91*(12), 4507–4518.

McAteer, K., Jing, Y., Kao, J., Taylor, J.-S., & Kennedy, M. A. (1998). Solution-state structure of a DNA dodecamer duplex containing a cis-syn thymine cyclobutane dimer, the major UV photoproduct of DNA. *Journal of Molecular Biology*, *282*(5), 1013–1032.

McKinnon, P. J. (2016). Topoisomerases and the regulation of neural function. *Nature Reviews Neuroscience*, *17*(11), 673–679.

Mees, A., Klar, T., Gnau, P., Hennecke, U., Eker, A. P., Carell, T., & Essen, L.-O. (2004). Crystal structure of a photolyase bound to a CPD-like DNA lesion after in situ repair. *Science*, *306*(5702), 1789–1793.

Meulenbroek, E. M., Peron Cane, C., Jala, I., Iwai, S., Moolenaar, G. F., Goosen, N., & Pannu, N. S. (2013). UV damage endonuclease employs a novel dual-dinucleotide flipping mechanism to recognize different DNA lesions. *Nucleic Acids Research*, *41*(2), 1363–1371.

Miaskiewicz, K., Miller, J., Cooney, M., & Osman, R. (1996). Computational simulations of DNA distortions by a cis, syn-cyclobutane thymine dimer lesion. *Journal of the American Chemical Society*, *118*(38), 9156–9163.

Michell, J. (1889). On the stability of a bent and twisted wire. *Messenger of Mathematics*, *11*, 181–184.

Min, J.-H., & Pavletich, N. P. (2007). Recognition of DNA damage by the Rad4 nucleotide excision repair protein. *Nature*, *449*, 570–575.

Minhas, V., Sun, T., Mirzoev, A., Korolev, N., Lyubartsev, A. P., & Nordenskiöld, L. (2019). Modeling DNA flexibility: comparison of force fields from atomistic to multiscale levels. *The Journal of Physical Chemistry B*, *124*(1), 38–49.

Mirny, L., & Dekker, J. (2022). Mechanisms of chromosome folding and nuclear organization: their interplay and open questions. *Cold Spring Harbor Perspectives in Biology*, *14*(7), a040147.

Mitchell, D. L., Vaughan, J. E., & Nairn, R. S. (1989). Inhibition of transient gene expression in Chinese hamster ovary cells by cyclobutane dimers and (6-4) photoproducts in transfected ultraviolet-irradiated plasmid DNA. *Plasmid*, *21*(1), 21–30.

Mitchell, J., Laughton, C., & Harris, S. A. (2011). Atomistic simulations reveal bubbles, kinks and wrinkles in supercoiled DNA. *Nucleic Acids Research*,

39(9), 3928–3938.

Mohammed, A. M., Šulc, P., Zenk, J., & Schulman, R. (2017). Self-assembling DNA nanotubes to connect molecular landmarks. *Nature Nanotechnology*, *12*(4), 312–316.

Moroz, J. D., & Nelson, P. (1997). Torsional directed walks, entropic elasticity, and DNA twist stiffness. *Proceedings of the National Academy of Sciences*, *94*(26), 14418–14422.

Moroz, J. D., & Nelson, P. (1998). Entropic elasticity of twist-storing polymers. *Macromolecules*, *31*(18), 6333–6347.

Mosconi, F., Allemand, J. F., Bensimon, D., & Croquette, V. (2009). Measurement of the torque on a single stretched and twisted DNA using magnetic tweezers. *Physical Review Letters*, *102*(7), 078301.

Nathan, D., & Crothers, D. M. (2002). Bending and flexibility of methylated and unmethylated EcoRI DNA. *Journal of Molecular Biology*, *316*(1), 7–17.

Neukirch, S., & Marko, J. F. (2011). Analytical description of extension, torque, and supercoiling radius of a stretched twisted DNA. *Physical Review Letters*, *106*(13), 138104.

Neuman, K. C., & Nagy, A. (2008). Single-molecule force spectroscopy: optical tweezers, magnetic tweezers and atomic force microscopy. *Nature Methods*, *5*(6), 491–505.

Niermann, M., Bolten, M., & Eimer, W. (1999). Optimization of the hydrodynamic bead model for the analysis of DNA conformations in solution. *The Journal of Physical Chemistry B*, *103*(45), 10065–10074.

Nomidis, S., Caraglio, M., Laleman, M., Phillips, K., Skoruppa, E., & Carlon, E. (2019). Twist-bend coupling, twist waves, and the shape of DNA loops. *Physical Review E*, *100*(2), 022402.

Oberstrass, F. C., Fernandes, L. E., & Bryant, Z. (2012). Torque measurements

reveal sequence-specific cooperative transitions in supercoiled DNA. *Proceedings of the National Academy of Sciences*, *109*(16), 6106–6111.

Odijk, T. (1995). Stiff chains and filaments under tension. *Macromolecules*, *28*(20), 7016–7018.

O'Nei, L. L., & Wiest, O. (2008). Structures and energetics of base flipping of the thymine dimer depend on DNA sequence. *The Journal of Physical Chemistry B*, *112*(13), 4113–4122.

Ott, K., Martini, L., Lipfert, J., & Gerland, U. (2020). Dynamics of the buckling transition in double-stranded DNA and RNA. *Biophysical Journal*, *118*(7), 1690–1701.

Ouldridge, T. E. (2012). *Coarse-grained modelling of DNA and DNA self-assembly*. Springer Science & Business Media.

Ouldridge, T. E., Louis, A. A., & Doye, J. P. (2011). Structural, mechanical, and thermodynamic properties of a coarse-grained DNA model. *The Journal of Chemical Physics*, *134*(8), 02B627.

Ouldridge, T. E., Louis, A. A., & Doye, J. P. K. (2010). Extracting bulk properties of self-assembling systems from small simulations. *Journal of Physics: Condensed Matter*, *22*, 104102.

Park, H., Zhang, K., Ren, Y., Nadji, S., Sinha, N., Taylor, J.-S., & Kang, C. (2002). Crystal structure of a DNA decamer containing a cis-syn thymine dimer. *Proceedings of the National Academy of Sciences*, *99*(25), 15965–15970.

Parker, J. B., Bianchet, M. A., Krosky, D. J., Friedman, J. I., Amzel, L. M., & Stivers, J. T. (2007). Enzymatic capture of an extrahelical thymine in the search for uracil in DNA. *Nature*, *449*(7161), 433–437.

Pauling, L., & Corey, R. B. (1953). A proposed structure for the nucleic acids. *Proceedings of the National Academy of Sciences of the United States of*

America, *39*(2), 84.

Pearlman, D. A., Holbrook, S. R., Pirkle, D. H., & Kim, S.-H. (1985). Molecular models for DNA damaged by photoreaction. *Science*, *227*(4692), 1304–1308.

Pérez, A., Castellazzi, C. L., Battistini, F., Collinet, K., Flores, O., Deniz, O., ... others (2012). Impact of methylation on the physical properties of DNA. *Biophysical Journal*, *102*(9), 2140–2148.

Pérez, A., Marchán, I., Svozil, D., Sponer, J., Cheatham III, T. E., Laughton, C. A., & Orozco, M. (2007). Refinement of the AMBER force field for nucleic acids: improving the description of α/γ conformers. *Biophysical Journal*, *92*(11), 3817–3829.

Pincet, F., & Husson, J. (2005). The solution to the streptavidin-biotin paradox: the influence of history on the strength of single molecular bonds. *Biophysical Journal*, *89*(6), 4374–4381.

Poetsch, A. R. (2020). The genomics of oxidative DNA damage, repair, and resulting mutagenesis. *Computational and Structural Biotechnology Journal*, *18*, 207–219.

Poppleton, E., Bohlin, J., Matthies, M., Sharma, S., Zhang, F., & Šulc, P. (2020). Design, optimization and analysis of large DNA and RNA nanostructures through interactive visualization, editing and molecular simulation. *Nucleic Acids Research*, *48*(12), e72–e72.

Postow, L., Hardy, C. D., Arsuaga, J., & Cozzarelli, N. R. (2004). Topological domain structure of the Escherichia coli chromosome. *Genes & Development*, *18*, 1766–1779.

Potoyan, D. A., Savelyev, A., & Papoian, G. A. (2013). Recent successes in coarse-grained modeling of DNA. *Wiley Interdisciplinary Reviews: Computational Molecular Science*, *3*(1), 69–83.

Protić-Sabljić, M., & Kraemer, K. H. (1985). One pyrimidine dimer inactivates expression of a transfected gene in xeroderma pigmentosum cells. *Proceedings of the National Academy of Sciences*, *82*(19), 6622–6626.

Pyne, A. L., Noy, A., Main, K. H., Velasco-Berrelleza, V., Piperakis, M. M., Mitchenall, L. A., … others (2021). Base-pair resolution analysis of the effect of supercoiling on DNA flexibility and major groove recognition by triplex-forming oligonucleotides. *Nature Communications*, *12*(1), 1–12.

Qu, H., Wang, Y., Tseng, C.-Y., & Zocchi, G. (2011). Critical torque for kink formation in double-stranded DNA. *Physical Review X*, *1*(2), 021008.

Qu, H., & Zocchi, G. (2011). The complete bending energy function for nicked DNA. *EPL (Europhysics Letters)*, *94*(1), 18003.

Racko, D., Benedetti, F., Dorier, J., Burnier, Y., & Stasiak, A. (2015). Generation of supercoils in nicked and gapped DNA drives DNA unknotting and postreplicative decatenation. *Nucleic Acids Research*, *43*(15), 7229–7236.

Randisi, F. (2019). *Theory and simulation of twisted DNA duplexes.* (PhD thesis, University of Oxford). Retrieved from https://ora.ox.ac.uk/objects/uuid:1b8cf9be-8034-4aed-b488-35e7a3c7c97f

Rao, S. N., Keepers, J. W., & Koliman, P. (1984). The structure of d (CGCGAAT [] TCGCG)-d (CGCGAATTCGCG): the incorporation of a thymine photodimer into a b-DNA helix. *Nucleic Acids Research*, *12*(11), 4789–4807.

Rhodes, D., & Klug, A. (1980). Helical periodicity of DNA determined by enzyme digestion. *Nature*, *286*(5773), 573–578.

Rohs, R., Jin, X., West, S. M., Joshi, R., Honig, B., & Mann, R. S. (2010). Origins of specificity in protein-DNA recognition. *Annual Review of Biochemistry*, *79*, 233–269.

Rovigatti, L., Šulc, P., Reguly, I. Z., & Romano, F. (2015). A comparison between parallelization approaches in molecular dynamics simulations on

GPUs. *Journal of Computational Chemistry*, *36*(1), 1–8.

Rybenkov, V. V., Vologodskii, A. V., & Cozzarelli, N. R. (1997). The effect of ionic conditions on DNA helical repeat, effective diameter and free energy of supercoiling. *Nucleic Acids Research*, *25*(7), 1412–1418.

Salerno, D., Tempestini, A., Mai, I., Brogioli, D., Ziano, R., Cassina, V., & Mantegazza, F. (2012). Single-molecule study of the DNA denaturation phase transition in the force-torsion space. *Physical Review Letters*, *109*(11), 118303.

Sancar, A. (2003). Structure and function of DNA photolyase and cryptochrome blue-light photoreceptors. *Chemical Reviews*, *103*(6), 2203–2238.

Sanij, E., Hannan, K. M., Yan, S., Xuan, J., Ahern, J. E., Chan, K. T., ... others (2019). Inhibition of RNA polymerase i transcription activates targeted DNA damage response and enhances the efficacy of PARP inhibitors in high-grade serous ovarian cancer. *bioRxiv*, 621623.

Sankararaman, S., & Marko, J. F. (2005). Formation of loops in DNA under tension. *Physical Review E*, *71*(2), 021911.

Schelvis, J. P., Zhu, X., & Gindt, Y. M. (2015). Enzyme–substrate binding kinetics indicate that photolyase recognizes an extrahelical cyclobutane thymidine dimer. *Biochemistry*, *54*(40), 6176–6185.

Schiffels, D., Liedl, T., & Fygenson, D. K. (2013). Nanoscale structure and microscale stiffness of DNA nanotubes. *ACS Nano*, *7*(8), 6700–6710.

Schlick, T., & Olson, W. K. (1992). Supercoiled DNA energetics and dynamics by computer simulation. *Journal of Molecular Biology*, *223*(4), 1089–1119.

Schneider, P. (2003). Endovascular skills: guidewire and catheter skills for endovascular surgery, 2003. *NY: Dekker, New York*.

Schvartzman, J. B., Martínez-Robles, M.-L., Hernández, P., & Krimer, D. B. (2013). The benefit of DNA supercoiling during replication. *Biochemical*

Society Transactions, *41*(2), 646–651.

Seeman, N. C., & Sleiman, H. F. (2017). DNA nanotechnology. *Nature Reviews Materials*, *3*(1), 1–23.

Seibert, E., Ross, J. A., & Osman, R. (2003). Contribution of opening and bending dynamics to specific recognition of DNA damage. *Journal of Molecular Biology*, *330*(4), 687–703.

Sengar, A., Ouldridge, T. E., Henrich, O., Rovigatti, L., & Šulc, P. (2021). A primer on the oxDNA model of DNA: When to use it, how to simulate it and how to interpret the results. *Frontiers in Molecular Biosciences*, *8*.

Sharma, M., Predeus, A. V., Mukherjee, S., & Feig, M. (2013). DNA bending propensity in the presence of base mismatches: implications for DNA repair. *The Journal of Physical Chemistry B*, *117*(20), 6194–6205.

Sheinin, M. Y., Li, M., Soltani, M., Luger, K., & Wang, M. D. (2013). Torque modulates nucleosome stability and facilitates H2A/H2B dimer loss. *Nature Communications*, *4*(1), 1–8.

Sinden, R. R., Carlson, J. O., & Pettijohn, D. E. (1980). Torsional tension in the DNA double helix measured with trimethylpsoralen in living E. coli cells: analogous measurements in insect and human cells. *Cell*, *21*(3), 773–783.

Sinden, R. R., & Pettijohn, D. E. (1981). Chromosomes in living Escherichia coli cells are segregated into domains of supercoiling. *Proceedings of the National Academy of Sciences*, *78*(1), 224–228.

Sinha, R. P., & Häder, D.-P. (2002). Uv-induced DNA damage and repair: a review. *Photochemical & Photobiological Sciences*, *1*(4), 225–236.

Skoko, D., Yan, J., Johnson, R. C., & Marko, J. F. (2005). Low-force DNA condensation and discontinuous high-force decondensation reveal a loop-stabilizing function of the protein Fis. *Physical Review Letters*, *95*(20), 208101.

Skoko, D., Yoo, D., Bai, H., Schnurr, B., Yan, J., McLeod, S. M., ... Johnson, R. C. (2006). Mechanism of chromosome compaction and looping by the Escherichia coli nucleoid protein Fis. *Journal of Molecular Biology*, *364*(4), 777–798.

Skoruppa, E., Laleman, M., Nomidis, S. K., & Carlon, E. (2017). DNA elasticity from coarse-grained simulations: The effect of groove asymmetry. *The Journal of Chemical Physics*, *146*(21), 214902.

Smith, S. B., Finzi, L., & Bustamante, C. (1992). Direct mechanical measurements of the elasticity of single DNA molecules by using magnetic beads. *Science*, *258*(5085), 1122–1126.

Snodin, B. E., Randisi, F., Mosayebi, M., Šulc, P., Schreck, J. S., Romano, F., ... others (2015). Introducing improved structural properties and salt dependence into a coarse-grained model of DNA. *The Journal of Chemical Physics*, *142*(23), 06B613_1.

Snodin, B. E., Romano, F., Rovigatti, L., Ouldridge, T. E., Louis, A. A., & Doye, J. P. (2016). Direct simulation of the self-assembly of a small DNA origami. *ACS Nano*, *10*(2), 1724–1737.

Snodin, B. E. K., Schreck, J. S., Romano, F., Louis, A. A., & Doye, J. P. K. (2019). Coarse-grained modelling of the structural properties of DNA origami. *Nucleic Acids Research*, *47*, 1585–1597.

Šponer, J., Riley, K. E., & Hobza, P. (2008). Nature and magnitude of aromatic stacking of nucleic acid bases. *Physical Chemistry Chemical Physics*, *10*(19), 2595–2610.

Stigter, D. (1975). The charged colloidal cylinder with a Gouy double layer. *Journal of Colloid and Interface Science*, *53*(2), 296–306.

Strick, T., Allemand, J.-F., Bensimon, D., & Croquette, V. (1998). Behavior of supercoiled DNA. *Biophysical Journal*, *74*(4), 2016–2028.

Strick, T., Dessinges, M., Charvin, G., Dekker, N., Allemand, J., Bensimon, D., & Croquette, V. (2002). Stretching of macromolecules and proteins. *Reports on Progress in Physics*, *66*(1), 1.

Sugasawa, K. (2016). Molecular mechanisms of DNA damage recognition for mammalian nucleotide excision repair. *DNA Repair*, *44*, 110–117.

Šulc, P., Romano, F., Ouldridge, T. E., Rovigatti, L., Doye, J. P., & Louis, A. A. (2012). Sequence-dependent thermodynamics of a coarse-grained DNA model. *The Journal of Chemical Physics*, *137*(13), 135101.

Swan, R. L., Cowell, I. G., & Austin, C. A. (2022). Mechanisms to repair stalled Topoisomerase ii-DNA covalent complexes. *Molecular Pharmacology*, *101*(1), 24–32.

Swope, W. C., Andersen, H. C., Berens, P. H., & Wilson, K. R. (1982). A computer simulation method for the calculation of equilibrium constants for the formation of physical clusters of molecules: Application to small water clusters. *The Journal of Chemical Physics*, *76*(1), 637–649.

Taylor, J. S., Garrett, D. S., Brockie, I. R., Svoboda, D. L., & Telser, J. (1990). Proton NMR assignment and melting temperature study of cis-syn and trans-syn thymine dimer containing duplexes of d(cgtattatgc)·d(gcataatacg). *Biochemistry*, *29*, 8858–8866.

Tempestini, A., Cassina, V., Brogioli, D., Ziano, R., Erba, S., Giovannoni, R., … Mantegazza, F. (2013). Magnetic tweezers measurements of the nanomechanical stability of DNA against denaturation at various conditions of pH and ionic strength. *Nucleic Acids Research*, *41*(3), 2009–2019.

ten Heggeler-Bordier, B., Wahli, W., Adrian, M., Stasiak, A., & Dubochet, J. (1992). The apical localization of transcribing RNA polymerases on supercoiled DNA prevents their rotation around the template. *The EMBO Journal*, *11*, 667–672.

Thompson, J., Silveira, M., Van der Heijden, G., & Wiercigroch, M. (2012). Helical post-buckling of a rod in a cylinder: with applications to drill-strings. *Proceedings of the Royal Society A: Mathematical, Physical and Engineering Sciences*, *468*(2142), 1591–1614.

Thompson, J. M. T. (2017). Instabilities of elastic and spinning systems: concepts and phenomena. *International Journal of Bifurcation and Chaos*, *27*(09), 1730029.

Tripathi, S., Brahmachari, S., Onuchic, J. N., & Levine, H. (2021). DNA supercoiling-mediated collective behavior of co-transcribing RNA polymerases. *bioRxiv*.

Tseng, Y., Lee, J. S., Kole, T. P., Jiang, I., & Wirtz, D. (2004). Micro-organization and visco-elasticity of the interphase nucleus revealed by particle nanotracking. *Journal of Cell Science*, *117*(10), 2159–2167.

Tullius, T. D., & Dombroski, B. A. (1985). Iron (ii) EDTA used to measure the helical twist along any DNA molecule. *Science*, *230*(4726), 679–681.

van den Broek, B., Lomholt, M. A., Kalisch, S.-M., Metzler, R., & Wuite, G. J. (2008). How DNA coiling enhances target localization by proteins. *Proceedings of the National Academy of Sciences*, *105*(41), 15738–15742.

van Loenhout, M. T., De Grunt, M., & Dekker, C. (2012). Dynamics of DNA supercoils. *Science*, *338*(6103), 94–97.

Velmurugu, Y., Chen, X., Sevilla, P. S., Min, J.-H., & Ansari, A. (2016). Twist-open mechanism of DNA damage recognition by the Rad4/XPC nucleotide excision repair complex. *Proceedings of the National Academy of Sciences*, *113*(16), E2296–E2305.

Veloso, A., Kirkconnell, K. S., Magnuson, B., Biewen, B., Paulsen, M. T., Wilson, T. E., & Ljungman, M. (2014). Rate of elongation by RNA polymerase ii is associated with specific gene features and epigenetic modifications.

Genome Research, *24*(6), 896–905.

Verdine, G. L., & Bruner, S. D. (1997). How do DNA repair proteins locate damaged bases in the genome? *Chemistry & Biology*, *4*(5), 329–334.

Verma, S. C., Qian, Z., & Adhya, S. L. (2019). Architecture of the Escherichia coli nucleoid. *PLOS Genetics*, *15*, e1008456.

Vilfan, I. D., Lipfert, J., Koster, D., Lemay, S., & Dekker, N. (2009). Magnetic tweezers for single-molecule experiments. *Handbook of Single-molecule Biophysics*, 371–395.

Vinograd, J., Lebowitz, J., Radloff, R., Watson, R., & Laipis, P. (1965). The twisted circular form of polyoma viral DNA. *Proceedings of the National Academy of Sciences of the United States of America*, *53*(5), 1104.

Visser, B. J., Sharma, S., Chen, P. J., McMullin, A. B., Bates, M. L., & Bates, D. (2022). Psoralen mapping reveals a bacterial genome supercoiling landscape dominated by transcription. *Nucleic Acids Research*, *50*(8), 4436–4449.

Vologodskii, A., & D. Frank-Kamenetskii, M. (2013). Strong bending of the DNA double helix. *Nucleic Acids Research*, *41*(14), 6785–6792.

Vologodskii, A. V., & Cozzarelli, N. R. (1994). Conformational and thermodynamic properties of supercoiled DNA. *Annual Review of Biophysics and Biomolecular Structure*, *23*(1), 609–643.

Wang, C.-I., & Taylor, J.-S. (1991). Site-specific effect of thymine dimer formation on dAn. dTn tract bending and its biological implications. *Proceedings of the National Academy of Sciences*, *88*(20), 9072–9076.

Wang, J. C. (1979). Helical repeat of DNA in solution. *Proceedings of the National Academy of Sciences*, *76*(1), 200–203.

Wang, M. D., Schnitzer, M. J., Yin, H., Landick, R., Gelles, J., & Block, S. M. (1998). Force and velocity measured for single molecules of RNA poly-

merase. *Science*, *282*(5390), 902–907.

Wang, M. D., Yin, H., Landick, R., Gelles, J., & Block, S. M. (1997). Stretching DNA with optical tweezers. *Biophysical Journal*, *72*(3), 1335–1346.

Wei, B., Dai, M., & Yin, P. (2012). Complex shapes self-assembled from single-stranded DNA tiles. *Nature*, *485*(7400), 623–626.

Whitelam, S., & Geissler, P. L. (2007). Avoiding unphysical kinetic traps in Monte Carlo simulations of strongly attractive particles. *The Journal of Chemical Physics*, *127*(15), 154101.

Wilson, T. J., Crystal, M. A., Rohrbaugh, M. C., Sokolowsky, K. P., & Gindt, Y. M. (2011). Evidence from thermodynamics that DNA photolyase recognizes a solvent-exposed CPD lesion. *The Journal of Physical Chemistry B*, *115*(46), 13746–13754.

Witz, G., & Stasiak, A. (2010). DNA supercoiling and its role in DNA decatenation and unknotting. *Nucleic Acids Research*, *38*(7), 2119–2133.

Wong, C. K., Tang, C., Schreck, J. S., & Doye, J. P. (2022). Characterizing the free-energy landscapes of dna origamis. *Nanoscale*, *14*(7), 2638–2648.

Wu, H.-Y., Shyy, S., Wang, J. C., & Liu, L. F. (1988). Transcription generates positively and negatively supercoiled domains in the template. *Cell*, *53*(3), 433–440.

Yan, Y., Ding, Y., Leng, F., Dunlap, D., & Finzi, L. (2018). Protein-mediated loops in supercoiled DNA create large topological domains. *Nucleic Acids Research*, *46*(9), 4417–4424.

Zakharova, S. S., Jesse, W., Backendorf, C., Egelhaaf, S. U., Lapp, A., & van der Maarel, J. R. (2002). Dimensions of plectonemically supercoiled DNA. *Biophysical Journal*, *83*(2), 1106–1118.

Zhabinskaya, D., & Benham, C. J. (2011). Theoretical analysis of the stress induced BZ transition in superhelical DNA. *PLoS Computational Biology*,

7(1), e1001051.

Zhang, C., Guttula, D., Liu, F., Malar, P. P., Ng, S. Y., Dai, L., ... Van Der Maarel, J. R. (2013). Effect of H-NS on the elongation and compaction of single DNA molecules in a nanospace. *Soft Matter*, *9*(40), 9593–9601.

Zhao, D., Liu, S., & Gao, Y. (2018). Single-molecule manipulation and detection. *Acta Biochimica et Biophysica Sinica*, *50*(3), 231–237.

Zhu, X., Ng, S. Y., Gupta, A. N., Feng, Y. P., Ho, B., Lapp, A., ... others (2010). Effect of crowding on the conformation of interwound DNA strands from neutron scattering measurements and Monte Carlo simulations. *Physical Review E*, *81*(6), 061905.

A | Appendix

A.1 DNA sequence used in the thymine dimer simulations

The position of the thymine dimer is indicated by circumflexes on the relevant thymines.

3'-AAGCCGGCCACGCGCTGTTCGGCCGGCATTTACACCAAACAGATTG
TCAGGAACTGTATCTTAGCTCCCGTTTCTGGACTTACGTGCTCAGGTGG
AAAACCTGGTAGACCTAACCGGACTCTACGCTTATGCCAGGGCAATCTT
CAACGATAGCTTTCCCTAGGCGGCTATAATCCACCCTACCTGTTT̂T̂TGGT
TCGAGGTCACGGATTCAAGATCTTGTCGGATACGGCGCGCGAGTCCACG
AGCCCTCGTTAGTTGTCCTCGCGGGAATAGCCGACGATTAATCTGAAAC
CGCCGTCGGGTCTCGTGATAGCTACATCGGTGGATAAACTTCCTAGGCG
CTAAGTCCACACACGCGCGCCCTATAGATGAGGACCACCAAGTCGAACC
GTGCGAATCGTCCGAGAATTCCCCCAACGACAAAATTTCGTGCGAAACG
GTTGCTAAAGGAATAAATGCGTCAGAGCGATTTAGGGGACCCCGCCCGT
GGTTTGGTAGGCTGTTGATTTCTTTCAGACTGTAAGGACCGGCCCAGCT
CTGCGAAGTGTGCTCGCTAGCCGGCACCGAAGACATACATTAAATGGAC
ACCCGGGAAGACGA-5'

A.2 Formula for the rate of change of end-to-end extension with the number of imposed turns

$$\frac{dL}{dN} = \frac{2\pi \left[1 - \frac{1}{2}\left(\frac{k_B T}{pF}\right)^{1/2} - \frac{C^2 P g \left(\frac{k_B T}{pF}\right)^{3/2}}{8(C_s k_B T)^2 \left(1 - \frac{P}{C_s}\right)}\right]}{\left[\frac{2Pg}{1-\frac{P}{C_s}}\right]^{1/2} \times \left(\frac{1}{P} - \frac{1}{C_s}\right)} \tag{A.1}$$

In Eq. A.1, g is the negative free energy of stretched and nicked (freely swiveling) DNA:

$$g = F - \left(\frac{k_B T \times F}{p}\right)^{1/2} \tag{A.2}$$

A.3 Parameters used in the theoretical treatment of tip-bubble plectonemes

Table A.1: List of parameters for negatively supercoiled dsDNA

	Value used	**Remarks**
DNA Torsional Modulus C	92 $k_{\mathrm{B}}T$nm	salt-dependent
Canonical Length of DNA L_0	199 nm	600 bps
Run initiation energy a	5 $k_{\mathrm{B}}T$	
Denaturation energy at run's edge b	25 $k_{\mathrm{B}}T$	
Bending persistence length p	45 nm	salt-dependent
Plectonemic Twist Stiffness P	23 $k_{\mathrm{B}}T$nm	salt-dependent
Helical pitch d	3.5 nm	
Measure of defect a_d	0.3	
Shape factor for plectonemic loop energy ρ_0	16	teardrop loop
Maximum value of kink parameter ϵ_m	0.4	

Table A.2: List of parameters for positively supercoiled dsDNA

	Value used	**Remarks**
P-DNA run initiation energy a_P	5 $k_{\mathrm{B}}T$	
P-DNA conversion energy at run's edge b_P	75 $k_{\mathrm{B}}T$	
Measure of defect ϵ_R	0.21	salt-dependent
Kink energy α_R	14 $k_{\mathrm{B}}T$	

A.4 Torque response curve of twist-induced denaturation

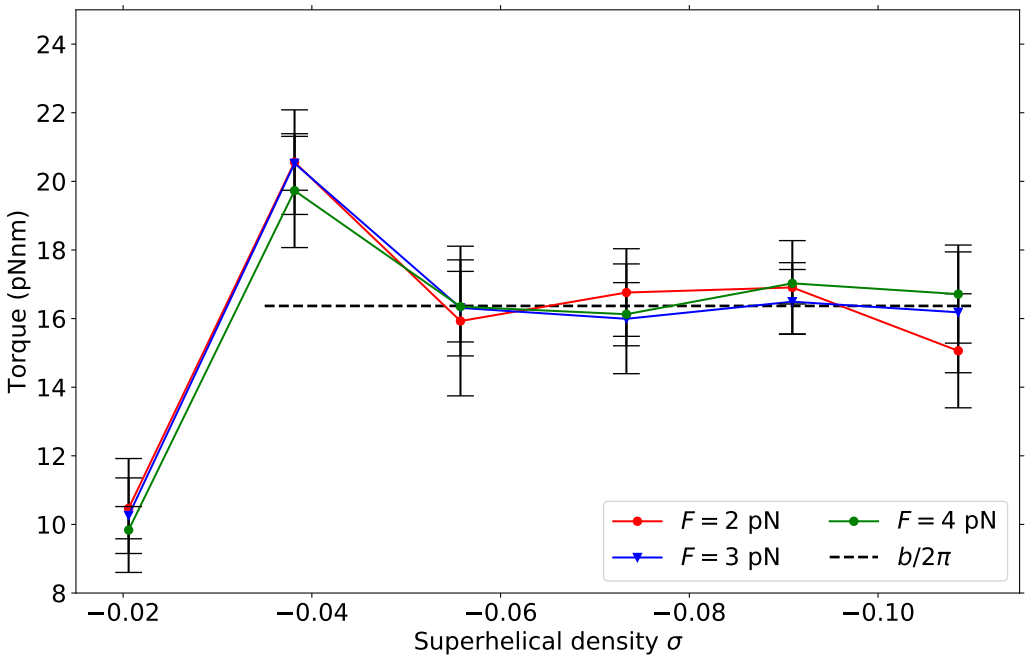


Figure A.1: Denaturation torque response curve of dsDNA with average-sequence oxDNA parameters. Compared to Fig. 4.5, the torque response curve obtained using average-sequence parameters shows a more distinct torque overshoot. Error bars represent SEM.

A.5 Sensitivity analysis

We vary the plectonemic twist stiffness P, torsional constant C and the measure of defect a_d to study their effects on the lower characteristic force F_{lc} (Eq. 4.18) and the bubble/tip-bubble boundary.

Reported values of the plectonemic twist stiffness P vary widely. Magnetic tweezer experiments by Kriegel *et al.* reported a P of 20 ± 4 $k_{\mathrm{B}}T$nm (Kriegel et al., 2017) for salt concentrations similar to the one used in our simulations while results from Brutzer *et al.* suggest a higher P of approximately 26 $k_{\mathrm{B}}T$nm at 100 mM Na^+ (Brutzer et al., 2010). Based on these reports, we choose to vary P from 20 $k_{\mathrm{B}}T$nm to 26 $k_{\mathrm{B}}T$nm for our analysis while keeping other parameters in the model fixed. Fig. A.2 shows the variation of F_{lc} with P for our dsDNA system at $\sigma \approx -0.073$. For the given range of P, the numerical value of the lower characteristic force remains a reasonable fit with the simulation results presented in Fig. 4.8.

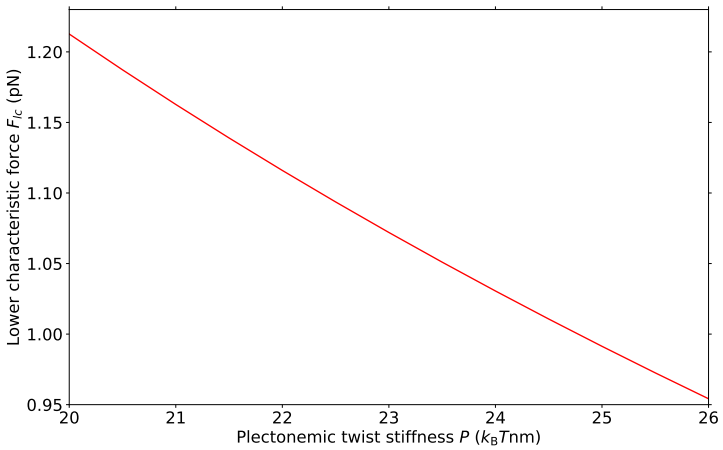


Figure A.2: Variation of the lower characteristic force F_{lc} with the plectonemic twist stiffness P.

The torsional modulus C of DNA at 100 mM NaCl has been experimentally mea-

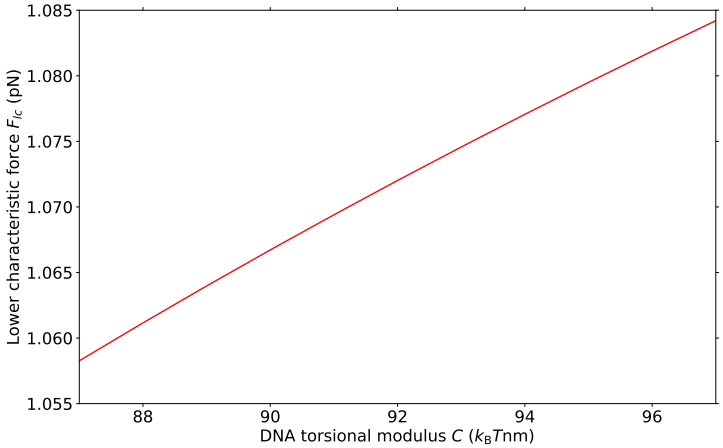


Figure A.3: Variation of the lower characteristic force F_{lc} with the torsional modulus C. Relative to its variation with P, the lower characteristic force is not as numerically sensitive to changes in C.

sured to be 94 ± 7 $k_BT$nm (Mosconi et al., 2009). This gives us a basis to study the variation in the lower characteristic force within the given margins of error in C. Fig. A.3 shows that the lower characteristic force is numerically less sensitive to changes in C compared to that of P. Next, we examine F_{lc}'s sensitivity to a_d.

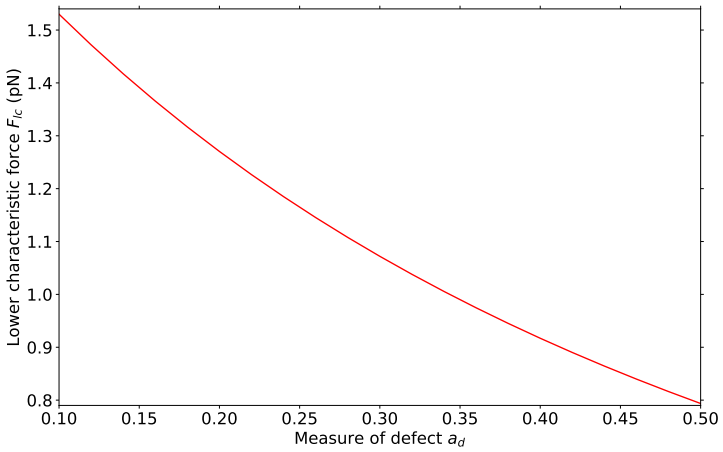


Figure A.4: Variation of F_{lc} with a_d. F_{lc} increases with a decreasing a_d. The theoretical value of F_{lc} fits well with our simulation results when a_d lies within the range of 0.25–0.5.

It is unclear what a good choice of a_d should be given the scarcity of relevant

experimental and simulation data. Measurements by Brahmachari *et al.* suggest that the value of a_d ranges from 0.35 if $N_d = 1$ represents 6 denatured base pairs to 0.45 if $N_d = 1$ represents 8 denatured base pairs (Brahmachari et al., 2018). However, these values of a_d were obtained using a much higher monovalent salt concentration than ours. oxDNA simulations of a system closer to our simulation set-up yield a range of 0.39 (6 denatured bps) to 0.52 (8 denatured bps) for a_d (P. R. Desai et al., 2020). These measurements provide us with an appropriate range of a_d to analyse F_{lc}'s sensitivity to the parameter. From Fig. A.4, we observe that the value of F_{lc} increases with a decreasing a_d. The theoretical value of F_{lc} remains a decent fit to our simulation results when a_d lies within the range of 0.25–0.5. We also examine how the theoretical bubble/tip-bubble boundary changes with a_d. Fig. A.5 shows that the gradient of the transition curve becomes more negative as the value of a_d decreases.

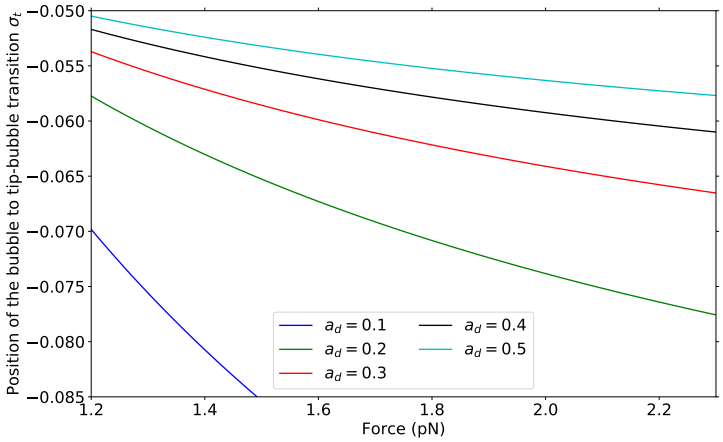


Figure A.5: a_d controls the slope of the bubble/tip-bubble boundary curve in the force-torsion space of negatively supercoiled dsDNA.

A.6 Alternative formulation of the free energy expression for tip-bubble plectoneme

Here, we present an alternative version to Eq. 4.14 for the tip-bubble plectoneme based on Salerno's model of DNA denaturation (i.e. Eq. 4.8):

$$\begin{aligned} E_{tip} =& \frac{1}{2}\frac{C_s}{L_0}(2\pi)^2(N - N_d - N_p)^2 + \alpha N_d \\ &+ 2(1 - a_d N_d)\sqrt{\rho_0 p k_{\mathrm{B}} T F} + E_{tail}(N_p - 1) + \Delta S \end{aligned} \tag{A.3}$$

The definitions of the terms used in Eq. A.3 remain the same as before. The entropic term ΔS is crucial when we consider defect-pinned plectonemes or tip-bubble plectonemes. To derive the state boundaries that involve tip-bubble plectonemes, we minimise Eq. A.3 with respect to N_d:

$$\frac{C_s}{L_0}(2\pi)^2(N - N_d - N_p) = \alpha - 2a_d N_d \sqrt{\rho_0 p k_{\mathrm{B}} T F} \tag{A.4}$$

At the state boundary between plectonemes and tip-bubble plectonemes, we match Eq. 4.5 with Eq. A.4 (i.e. set $N_p = \bar{N}_p$). This gives us:

$$N_d = \frac{E_{tail} - (\alpha - 2a_d\sqrt{\rho_0 p k_{\mathrm{B}} T F})}{\frac{C_s}{L_0}(2\pi)^2} \tag{A.5}$$

Eq. A.5 provides a physically intuitive description of the origin of tip-bubbles. For tip-bubbles to form (i.e. N_d is positive), E_{tail} has to be larger than $\alpha - 2a_d\sqrt{\rho_0 p k_{\mathrm{B}} T F}$. As such, the boundary between plectonemes and tip-bubble plectonemes is given by:

$$E_{tail} = \alpha - a_d E_{loop} \tag{A.6}$$

A.7 Denaturation transition point for dsDNA with defect X

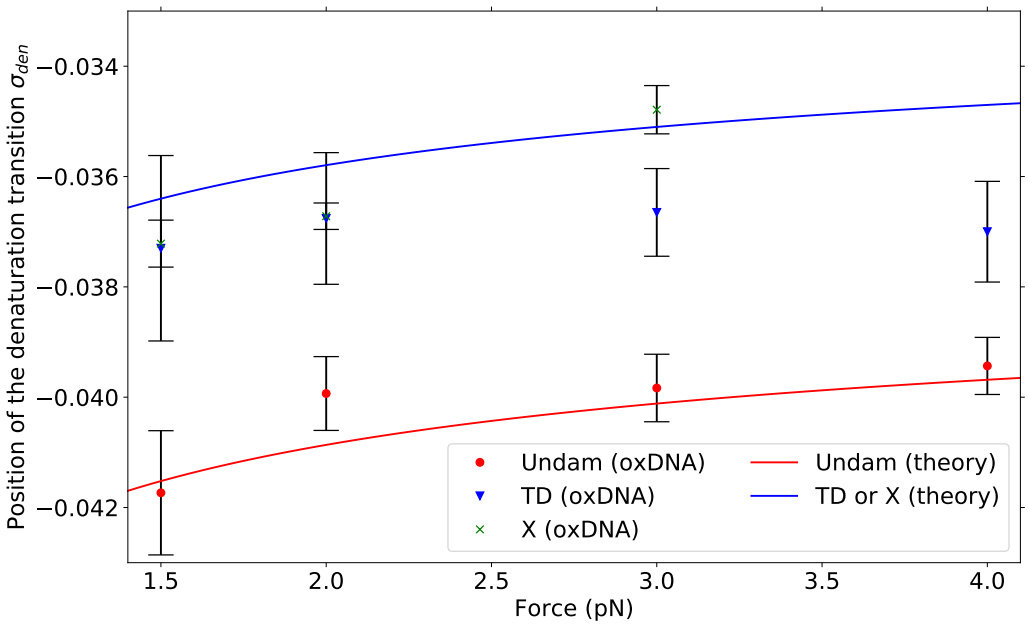


Figure A.6: The shift in the denaturation transition point for defect X-containing dsDNA is similar to that of the TD-containing dsDNA at $F \leq 2$ pN. This justifies the use of $\Delta a = 3\,k_{\mathrm{B}}T$ for defect X-containing dsDNA.

A.8 Supplementary data for bacterial nucleoid simulations

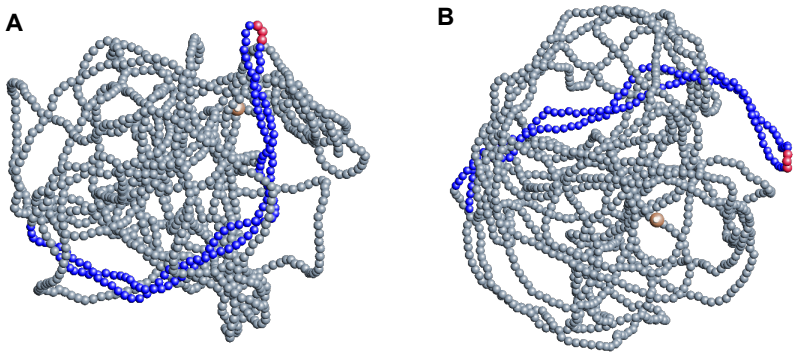


Figure A.7: Snapshots of defect localisation at a plectoneme tip in a nucleoid system with an (A) RNAP rotation period of 1×10^5 TEP units, and (B) RNAP rotation period of 1×10^6 TEP units. In (A), the snapshot was taken when the RNAP has made 300 rotations. In (B), the RNAP has made approximately 50 rotations.

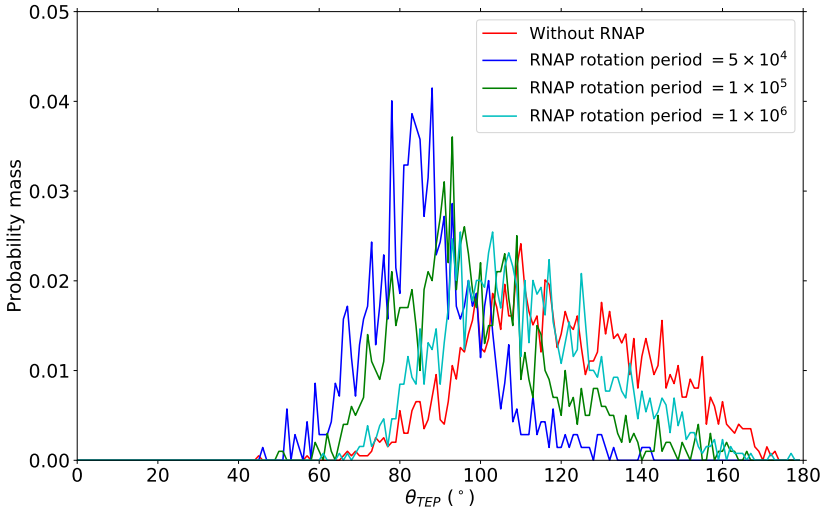


Figure A.8: Effect of RNAP rotation period on the θ_{TEP} distributions for nucleoid systems. As the rotational speed increases, the defect-containing end-loop becomes tighter in size. This effect is evident in the shift in the peak of the θ_{TEP} distribution to lower angular values.